optica

optica

In situ spectroscopic characterization of a terahertz resonant cavity

KIMBERLY S. REICHEL,[1] KRZYSZTOF IWASZCZUK,[2] PETER U. JEPSEN,[2] RAJIND MENDIS,[1] AND DANIEL M. MITTLEMAN[1,*]

[1]Department of Electrical and Computer Engineering, Rice University, MS-378, Houston, Texas 77005, USA

[2]DTU Fotonik, Technical University of Denmark, DK-2800 Kongens Lyngby, Denmark

*Corresponding author: daniel@rice.edu

In many cases, the characterization of the frequency-dependent electric field profile inside a narrowband resonator is challenging, either due to limited optical access or to the perturbative effects of invasive probes. An isolated groove inside a terahertz parallel-plate waveguide provides an opportunity to overcome these challenges, as it forms a narrowband resonator and also offers direct access to the resonant cavity via the open sides of the waveguide. We characterize the spatially varying spectral response of such a resonator using a noninvasive probe. We observe a frequency-dependent field enhancement, which varies depending on the location of the probe within the cavity. This spectral dependence cannot be observed using conventional far-field measurements. © 2014 Optical Society of America

High quality-factor (Q) resonators are important in many areas of optics [1]. In nearly all cases, the characterization of such resonators takes place in the far field, although a few measurements of near-field emission have been reported at optical [2,3] and microwave [4] frequencies in photonic crystal cavity resonators. Even in these cases, the near-field measurement technique is generally invasive, since it often involves a scattering tip or tapered optical fiber immersed in the near field of the resonator. This can perturb the field distribution under study [5], and can even lead to frequency-dependent filtering that obscures the spectral response of the object under study [6]. It is very rare to find examples of an artificial high-Q cavity

being probed noninvasively and *in situ*. Yet, this type of measurement can give new information that is not available in the far field. In this Letter, we experimentally access and characterize a resonant cavity *in situ*, in the terahertz (THz) range, without perturbing the field distribution inside the cavity. We show that these results give new information on the frequency-dependent field enhancement that goes beyond what can be inferred from far-field measurements.

Typically, information about the internal dynamics of a resonator can be accessed only via numerical simulation, with experimental studies limited to the region outside the resonator (e.g., see Fig. 1). Our method for noninvasive *in situ* probing is inspired by a novel adaptation of the air-biased coherent detection (ABCD) technique [7] for measuring high-field terahertz transients. Recently, ABCD has been used to characterize the electric field distribution inside an adiabatically tapered THz parallel-plate waveguide (PPWG) [7,8]. Here, we employ an untapered PPWG with a resonant cavity integrated into one of the plates [9,10]. We have previously studied these waveguide-integrated resonators, and characterized the high Q-factor ($Q \sim 95$) resonance [11–13] when the waveguide is excited in the TE_1 mode. By combining these resonant cavity waveguides with the ABCD technique for noninvasive detection, we are able to measure the broadband THz field *in situ*. We also present computational electromagnetic (CEM) simulations to support these experimental results.

As the platform of this experiment, we investigate PPWGs with various resonant cavity groove dimensions, including rectangular and triangular shapes. The simulations of the rectangular and triangular cavities are very similar, having a double lobe shape at the resonance as seen in Fig. 1(b), implying the measured effect is the same for either groove shape. We display results from both rectangular and triangular grooves in order to illustrate the generality of this phenomenon, which is not limited to one particular groove geometry. The orientation of the waveguide is such that the positive z direction is the forward-propagating direction and the groove is located at the $z = 0$
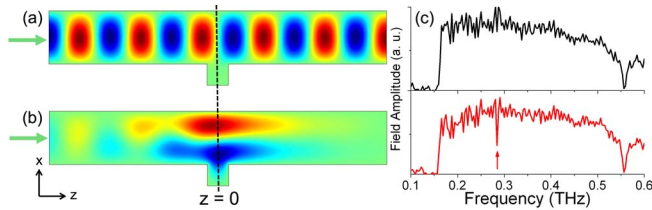
Fig. 1. Computational FEM simulation results showing electric field distribution inside a PPWG with an integrated resonant cavity. Here, the polarization is in the y direction, the plate separation is 1 mm, and the groove width and depth are 400 μm. The waveguide in (a) is excited at 300 GHz, off-resonance and (b) is excited at 295 GHz, on-resonance. The color scale is 10 times greater in (b) than (a), revealing a 10× field enhancement at the resonance. The green arrows indicate the propagation direction of the incident THz field and the dashed line indicates the center of the groove, which we define as $z = 0$. (c) Typical experimental measurement of the resonance in the far field, obtained by measurement of the total transmission through the waveguide with a groove (bottom plot, red curve), compared to one without a groove (top plot, black curve). Both curves exhibit a cutoff at $f_c = 0.15$ THz, and a strong water vapor absorption line at 0.56 THz, while the resonance indicated by a red arrow at $f_0 = 285$ GHz appears in the bottom curve attributable to the resonant cavity groove.

position (halfway along the waveguide length). We fabricate the PPWG out of aluminum with a width of 5 mm, propagation length of 9 mm, and plate separation of 1 mm. In the experiments, the measured resonant frequency may differ slightly from the simulation-predicted resonant frequency, indicating that either the plate separation is slightly larger or smaller than 1 mm or that the fabricated groove may differ from the designed dimensions [11].

To excite the waveguide, we use a near-infrared (NIR) beam from a regenerative Ti:Sapphire femtosecond laser amplifier (1 kHz, 100 fs, 800 nm) to generate broadband (50 GHz–2 THz) pulses via tilted pulse-front optical rectification in a LiNbO$_3$ crystal [14]. This radiation is coupled into the waveguide such that the polarization of the THz electric field is parallel to the plates in order to excite the TE$_1$ mode [15]. This propagating THz field is detected inside the waveguide using the ABCD method, which measures the second harmonic (400 nm) light generated from the interaction between a focused NIR probe (in this case, beam waist = 13 μm, Rayleigh range = 637 μm) and THz field in the presence of an external DC field of ±3 kV at 500 Hz, as described in Ref. [16]. As first presented in Ref. [7], the PPWG itself is used as the electrodes for the DC bias. This creates a detection region between the metal plates that enables field measurements inside the waveguide, at any position along its length. By comparing the detected second harmonic intensity at two different DC biases [8], we estimate that the peak THz field inside the waveguide is 340 kV/cm. Evidently, this all-optical method is noninvasive since it does not disturb the guided THz wave.

We carry out CEM simulations in both the frequency domain and the time domain. Figures 1(a) and 1(b) show results of the frequency-domain FEM (finite element method) simulation in the off-resonance and on-resonance case for a PPWG

with a square cavity of size 400 μm in groove width and depth. The simulation region is the air space between the two metal plates, which are represented by perfect electric conductor on the top and bottom, and scattering boundary conditions on the left and right, where the electric field is incident from the left. In the off-resonance case, we clearly see the propagation of the TE$_1$ mode, almost unperturbed by the presence of the cavity. In the on-resonance case, the electric field is strongly confined to the resonant cavity region, forming a pattern with two lobes and a node halfway between the plates. The range of the false color scale of Fig. 1(b) is 10× greater than in Fig. 1(a), showing a strong field enhancement for resonant excitation.

To explore broadband frequency-dependent effects, we also carry out time-domain FDTD (finite-difference time-domain) simulations. The same boundary conditions are used to represent the PPWG, but here we excite with a single-cycle pulse (3 dB bandwidth of 90–560 GHz) that is also polarized to excite the TE$_1$ mode. The resonance due to the groove causes a long ringing in the time domain, but we use only about a 100 ps time window so as to have a better comparison to our experiments in which the length of the measured time axis is limited by the optical delay line. The results of the time-domain simulations are compared to the experimental results, as discussed below.

We employ two different geometrical configurations to make use of ABCD. For the collinear configuration shown in Fig. 2(a), the probe is focused to a particular point within the waveguide and propagates along the same optical axis as the THz beam. This geometry achieves maximum detection of the second harmonic signal, since the polarization of the probe is parallel to the bias field [Fig. 2(c)], i.e., perpendicular to the plate surfaces [17]. In this geometry, the spatial resolution originates from the focusing of the optical probe beam, since the THz-field-assisted second harmonic radiation is largely generated at the probe beam focus where the intensity is highest. Another alternative [Fig. 2(b)] is to angle the probe beam propagation direction with respect to the THz beam. This provides improved spatial resolution along the THz propagation direction, while still maintaining the perpendicular polarization (with respect to the plate surfaces) of the probe beam. In both of these configurations, the probe beam focal point
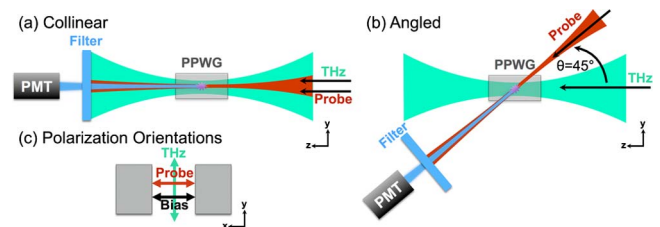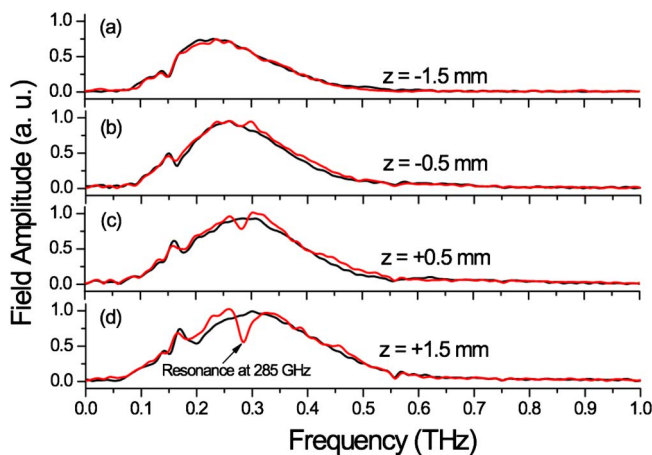

Fig. 2. Diagram of experimental detection setup probing inside the waveguide. Black arrows indicate propagation direction of the THz (green) and the NIR probe (red) beams. Focusing the probe using a 100 mm focal length lens and modified ABCD technique, the probe and THz fields interact within the bias field between the waveguide plates, generating the second harmonic at 400 nm (blue), which is filtered and detected via a photomultiplier tube (PMT). Two configurations are used: (a) collinear, and (b) angled, where $\theta = 45°$. The polarization directions of the THz, NIR, and DC bias fields are illustrated in (c).
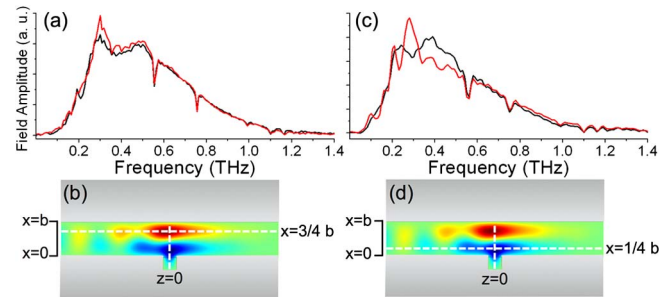
can be moved along the waveguide (z axis), and in particular can be situated in the section of the waveguide in which the groove (resonant cavity) is located. We also note that the focal spot can be translated between the two plates along the x axis to independently probe the two lobes of the resonating mode shown by the simulation in Fig. 1(b). Interestingly, the measured field enhancement factors in these two locations have different spectral behaviors.

We use the angled configuration [Fig. 2(b)] to probe along the length of the waveguide, thereby characterizing the spectral response both before and after the resonant cavity. For this experiment, we employed a PPWG with a 60° triangular groove and a depth of 265 μm, with expected resonance at $f_0 = 299$ GHz from simulation. We obtain measurements along the length of the waveguide by translating the probe beam along the propagation direction. We use a bare PPWG (without cavity) as a reference to compare to the grooved PPWG (with cavity). In Fig. 3, the measured spectra are plotted at selected positions, showing the emergence and development of the resonance. For $z < 0$, the THz pulse is measured at a spatiotemporal location such that it has not yet reached the groove at $z = 0$, and thus the spectra overlap. For $z > 0$, the pulse is measured at a later time after it has passed the resonant cavity. The cavity acts as a filter, collecting a certain narrow range of frequencies while allowing other frequencies to pass. Thus, after propagating past the groove, a narrow band of spectral components has been removed from the broadband spectrum of the incident wave, appearing as a dip in the spectra in Figs. 3(c) and 3(d). This result validates the experimental procedure and confirms that we can spatially isolate the resonant cavity with the optical probe.

To directly probe the region containing the resonant cavity, we use the collinear configuration [Fig. 2(a)]. We use the same PPWG dimensions but now with a square cavity of 400 μm width and depth that was used in Fig. 1. Again, we compare a bare reference PPWG to the grooved PPWG, which is shown

Fig. 4. Evidence of field enhancement at the narrowband resonance frequency and additional broadband features due to the cavity, observed by comparing a bare reference PPWG (black curves) to a PPWG with a resonant cavity (red curves). Experimental measurements in the collinear configuration where the probe is focused to (a) the top lobe with the position denoted in schematic (b), and (c) the bottom lobe with the position denoted in schematic (d). The dips at 0.56 and 0.75 THz in the experimental measurements (a) and (c) are water vapor absorption lines, and the schematics in (b) and (d) are obtained from FEM simulation.

in Figs. 4(a) and 4(c). Here, the focus of the probe beam is situated at the $z = 0$ position (centered over the groove), and placed either closer to the top plate at $x = \frac{3}{4}b$ [Fig. 4(b)] or bottom plate at $x = \frac{1}{4}b$ [Fig. 4(d)] to investigate the two lobes observed from simulation. To further analyze these results, we normalize the spectra obtained with the waveguide containing a groove to those without a groove for both experiment and simulation in order to derive the field enhancement, which is shown in Figs. 5(a)–5(d).

These results clearly indicate both a narrowband ($\omega/\Delta\omega \sim 20$) field enhancement at the resonant frequency and also an asymmetric broadband ($\omega/\Delta\omega \sim 3$) response on the high-frequency side of the resonance that is unanticipated from far-field measurements. Here, ω is the center frequency and $\Delta\omega$ is the bandwidth. Figure 5(a) shows results for the probe aligned closer to the top waveguide plate. We see the largest electric field at f_0, but we also see a weaker broadband enhancement, extending up to about 415 GHz (the location of the next higher cavity resonance). Throughout this spectral range, the field at this location is stronger with the groove as
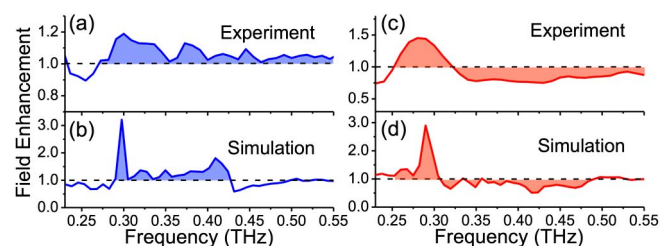

Fig. 3. Measurements in the angled configuration [Fig. 2(b)] of a PPWG containing a resonant cavity at $z = 0$ (red curves) and reference measurements of a PPWG without a cavity (black curves), where the measurement was taken closer to the plate with the groove. This shows the resonant feature due to the groove emerging inside the waveguide with increasing distance in the propagation direction from (a)–(d).

Fig. 5. Measured and simulated field enhancement (the spectral response from a waveguide with a resonant cavity, normalized to the response of a waveguide without a cavity). In (a) and (b), the measurement point is closer to the upper waveguide plate, while in (c) and (d) it is near the lower plate, as in the schematics of Figs. 4(b) and 4(d). For a broad range of frequencies above the fundamental resonance at 295 GHz, both the measurements and simulations indicate a greater than unity field enhancement near the upper waveguide plate, and a less than unity enhancement near the lower plate.
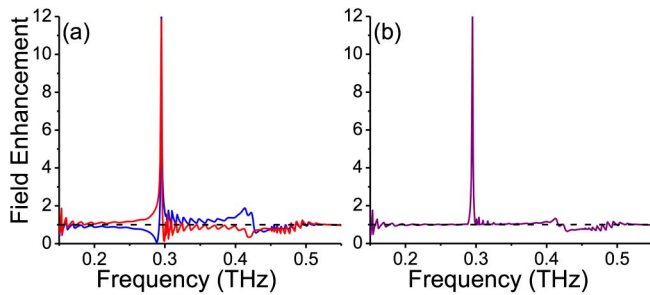
Fig. 6. Simulated field enhancement, extracted from simulations with a longer time window of 1200 ps. When the spectra extracted from the top (blue) and bottom (red) of the waveguide (a) are superposed, (b) the very narrow resonance remains but the broad spectral features cancel out. Thus, the asymmetrical field enhancement inside the waveguide cannot readily be observed by far-field measurements outside the waveguide, which are only sensitive to the superposed result.

compared to without it. At even higher frequencies, however, the spectra of the sample and reference coincide almost precisely in Figs. 4(a) and 4(c), indicating no groove-induced field enhancement. Additionally, the result from the time-domain simulation, shown in Fig. 5(b), exhibits qualitatively the same effect, with both a narrowband and a broadband component. In contrast, when the probe is aligned closer to the bottom plate [Fig. 5(c)], we again see the largest electric field at the resonant frequency f_0, but here the broadband region shows a *diminished* field strength with the groove as compared to without (i.e., a field enhancement factor less than unity). Again, this result is qualitatively reproduced by the time-domain simulation [Fig. 5(d)].

This analysis more clearly shows the nature of the spectrally asymmetric field enhancement inside the waveguide. Over the range between the first resonance and the next higher-order resonance, there is a field enhancement greater than unity near the upper waveguide plate, and less than unity near the lower one. These results strongly contrast with far-field transmission measurements, which show modifications to the transmission only in a very narrow frequency range near f_0 [Fig. 1(c)].

To explain this unanticipated broadband effect, we look more closely at the FDTD simulations. In Fig. 6, we use a longer time window of 1200 ps to provide higher spectral resolution and a more complete picture of the dynamics. Figure 6(a) shows the computed field enhancement factors near the top and bottom waveguide plates. Here, we see dramatically the field enhancement at the resonance and the distinct spectral response at higher frequencies. When we add these two curves together to compute a superposed field enhancement factor in Fig. 6(b), the broadband component cancels, leaving only the narrowband resonance at f_0, as observed in far-field measurements. It is reasonable to expect an asymmetric response inside the waveguide with respect to the horizontal mirror plane of the waveguide, since the resonator is located only on the bottom plate, breaking the symmetry. Even so, the nearly perfect cancellation of the broadband asymmetric response in the far

field is surprising. This serves as a strong argument that the ability to directly probe the resonant cavity inside the waveguide reveals unanticipated effects that cannot easily be observed outside the waveguide.

We have investigated *in situ* a resonant cavity inside a PPWG through both experiment and simulation. We have seen the emergence of the resonance as a function of propagation length, and also resolved an asymmetric frequency response over a broader bandwidth inside the waveguide. Through the application of nonlinear second-harmonic generation in ABCD, we have shown the ability to experimentally measure narrowband resonant features of a high-Q cavity inside a waveguide that has yielded new information that is not available in the far field.

REFERENCES

1. K. J. Vahala, Nature **424**, 839 (2003).
2. P. Kramper, M. Kafesaki, C. M. Soukoulis, A. Birner, F. Müller, U. Gösele, R. B. Wehrspohn, J. Mlynek, and V. Sandoghdar, Opt. Lett. **29**, 174 (2004).
3. N. Louvion, A. Rahmani, C. Seassal, S. Callard, D. Gérard, and F. de Fornel, Opt. Lett. **31**, 2160 (2006).
4. D. A. Usanov, S. A. Nikitov, A. V. Skripal, and A. P. Frolov, J. Commun. Technol. Electron. **58**, 1130 (2013).
5. G. Le Gac, A. Rahmani, C. Seassal, E. Picard, E. Hadji, and S. Callard, Opt. Express **17**, 21672 (2009).
6. K. Wang, D. M. Mittleman, N. C. J. van der Valk, and P. C. M. Planken, Appl. Phys. Lett. **85**, 2715 (2004).
7. K. Iwaszczuk, A. Andryieuski, A. Lavrinenko, X.-C. Zhang, and P. U. Jepsen, Appl. Phys. Lett. **99**, 071113 (2011).
8. K. Iwaszczuk, A. Andryieuski, A. Lavrinenko, X. Zhang, and P. U. Jepsen, Opt. Express **20**, 8344 (2012).
9. R. Mendis and D. M. Mittleman, Opt. Express **17**, 14839 (2009).
10. R. Mendis, V. Astley, J. Liu, and D. M. Mittleman, Appl. Phys. Lett. **95**, 171113 (2009).
11. V. Astley, B. McCracken, R. Mendis, and D. M. Mittleman, Opt. Lett. **36**, 1452 (2011).
12. V. Astley, K. S. Reichel, J. Jones, R. Mendis, and D. M. Mittleman, Appl. Phys. Lett. **100**, 231108 (2012).
13. V. Astley, K. S. Reichel, J. Jones, R. Mendis, and D. M. Mittleman, Opt. Express **20**, 21766 (2012).
14. M. C. Hoffmann and J. A. Fülöp, J. Phys. D. **44**, 083001 (2011).
15. R. Mendis and D. M. Mittleman, J. Opt. Soc. Am. B **26**, A6 (2009).
16. N. Karpowicz, J. Dai, X. Lu, Y. Chen, M. Yamaguchi, H. Zhao, X.-C. Zhang, L. Zhang, C. Zhang, M. Price-Gallagher, C. Fletcher, O. Mamer, A. Lesimple, and K. Johnson, Appl. Phys. Lett. **92**, 011131 (2008).
17. J. Zhang, Opt. Lett. **39**, 5317 (2014).

Direct measurement of light–matter energy exchange inside a microcavity

A. D. Jameson,[1] J. L. Tomaino,[1] Y.-S. Lee,[1,*] G. Khitrova,[2] H. M. Gibbs,[2] C. N. Böttge,[3] A. C. Klettke,[3] M. Kira,[3] and S. W. Koch[3]

[1]Department of Physics, Oregon State University, Corvallis, Oregon 97331, USA

[2]College of Optical Sciences, The University of Arizona, Tucson, Arizona 85721, USA

[3]Department of Physics and Material Sciences Center, Philipps-Universität Marburg, Renthof 5, 35032 Marburg, Germany

*Corresponding author: leeys@physics.oregonstate.edu

We demonstrate that one can directly measure the time evolution of light–matter interaction in a semiconductor microcavity by tracking how the optical response is changed by strong single-cycle terahertz (THz) pulses. A short THz pulse transiently interrupts the interaction of the quantum-well microcavity with the light mode and resets the polaritonic light–matter oscillations at THz frequencies. This THz-reset protocol can provide novel insights into the light–matter coupling dynamics in a wide range of photonic materials such as plasmonic and organic systems. © 2014 Optical Society of America

1. INTRODUCTION

Understanding the dynamics of light–matter coupling in semiconductors is not only of fundamental interest but also of great importance for the development of ultra-high-speed communication [1] and computing [2]. State-of-the-art electronics have already reached 100 GHz switching rates [3–6], and further improvements challenge the fundamental limitations. Whereas light–matter interactions are widely studied in many different systems, the detailed coupling dynamics in semiconductor heterostructures is poorly understood, because it involves ultrafast many-body interactions. We directly measure the time evolution of light–matter interaction in a quantum-well (QW) microcavity, employing transient terahertz (THz) excitations in the light–matter coupled system.

QWs embedded in an optical microcavity are widely utilized to explore how light–matter coupling can be harnessed in condensed-matter systems [7] and to understand quantum-optical effects in semiconductors [8–15]. In such configurations, the light–matter coupling proceeds as a polariton with the periodic exchange of energy between the QW polarization and the intracavity field, in analogy with two coupled harmonic oscillators. Figure 1 schematically shows such a periodic evolution; the shaded areas represent the polarization P (gray) and the light components E (yellow) of the polariton. As a principal idea of our measurement scheme, we use two distinctly different excitation pulses, where the first (pump) pulse creates the polariton and the second (reset) pulse destroys its polarization component, i.e., it eliminates one of the two coupled oscillators. The solid lines in Fig. 1 illustrate how the reset pulse modifies P (blue) and E (red) for two different arrival times indicated by the dashed lines. When the polariton is dominantly polarization-like (upper part), the reset pulse removes most of the polarization. Since the polariton was essentially "stored" in the P component at the moment of reset, the subsequent polariton dynamics is strongly modified. When the reset acts on a polariton at a moment in time where it is predominantly light-like (lower part), the polariton dynamics remains basically unchanged. Therefore, the effect of the reset pulse on the polariton dynamics depends directly on the time evolution of the light–matter coupling as a polariton; the evolution time is simply defined by the delay between the pump
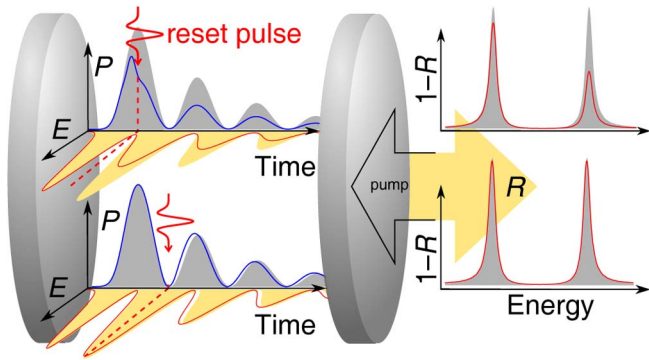
Fig. 1. Pump–reset protocol for a cavity polariton. The microcavity (disks) is irradiated with an optical pump pulse (arrow, left) to generate a cavity polariton. Subsequently, the QW polarization (P) and the cavity field (E) periodically exchange energy. A reset pulse (wave symbols) removes the polarization at two exemplary times (dashed lines). The reset-induced changes are revealed in modulations of the pump-reflection spectrum ($1 - R$, solid red lines), where the shaded areas correspond to the spectra without the reset.

and reset pulses. Since the polariton oscillations produce two normal-mode resonances in the pump-reflection spectrum R, the light–matter dynamics can be directly recorded in the changes of R as a function of the pump–reset delay.

2. METHODS

To realize the pump–reset protocol, we use a combination of optical and THz spectroscopy, where the optical pulse creates the polariton and a single-cycle THz pulse [16] resets the QW polarization. During the past decade, similar schemes have been used successfully to characterize many-body physics ranging from dynamical buildup of Coulomb screening [17] on the femtosecond time scale to exciton-formation dynamics [18] on the nanosecond time scale. In our recent study [19], we demonstrated that only the polarization part of the polariton can be efficiently converted into optically dark $2p$-exciton states when the sample is subjected to THz fields. In this work, we apply a THz π pulse to move an s-like polarization into an optically dark p-like state. This process essentially resets, i.e., switches off, the optical light–matter coupling, because the p-like states cannot couple to the cavity. By using a strong single-cycle THz pulse, the corresponding reset proceeds on a subpicosecond time scale [20].

In our sample, QWs are positioned within an optical cavity. Therefore, the optical pulse couples into the cavity and the cavity photons interact with the QWs, which generates the polaritons. At the same time, the THz pulse propagates nearly freely to reset the polarization to optically dark states at a desired moment t_{THz}. We control the pump–reset delay $\Delta t = t_{THz} - t_{opt}$, where t_{THz} and t_{opt} refer to the arrival times of the peak THz and optical fields, respectively, to the QW. The optical and THz pulses have average photon energies of 1.49 eV and 4.2 meV, respectively. We will demonstrate that by adjusting the pump–reset delay Δt, we can directly characterize the time evolution of the polaritonic light–matter interaction.

We generated the optical-pump and THz-reset pulses using 800 nm, 80 fs, 1 mJ pulses from a 1 kHz Ti:sapphire amplifier (Coherent Inc., Legend). The optical beam was split into two components: the major portion for THz-reset pulses and the minor portion for the optical-pump pulses. Using a small portion of the pulse energy (10 μJ), we produced weak 830 nm, 100 fs optical pulses by white-light continuum generation in a 1 mm quartz crystal with a bandpass filter (central wavelength, 830 nm; bandwidth, 10 nm). The major portion of the optical beam was used to generate single-cycle THz pulses via optical rectification in a 1 mm ZnTe crystal. The incident optical pulse energy was 0.8 mJ, irradiated on a 3 mm spot in the ZnTe crystal. The THz pulses were collimated with an off-axis parabolic mirror, and the THz beam diameter was measured as 1.5 mm at the focus. The THz pulses were measured using electro-optical sampling in a 1 mm ZnTe crystal. We also measured THz pulse energy using a Si bolometer at liquid helium (L-He) temperature. The THz electric field amplitude at the peak was estimated as 10 kV/cm when the optical pump pulse energy was 0.8 mJ. The QW microcavity sample consisted of 10 $In_{0.04}Ga_{0.96}As$ QWs in a $11\lambda/2$ microcavity with distributed Bragg reflectors designed for 99.4% reflectivity. The cavity was wedged so that we could tune the cavity resonance by scanning the optical beam across the sample. The sample temperature was maintained at 5 K in a L-He cryostat.

3. RESULTS AND DISCUSSION

Figure 2 shows the experimental reflectivity R at zero detuning measured with (solid lines) and without (shaded area) additional THz pulses. Without the THz reset, $1 - R$ shows two resonances, the low-energy peak (LEP) and the high-energy peak (HEP), resulting from the polariton splitting between the uncoupled exciton and cavity resonances. The high
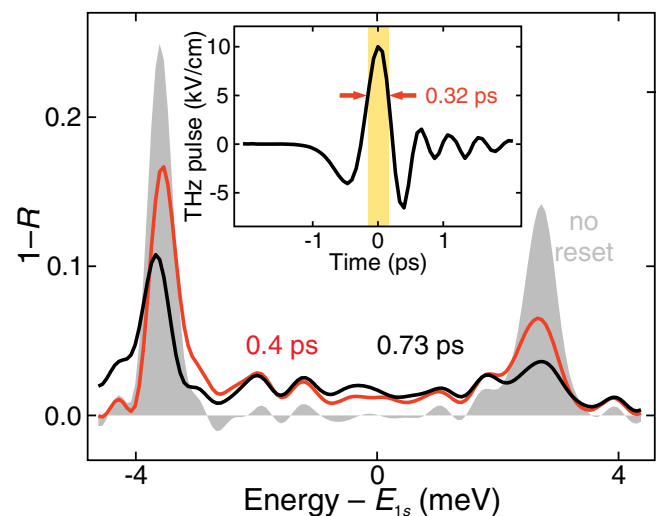
Fig. 2. Demonstration of pump–reset protocol. The measured optical reflection spectra ($1 - R$) at zero detuning without additional THz excitation (shaded) are compared to those with THz pulses at time delays of 0.4 ps (red line) and 0.73 ps (black line) between optical and THz excitation. The inset shows the experimental single-cycle THz-reset pulse. Figure S2 in Supplement 1 shows the THz power spectrum.

splitting-to-linewidth ratio indicates that the microcavity is in the nonperturbative regime of normal-mode coupling. This splitting amounts to 6.3 meV in our sample, which corresponds to an oscillation period of 0.66 ps. In order to clearly resolve these polariton oscillations, the reset process has to be shorter than half of this period 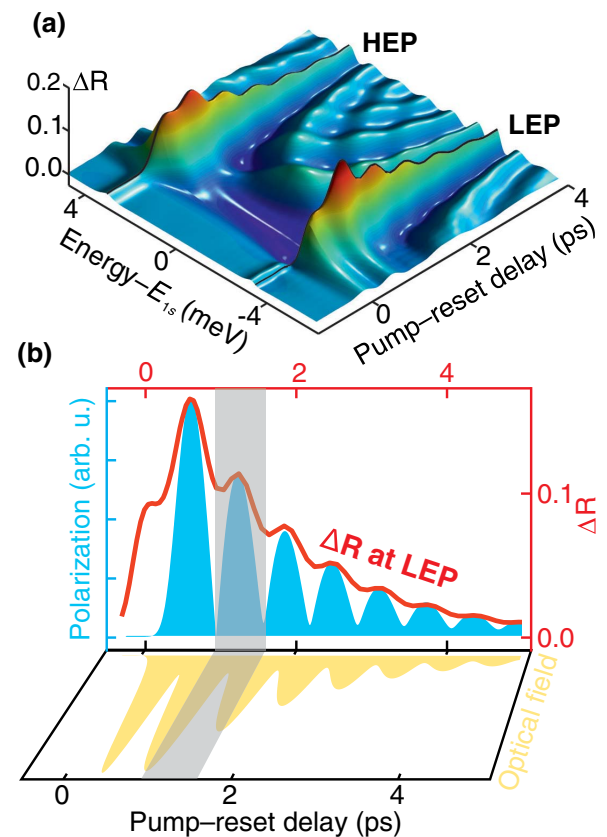(see Fig. 1). For this purpose, we use the shortest possible single-cycle THz pulse, which is frequency matched to convert the polarization part of the polariton from the excitonic 1s into the dark exciton states. The temporal profile of the THz pulse is shown in the inset of Fig. 2. The reset time is expected to be much shorter than the reset-pulse duration, because the THz-induced reset is an extreme nonlinear process and hence most efficient near the main peak. To characterize the THz-reset capabilities of our setup, Fig. 2 shows the $1 - R$ spectra measured at a 5 K sample temperature. Here, we employ THz resets at delays of $\Delta t = 0.4$ ps (red line) and $\Delta t = 0.73$ ps (black line) with respect to the optical pump. The delay difference was chosen to match the light-to-polarization conversion time 0.33 ps. As we can see in Fig. 2, the high-energy polariton peak shows a 1.8 times higher $1 - R$ resonance for the 0.4 ps than for the 0.73 ps pump–THz delay. Even though the 0.4 ps pump–reset delay corresponds to the weak reset, the $1 - R$ changes are still appreciable due to the relatively long overall THz pulse duration (0.9 ps). Nonetheless, the strong reset at 0.73 ps yields much
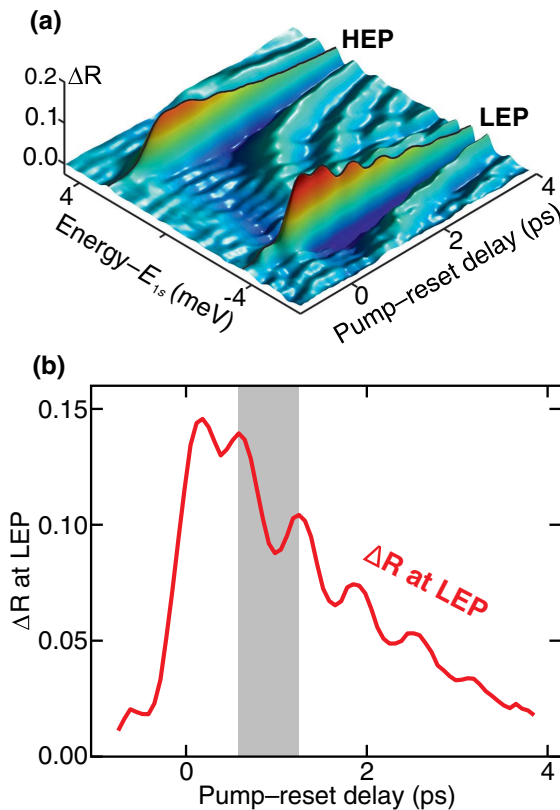
larger changes, indicating that the THz-reset time is shorter than 0.33 ps. This confirms that we may indeed directly resolve the polariton interaction dynamics with the proposed protocol.

In order to resolve the polariton dynamics in the time domain, we measure the reflectivity difference $\Delta R = R_0 - R_{reset}$ with (R_{reset}) and without (R_0) the THz-reset pulse. The measured ΔR spectra at zero detuning are shown in Fig. 3(a) as a function of pump–reset delay Δt. Here, the pump–reset delay is counted as positive when the THz-reset pulse arrives at the sample after the optical pulse. The short rising time of the peaks, ~0.3 ps, indicates that the light–matter coupling in the microcavity is turned off within less than one cycle of the THz pulse [8] and the light–matter interaction is in the regime of carrier-wave Rabi flopping [21]. We observe that both peaks decrease with increasing time delay due to the finite coherence lifetime in the system [22]. Additionally, ΔR exhibits its pronounced polariton oscillations as a function of pump–reset delay, just as the ideal operation of Fig. 1 suggests. To examine the oscillations in more detail, Fig. 3(b) shows a temporal slice of the ΔR data, measured at the LEP. We observe that the oscillation period 0.66 ps (gray-shaded area) perfectly matches the behavior predicted by the reset protocol. These results strongly suggest that we have directly measured the temporal evolution of the light–matter interaction.

Fig. 3. Direct measurement of polariton oscillations. (a) The experimentally measured differential reflectivity $\Delta R = R_0 - R_{reset}$ at zero detuning is plotted as a function of energy and time delay between the optical pump and the THz-reset pulses with $E_{THz} = 10$ kV/cm; (b) slice through the low-energy peak. The oscillation period is 0.66 ps (shaded area), corresponding to the LEP–HEP energy splitting of 6.3 meV.

Fig. 4. Computed polariton oscillations in pump–reset protocol. (a) The computed differential reflectivity $\Delta R = R_0 - R_{reset}$ at zero detuning is plotted as a function of energy and time delay between the optical pump and the THz-reset pulses; (b) slice through the low-energy peak (red solid line), polarization (blue-shaded area), and optical field (yellow-shaded area) at the QW position. The oscillation period is 0.66 ps (gray-shaded areas).

To verify this intriguing prospect, we use our fully microscopic theory [22–24] to simulate the experimental results of Fig. 3. The theoretical analysis determines the light–matter interaction microscopically and self-consistently using the Maxwell–semiconductor Bloch equations extended to THz fields [22,23]. In Supplement 1, we show that excitation-induced effects play an important role in the microscopic analysis. The computed ΔR spectra are presented in Fig. 4(a) as a function of pump–reset delay. Our theory explains the experimental observations concerning the polariton-peak position, the decay of ΔR, and the oscillation structure very well. Most important, the oscillations exhibit the same period (0.66 ps) as the experimental data. The LEP oscillations, in both experiment and theory, are larger than the HEP oscillations because the higher-lying exciton resonances damp mainly the HEP oscillations, which is verified by a switch-off analysis in Supplement 1. The experiment includes the well-known disorder effects in the sample [25], which explains the more pronounced oscillations of the computed HEP compared with the experiment.

Both experiment and theory ΔR show a pronounced spectrotemporal interference pattern between the HEP and LEP for the positive pump–reset time delay. The THz reset pulse simultaneously drives the LEP-to-$2p$ and HEP-to-$2p$ transitions in the Λ system and gives rise to quantum interference between the two transition pathways. This observation confirms that the light–matter interaction in the microcavity is a coherent dynamics. Our computations assign the reset processes to extreme nonlinear effects, because a significant portion of the optically induced $1s$ polarization is transferred to higher states by the THz-reset pulse.

A detailed analysis verifies that the measured ΔR directly detects the polariton dynamics. Figure 4(b) compares the polarization (blue-shaded area) and optical field (yellow–shaded area) at the QW position with ΔR at the LEP. We find that polarization and optical field show alternating maxima and minima, oscillating with the corresponding oscillation period 0.66 ps (gray-shaded areas). At the same time, the maxima of ΔR exactly coincide with the maxima of the polarization part of the polariton. These results confirm that the THz pulse resets the pure polarization component, resulting in direct detection of the polariton, as described in Fig. 1.

We confirm next that the reset protocol is also valid at nonzero cavity detunings. Figure 5(a) shows that the temporal evolution of the measured ΔR at the LEP exhibits clear polariton oscillations for different cavity detunings at $\delta_c = -1.9$, -0.3, and 0.4 meV. In particular, the largest and the smallest detunings produce oscillations that are out of phase already after two oscillations. To confirm that the oscillation period matches the polariton splitting, we have determined the splitting from the energy difference of the LEP and HEP and converted this number to the predicted oscillation period T_{osc}. The measured reset period (squares) and the computed T_{osc} (gray solid line) are shown in Fig. 5(b) as function of the cavity detuning. We conclude that the oscillation period is consistent with the polariton mode splitting, establishing a complementary verification for the reset protocol. As precise numbers, the oscillation period changes little in the anticrossing region
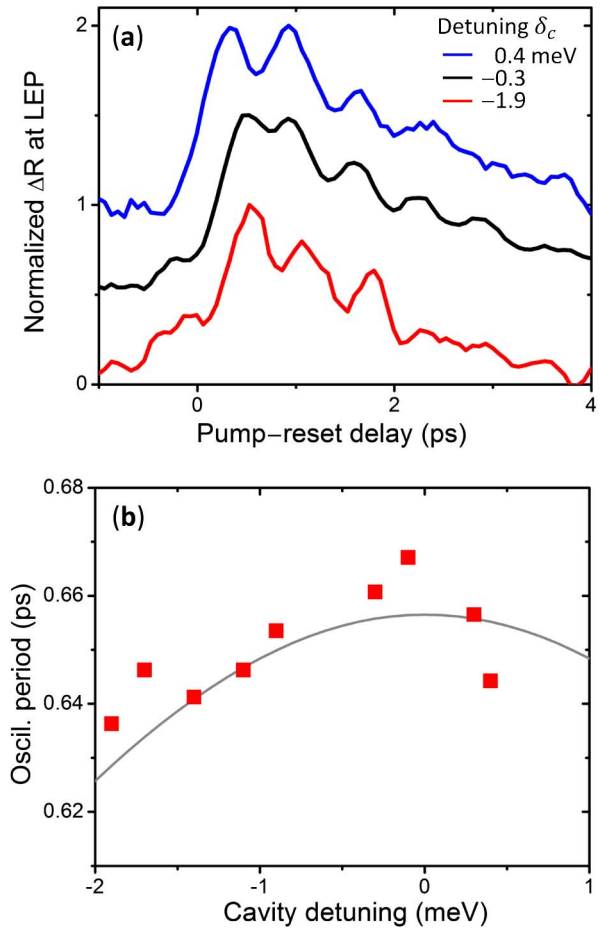
Fig. 5. Cavity-detuning-dependent polariton oscillation. (a) Time slices of polariton oscillation through the low-energy peak at $\delta_c = -1.9$, -0.3, and 0.4 meV. The curves are vertically offset for clarity. (b) Polariton oscillation period versus cavity detuning. The red squares indicate experimental data, and the gray line is a theoretical curve obtained from calculated polariton mode splitting.

between $\delta_c = -1.0$ and $+1.0$ meV and undergoes a small reduction at a relatively large detuning (e.g., 0.63 ps at $\delta_c = -2.0$ meV). Nevertheless, this change is large enough to produced clear changes in the measurements, as discussed above.

4. SUMMARY

In summary, our theory–experiment comparison demonstrates that one can directly measure the time evolution of the light–matter interaction with the proposed pump–reset protocol. The protocol is based on a sequence where a pump transiently creates the polaritons of both modes inside a QW microcavity and a single-cycle THz pulse resets the polarization components of the polaritons. The time evolution of the polaritons shows up as distinct oscillations in the pump-reflection spectrum. The optical-pump/THz-reset protocol is widely applicable to studying light–matter interaction in photonic materials. In most of the photonic systems, the optical pump excites band-to-band transitions and the THz-reset pulse induces intraband transitions, involving very different energy

ranges and final states, analogous to the semiconductor microcavity studied in this work. An immediate application of the protocol would be to study the light–matter coupling dynamics in plasmonic [26–29] and organic [30,31] devices.

See Supplement 1 for supporting content.

REFERENCES

1. D. Powell, "Lasers boost space communications," Nature **499**, 266–267 (2013).
2. T. D. Ladd, F. Jelezko, R. Laflamme, Y. Nakamura, C. Monroe, and J. L. O'Brien, "Quantum computers," Nature **464**, 45–53 (2010).
3. R. J. Warburton, C. Schäflein, D. Haft, F. Bickel, A. Lorke, K. Karrai, J. M. Garcia, W. Schoenfeld, and P. M. Petroff, "Optical emission from a charge-tunable quantum ring," Nature **405**, 926–929 (2000).
4. F. N. Xia, M. Steiner, Y. M. Lin, and P. Avouris, "A microcavity-controlled, current-driven, on-chip nanotube emitter at infrared wavelengths," Nat. Nanotechnol. **3**, 609–613 (2008).
5. N. M. Gabor, Z. H. Zhong, K. Bosnick, J. Park, and P. L. McEuen, "Extremely efficient multiple electron-hole pair generation in carbon nanotube photodiodes," Science **325**, 1367–1371 (2009).
6. S. Koenig, D. Lopez-Diaz, J. Antes, F. Boes, R. Henneberger, A. Leuther, A. Tessmann, R. Schmogrow, D. Hillerkuss, R. Palmer, T. Zwick, C. Koos, W. Freude, O. Ambacher, J. Leuthold, and I. Kallfass, "Wireless sub-THz communication system with high data rate," Nat. Photonics **7**, 977–981 (2013).
7. G. Khitrova, H. M. Gibbs, F. Jahnke, M. Kira, and S. W. Koch, "Nonlinear optics of normal-mode-coupling semiconductor microcavities," Rev. Mod. Phys. **71**, 1591–1639 (1999).
8. G. Günter, A. A. Anappara, J. Hees, A. Sell, G. Biasiol, L. Sorba, S. de Liberato, C. Ciuti, A. Tredicucci, A. Leitenstorfer, and R. Huber, "Sub-cycle switch-on of ultrastrong light–matter interaction," Nature **458**, 178–181 (2009).
9. Y.-S. Lee, T. B. Norris, M. Kira, F. Jahnke, S. W. Koch, G. Khitrova, and H. M. Gibbs, "Quantum correlations and intraband coherences in semiconductor cavity QED," Phys. Rev. Lett. **83**, 5338–5341 (1999).
10. J. P. Reithmaier, G. Sęk, A. Löffler, C. Hofmann, S. Kuhn, S. Reitzenstein, L. V. Keldysh, V. D. Kulakovskii, T. L. Reinecke, and A. Forchel, "Strong coupling in a single quantum dot-semiconductor microcavity system," Nature **432**, 197–200 (2004).
11. T. Yoshie, A. Scherer, J. Hendrickson, G. Khitrova, H. M. Gibbs, G. Rupper, C. Ell, O. B. Shchekin, and D. G. Deppe, "Vacuum Rabi splitting with a single quantum dot in a photonic crystal nanocavity," Nature **432**, 200–203 (2004).
12. K. Hennessy, A. Badolato, M. Winger, D. Gerace, M. Atatüre, S. Gulde, S. Fält, E. L. Hu, and A. Imamoğlu, "Quantum nature of a strongly coupled single quantum dot-cavity system," Nature **445**, 896–899 (2007).
13. H. Deng, G. Weihs, C. Santori, J. Bloch, and Y. Yamamoto, "Condensation of semiconductor microcavity exciton polaritons," Science **298**, 199–202 (2002).
14. J. Kasprzak, M. Richard, S. Kundermann, A. Baas, P. Jeambrun, J. M. J. Keeling, F. M. Marchetti, M. H. Szymańska, R. André, J. L. Staehli, V. Savona, P. B. Littlewood, B. Deveaud, and L. S. Dang, "Bose–Einstein condensation of exciton polaritons," Nature **443**, 409–414 (2006).
15. R. Balili, V. Hartwell, D. Snoke, L. Pfeiffer, and K. West, "Bose–Einstein condensation of microcavity polaritons in a trap," Science **316**, 1007–1010 (2007).
16. J. R. Danielson, Y.-S. Lee, J. P. Prineas, J. T. Steiner, M. Kira, and S. W. Koch, "Interaction of strong single-cycle terahertz pulses with semiconductor quantum wells," Phys. Rev. Lett. **99**, 237401 (2007).
17. R. Huber, F. Tauser, A. Brodschelm, M. Bichler, G. Abstreiter, and A. Leitenstorfer, "Femtosecond buildup of Coulomb screening in photoexcited GaAs probed via ultrabroadband THz spectroscopy," J. Lumin. **94–95**, 555–558 (2001).
18. R. A. Kaindl, M. A. Carnahan, D. Hägele, R. Lövenich, and D. S. Chemla, "Ultrafast terahertz probes of transient conducting and insulating phases in an electron–hole gas," Nature **423**, 734–738 (2003).
19. J. L. Tomaino, A. D. Jameson, Y.-S. Lee, G. Khitrova, H. M. Gibbs, A. C. Klettke, M. Kira, and S. W. Koch, "Terahertz excitation of a coherent Λ-type three-level system of exciton-polariton modes in a quantum-well microcavity," Phys. Rev. Lett. **108**, 267402 (2012).
20. A. D. Jameson, J. L. Tomaino, Y. Lee, J. P. Prineas, J. T. Steiner, M. Kira, and S. W. Koch, "Transient optical response of quantum well excitons to intense narrowband terahertz pulses," Appl. Phys. Lett. **95**, 201107 (2009).
21. O. D. Mücke, T. Tritschler, M. Wegener, U. Morgner, and F. X. Kärtner, "Signatures of carrier-wave Rabi flopping in GaAs," Phys. Rev. Lett. **87**, 057401 (2001).
22. M. Kira and S. W. Koch, "Many-body correlations and excitonic effects in semiconductor spectroscopy," Prog. Quantum Electron. **30**, 155–296 (2006).
23. J. T. Steiner, M. Kira, and S. W. Koch, "Optical nonlinearities and Rabi flopping of an exciton population in a semiconductor interacting with strong terahertz fields," Phys. Rev. B **77**, 165308 (2008).
24. M. Kira and S. W. Koch, *Semiconductor Quantum Optics*, 1st ed. (Cambridge University, 2011).
25. M. Gurioli, F. Bogani, D. S. Wiersma, P. Roussignol, G. Cassabois, G. Khitrova, and H. Gibbs, "Experimental study of disorder in a semiconductor microcavity," Phys. Rev. B **64**, 165309 (2001).
26. B. Min, E. Ostby, V. Sorger, E. Ulin-Avila, L. Yang, X. Zhang, and K. Vahala, "High-Q surface-plasmon-polariton whispering-gallery microcavity," Nature **457**, 455–458 (2009).
27. D. Chanda, K. Shigeta, T. Truong, E. Lui, A. Mihi, M. Schulmerich, P. V. Braun, R. Bhargava, and J. A. Rogers, "Coupling of plasmonic and optical cavity modes in quasi-three-dimensional plasmonic crystals," Nat. Commun. **2**, 479 (2011).
28. P. Berini and I. de Leon, "Surface plasmon-polariton amplifiers and lasers," Nat. Photonics **6**, 16–24 (2012).
29. T. Volz, A. Reinhard, M. Winger, A. Badolato, K. J. Hennessy, E. L. Hu, and A. Imamoğlu, "Ultrafast all-optical switching by single photons," Nat. Photonics **6**, 607–611 (2012).
30. V. Bulovic, V. G. Kozlov, V. B. Khalfin, and S. R. Forrest, "Transform-limited, narrow-linewidth lasing action in organic semiconductor microcavities," Science **279**, 553–555 (1998).
31. S. Kéna-Cohen and S. R. Forrest, "Room-temperature polariton lasing in an organic single-crystal microcavity," Nat. Photonics **4**, 371–375 (2010).

optica

Fast and highly resolved capture of the joint spectral density of photon pairs

Bin Fang,[1,*] Offir Cohen,[2] Marco Liscidini,[3] John E. Sipe,[4] and Virginia O. Lorenz[1]

[1]Department of Physics and Astronomy, University of Delaware, Newark, Delaware 19716, USA

[2]Joint Quantum Institute, National Institute of Standards and Technology & University of Maryland, Gaithersburg, Maryland 20849, USA

[3]Department of Physics, University of Pavia, Via Bassi 6, I-27100 Pavia, Italy

[4]Department of Physics and Institute for Optical Sciences, University of Toronto, 60 St. George Street, Ontario M5S 1A7, Canada

*Corresponding author: bfang@udel.edu

Controlling the spatial and spectral–temporal properties of photon pairs produced in artificially structured materials is fundamental to the realization of numerous photonic quantum information applications. Tailoring the joint spectral properties of photon pairs is of particular importance for applications relying on time–energy entanglement, high-visibility interference, and heralding. Yet measuring the joint spectral properties is a time-consuming task requiring coincidence counting, typically resulting in low-resolution spectra with a poor signal-to-noise ratio. In this work we capture the joint spectral correlations of photon pairs that would be produced in optical fibers with unprecedented speed, resolution, and signal-to-noise ratio, using a scheme based on stimulated four-wave mixing. We also illustrate that this technique can be used in engineering joint spectral correlations, making it a powerful tool for studying quantum states. © 2014 Optical Society of America

Some of the most promising strategies for enabling quantum information applications rely on photonic quantum states produced in artificially structured materials. These strategies take advantage of the wide tunability of the spontaneous four-wave mixing (SFWM) interaction and the single-mode nature and compactness of the structures to generate photons with specific spatial and spectral–temporal properties [1–11]. The design of the joint spectral properties of photon pairs [12–14] is of particular importance, as many protocols rely on specific types of spectral correlations, such as strongly correlated photons for time–energy entanglement [15] and uncorrelated photons for high-visibility interference and heralding [16].

Quantum correlated photon pairs [9] are typically described using a biphoton wave function, or equivalently a joint spectral amplitude. With knowledge of the joint spectral amplitude, we can extract information about the different degrees of freedom of the photon pairs and their quantum correlations. To date, measurement of the properties of the joint spectral amplitude and its magnitude [12,17–20] has been nontrivial, typically relying on single-photon detection, which results in slow characterization and low resolution. Recently, a simple relation between spontaneous and stimulated emission of photon pairs in second-order nonlinear materials was demonstrated theoretically [21], implying that the joint spectral amplitude of photon pairs that would be generated in the spontaneous process can be measured through the corresponding stimulated process. This was recently confirmed for photon pairs generated by spontaneous parametric downconversion in AlGaAs waveguides [22].

In this work, we experimentally demonstrate that the protocol in [21] is more general, and it can be applied to photon-pair generation based on higher-order nonlinear processes. We use stimulated four-wave mixing to capture, with unprecedented speed and resolution, the joint spectral density (JSD) of photon pairs that would be generated by SFWM in an optical fiber. The generation of photon pairs in this system has been studied for more than a decade, and yet our experimental results reveal details of the JSD that have never been observed before. We also illustrate how this technique can serve as a tool in the engineering of joint spectral properties.

In the silica fiber used in our experiments, the photon pairs are generated with the same linear polarization, and their state can be written as [12]

$$|\Psi\rangle = \iint d\omega_s d\omega_i f(\omega_s, \omega_i)|\omega_s, \omega_i\rangle, \qquad (1)$$

where $|\omega_s, \omega_i\rangle$ is the quantum state with the signal (idler) at angular frequency ω_s (ω_i) and $f(\omega_s, \omega_i)$ is the joint spectral amplitude. Thus the measurement of $|f(\omega_s, \omega_i)|^2$, called the JSD, allows one to obtain some information about the quantum correlations. Traditionally, its determination follows a statistical approach, based on spectrally resolved coincidence experiments [12,18,19]. This approach is time consuming and has low resolution, due to the low generation rate of photon pairs. An example of a state-of-the-art JSD measurement performed using coincidence counting for a 10 cm long polarization-maintaining fiber (PMF; Fibercore HB800G) is used for comparison, kindly provided by Smith *et al.* [12]. Here we apply a stimulated-emission-based measurement, in which the detected signal is much larger than that measured in the coincidence experiment, and thus the speed and signal-to-noise ratio are greatly improved. Indeed, the number of photon pairs emitted in the stimulated process is proportional to the number that would be emitted in the spontaneous process, with a proportionality constant approximately equal to the average number of photons in the stimulating seed [21]:

$$\frac{\langle n_{\omega_s}\rangle_{A_{\omega_i}}}{\langle n_{\omega_s} n_{\omega_i}\rangle} \approx |A_{\omega_i}|^2, \qquad (2)$$

where $\langle n_{\omega_s}\rangle_{A_{\omega_i}}$ is the average number of signal photons with frequency ω_s stimulated by an idler seed with frequency ω_i, $\langle n_{\omega_s} n_{\omega_i}\rangle$ is the average number of photon pairs that would be generated in the spontaneous process, and $|A_{\omega_i}|^2$ is the average photon number within the coherence time of the seed. Thus, one can extract the information to reconstruct the JSD by measuring the output signal. The captured JSD has a high fidelity with theoretical predictions.

Our experimental setup is shown in Fig. 1. A Ti:sapphire laser generates pump pulses centered at 710 nm with an ~3 nm full width at half-maximum (FWHM) bandwidth. The pump is coupled into an ~10 cm long PMF (Nufern PM630-HP with a birefringence of 3.3×10^{-4}). A half-wave plate (HWP) is placed in front of the fiber to rotate the polarization of the pump such that it propagates along the slow axis of the fiber. When used for SFWM, two sideband photons, the signal at 626 nm and the idler at 820 nm, are spontaneously emitted with polarization orthogonal to the pump [12]. In the
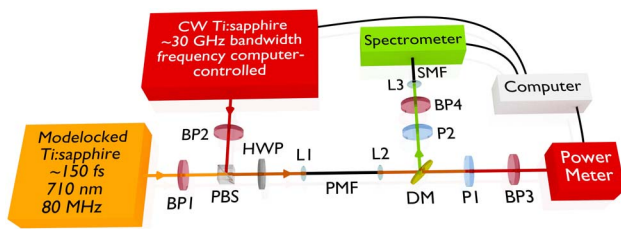
stimulated experiment, a tunable continuous-wave (CW) Ti:sapphire laser within the idler bandwidth is used as a seed to stimulate the emission of signal photons. A polarizing beam splitter (PBS) is used to combine the pump and seed before they enter the fiber. A dichroic mirror (DM) (Semrock FF685-Di02) separates the signal and idler photons. The signal is collected by a single-mode fiber (SMF) and sent to a spectrometer (Andor SR-303i-A). The power of the seed is detected by a power meter. The power for each slice (i.e., the measured signal spectrum for each idler seed wavelength) is used to normalize the corresponding spectrum taken by the spectrometer. We obtain slices of the JSD along the wavelength of the signal as we scan the seed across the idler bandwidth. The wavelength of the seed for each slice is also recorded. All the data are sent to a computer to directly generate the final joint spectrum.

A total pump power of 10 mW is coupled into the fiber. The stimulated process strongly enhances the signal, such that only 10 mW average seed power is used in our measurements to avoid saturation of the spectrometer when set to its shortest acquisition time, which is 10 ms per scan. We measure the dependence of the stimulated signal power on the seed power at fixed idler central wavelength. The result, shown in Fig. 2, confirms that the stimulated signal power varies linearly with the seed power, in agreement with Eq. (2).

The measured JSD is shown in Fig. 3(b). The sidelobes on either side of the central lobe are due to the sudden onset and end of the nonlinear interaction in the fiber [12,23]. The sidelobes are much less intense than the central lobe, and thus they are difficult to observe using the traditional JSD measurements in the spontaneous regime, such as that shown in Fig. 3(a). The stimulated-emission-based measurement gives a resolution of approximately 60 pm × 100 pm (signal × idler) per pixel. The resolution of the signal wavelength axis is determined by the resolution of the spectrometer, while the resolution of the idler wavelength axis can be controlled by the step size of the frequency scan.

To compare with the theory, we calculate the JSD numerically, using a standard approach in quantum optics that consists of finding the Hamiltonian of the FWM interaction
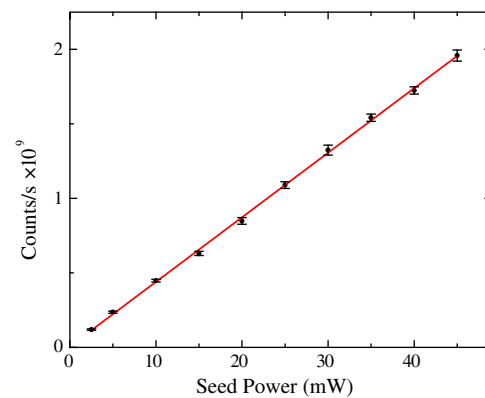

Fig. 1. Schematic of the experimental setup. BP1–4, bandpass filter; PBS, polarizing beam splitter; HWP, half-wave plate; L1–3, lens; PMF, polarization-maintaining fiber; DM, dichroic mirror; P1–2, polarizer; SMF, single-mode fiber.

Fig. 2. Power dependence of the stimulated photon counts. The black squares are the measured counts, with error bars indicating the standard deviation across 20 measurements. The red line is a linear least-squares fit.
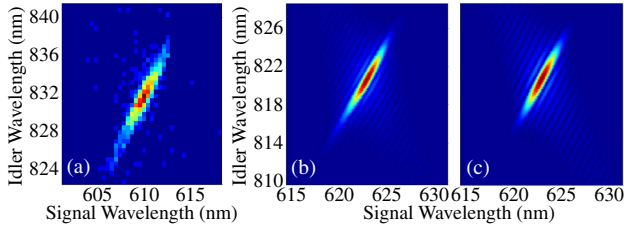
**Fig. 3.** (a) JSD measured by coincidence counting, provided by Smith *et al.* [12], (b) JSD measured by stimulated four-wave mixing, (c) numerical calculation of the JSD. Note the high resolution and low noise in (b) compared with (a). Also note that the measurements in (a) are taken for a fiber different from the one in (b), resulting in a generally different JSD.

Fig. 4. Measured JSDs for fiber lengths of (a) 2.6 cm, (b) 1.6 cm, and (c) 1.1 cm. From (a)–(c), the spectral correlation changes from correlated to nearly uncorrelated to anticorrelated as the length of the fiber decreases.

and calculating the evolution of the pump state [24]. In our birefringent optical fibers, as in Smith *et al.* [12], the resulting JSD can be written as

$$|f(\omega_s, \omega_i)|^2 = \left| \int d\omega_p \alpha(\omega_p)\alpha(\omega_s + \omega_i - \omega_p)\phi(\omega_s, \omega_i) \right|^2,$$

$$(3)$$

where $\alpha(\omega_p)$ is the pump envelope function (assumed to be Gaussian) and $\phi(\omega_s, \omega_i) = \operatorname{sinc}(\Delta k L/2)\exp(i\Delta k L/2)$ is the phase-matching function, where L is the length of the fiber and $\Delta k = 2n(\omega_p)\omega_p/c - n(\omega_s)\omega_s/c - n(\omega_i)\omega_i/c + \Delta n\omega_p/c$ is the phase mismatch, with $n(\omega)$ being the refractive index given by the Sellmeier equation of bulk silica, Δn the birefringence of the fiber, and c the speed of light in free space. As in earlier studies [12], we are working in a low-pump-power regime in which self- and cross-phase modulation can be safely neglected. The calculated JSD, plotted in Fig. 3(c), has ~94% fidelity to the experimental JSD. The clear presence of the weak sidelobes in the stimulated measurement demonstrates that this approach provides access to properties of the JSD that cannot be detected using traditional coincidence-counting techniques. The signal photon count rate when the idler seed wavelength is at the peak of the JSD is ~4.5×10^8 photons/s. Compared to the traditional coincidence-counting method [18], which has a resolution of ~0.5 nm and a count rate that requires hours to obtain a full JSD, the improvement is substantial. The whole measurement can be done within 10 min. Most of the time is spent by the computer-controlled mechanical turning of an actuator to control the seed wavelength. Many more investigations of photon-pair correlations can be pursued with the benefit of this efficient measurement technique.

Finally, we illustrate how this technique can be used as an aid in engineering joint spectral correlations of the photon pairs. In general, the photon pairs can range from correlated to uncorrelated; the latter has wide use in quantum schemes requiring pure heralded single-photon states. Although a full engineering study would require determination of the joint spectral amplitude, the JSD is the most important part for identifying when conditions have been achieved for the generation of uncorrelated photons, as the joint spectral phase typically varies little across the range in which the flux of
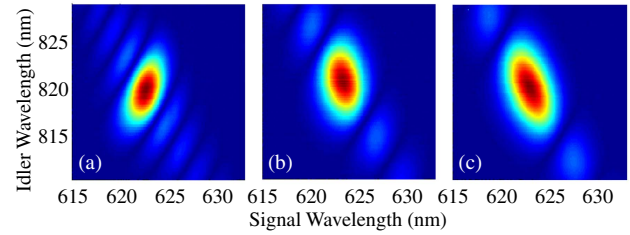
generated pairs is appreciable; thus, any improvement in determining the JSD will facilitate the design process. As an example, in this study we tailor the JSD by changing the length of the fiber; for fiber lengths of 2.6, 1.6, and 1.1 cm, we use the stimulated FWM technique to capture the JSDs. Figure 4 shows the results for the different fiber lengths, indicating that the photons change from correlated to anticorrelated as the fiber is shortened. The data suggest that a length close to 1.6 cm is the best candidate for producing nearly uncorrelated photons, a result that has been achieved much faster than previous techniques that rely on the spontaneous generation of the photon pairs would allow.

In summary, we have successfully demonstrated that the JSD of photon pairs that would be produced by SFWM can be obtained from the results of a stimulated four-wave mixing experiment. The stimulated emission allows us to capture the full JSD in a few minutes, with a resolution as fine as 60 pm, and using a standard spectrometer. This represents an improvement of about an order of magnitude in resolution per axis (two orders of magnitude per unit area) with respect to a typical coincidence experiment, which would take several hours and require single-photon detectors. This measurement has required only a few minutes, less than a tenth the time reported in Ref. [22], demonstrating that the full potential of this technique has yet to be completely exploited. The ability to quickly determine JSDs with high resolution is essential for the efficient design of systems to produce quantum correlated photons with desired properties, and so we can expect that the technique demonstrated here will become central in engineering systems to produce pairs of photons by SFWM. We expect it will also become the preferred technique in future studies of the physics of various states of photon pairs that can be produced by parametric fluorescence in fibers as well as integrated devices.

REFERENCES

1. J. B. Spring, P. S. Salter, B. J. Metcalf, P. C. Humphreys, M. Moore, N. Thomas-Peter, M. Barbieri, X.-M. Jin, N. K. Langford, W. S. Kolthammer, M. J. Booth, and I. A. Walmsley, Opt. Express **21**, 13522 (2013).
2. M. A. Hall, J. B. Altepeter, and P. Kumar, Phys. Rev. Lett. **106**, 053901 (2011).
3. K. Garay-Palmett, H. J. McGuinness, O. Cohen, J. S. Lundeen, R. Rangel-Rojo, A. B. U'ren, M. G. Raymer, C. J. McKinstrie, S. Radic, and I. A. Walmsley, Opt. Express **15**, 14870 (2007).
4. J. Fan, M. D. Eisaman, and A. Migdall, Opt. Express **15**, 18339 (2007).
5. Q. Lin and G. P. Agrawal, Opt. Lett. **31**, 3140 (2006).
6. J. E. Sharping, K. F. Lee, M. A. Foster, A. C. Turner, B. S. Schmidt, M. Lipson, A. L. Gaeta, and P. Kumar, Opt. Express **14**, 12388 (2006).
7. K. Harada, H. Takesue, H. Fukuda, T. Tsuchizawa, T. Watanabe, K. Yamada, Y. Tokura, and S. Itabashi, Opt. Express **16**, 20368 (2008).
8. J. W. Silverstone, D. Bonneau, K. Ohira, N. Suzuki, H. Yoshida, N. Iizuka, M. Ezaki, C. M. Natarajan, M. G. Tanner, and R. H. Hadfield, Nat. Photonics **8**, 104 (2014).
9. J. Rarity, J. Fulconis, J. Duligall, W. Wadsworth, and P. Russell, Opt. Express **13**, 534 (2005).
10. X. Li, J. Chen, P. Voss, J. Sharping, and P. Kumar, IEEE Photon. Technol. Lett. **14**, 983 (2002).
11. Y. Kang, J. Ko, S. Lee, S.-K. Choi, B. Kim, and H. Park, Phys. Rev. Lett. **109**, 020502 (2012).
12. B. J. Smith, P. Mahou, O. Cohen, J. S. Lundeen, and I. A. Walmsley, Opt. Express **17**, 23589 (2009).
13. O. Cohen, J. Lundeen, B. Smith, G. Puentes, P. Mosley, and I. Walmsley, Phys. Rev. Lett. **102**, 123603 (2009).
14. X. Li, P. L. Voss, J. E. Sharping, and P. Kumar, Phys. Rev. Lett. **94**, 053601 (2005).
15. J. D. Franson, Phys. Rev. Lett. **62**, 2205 (1989).
16. E. Knill, R. Laflamme, and G. J. Milburn, Nature **409**, 46 (2001).
17. Y.-H. Kim and W. P. Grice, Opt. Lett. **30**, 908 (2005).
18. H. S. Poh, C. Y. Lum, I. Marcikic, A. Lamas-Linares, and C. Kurtsiefer, Phys. Rev. A **75**, 043816 (2007).
19. M. Avenhaus, A. Eckstein, P. J. Mosley, and C. Silberhorn, Opt. Lett. **34**, 2873 (2009).
20. R. Z. Vered, Y. Ben Or, M. Rosenbluh, and A. Pe'er, New J. Phys. **16**, 053012 (2014).
21. M. Liscidini and J. E. Sipe, Phys. Rev. Lett. **111**, 193602 (2013).
22. A. Eckstein, G. Boucher, A. Lemaître, P. Filloux, I. Favero, G. Leo, J. E. Sipe, M. Liscidini, and S. Ducci, Laser Photon. Rev. **8**, L76 (2014).
23. B. Fang, O. Cohen, J. B. Moreno, and V. O. Lorenz, Opt. Express **21**, 2707 (2013).
24. J. Chen, X. Li, and P. Kumar, Phys. Rev. A **72**, 033801 (2005).

optica

Single-pixel infrared and visible microscope

Neal Radwell,[1,*] Kevin J. Mitchell,[1] Graham M. Gibson,[1] Matthew P. Edgar,[1] Richard Bowman,[2] and Miles J. Padgett[1]

[1]SUPA, School of Physics and Astronomy, University of Glasgow, Glasgow G12 8QQ, UK

[2]Department of Physics, University of Cambridge, Cambridge CB3 0HE, UK

*Corresponding author: neal.radwell@glasgow.ac.uk

Microscopy is an essential tool in a huge range of research areas. Until now, microscopy has been largely restricted to imaging in the visible region of the electromagnetic spectrum. Here we present a microscope system that uses single-pixel imaging techniques to produce images simultaneously in the visible and short-wave infrared. We apply our microscope to the inspection of various objects, including a silicon CMOS sensor, highlighting the complementarity of the visible and shortwave infrared wavebands. The system is capable of producing images with resolutions between 32×32 and 128×128 pixels at corresponding frame rates between 10 and 0.6 Hz. We introduce a compressive technique that does not require postprocessing, resulting in a predicted frame rate increase by a factor 8 from a compressive ratio of 12.5% with only 28% relative error.   © 2014 Optical Society of America

1. INTRODUCTION

Imaging allows us to understand the world in which we live. Digital imaging has traditionally been based on a detector array that can detect variations in light intensities with spatial resolution. Recently, however, there have been rapid developments of a technology capable of imaging without a detector array, using only a single pixel. This so-called "single-pixel imaging" [1] allows imaging in which a reduction in camera complexity is gained at the cost of increased computational time. While it is true that in the visible region of the spectrum the development of detector arrays has reached the stage where this trade-off is not beneficial, it is in other regions of the electromagnetic spectrum where this technology can provide huge benefits.

In this work we present an application of single-pixel imaging to the field of microscopy [2]. Microscopy is typically performed in the visible region of the spectrum where camera technology is extremely well developed. Microscopy in other regions of the spectrum, such as infrared or ultraviolet, traditionally requires expensive cameras. Single-pixel imaging is, therefore, an attractive prospect as it allows the development of imaging systems that can be significantly cheaper than

current camera technology. This may allow imaging at previously undeveloped wavelengths, increasing the range of spectral imaging [3].

Single-pixel imaging has previsouly been applied to a microscope, e.g., Wu et al. [4] and Studer et al. [5]. In [5] they image hyperspectrally across the visible spectrum. Here we present a prototype single-pixel microscope that images not only in the traditional visible spectrum but also simultaneously in the short-wave infrared (SWIR). Previous work in single-pixel imaging has utilized compressive sensing [6–9], which minimizes the number of measurements required to produce an image. However, these compressive approaches result in long image reconstruction times of minutes to hours and, hence, low frame rates. To better suit the operational needs of a microscope, here we concentrate on methods to produce images at video rates.

As an alternative to a detector array, single-pixel imaging shifts the spatial information away from the detector and onto a set of masks. If the image is masked such that some of the light is blocked and some passes to create a signal on a single detector, then this signal contains information about how similar the mask is to the image. If many different masks are used,

their shapes and corresponding signals can be combined to infer a reconstruction of the image. An intuitive set of masks would scan a single bright pixel to build up the image as in confocal microscopy [10]. However, for systems in which the source is not also scanned, these masks waste most of the light, resulting in very poor signal-to-noise ratios (SNRs). An ideal set of masks would therefore have an equal amount of bright and dark pixels.

A commonly used set of such binary masks is the Hadamard set [11]. Each mask in this set is orthogonal to every other mask, which, in the absence of noise, allows perfect reconstruction of the image when the number of masks equals the number of pixels. This number is large even for images with a moderate resolution (4096 measurements required for a resolution of 64×64 pixels), which has lead to the development of compressive techniques.

Compressive imaging methods allow images to be reconstructed using a number of masks that is only a fraction of the number of pixels. These methods are usually reliant on iterative algorithms to solve optimization problems that are computationally difficult. This can result in long reconstruction times measured in minutes or hours. Recent developments make progress toward compressive video reconstruction [12–18], with emphasis on developing methods to reduce computational time [19,20]; however, in this paper we concentrate on compressive techniques that do not require computationally expensive reconstruction and are therefore able to provide near video frame rates.

Our microscope design is shown in Fig. 1(b) and is based on a modified Zeiss Axiovert 200. The halogen light source has been removed and the illumination is provided by a white-light LED in addition to a SWIR source comprising a superluminescent diode emitting at 1550 nm (Thorlabs S5FC1005S). The objective lens is a reflecting objective with a broadband aluminium coating, providing an image plane with 36× magnification at 0.52 NA (Newport 50102-01) . Two parabolic mirrors then re-image this plane onto a digital mirror device (DMD). This optical system provides a field of view of 381 μm, giving physical resolution of 12, 6, and 3 μm for mask sizes of 32×32, 64×64, and 128×128, respectively.

The DMD is a Vialux ALP 4.2 model with 1024×768 pixels, a binary pattern switching rate of 22 kHz, and onboard storage for up to 45,000 patterns. As illustrated in Fig. 1(a), the micromirrors can be orientated either +24 or –24 deg with respect to the normal incidence input beam. Two pick-off mirrors are positioned to steer these beams through a collection lens and into a single-pixel detector. One arm has an amplified photodiode sensitive in the visible (Thorlabs PDA100A) and the other has a large area Ge detector (Thorlabs FDG1010) amplified by a Thorlabs PDA 200C.

The whole optical system is composed of a mixture of lenses and curved mirrors. To provide maximum imaging performance over as large a wavelength range as possible, all imaging optics prior to the DMD are reflecting, specifically to avoid any chromatic aberrations. Imaging is not required after the DMD and, therefore, lenses are used to collect light into the single pixel detectors. In addition to this collection lens, a field lens is
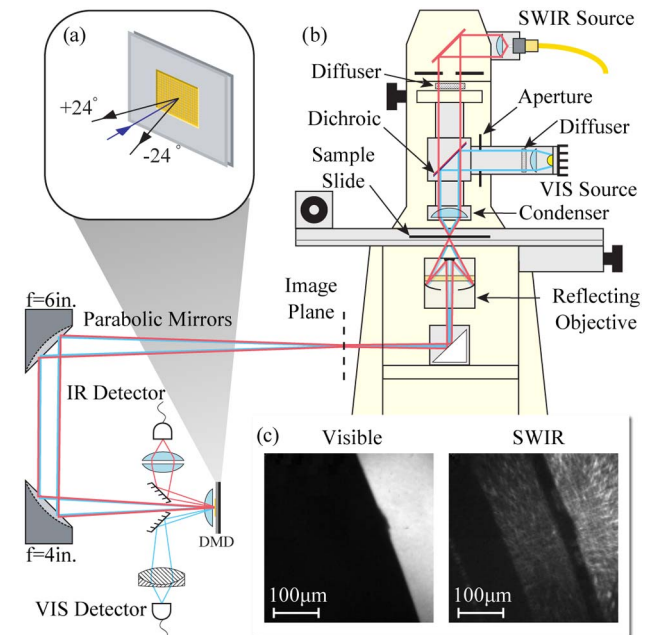
Fig. 1. Experimental setup and dual band images. (a) Sketch of the DMD operation. The input beam can be diverted, pixel by pixel, into one of two output arms. (b) Experimental setup. The diffuser (aperture) in the SWIR (visible) illumination arm can be removed (closed) to switch to a dark field configuration. (c) Reconstructed images from the visible and SWIR detectors of a silicon CMOS chip edge. The resolution is 128×128 and the images are the result of five averages and have been upscaled to 256×256 using linear interpolation.

placed as close to the DMD plane as possible in order to reduce the size of the beam in the collection arms.

2. RESULTS

A. Optical Modes

To illustrate the dual, visible/SWIR, waveband capability provided by the microscope, we image a silicon CMOS chip. The visible and infrared images are shown in Fig. 1(c). Since silicon is opaque to visible light, the edge of the chip appears as a sharp boundary in the visible image. The infrared light, on the other hand, is partially transmitted by silicon and this image shows additional features. The example in Fig. 1(c) shows that there is a band of silicon near the edge of the chip, with metal on either side that appears opaque (black). We note that the single-pixel approach has the advantage of perfect spatial registration between the two images since the spatial information is dictated by the DMD.

The flexibility of the microscope is further extended with the addition of a "dark-field" imaging configuration for both SWIR and visible. Examples of the images obtained for bright- and dark-field modes can be seen in Fig. 2. The sample comprises an amalgamation of 200 nm sized gold beads and, by comparing the bright-field images, it is apparent that the beads are almost transparent at the SWIR wavelength. If we switch to dark-field imaging, however, the results in the visible and IR are similar. The bright field measures the absorption of the sample, while the dark field measures scattering.

Channel	Visible	SWIR
Bright Field		
Dark Field		
Resolution	128 x 128	128 x 128
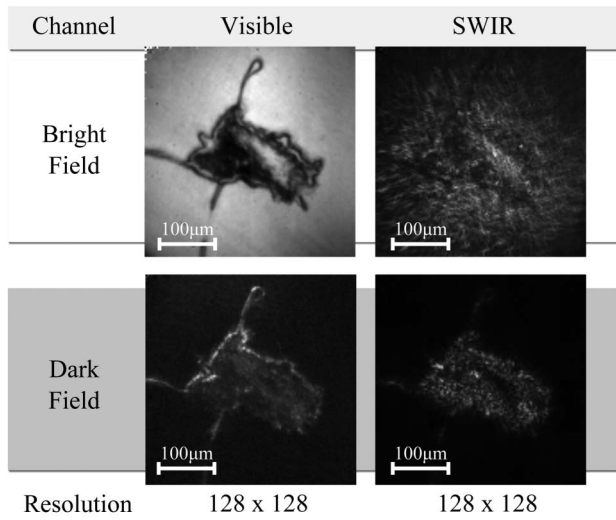
Fig. 2. Optical modes. Comparison of bright- and dark-field operating modes. The visible and SWIR images were acquired simultaneously, but the sets of bright- and dark-field images were from separate acquisitions. The images are the result of five averages and have been upscaled to 256 × 256 using linear interpolation.

B. Image Reconstruction Modes

The nature of single-pixel imaging enforces a reciprocal relationship between frame rate and image resolution, and we have therefore designed several different modes of operation to give the widest possible range of utility.

The most basic operating mode allows the user to adjust the resolution and corresponding frame rate to suit their needs. The reconstructions are formed from a full set of masks in order to give the best possible reconstruction. The quality of the reconstruction is dependent on the SNR of the system. This can be maximized by taking a differential measurement between each mask and its inverse, effectively throwing away noise below the pattern display rate. The resulting SNR of the reconstructed images is of order 115 and 95 (taken from images in the right hand column of Fig. 5) for the visible and SWIR arms, respectively.
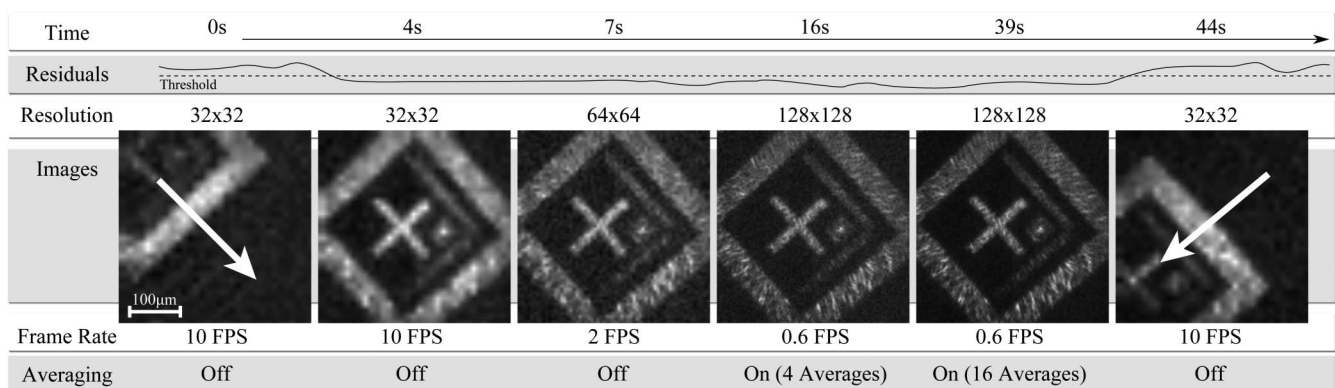
For a given resolution, the frame rate is simply a function of the number of masks and the mask display rate. The resulting frame rate is then $R_{\mathrm{Patt}}/2N$ where R_{Patt} is the pattern display rate and N is the number of a pixels in the image. For our particular DMD, the pattern display rate of 22 kHz results in a frame rate of 10 Hz at 32 × 32 and 0.6 Hz at 128 × 128.

We expand upon this "standard" operational mode to provide a user-friendly "adaptive" mode that provides the benefits of both high frame rate and high resolution. Typical use of a microscope involves two distinct stages, an initial stage in which the user searches around the sample for a particular feature of interest, and a subsequent stage in which they wish to image the feature with as high a resolution as possible.

This adaptive mode constantly compares the current signal from the single-pixel with the equivalent signal from the previous frame in order to determine if the sample is moving. If the difference between current and previous signals exceeds some threshold, then the sample is judged to be moving and the frame rate remains high. Otherwise, after a fixed number of frames the program increases the resolution from the base 32 × 32 to 64 × 64 and then to 128 × 128, so long as the sample is still not judged to be moving. Any movement in the sample resets this process and returns to the high-frame-rate mode.

An example image sequence for the adaptive mode is shown in Fig 3. It shows an image of a patterned contact on a CMOS chip that, in the first image, is moving. The program compares the signals from one frame to the next, detects movement, and, as a result, maintains a high frame rate with low resolution. After a few seconds, the contact is stationary and having detected no movement, the program doubles the resolution. After 16 s there is still no movement so the resolution is doubled again to the maximum value of 128 × 128 pixels. The image is still stationary, so the program now begins to average the data, improving the signal to noise of the image further. After 44 s, the sample begins to move again; the program detects this and switches back into high-frame-rate mode.

The standard and adaptive modes have both used a complete set of Hadamard masks for image reconstruction. A further approach, which we call "evolutionary mode", can

Time	0s	4s	7s	16s	39s	44s
Residuals						
Resolution	32x32	32x32	64x64	128x128	128x128	32x32
Images						
Frame Rate	10 FPS	10 FPS	2 FPS	0.6 FPS	0.6 FPS	10 FPS
Averaging	Off	Off	Off	On (4 Averages)	On (16 Averages)	Off

Fig. 3. Transmission images of a silicon CMOS chip captured in the SWIR band. The picture series shows a typical timeline when using sharpen mode. The resolution and averaging is controlled automatically based on the residuals. The line showing residuals is only for illustration and is not quantitatively accurate. The arrows indicate that the object in the scene is moving. The sample is entirely absorbing in the visible and thus no visible image is shown. All images have been upscaled to 256 × 256 using linear interpolation.

reconstruct an image from a subset of masks and is therefore compressive. However, unlike most forms of compressive imaging it is not computationally intensive and so is compatible with video frame rates.

The fundamental idea behind our evolutionary mode is outlined in Fig. 4. For the image in Fig. 4(a) a numerical prediction is made of the anticipated signal corresponding to each mask in a complete Hadamard set. The signals are then ordered in a sequence with the largest first, and the result is shown in Fig. 4(b). If we wish to re-image the same object using less than a full set of masks we should start with the masks producing the largest signal, but how many masks do we need? A good estimate can be obtained by summing the signals within a subset and comparing that with the total of all signals. As can be seen, the largest 25% of the signals accounts for 70% of the total signal. The reconstructions corresponding to various subsets are shown in Fig. 4(c) and reveal that as few as 12.5% of the masks produce a good reconstruction with only 28% relative error.

However, this reduction in itself is not directly useful for imaging since one would have to know the object *a priori*. The evolutionary mode takes this insight and expands it. Let us consider an image with a resolution of 64×64 pixels; to be compressive, we wish to use only 1024 patterns, giving a compressive ratio of 25%. To optimize the choice of masks we keep a fraction of the 1024 masks with the highest signals from the previous frame, replacing the rest with randomly chosen masks from the full set. This continued optimization allows good masks to be filtered into the set of 1024 after several frames.

The experimental realization of this method is shown in Fig. 5. The images show the visible and SWIR images of two shapes, a metal tip in the lower left and a silicon edge

Fig. 5. Experimental results of the evolutionary mode. The images are taken simultaneously from the visible and SWIR channels, and the images are reconstructed from the number of patterns shown underneath. The images are the result of five averages and have been upscaled to 256×256 using linear interpolation.

in the upper right. The transmission of silicon in the infrared leads to it appearing almost invisible in the SWIR channel. We see that the image quality remains high even for a low number of patterns and that this low number of patterns also results in a significant boost to the frame rate.

The fraction of patterns to retain and the number to randomize from one frame to the next can be controlled, allowing control of the final image quality and speed of adaptability. In the example shown in Fig. 5 we use a 25% compression (1024 masks) wherein we retain 70% and randomize 30%, a ratio that we find is a good balance between image quality and speed of response. This results in the image quality shown in Fig. 5, and, if the objects in the scene move, the image returns to this quality within 2 or 3 s.

Evolutionary mode has the further advantage that it provides an increased robustness to noise. If the noise level is fixed, for instance, detector noise due to dark counts, then the SNR scales directly with signal strength. Evolutionary mode uses only the largest signals with the highest SNR and is therefore robust to this type of noise. Extreme cases with significant noise can result in the evolutionary mode reconstruction having even lower absolute error than a reconstruction from a full set.

3. CONCLUSIONS

We have demonstrated a prototype microscope system based on a single-pixel approach to image simultaneously in the visible and SWIR at frame rates approaching video rates. We demonstrate imaging in visible and SWIR with perfect pixel registration, both in standard bright-field and dark-field configurations. We have furthermore demonstrated that the instrument has a high degree of flexibility, switching from a high frame rate to high resolution automatically. We have also introduced a compressive technique that allows high resolution in tandem with high frame rate by basing our reconstruction on only the important patterns. All of these factors result in a microscope system that can produce images in multiple spectral bands simultaneously and gives great flexibility to tune its operation to suit a variety of applications. In comparison with

Fig. 4. Hadamard spectrum analysis and subset reconstruction. (a) Original image taken with a standard optical microscope. (b) Signal strength for each Hadamard pattern, ordered with largest signal first and plotted in log space for clarity. The lines are drawn at specific numbers of patterns and the number above is the percentage of total signal contained within that subset. (c) Numerical simulation reconstructions formed from subsets of patterns and signals. The subsets start with the largest signal and include ever smaller signals up to the number of patterns listed. The relative error is obtained from the absolute difference to a 4096 pattern reconstruction.

commercially available systems based on standard microscopes utilizing IR cameras, this prototype system offers hyperspectrality and significant cost savings, at the expense of some performance in terms of frame rate and resolution. Furthermore, the current implementation extends the detection bandwidth into the SWIR, but this technique can be applied to a wide variety of wavelengths.

FUNDING INFORMATION

ACKNOWLEDGMENT

REFERENCES

1. M. F. Duarte, M. A. Davenport, D. Takhar, J. N. Laska, T. Sun, K. F. Kelly, and R. G. Baraniuk, "Single-pixel imaging via compressive sampling," IEEE Signal Process. Mag. **25**(2), 83–91 (2008).
2. J. Mertz, *Introduction to Optical Microscopy* (Roberts, 2010).
3. T. Zimmermann, J. Rietdorf, and R. Pepperkok, "Spectral imaging and its applications in live cell microscopy," FEBS Lett. **546**, 87–92 (2003).
4. Y. Wu, P. Ye, I. O. Mirza, G. R. Arce, and D. W. Prather, "Experimental demonstration of an optical-sectioning compressive sensing microscope (CSM)," Opt. Express **18**, 24565–24578 (2010).
5. V. Studer, J. Bobin, M. Chahid, H. S. Mousavi, E. Candes, and M. Dahan, "Compressive fluorescence microscopy for biological and hyperspectral imaging," Proc. Natl. Acad. Sci. USA **109**, E1679–E1687 (2012).
6. D. L. Donoho, "Compressed sensing," IEEE Trans. Inf. Theory **52**, 1289–1306 (2006).
7. E. J. Candès, J. Romberg, and T. Tao, "Robust uncertainty principles: exact signal reconstruction from highly incomplete frequency information," IEEE Trans. Inf. Theory **52**, 489–509 (2006).
8. N. Pitsianis, D. Brady, A. Portnoy, X. Sun, T. Suleski, M. Fiddy, M. Feldman, and R. TeKolste, "Compressive imaging sensors," Proc. SPIE **6232**, 62320A (2006).
9. E. J. Candès and M. B. Wakin, "An introduction to compressive sampling," IEEE Signal Process. Mag. **25**(2), 21–30 (2008).
10. C. J. R. Sheppard and T. Wilson, "Image formation in confocal scanning microscopes," Optik **55**, 331–342 (1980).
11. W. Pratt, J. Kane, and H. C. Andrews, "Hadamard transform image coding," Proc. IEEE **57**, 58–68 (1969).
12. R. Marcia and R. M. Willett, "Compressive coded aperture video reconstruction," in *Proceedings of European Signal Processing Conference (EUSIPCO)* (2008).
13. J. Zheng and E. L. Jacobs, "Video compressive sensing using spatial domain sparsity," Opt. Eng. **48**, 087006 (2009).
14. Z. Liu, A. Y. Elezzabi, and H. V. Zhao, "Maximum frame rate video acquisition using adaptive compressed sensing," IEEE Trans. Circuits Syst. Video Technol. **21**, 1704–1718 (2011).
15. J. E. Fowler, S. Mun, and E. W. Tramel, "Block-based compressed sensing of images and video," Found. Trends Signal Process. **4**, 297–416 (2012).
16. L. Xu, A. Sankaranarayanan, C. Studer, Y. Li, R. G. Baraniuk, and K. F. Kelly, "Multi-scale compressive video acquisition," in *Computational Optical Sensing and Imaging* (Optical Society of America, 2013), paper CW2 C.4.
17. P. Llull, X. Liao, X. Yuan, J. Yang, D. Kittle, L. Carin, G. Sapiro, and D. J. Brady, "Coded aperture compressive temporal imaging," Opt. Express **21**, 10526–10545 (2013).
18. I. Noor and E. L. Jacobs, "Adaptive compressive sensing algorithm for video acquisition using a single-pixel camera," J. Electron. Imaging **22**, 021013 (2013).
19. A. C. Sankaranarayanan, C. Studer, and R. G. Baraniuk, "CS-MUVI: video compressive sensing for spatial-multiplexing cameras," in *International Conference on Computational Photography (ICCP)* (IEEE, 2012).
20. T. Goldstein, L. Xu, K. F. Kelly, and R. Baraniuk, "The STONE transform: multi-resolution image enhancement and real-time compressive video," arXiv:1311.3405 (2013).

optica

Frequency-comb-based remote sensing of greenhouse gases over kilometer air paths

G. B. RIEKER,[1,2,*] F. R. GIORGETTA,[1] W. C. SWANN,[1] J. KOFLER,[3] A. M. ZOLOT,[1] L. C. SINCLAIR,[1] E. BAUMANN,[1] C. CROMER,[1] G. PETRON,[3] C. SWEENEY,[3] P. P. TANS,[3] I. CODDINGTON,[1] AND N. R. NEWBURY[1,4]

[1]National Institute of Standards and Technology, Boulder, Colorado 80305, USA

[2]University of Colorado-Boulder, Boulder, Colorado 80309, USA

[3]National Oceanic and Atmospheric Administration, Boulder, Colorado 80305, USA

[4]e-mail: nathan.newbury@nist.gov

*Corresponding author: greg.rieker@colorado.edu

Increasing our understanding of regional greenhouse gas transport, sources, and sinks requires accurate, precise, continuous measurements of small gas enhancements over long ranges. We demonstrate a coherent dual frequency-comb spectroscopy technique capable of achieving these goals. Spectra are acquired spanning 5990 to 6260 cm^{-1} (1600–1670 nm) covering ∼700 absorption features from CO_2, CH_4, H_2O, HDO, and $^{13}CO_2$, across a 2 km path. The spectra have sub-1-kHz frequency accuracy, no instrument lineshape, and a 0.0033 cm^{-1} point spacing. They are fit with different absorption models to yield dry-air mole fractions of greenhouse gases. These results are compared with a point sensor under well-mixed conditions to evaluate the accuracy of models critical to global satellite-based trace gas monitoring. Under heterogeneous conditions, time-resolved data demonstrate tracking of small variations in mole fractions, with a precision <1 ppm for CO_2 and <3 ppb for CH_4 in 5 min. Portable systems could enable regional monitoring. © 2014 Optical Society of America

OCIS codes: (300.6300) Spectroscopy, Fourier transforms; (280.1120) Air pollution monitoring; (010.0280) Remote sensing and sensors.

http://dx.doi.org/10.1364/OPTICA.1.000290

1. INTRODUCTION

Absorption spectroscopy over open paths provides a means of remotely sensing changes in greenhouse gas mole fractions—a critical need for greenhouse gas transport, source, and sink studies as well as future regulatory monitoring [1–3]. It is implemented in satellite instruments, upward-looking Fourier transform spectrometers (FTS), and ground-based FTS and laser spectrometers [4–11]. Ideally, these systems should detect the dry-air mole fractions (which correct for variable dilution by water vapor) of multiple gases over long paths with high precision and reproducibility to enable mapping of small gradients in both space and time. However, absorption spectroscopy faces two distinct challenges. First, spectral databases

required to convert absorption to concentrations cannot support the desired reproducibility between instruments of 0.1 ppm CO_2 and 2 ppb CH_4 for background greenhouse gas monitoring [12], and less than 1 ppm CO_2 for urban enhancement monitoring [13–15]. Second, there is a lack of portable, long-path, multigas sensors with high reproducibility to support regional monitoring. Portable FTS is limited to sub-kilometer paths and ∼5%–10% uncertainty because of divergent sources and broad instrument lineshapes [10,16]. Therefore, regional studies use flushed-cell point sensors calibrated via a reference gas [17,18]. In contrast, accurate open-air path systems could provide continuous path-averaged mole fractions that avoid representation errors associated with point sensors [3,19].

Dual frequency-comb spectroscopy (DCS) is a promising solution to both challenges. DCS [20–31] has broadband spectral coverage for multispecies detection, a bright diffraction-limited source for high signal-to-noise ratio (SNR) over multikilometer ranges, a rapid update rate for immunity to turbulence-induced optical intensity fluctuations, and, importantly, can sample the transmission on a comb tooth-by-tooth basis for high-accuracy spectra. Here, we show that the full advantages of DCS can be applied to quantitative outdoor sensing of greenhouse gases. Our measured spectra span 80,000 comb teeth covering 5990 to 6260 cm^{-1} (1600 to 1670 nm) with absorbance noise below 5×10^{-4}. Data are acquired at the comb-tooth separation of 0.0033 cm^{-1} (100 MHz), with negligible instrument lineshape since the comb teeth are essentially delta functions in frequency. We demonstrate simultaneous retrieval of dry-air mole fractions of CO_2, CH_4, H_2O, HDO, and $^{13}CO_2$ and air temperature over a 2 km turbulent air path. During well-mixed atmospheric conditions, these data enable high-resolution evaluation of spectral absorption models and, when combined with laboratory measurements, should lead to improved spectral absorption models critical for open long-path remote sensing [13,32].

Moreover, the advent of portable frequency combs [33] should enable field-deployable DCS to support verification and monitoring of emissions of distributed sources (e.g., carbon sequestration [11] and gas development sites [2,34]) and larger-scale monitoring networks. As an initial demonstration, time-resolved dry-air mole fractions were acquired continuously over three days. The DCS data compare well with a nearby point sensor for large-scale fluctuations with much lower sensitivity to local concentration spikes. One-sigma stabilities of <1 ppm (μ mol/mol) for CO_2 and <3 ppb (nmol/mol) for CH_4 are reached at 5 min averaging. Absolute agreement is limited by the current spectral databases to ~1%–2% and by variability in sampled regions. Future optimized systems with higher power and extended spectral coverage [29,35–40] could reach similar stabilities in seconds, over 10 km, while sensing additional species, isotopologues, and oxygen [28]. Finally, the absence of instrument lineshapes should enable direct cross comparison of retrievals between systems, times, and locations.

2. OPEN-AIR DUAL-COMB SPECTROMETER

Figure 1 shows the experimental setup. In dual-comb spectroscopy [20–30], two frequency combs are arranged to have offset repetition rates (f_r and $f_r + \Delta f_r$). When combined, the resulting heterodyne signal is an rf frequency comb, where each rf comb tooth is spaced by Δf_r, and has a one-to-one relationship with a specific pair of optical comb teeth [see Fig. 1(a)]. Therefore, this rf spectrum is simply scaled to reproduce the optical spectrum.

Here, we implement DCS with two mutually coherent erbium-doped fiber frequency combs ($f_r \sim 100$ MHz, $\Delta f_r = 444$ Hz) with relative ~1 Hz comb linewidth and with each comb tooth's frequency known to better than 1 kHz [23] (see Supplement 1). The comb spectra are centered within the atmospheric water-vapor window near 1.6 μm and further shaped to cover both a portion of the CH_4 tetradecad and a CO_2 combination band. The choice of $\Delta f_r = 444$ Hz allows an alias-free optical bandwidth of $f_r^2/(2\Delta f_r) = 375$ cm^{-1}, which covers both absorption bands simultaneously [22]. The comb outputs are combined and transmitted over a 2 km folded open-air path on the NIST Boulder campus [see Figs. 1(b) and 1(c)]. This 2 km path length exceeds previous laboratory-based DCS using either multipass cells or resonant cavities.

Figures 1(d) and 1(e) show the resulting high SNR transmission spectrum acquired over ~170 min under relatively constant temperature and pressure across the measurement path (see Supplement 1). The overall shape corresponds to the spectrally filtered comb light. The stronger CO_2, H_2O, and CH_4 absorption lines appear as sharp dips of up to 15% with many weaker CH_4, CO_2, and H_2O, HDO, and $^{13}CO_2$ lines observed down to 10^{-3} absorbance. There are ~80,000 comb-tooth pairs across the 267 cm^{-1} window. With the spectral shaping, about half of these, or ~40,000 comb-tooth pairs, compose the measured spectrum. Each comb-tooth pair contributes a distinct data point in the transmitted spectrum with kilohertz-level frequency uncertainty (corresponding to a resolving power of 10^{11}), spaced at $f_r = 100$ MHz (0.0033 cm^{-1}), and with SNR in the signal intensity exceeding 3000:1 for these long time-averaged data. Even higher SNR values would be possible except that we aggressively limited the transmitted power to avoid any lineshape distortions due to detector nonlinearity [23,29]. These data were acquired with coherent summing (see Supplement 1), but continuous time data confirmed ~Hz linewidth between the detected pairs of frequency-comb teeth. The quality of these data is consistent with previous ultrahigh-resolution laboratory DCS spectra and demonstrates that the fundamental properties of coherent DCS—namely high resolution, high accuracy, broad bandwidth, and high SNR—can be directly translated to field-based measurements.

Turbulence is a concern for high-resolution open-air path spectroscopy as it can easily cause strong (100%) and fast (>100 Hz) optical intensity modulation, potentially leading to excess noise in the measured optical transmission spectrum. The power spectral density related to turbulence-induced intensity noise falls off strongly as $f^{-8/3}$ beyond the characteristic cutoff Fourier frequency, $f_c \approx U/\sqrt{2\pi L \lambda}$, where U is the wind speed, λ is the optical wavelength, and L is the path length [41]. Here, f_c is tens of hertz. In comparison, the DCS effectively acquires a single spectrum within $1/\Delta f_r = 1/444$ s. In other words, since $f_c < \Delta f_r$, the turbulence intensity noise is effectively frozen during a single spectrum. Rain, light fog, or clipping of the beam at the telescope will reduce the SNR if there is significant attenuation, but should not distort the spectrum for similar reasons. Of course, some turbulence-induced fluctuations do occur on the timescale of a single interferogram, but a more rigorous discussion (see Fig. 1 of Supplement 1) shows they appear as multiplicative noise that is below the overall noise floor. Turbulence can also cause optical
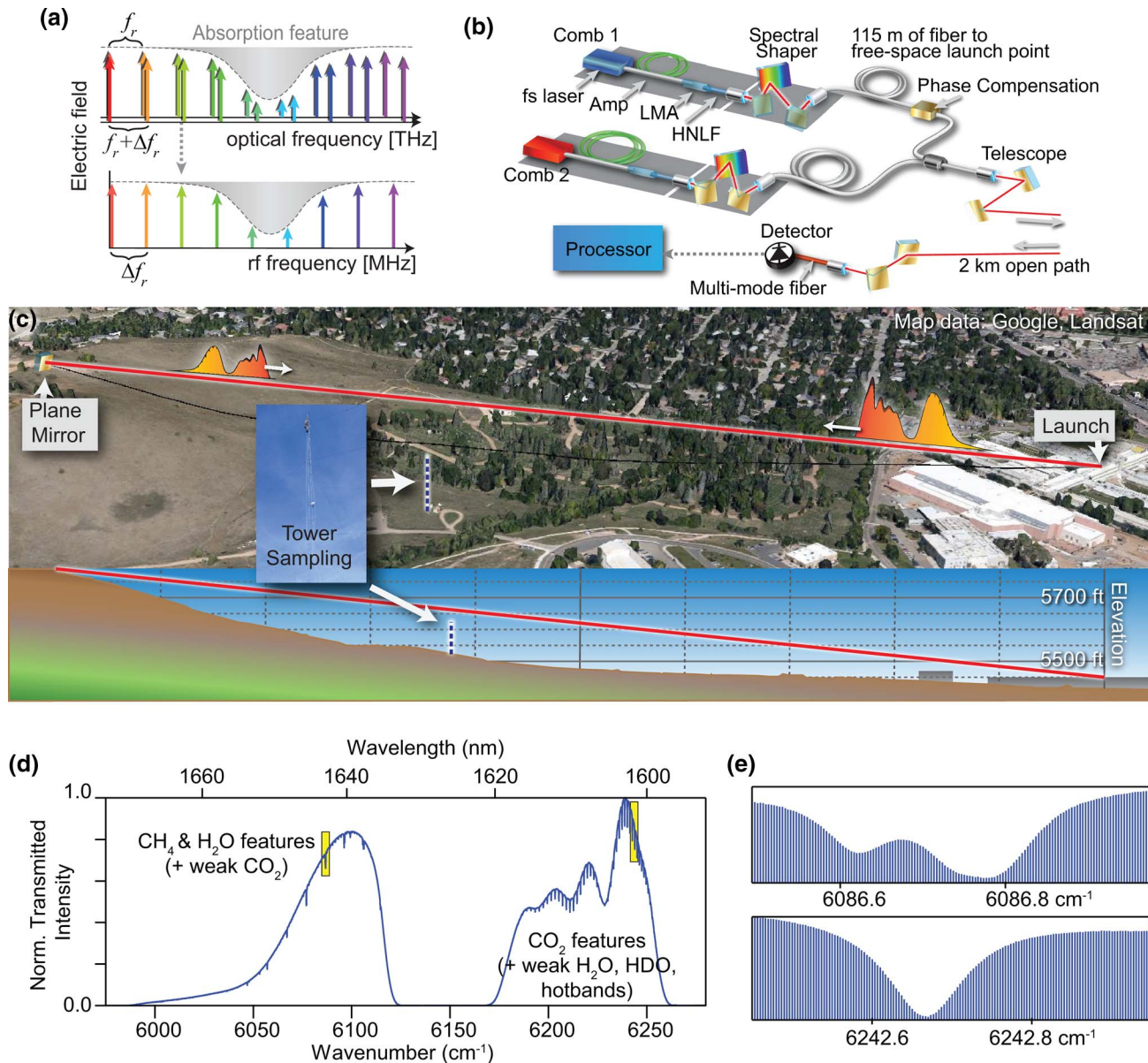
Fig. 1.   Open-air path greenhouse gas sensing through dual-comb spectroscopy. (a) DCS concept: two combs with slightly different tooth spacing interfere on a detector, giving a third rf comb with a one-to-one mapping to the optical comb teeth. (The actual experiment spans $\sim 10^5$ comb teeth.) (b) Experimental setup: two combs are amplified, pulse-compressed in large mode area (LMA) fiber, spectrally broadened in highly nonlinear fiber (HNLF), and filtered to generate light covering the spectral bands of interest. Two fibers carry the comb light to the rooftop, where the light is combined and launched in a ~ 40 mm beam ($1/e^2$ diameter), and reflected from a 50 cm diameter plane mirror located 1 km distant. The return light is coupled to a multimode fiber and detected. The transmitted light power was limited to 1.5 mW so that the maximum received power was always below a conservative detector nonlinearity threshold of 50 μW average power (500 fJ pulse energy). (c) Location of the 2 km interrogation path (red line, ground projection represented by black line), the tower with the point sensor intake (inset), and elevation of the beam path (bottom inset). (d) Example transmitted intensity showing the smoothly varying comb intensity and abrupt dips due to absorption. (e) Expanded view of absorption features. The typical gas absorption lines have ~ 40 teeth across each ~ 4 GHz wide line (top, several transitions from the $2\nu 3$ level of the CH_4 tetradecad; bottom, R20 transition of the $30013 \leftarrow 00001$ band of CO_2).

wavefront distortions and phase noise on the comb lines [41,42]. However, since both combs are copropagating, these effects are common mode and ultimately negligible. This relative immunity of DCS to turbulence is in strong contrast to high-resolution FTS or conventional swept laser spectroscopy, which have longer acquisition periods. Finally, as a coherent system, DCS is unaffected by collected sunlight because of the narrow heterodyne detection bandwidth.

## 3. MEASUREMENTS UNDER WELL-MIXED ATMOSPHERIC CONDITIONS

The DCS spectra provide a direct means to validate current and future spectral databases and absorption models since the spectra are free from instrument distortions and the DCS horizontal path avoids the atmospheric modeling that is required with up-looking total column measurements [7,14]. The transmission spectrum shown in Fig. 1(d) is

converted to absorbance by normalizing out the overall comb spectrum and applying Beer's law. Initially, we acquired a reference spectrum without the air path, but this approach introduced additional baseline etalons. Therefore, we instead normalized out the smoothly varying comb spectrum through piecewise baseline fitting (see Supplement 1), as is done for FTIR spectra. The resulting absorbance spectrum, shown in Fig. 2, can then be fit using different absorption models to

both assess those models and find the path-averaged dry-air mole fractions of various greenhouse gas species.

We separately fit the lower (6050 to 6120 cm^{-1}) and upper (6180 to 6260 cm^{-1}) spectral windows. Within a spectral window, we fit the entire absorption spectrum at once. The only inputs to the fits are the measured atmospheric pressure (from calibrated pressure gauges at each end of the path) and the absorption models. The fitted parameters are the overall gas
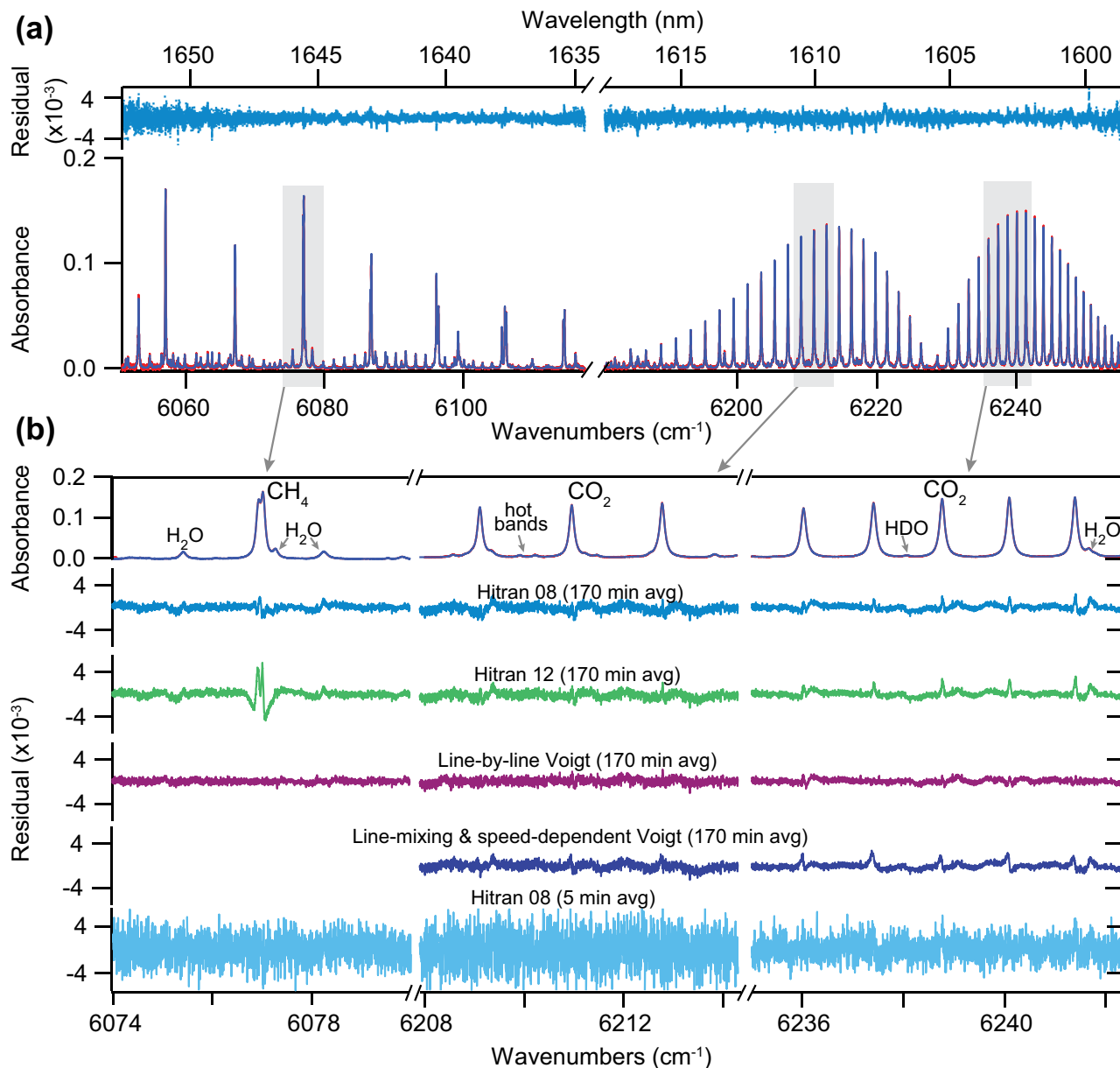
Fig. 2. Baseline-corrected absorbance from the transmission spectrum of Fig. 1(d). (a) The left spectrum mainly comprises CH_4 and H_2O lines, with some weaker CO_2 lines, while the right spectrum shows the $30013 \leftarrow 00001$ CO_2 band, CO_2 hot bands, and H_2O, $^{13}CO_2$, and HDO features. The data (red line), fit with HITRAN 2008 (blue line, indistinguishable from the data), and residuals (upper blue line) are shown. There are ~40,000 data points, or comb teeth, spaced at 100 MHz across the spectral windows. (b) Expanded view of a few representative lines along with residuals for fits to the HITRAN 2008 model [44], the HITRAN 2012 model [43], the line-mixing and speed-dependent model of Ref. [14], and line-by-line Voigt fits to each line. Also shown are the fit residuals for a 5 min time average, identical to those used in the time-resolved data of Fig. 3. The noise per comb tooth (in absorbance units) for the 5 min averaged spectra is 2.0×10^{-3}, 2.7×10^{-3}, and 1.7×10^{-3} for the three windows shown, with the differences attributable to different spectral intensities. For the 170 min average, the noise decreases with the square root of time, as expected, to 3.5×10^{-4}, 5.1×10^{-4}, and 3.0×10^{-4}, respectively. However, there are clear residuals near the spectral lines due to mismatch between the measured lineshapes and absorption models.

Table 1.   Mole Fractions Retrieved from Fits of the Absorbance Spectrum of Fig. 2 with Four Absorption Models: HITRAN 2008 [44], HITRAN 2012 [43], Line-Mixing Speed-dependent Voigt (LM/SD) [14], and Toth et al. [48][a]

	Mole Fraction Retrieval (ppm)				Systematic Unc. (ppm)	
	Hitran 08	**Hitran 12**	**LM/SD**	**Toth**	**Excluding Spectral Model**	
CO_2	408.7	407.7	404.7	406.2	0.8	0.21%
CH_4	1.878	1.985	—	—	0.009	0.45%
H_2O	3223	3217	—	—	22	0.73%
HDO	1.13	0.97	—	—	0.13	11%
$^{13}CO_2$	4.5	4.4	—	4.2	1.7	37%

[a]The final column reports the systematic (type B) uncertainty of the dual-comb spectrometer, excluding the model dependence captured in the first columns (see text).

concentrations of CO_2, $^{13}CO_2$, H_2O, CH_4, and HDO, and temperature. The fit to the upper spectral window includes a fit for temperature based on the band-wide CO_2 absorption; in this way the path-averaged temperature is extracted directly instead of using colocated temperature sensors that can suffer from solar loading. The CO_2 and $^{13}CO_2$ mole fractions were extracted from the fit to the upper spectral region, while the CH_4, H_2O, and HDO mole fractions were extracted from the fit to the lower spectral region (although there are CO_2 lines present as well). More than 300 spectral lines are included in the lower spectral window and 400 in the upper spectral window.

Absorption models for species in this region are evolving. The models consist of a set of spectral parameters that describe the temperature-, pressure-, and concentration-dependent strength, location, and width of each absorption feature, along with a lineshape profile model. Figure 2 shows the results of fits using the High-Resolution Transmission Molecular Absorption Database (HITRAN) 2012 [43] and 2008 [44]. The standard deviation of the residuals is $\sim 2 \times 10^{-3}$ absorbance units for 5 min averages at the 100 MHz (0.0033 cm^{-1}) point spacing, dropping to $< 5 \times 10^{-4}$ at 170 min. When scaled to the same resolution, this SNR is comparable to high-resolution solar, up-looking FTS spectra (but in a more compact, potentially portable instrument package without long, moving interferometer arms). For the upper spectral region, fits using the similar HITRAN 2012 [43] and 2008 [44] databases result in peak residuals below 3×10^{-3}, except for one errant line near 187.38 THz (coincident with a reported weak HDO line in HITRAN 2008). For the lower spectral region, HITRAN 2012 has methane parameters quite different from HITRAN 2008, and this difference is strongly reflected in the residuals, as well as the concentrations as discussed in Table 1.

The Voigt profile used with the HITRAN databases [43,44] neglects, among other things, coupling between energy states of nearby transitions (line mixing) and the effect of collisions on the Doppler contribution to the lineshape (speed dependence). Therefore, concentrations extracted using the Voigt profiles have been shown to lead to inaccurate atmospheric retrievals [45]. Figure 2(b) also shows residuals to a fit using a lineshape model and a corresponding spectral parameter database that includes line-mixing and speed-dependent Voigt profiles and was developed to support accurate satellite-based trace gas monitoring [14,46,47]. Residuals remain, with quite different structures compared to the other models; however, the fitted concentration using the

line-mixing and speed-dependent model should have the highest accuracy.

Figure 2(b) also contains residuals resulting from a line-by-line Voigt profile fit where the collisional linewidth, line center, and line strength are finally allowed to vary on a line-by-line basis. Though this fit overlooks the quantum-mechanical basis of the previous spectral databases, the small residual may indicate that the largest sources of error in absorption models are the spectral parameters (line strength, line center, broadening coefficients, etc.) rather than deviations from the Voigt lineshape model.

Table 1 compares the mole fractions extracted using the different absorption models. There is a significant model-dependent spread. For CO_2, all four absorption models rely on analysis of the same underlying laboratory FTS data, so this spread emphasizes the consequences of different lineshape models. As mentioned above, among the models considered here the line-mixing, speed-dependent Voigt profile (LM/SD) and corresponding spectral parameter database [14,46,47] is expected to yield the most accurate results for CO_2. Table 1 also reports the DCS systematic uncertainty excluding the model-dependent effects. The uncertainty is based on the root-mean-square of the sensitivities of the retrieved mole fractions to several different factors: maximum pressure and temperature path inhomogeneities (± 500 Pa and 6 K, respectively), uncertainty in path length (± 20 cm) and air pressure (± 30 Pa), and baseline correction. Baseline correction is the largest contributor (by a factor of 10 or more) in particular due to an etalon ripple with absorbance amplitude 10^{-3} (see Supplement 1). For CO_2, the other factors contribute below 0.06 ppm uncertainty.

Table 2.   Comparison of the Mole Fractions Obtained with the Dual-Comb Spectrometer and the Tower-Mounted Point Sensor under the Well-Mixed, Stable Atmospheric Conditions of Fig. 2[a]

Mole Fraction (ppm)	DCS	Tower Sensor	Difference	
CO_2	404.7 ± 0.8	397.6 ± 0.06	7.1	1.78%
CH_4	1.878 ± 0.009	1.874 ± 0.002	0.004	0.20%
H_2O	3223 ± 22	3168 ± 95	55	1.74%

[a]For the DCS, the dry-air mole fraction of CO_2 is retrieved from the LM/SD fit, and the dry-air CH_4 and H_2O ratios are retrieved from the HITRAN 2008 fit.

Table 2 compares the DCS to the tower-mounted point sensor. For CO_2, there is 1.8% offset with the LM/SD fits, which increases to 2.8% for the HITRAN 2008 fits. Under the windy, well-mixed atmospheric conditions for these data, the DCS and tower-mounted point sensor should measure almost identical mole fractions. Given that the point sensor is calibrated directly against the World Meteorological Organization (WMO) reference gas (see Supplement 1), we attribute most of the offset to the DCS retrieval and specifically to the line strengths of the absorption model. For CH_4, the DCS analyzed with the HITRAN 2008 database is in excellent agreement with the tower sensor (although the fits to HITRAN 2012 exhibit a 5.7% offset from the tower sensor). For H_2O, the two systems agree to within the uncertainty of the tower sensor.

The main conclusion—that better absorption models are needed to support accurate greenhouse gas monitoring—very much echoes the significant body of work in support of satellite measurements. Subpercent uncertainties in retrieved gas concentrations will require improvements in the spectral database, possibly through laboratory frequency-comb or cavity ring-down systems [23,29,49,50]. Finally, while DCS does rely on accurate spectral databases (as with any open-air path absorption technique), it should be straightforward to reanalyze DCS spectra as the databases are refined. In fact, this feature of the dual-comb spectra is important for accurate greenhouse gas monitoring. Whereas extractive flushed-cell sampling instruments rely on reference gas calibrations that must be performed periodically to maintain accuracy and cross-instrument comparability, the measured dual-comb
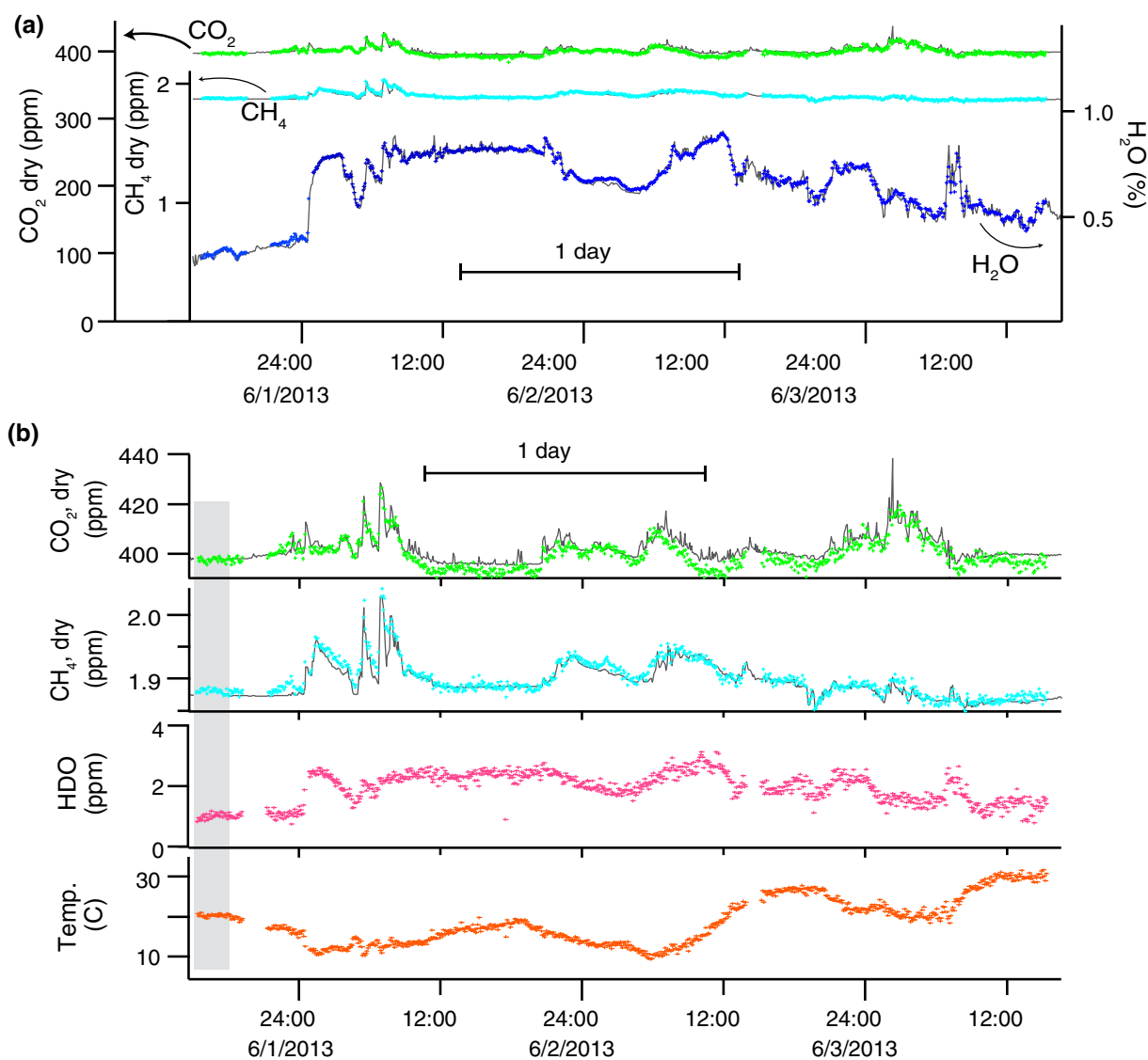
Fig. 3. Time-resolved mole fractions. (a) Time dependence of the dry-air mole fraction for CO_2 (green), CH_4 (light blue), and water (dark blue) retrieved from the DCS and the corresponding values from the tower-mounted point sensor (black line) at 5 min periods over three days. (b) Time dependence of CO_2 and CH_4 with an expanded y axis. Also shown are the time dependence of HDO (pink) and the retrieved path-averaged temperature (orange). All data are from the fit with the absorption model based on HITRAN 2008. The DCS CO_2 mole fraction has been scaled to remove the 2.8% offset between the DCS and the tower-mounted sensor over the initial ~3 h period (shaded region) where the atmosphere was well-mixed and the measurement path was upwind from the NIST central utility plant.

spectra from multiple instruments can be compared directly and indefinitely. Therefore, the retrieved mole fractions can be similarly compared when the spectra are fit with an accurate, bias-free absorption model. For example, as water-broadening coefficients for CO_2 and CH_4 become available, these effects can be included without the empirical corrections needed with flushed-cell point sensors [18].

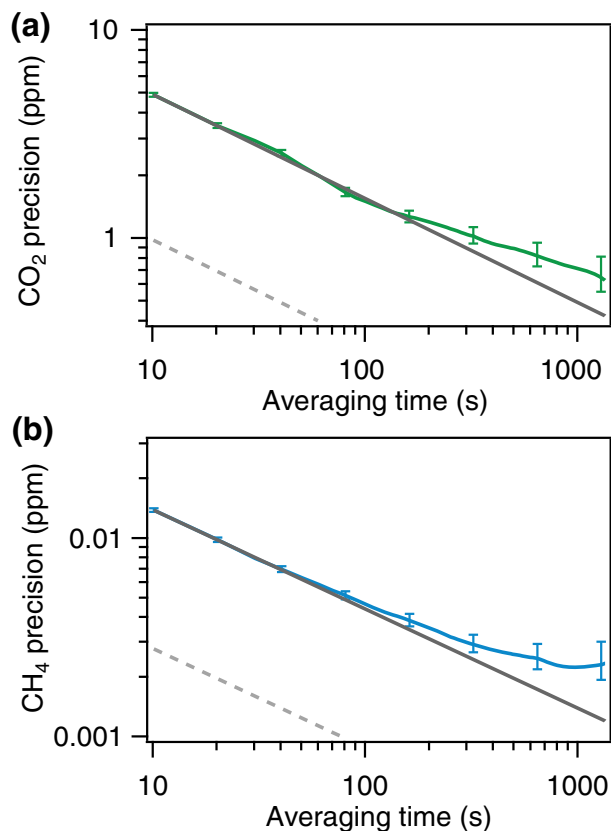## 4. TIME-RESOLVED MEASUREMENTS OF THE DRY-AIR MOLE FRACTIONS OVER A THREE-DAY PERIOD

The data of Fig. 2 were acquired over a windy, well-mixed period in which the mole fractions were quite stable. Normally, the mole fractions will vary significantly from nearby sources and sinks, and as the planetary boundary-layer height changes. We can analyze these time variations using the same fitting procedures described above. Figure 3 shows the results over a three-day period at 5 min averaging, analyzed with the HITRAN 2008 spectral database. The path-averaged air temperature is extracted directly from the fit to the

Fig. 4. Precision (Allan deviation) from data acquired during high-wind periods with a stable, well-mixed atmosphere. (a) CO_2 precision (green) versus averaging time, τ, which follows $15\sqrt{\tau}$/ppm, where τ is in seconds (gray line), or 0.86 ppm at 5 min. At longer times, actual atmospheric mole fraction variations cause a decrease in the slope. A modest increase of the launched power up to the eye-safe limit of 9.6 mW (or alternatively an increased receive aperture) would yield the improved precision of $3\sqrt{\tau}$/ppm (dashed gray line). (b) CH_4 precision (blue) follows a scaling of $40\sqrt{\tau}$/ppb (gray line) or 2.3 ppb at 5 min. Again, modest power increases, or increased receive aperture, would yield the improved precision of $8\sqrt{\tau}$/ppb (dashed gray line).

$30013 \leftarrow 00001$ CO_2 spectral band, placing even greater reliance on accurate spectral parameters.

During periods of wind and daytime thermal turbulence, the dry-air mole fractions reported by both the DCS and the tower-mounted point sensor are relatively flat. During low wind and nighttime boundary-layer settling, both show strong variations in time. However, as expected, the point sensor is much more susceptible to short spikes from local plumes. (For comparison purposes, the tower-sensor data are averaged to 5 min here; at shorter timescales the spikes are even more pronounced.) Moreover, statistically significant offsets are common between the point sensor and the path-averaged DCS results, which is not surprising given the presence of localized emissions from vehicles, the NIST central utility plant (just south of the air path), and a nearby roadway. The comparison emphasizes the quantitative differences that can arise between a single point sensor and a path-averaged system. One expects the path-averaged system to connect more directly to kilometer-scale regional transport models. Moreover, with the addition of multiple reflectors the same DCS system could interrogate multiple displaced paths [11], providing even greater utility to regional models.

The overall sensitivity, or precision, of the DCS is calculated directly as the Allan deviation over a period of relative stability, as shown in Fig. 4. The optimal averaging time period depends on the timescale of the atmospheric fluctuations; we selected 5 min for Fig. 3, which also leads to a precision comparable to the systematic uncertainty (Table 2). However, operation over longer distances, at the full eye-safe power level of 9.6 mW, or at longer wavelengths where the absorption is tenfold stronger, will all dramatically improve the precision. In addition, stronger absorption lines will reduce the systematic uncertainty that is dominated by baseline ripple (etalons).

5. CONCLUSION

We demonstrate that DCS is ideally suited to the challenges associated with accurate sensing of atmospheric trace gases across open-air paths; it combines broadband spectral coverage for accurate multispecies detection with a diffraction-limited laser output for high sensitivity over multikilometer air paths. Equally important, its high acquisition speed achieves immunity to turbulence-induced intensity noise, and its negligible instrument lineshape enables high accuracy and ultimately accurate cross comparison of spectra (and therefore concentrations) acquired with different systems, at different times and locations. We demonstrate these capabilities over a 2 km open-air path with an initial system that measures CO_2, $^{13}CO_2$, CH_4, H_2O, HDO, and air temperature. Future broader bandwidth systems will detect more species, while higher power output will further improve the sensitivity. DCS data can support the development of accurate absorption models used in global, satellite-based greenhouse gas monitoring. Moreover, with the recent advancement of portable, high-performance frequency combs [33], there is no technological barrier to regional deployment of fielded DCS systems that have costs comparable to high-performance point sensors and are capable

of autonomous, eye-safe, around-the-clock monitoring of multiple gas species over multiple optical paths.

REFERENCES

1. C. Le Quere, M. R. Raupach, J. G. Canadell, G. Marland, L. Bopp, P. Ciais, T. J. Conway, S. C. Doney, R. A. Feely, P. Foster, P. Friedlingstein, K. Gurney, R. A. Houghton, J. I. House, C. Huntingford, P. E. Levy, M. R. Lomas, J. Majkut, N. Metzl, J. P. Ometto, G. P. Peters, I. C. Prentice, J. T. Randerson, S. W. Running, J. L. Sarmiento, U. Schuster, S. Sitch, T. Takahashi, N. Viovy, G. R. van der Werf, and F. I. Woodward, "Trends in the sources and sinks of carbon dioxide," Nat. Geosci. **2**, 831–836 (2009).
2. D. R. Caulton, P. B. Shepson, R. L. Santoro, J. P. Sparks, R. W. Howarth, A. R. Ingraffea, M. O. L. Cambaliza, C. Sweeney, A. Karion, K. J. Davis, B. H. Stirm, S. A. Montzka, and B. R. Miller, "Toward a better understanding and quantification of methane emissions from shale gas development," Proc. Natl. Acad. Sci. USA **111**, 6237–6242 (2014).
3. M. R. Raupach, P. J. Rayner, D. J. Barrett, R. S. DeFries, M. Heimann, D. S. Ojima, S. Quegan, and C. C. Schmullius, "Model-data synthesis in terrestrial carbon observation: methods, data requirements and data uncertainty specifications," Glob. Chang. Biol. **11**, 378–397 (2005).
4. D. M. Hammerling, A. M. Michalak, C. O'Dell, and S. R. Kawa, "Global CO_2 distributions over land from the Greenhouse Gases Observing Satellite (GOSAT)," Geophys. Res. Lett. **39**, paper L08804 (2012).
5. J. O. Day, C. W. O'Dell, R. Pollock, C. J. Bruegge, D. Rider, D. Crisp, and C. E. Miller, "Preflight spectral calibration of the orbiting carbon observatory," IEEE Trans. Geosci. Remote Sens. **49**, 2793–2801 (2011).
6. C. Frankenberg, J. F. Meirink, M. van Weele, U. Platt, and T. Wagner, "Assessing methane emissions from global space-borne observations," Science **308**, 1010–1014 (2005).
7. D. Wunch, G. C. Toon, J.-F. L. Blavier, R. A. Washenfelder, J. Notholt, B. J. Connor, D. W. T. Griffith, V. Sherlock, and P. O. Wennberg, "The total carbon column observing network," Phil. Trans. R. Soc. B **369**, 2087–2112 (2011).
8. A. Ramanathan, J. Mao, G. R. Allan, H. Riris, C. J. Weaver, W. E. Hasselbrack, E. V. Browell, and J. B. Abshire, "Spectroscopic measurements of a CO_2 absorption line in an open vertical path using an airborne lidar," Appl. Phys. Lett. **103**, 214102 (2013).
9. D. K. MikelU. S. Environmental Protection Agency, Optical Remote Sensing for Measurement and Monitoring of Emissions Flux (n.d.), EPA Handbook, Office of Air Quality Planning and Standards, Air quality analysis division, Measurement technology group.
10. G. M. Russwurm and J. W. Childers, "Open-path Fourier transform infrared spectroscopy," in *Handbook of Vibrational Spectroscopy* (Wiley, 2006), pp. 1750–1773

11. S. D. Humphries, A. R. Nehrir, C. J. Keith, K. S. Repasky, L. M. Dobeck, J. L. Carlsten, and L. H. Spangler, "Testing carbon sequestration site monitor instruments using a controlled carbon dioxide release facility," Appl. Opt. **47**, 548–555 (2008).
12. W. Brand, ed., "15th WMO/IAEA Meeting on Carbon Dioxide, Other Greenhouse Gases, and Related Measurement Techniques," GAW Report No. 194 (World Meteorological Organization, 2009).
13. C. E. Miller, D. Crisp, P. L. DeCola, S. C. Olsen, J. T. Randerson, A. M. Michalak, A. Alkhaled, P. Rayner, D. J. Jacob, P. Suntharalingam, D. B. A. Jones, A. S. Denning, M. E. Nicholls, S. C. Doney, S. Pawson, H. Boesch, B. J. Connor, I. Y. Fung, D. O'Brien, R. J. Salawitch, S. P. Sander, B. Sen, P. Tans, G. C. Toon, P. O. Wennberg, S. C. Wofsy, Y. L. Yung, and R. M. Law, "Precision requirements for space-based X-CO_2 data," J. Geophys. Res.: Atmos. **112**, D10314 (2007).
14. D. R. Thompson, D. Chris Benner, L. R. Brown, D. Crisp, V. Malathy Devi, Y. Jiang, V. Natraj, F. Oyafuso, K. Sung, D. Wunch, R. Castaño, and C. E. Miller, "Atmospheric validation of high accuracy CO_2 absorption coefficients for the OCO-2 mission," J. Quant. Spectrosc. Radiat. Transfer **113**, 2265–2276 (2012).
15. K. L. Mays, P. B. Shepson, B. H. Stirm, A. Karion, C. Sweeney, and K. R. Gurney, "Aircraft-based measurements of the carbon footprint of Indianapolis," Environ. Sci. Technol. **43**, 7816–7823 (2009).
16. T. E. L. Smith, M. J. Wooster, M. Tattaris, and D. W. T. Griffith, "Absolute accuracy and sensitivity analysis of OP-FTIR retrievals of CO_2, CH_4 and CO over concentrations representative of "clean air" and "polluted plumes"," Atmos. Meas. Tech. **4**, 97–116 (2011).
17. W. Peters, A. R. Jacobson, C. Sweeney, A. E. Andrews, T. J. Conway, K. Masarie, J. B. Miller, L. M. P. Bruhwiler, G. Pétron, A. I. Hirsch, D. E. J. Worthy, G. R. van der Werf, J. T. Randerson, P. O. Wennberg, M. C. Krol, and P. P. Tans, "An atmospheric perspective on North American carbon dioxide exchange: Carbon-Tracker," Proc. Natl. Acad. Sci. USA **104**, 18925–18930 (2007).
18. C. W. Rella, H. Chen, A. E. Andrews, A. Filges, C. Gerbig, J. Hatakka, A. Karion, N. L. Miles, S. J. Richardson, M. Steinbacher, C. Sweeney, B. Wastine, and C. Zellweger, "High accuracy measurements of dry mole fractions of carbon dioxide and methane in humid air," Atmos. Meas. Tech. **6**, 837–860 (2013).
19. P. Ciais, P. Rayner, F. Chevallier, P. Bousquet, M. Logan, P. Peylin, and M. Ramonet, "Atmospheric inversions for estimating CO_2 fluxes: methods and perspectives," Climatic Change **103**, 69–92 (2010).
20. F. Keilmann, C. Gohle, and R. Holzwarth, "Time-domain mid-infrared frequency-comb spectrometer," Opt. Lett. **29**, 1542–1544 (2004).
21. A. Schliesser, M. Brehm, F. Keilmann, and D. van der Weide, "Frequency-comb infrared spectrometer for rapid, remote chemical sensing," Opt. Express **13**, 9029–9038 (2005).
22. I. Coddington, W. C. Swann, and N. R. Newbury, "Coherent dual-comb spectroscopy at high signal-to-noise ratio," Phys. Rev. A **82**, 043817 (2010).
23. A. M. Zolot, F. R. Giorgetta, E. Baumann, J. W. Nicholson, W. C. Swann, I. Coddington, and N. R. Newbury, "Direct-comb molecular spectroscopy with accurate, resolved comb teeth over 43 THz," Opt. Lett. **37**, 638–640 (2012).
24. T. Ideguchi, A. Poisson, G. Guelachvili, N. Picqué, and T. W. Hänsch, "Adaptive real-time dual-comb spectroscopy," Nat. Commun. **5**, 3375 (2014).
25. B. Bernhardt, A. Ozawa, P. Jacquet, M. Jacquey, Y. Kobayashi, T. Udem, R. Holzwarth, G. Guelachvili, T. W. Hänsch, and N. Picqué, "Cavity-enhanced dual-comb spectroscopy," Nat. Photonics **4**, 55–57 (2009).
26. J. Roy, J.-D. Deschênes, S. Potvin, and J. Genest, "Continuous real-time correction and averaging for frequency comb interferometry," Opt. Express **20**, 21932–21939 (2012).
27. S. Boudreau, S. Levasseur, C. Perilla, S. Roy, and J. Genest, "Chemical detection with hyperspectral lidar using dual frequency combs," Opt. Express **21**, 7411–7418 (2013).

28. S. Potvin and J. Genest, "Dual-comb spectroscopy using frequency-doubled combs around 775 nm," Opt. Express **21**, 30707–30715 (2013).

29. E. Baumann, F. R. Giorgetta, W. C. Swann, A. M. Zolot, I. Coddington, and N. R. Newbury, "Spectroscopy of the methane ν_3 band with an accurate midinfrared coherent dual-comb spectrometer," Phys. Rev. A **84**, 062513 (2011).

30. D. A. Long, A. J. Fleisher, K. O. Douglass, S. E. Maxwell, K. Bielska, J. T. Hodges, and D. F. Plusquellic, "Multiheterodyne spectroscopy with optical frequency combs generated from a continuous-wave laser," Opt. Lett. **39**, 2688–2690 (2014).

31. T. Ideguchi, S. Holzner, B. Bernhardt, G. Guelachvili, N. Picqué, and T. W. Hänsch, "Coherent Raman spectro-imaging with laser frequency combs," Nature **502**, 355–358 (2013).

32. S. Houweling, F.-M. Breon, I. Aben, C. Rödenbeck, M. Gloor, M. Heimann, and P. Ciais, "Inverse modeling of CO_2 sources and sinks using satellite data: a synthetic inter-comparison of measurement techniques and their performance as a function of space and time," Atmos. Chem. Phys. **4**, 523–538 (2004).

33. L. C. Sinclair, I. Coddington, W. C. Swann, G. B. Rieker, A. Hati, K. Iwakuni, and N. R. Newbury, "Operation of an optically coherent frequency comb outside the metrology lab," Opt. Express **22**, 6996–7006 (2014).

34. A. Karion, C. Sweeney, G. Pétron, G. Frost, R. Michael Hardesty, J. Kofler, B. R. Miller, T. Newberger, S. Wolter, R. Banta, A. Brewer, E. Dlugokencky, P. Lang, S. A. Montzka, R. Schnell, P. Tans, M. Trainer, R. Zamora, and S. Conley, "Methane emissions estimate from airborne measurements over a western United States natural gas field," Geophys. Res. Lett. **40**, 4393–4397 (2013).

35. A. Schliesser, N. Picqué, and T. W. Hänsch, "Mid-infrared frequency combs," Nat. Photonics **6**, 440–449 (2012).

36. F. Adler and S. A. Diddams, "High-power, hybrid Er:fiber/Tm:fiber frequency comb source in the 2 μm wavelength region," Opt. Lett. **37**, 1400–1402 (2012).

37. T. J. Kippenberg, R. Holzwarth, and S. A. Diddams, "Microresonator-based optical frequency combs," Science **332**, 555–559 (2011).

38. A. Hugi, G. Villares, S. Blaser, H. C. Liu, and J. Faist, "Mid-infrared frequency comb based on a quantum cascade laser," Nature **492**, 229–233 (2012).

39. Z. Zhang, T. Gardiner, and D. T. Reid, "Mid-infrared dual-comb spectroscopy with an optical parametric oscillator," Opt. Lett. **38**, 3148–3150 (2013).

40. N. Leindecker, A. Marandi, R. L. Byer, K. L. Vodopyanov, J. Jiang, I. Hartl, M. Fermann, and P. G. Schunemann, "Octave-spanning ultra-fast OPO with 2.6–6.1 μm instantaneous bandwidth pumped by femtosecond Tm-fiber laser," Opt. Express **20**, 7046–7053 (2012).

41. A. Ishimaru, *Wave Propagation and Scattering in Random Media* (Academic, 1978).

42. L. C. Sinclair, F. R. Giorgetta, W. C. Swann, E. Baumann, I. Coddington, and N. R. Newbury, "Optical phase noise from atmospheric fluctuations and its impact on optical time-frequency transfer," Phys. Rev. A **89**, 023805 (2014).

43. L. S. Rothman, I. E. Gordon, Y. Babikov, A. Barbe, D. Chris Benner, P. F. Bernath, M. Birk, L. Bizzocchi, V. Boudon, L. R. Brown, A. Campargue, K. Chance, E. A. Cohen, L. H. Coudert, V. M. Devi, B. J. Drouin, A. Fayt, J.-M. Flaud, R. R. Gamache, J. J. Harrison, J.-M. Hartmann, C. Hill, J. T. Hodges, D. Jacquemart, A. Jolly, J. Lamouroux, R. J. Le Roy, G. Li, D. A. Long, O. M. Lyulin, C. J. Mackie, S. T. Massie, S. Mikhailenko, H. S. P. Müller, O. V. Naumenko, A. V. Nikitin, J. Orphal, V. Perevalov, A. Perrin, E. R. Polovtseva, C. Richard, M. A. H. Smith, E. Starikova, K. Sung, S. Tashkun, J. Tennyson, G. C. Toon, V. G. Tyuterev, and G. Wagner, "The HITRAN 2012 molecular spectroscopic database," J. Quant. Spectrosc. Radiat. Transfer **130**, 4–50 (2013).

44. L. S. Rothman, I. E. Gordon, A. Barbe, D. C. Benner, P. E. Bernath, M. Birk, V. Boudon, L. R. Brown, A. Campargue, J. P. Champion, K. Chance, L. H. Coudert, V. Dana, V. M. Devi, S. Fally, J. M. Flaud, R. R. Gamache, A. Goldman, D. Jacquemart, I. Kleiner, N. Lacome, W. J. Lafferty, J. Y. Mandin, S. T. Massie, S. N. Mikhailenko, C. E. Miller, N. Moazzen-Ahmadi, O. V. Naumenko, A. V. Nikitin, J. Orphal, V. I. Perevalov, A. Perrin, A. Predoi-Cross, C. P. Rinsland, M. Rotger, M. Simeckova, M. A. H. Smith, K. Sung, S. A. Tashkun, J. Tennyson, R. A. Toth, A. C. Vandaele, and J. Vander Auwera, "The HITRAN 2008 molecular spectroscopic database," J. Quant. Spectrosc. Radiat. Transfer **110**, 533–572 (2009).

45. J.-M. Hartmann, H. Tran, and G. C. Toon, "Influence of line mixing on the retrievals of atmospheric CO_2 from spectra in the 1.6 and 2.1 μm regions," Atmos. Chem. Phys. **9**, 7303–7312 (2009).

46. V. M. Devi, D. C. Benner, L. R. Brown, C. E. Miller, and R. A. Toth, "Line mixing and speed dependence in CO_2 at 6227.9 cm−1: con-strained multispectrum analysis of intensities and line shapes in the 30013 ← 00001 band," J. Mol. Spectrosc. **245**, 52–80 (2007).

47. A. Predoi-Cross, A. R. W. McKellar, D. C. Benner, V. M. Devi, R. R. Gamache, C. E. Miller, R. A. Toth, and L. R. Brown, "Temperature dependences for air-broadened Lorentz half-width and pressure shift coefficients in the 30013 ← 00001 and 30012 ← 00001 bands of CO_2 near 1600 nm," Can. J. Phys. **87**, 517–535 (2009).

48. R. A. Toth, L. R. Brown, C. E. Miller, V. M. Devi, and D. C. Benner, "Spectroscopic database of CO_2," J. Quant. Spectrosc. Radiat. Transfer **109**, 906–921 (2008).

49. G.-W. Truong, K. O. Douglass, S. E. Maxwell, R. D. van Zee, D. F. Plusquellic, J. T. Hodges, and D. A. Long, "Frequency-agile, rapid scanning spectroscopy," Nat. Photonics **7**, 532–534 (2013).

50. D. A. Long, A. Cygan, R. D. van Zee, M. Okumura, C. E. Miller, D. Lisak, and J. T. Hodges, "Frequency-stabilized cavity ring-down spectroscopy," Chem. Phys. Lett. **536**, 1–8 (2012).

optica

Controlling free-carrier temporal effects in silicon by dispersion engineering

ANDREA BLANCO-REDONDO,[1,2,*] DANIEL EADES,[1] JUNTAO LI,[3,4] SIMON LEFRANCOIS,[1] THOMAS F. KRAUSS,[3,5] BENJAMIN J. EGGLETON,[1] AND CHAD HUSKO[1,6]

[1]*Centre for Ultrahigh bandwidth Devices for Optical Systems (CUDOS), Institute of Photonics and Optical Science (IPOS), School of Physics, The University of Sydney, NSW 2006, Australia*

[2]*Aerospace Unit, Industry and Transport Division, Tecnalia, Parque Tecnologico de Bizkaia, Ibaizabal Bidea, Edificio 202 E-48170 Zamudio, Bizkaia, Spain*

[3]*School of Physics and Astronomy, University of St Andrews, St Andrews, Fife KY16 9SS, UK*

[4]*State Key Laboratory of Optoelectronic Materials and Technologies, Sun Yat-sen University, Guangzhou 510275, China*

[5]*Department of Physics, University of York, York, YO10 5DD, UK*

[6]*e-mail: husko@physics.usyd.edu.au*

*Corresponding author: andrea.blanco@tecnalia.com

Nonlinear silicon photonics will play an important role in future integrated opto-electronic circuits. Here we report temporal pulse broadening induced by the dynamic interplay of nonlinear free-carrier dispersion coupled with group-velocity dispersion in nanostructured silicon waveguides for the first time, to the best of our knowledge. Further, we demonstrate that the nonlinear temporal dynamics are supported or countered by third-order dispersion, depending on the sign. Our time-domain measurements of the subpicojoule pulse dynamics are supported by strong agreement with numerical modeling. In addition to the fundamental nonlinear optical processes unveiled here, these results highlight dispersion engineering as a powerful tool for controlling free-carrier temporal effects. © 2014 Optical Society of America

1. INTRODUCTION

Understanding and controlling nonlinear optical processes in silicon [1–7] will be essential in low-cost, high-volume fabrication of integrated opto-electronic chips [8]. On-chip demonstrations of $\chi^{(3)}$ processes in silicon include soliton compression [3], supercontinuum generation [4], photon pair generation [5], Raman lasing [6], and third-harmonic generation [7], as well as applications in optical communications, interconnects, and switching [9–13]. The advantages of silicon for nonlinear photonic devices include its large Kerr nonlinearity and its capacity for subwavelength confinement of light. Combined with the potential for monolithically integrating photonics and micro-electronics in a single complementary metal-oxide-semiconductor (CMOS) platform [14], silicon

continues to attract considerable attention from researchers around the world. It is clear that a deeper understanding of the physics of nonlinear pulse propagation in silicon is essential from both fundamental and practical points of view.

There are several optical nonlinearities present in silicon. In addition to the desirable $\chi^{(3)}$ Kerr effect (n_2), a major impairment to the development of nonlinear photonic devices in silicon is the presence of strong two-photon absorption (TPA) in the telecommunications band. The primary response of this nonlinear absorption is the reduction of pulse intensity I and consequent clamping of the optical Kerr effect [15]. Recently we showed that cross-TPA in silicon affects photon pair sources even at very low power levels [16]. In addition, TPA also impacts the pulse dynamics through a second

mechanism: the photogeneration of free carriers, which has been shown to greatly distort nonlinear pulse propagation in silicon [3,17].

Since the free-carrier density N_c is generated by the intensity-dependent TPA mechanism, the resulting free-carrier refractive index change Δn_{FC} is also nonlinear. Here $\Delta n_{FC} = n_{FC} N_c(I)$, where n_{FC} is the free-carrier dispersion (FCD) coefficient, which can be derived from the Drude model [18]. Note that n_{FC} is a material parameter dependent on fundamental quantities and has a negative sign: $n_{FC} = (-e^2/(2n_0\epsilon_0\omega^2))(m_e^{*-1} + m_h^{*-1})$, where e is the elementary charge, n_0 is the linear refractive index, ϵ_0 is the vacuum permittivity, ω is the angular frequency, and $m_{e/h}^*$ is the effective mass of the electrons/holes in the semiconductor. We recognize this as the general case of plasma dispersion, where the refractive index goes down with increasing carrier density. The total index of refraction in the silicon waveguide here is thus described by $n = n_o + n_2 I + n_{FC} N_c(I)$. In our investigation, we are in a regime in which both the Kerr and FCD effects play a role with FCD ultimately dominating the system. Associated with free-carrier dispersion (FCD) is free-carrier absorption (FCA), which has a relatively minor impact here.

Interplay between linear and nonlinear phase modulations leads to interesting dynamics not possible when either of these effects is present alone. A notable example is higher-order soliton formation, which requires both nonlinear self-phase modulation (SPM) and linear group-velocity dispersion (GVD) to observe temporal pulse narrowing [19,20]. While these effects are fundamentally dynamic interactions, to date the majority of investigations of nonlinear wave propagation in silicon have targeted the spectral domain [4–7,9,15,21]. This is likely due to the significant challenges in characterizing ultrashort pulses in the time domain, especially for the subpicojoule energies required in nanophotonic structures. Specifically, many temporal characterization techniques rely on nonlinear gating methods such as frequency-resolved optical gating, which require minimum power thresholds. Indeed, only last year free-carrier-induced temporal acceleration of picosecond optical pulses in semiconductor waveguides was identified [19]. Acceleration is defined as a reduced time-of-flight compared to linear propagation. These observations were enabled by direct time-domain measurements building on an earlier demonstration of soliton compression [20]. More recently we reported these effects in silicon [3].

Here we report the first description, to the best of our knowledge, of temporal broadening due to dynamic interaction between nonlinear-induced FCD and linear GVD in nanostructured waveguides made of silicon. While these effects have been studied separately, the observations presented here arise uniquely from their simultaneous interaction in the system. In addition, we unveil the role of the third-order dispersion (TOD) interacting with FCD, which, to our knowledge, is also not described in the present literature. We further demonstrate that TOD can either counteract or support the FCD-GVD effect. Critically, the ability to independently tune the dispersion and the nonlinearity in the photonic crystal waveguide (PhC-wg) enables our examination into distinct nonlinear regimes simply by changing the input wavelength

of the pulses. This allows us to understand the basic physics in silicon waveguides for a wide range of parameters. We measure the dynamics of electric field evolution of the subpicojoule pulses with an ultrasensitive linear frequency-resolved electrical gating (FREG) [22] technique. The FREG measurements are supported by strong agreement with a generalized nonlinear Schrödinger equation (GNLSE) model. We further demonstrate that dispersion engineering is a powerful control mechanism for free-carrier temporal effects. In addition to our main goal of elucidating the fundamental light–matter interaction of FCD-GVD dynamics in silicon waveguides, these results provide direct insight into fundamental nonlinear optical processes and means to control free-carrier effects in silicon waveguides for potential applications in optical interconnects [23].

2. DISPERSION ENGINEERED SILICON WAVEGUIDES AND DESCRIPTION OF THE EXPERIMENT

The sample is a dispersion engineered slow-light silicon PhC-wg of length $L = 396$ μm [24]. The measured group index (n_g), the GVD (β_2), and the TOD (β_3) vary with wavelength as shown in Fig. 1(a). In addition to many degrees of freedom for dispersion engineering, the photonic crystal also significantly enhances the nonlinear optical interactions due to a reduction in the group velocity in the structure known as slow light. The reduced group velocity $v_g = c/n_g$ yields a larger electric field for a given power, as well as a longer effective optical path length [25]. The exact slow-light scaling of the nonlinear parameters is given in Section 3 and discussed in detail in Supplement 1. We note that the slow-light-enhanced
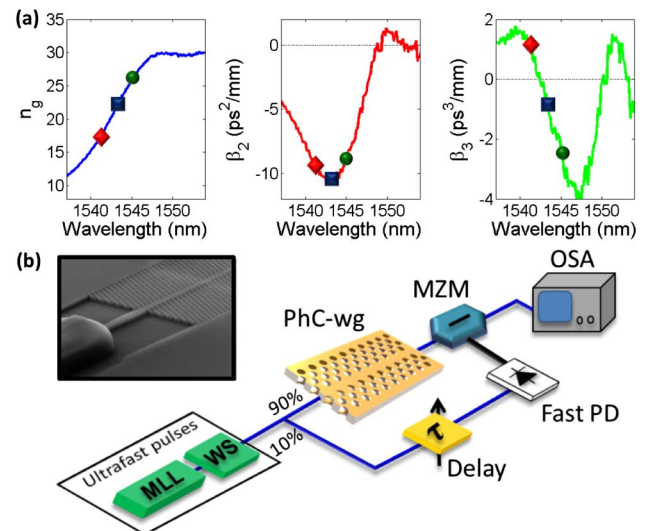
Fig. 1. Sample parameters and temporal characterization setup. (a) Measured group index (blue line), and second-order (red line) and third-order (green line) dispersion of the photonic crystal waveguide. The markers represent the values for the measured wavelengths. (b) Experimental FREG setup, consisting of the following: MML, mode-locked laser; WS, pulse shaper; PhC-wg, photonic crystal waveguide; τ variable delay; PD, fast photodiode; MZM, Mach–Zehnder modulator; OSA, optical spectrum analyzer. The inset shows a scanning electron micrograph of our silicon PhC-wg device.

nonlinearity discussed here is derived from the *structure*. In contrast, *material* slow light from atomic and related systems does not exhibit enhanced nonlinear effects [26].

In order to obtain a complete temporal and spectral characterization of the ultrafast pulses propagating through the PhC-wg, we have built a FREG apparatus [22] in a cross-correlation configuration as shown in Fig. 1(b). The FREG technique is a subclass of spectrographic techniques including frequency-resolved optical gating [27]. With the FREG we measure a series of spectrograms $S(\omega, \tau)$, gated optical power versus frequency ω and delay τ, for varying input powers. The spectrogram $S(\omega, \tau)$ is defined as

$$S(\omega, \tau) = \left| \int_{-\infty}^{+\infty} E(t) R(t - \tau) \exp(-i\omega t) \mathrm{d}t \right|^2. \quad (1)$$

Using a numerical algorithm, we extract the complex electrical field of the optical pulse $E(t)$, the electronic gate $R(t)$, and the phase $\exp(-i\omega t)$ from the experimental spectrogram [28]. Note that while we experimentally measure λ, we change this to ω for the numerical algorithm. Importantly, this technique yields information beyond what is available from autocorrelation or optical spectrum analyzer (OSA) measurements alone. The FREG technique provides us with ultrasensitive (up to 10^{-17} J) time- and phase-resolved measurements of the picosecond pulses at the output of the PhC-wg. Further details of the FREG technique are discussed in Supplement 1.

3. MODELING THE INTERACTION OF FREE-CARRIER EFFECTS AND DISPERSION

In order to understand the physics behind the observed temporal dynamics, we employ a model based on a GNLSE. In addition to dispersion and SPM, this incorporates TPA, FCD, and FCA present in silicon [17]:

$$\frac{\partial A}{\partial z} = -\frac{\alpha_l}{2} A - i \frac{\beta_2}{2} \frac{\partial^2 A}{\partial t^2} + \frac{\beta_3}{6} \frac{\partial^3 A}{\partial t^3}$$
$$+ \left(i\gamma - \frac{\gamma_{\mathrm{TPA}}}{2} \right) |A|^2 A + \left(i k_0 n_{\mathrm{FC}} - \frac{\sigma}{2} \right) N_c A. \quad (2)$$

Here $A(z, t)$ is the slowly varying amplitude of the pulse, and time t is in the frame of the pulse. The input pulse peak power is $P_0 = |A(0, 0)|^2$, α_l represents the linear loss, $\beta_n = d^n \beta(\omega)/d\omega^n$ is the nth-order dispersion of the propagation constant $\beta(\omega)$, and k_0 is the vacuum wavevector. The nonlinear SPM and TPA parameters are $\gamma = k_0 n_2 / A_{\mathrm{eff}}$ and $\gamma_{\mathrm{TPA}} = \alpha_{\mathrm{TPA}} / A_{\mathrm{eff}}$, respectively. The waveguide mode area is A_{eff}. The bulk nonlinear parameters are the intensity-dependent refractive index n_2 and TPA coefficient α_{TPA} [29]. The FCD refractive index coefficient is n_{FC}, and σ is the FCA cross section.

The free-carrier density is $N_c(z, t)$, and the generation of the TPA-induced free carriers obeys the following rate equation:

Table 1. Measured Parameters and Ratios for the Wavelengths Studied[a]

λ_0 (nm)	n_g	β_2 ($\frac{\mathrm{ps}^2}{\mathrm{mm}}$)	β_3 ($\frac{\mathrm{ps}^3}{\mathrm{mm}}$)	$\frac{L}{L_{\mathrm{FCD}}}$	$\frac{L_D}{L_{\mathrm{FCD}}}$	$\frac{L_{\mathrm{NL}}}{L_{\mathrm{FCD}}}$	$\frac{L_D}{L_{D'}}$
1541	17.9	−9.6	1.1	4.7	0.78	1.7	0.15
1543	22.4	−10.1	−0.92	6.5	1.0	1.8	0.11
1545	26.2	−8.4	−2.6	5.8	1.1	1.6	0.38

[a]Nonlinear lengths are calculated for $P_0 = 3$ W.

$$\frac{\partial N_c}{\partial t} = \rho_{\mathrm{FC}} |A|^4 - \frac{N_c}{\tau_c}. \quad (3)$$

We have defined the power-normalized carrier generation rate $\rho_{\mathrm{FC}} = \alpha_{\mathrm{TPA}} / (2h\nu_0 A_{\mathrm{eff}}^2)$, with the photon energy $h\nu_0$, and $\tau_c \sim 0.5$ ns is the carrier lifetime [15].

For our silicon PhC-wg the linear loss is $\alpha_l = 60$ dB/cm [24]. The dispersion values β_n and group indices n_g at the chosen wavelengths are given in Table 1. The effective area A_{eff} is calculated using the MPB package [30], being 0.28, 0.34, and 0.44 μm² for 1541, 1543, and 1545 nm, respectively. The slow-light enhancement of nonlinearity is included in the GNLSE model by scaling the relevant parameters by the slow-down factor $S = v_p / v_g = n_g / n_0$, where v_p is the phase velocity and n_0 is the bulk refractive index (for silicon we use $n_0 = 3.46$) [15]. As detailed in Supplement 1, the GNLSE describes our experiment when we replace the nonlinear bulk parameters with the following slow-light-scaled values [31]: $n_2 = S^2 \cdot 6 \cdot 10^{-18}$ m²/W, $\alpha_{\mathrm{TPA}} = S^2 \cdot 10 \cdot 10^{-12}$ m/W, $n_{\mathrm{FC}} = S \cdot -6 \cdot 10^{-27}$ m³, and $\sigma = S \cdot 1.45 \cdot 10^{-21}$ m² [18,29]. The FCD parameter used here differs slightly from our previous experiment due to the fact that n_{FC} depends on the exact free-carrier concentration and distribution, which vary somewhat with the exact powers and pulse durations used [3,18]. We emphasize that the physical effects described by this equation are general to all silicon waveguides.

4. TIME-RESOLVED MEASUREMENTS AND PHYSICAL LENGTH SCALES IN SILICON WAVEGUIDES

We first characterized the input pulses with the FREG by bypassing the sample. Figure 2(a) shows a measured spectrogram (top), which we take before the pulse is input into the PhC-wg. Then we inject 1.3 ps pulses at 1541, 1543, and 1545 nm into the PhC-wg, gradually increasing the input power and recording their output spectrograms using our FREG arrangement. The pulse duration is defined for Gaussian pulses at full width-half-maximum T_{FWHM}. In the spectrograms shown in Fig. 2(a), increasing blue shift and acceleration (diminished time of flight) are observed with increasing input power for the 1543 nm input wavelength. Similar blue-shift and acceleration trends were observed for the other two input wavelengths. However, Fig. 2(b), showing the T_{FWHM} of the retrieved output pulses, clearly indicates distinct pulse temporal dynamics for each measured wavelength. In Fig. 2(b) we highlight three key regimes dominated by linear dispersion (red), Kerr and dispersion (yellow), as well
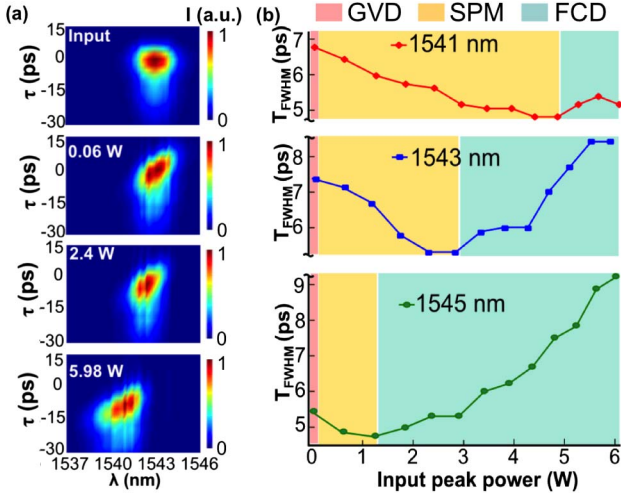
Fig. 2. Frequency-resolved electrical gating (FREG) measurements. (a) Experimental spectrograms at the input (waveguide bypassed) and output for three different coupled peak powers at 1543 nm. The cross-correlation delay is τ. (b) Measured pulse durations as a function of coupled peak power for three different wavelengths. Color-shaded regions indicate the dominant effect: dispersive broadening (GVD, red), Kerr-induced narrowing (SPM, yellow), and free-carrier dispersion broadening (FCD, blue).

Fig. 3. Ratios of key physical length scales in silicon waveguides for the 1543 nm case. As L_{FCD} and L_{NL} are power dependent, we show the relative balance of the characteristic length scales as a function of coupled power. The other wavelengths exhibit similar behavior.
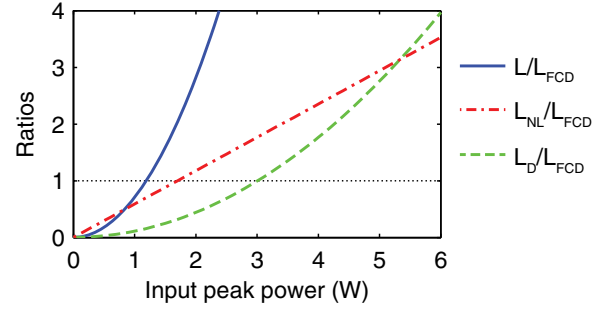
as FCD and dispersion (blue). In this paper we describe the physical origin of these dynamics.

To elucidate the driving effects behind the temporal regimes observed in Fig. 2, we quantify the strengths of the various linear and nonlinear effects (GVD, TOD, Kerr, FCD) using the associated length scales (L_D, L'_D, L_{NL}, L_{FCD}). Devices longer than these length scales will exhibit the properties described by these effects. For example, dispersive temporal broadening of $\sqrt{2}T_{FWHM}$ occurs when $L = L_D$ for Gaussian pulses. The dispersion length $L_D = T_0^2/|\beta_2|$ and TOD length $L'_D = T_0^3/|\beta_3|$ are linear effects with $T_0 = T_{FWHM}/1.665$ being the pulse duration for Gaussian pulses. The nonlinear length $L_{NL} = 1/(\gamma P_0)$ describes the strength of SPM [32]. The characteristic FCD length,

$$L_{FCD} = \frac{1}{k_0|n_{FC}|\rho_{FC}P_0^2 T_0}, \qquad (4)$$

is obtained by normalizing the GNLSE. Note that this length scale is valid for free carriers generated by TPA, but can be generalized to n-photon aborption. We show the derivation of L_{FCD} and a related FCA length scale in Supplement 1. The strength of nonlinear effects (Kerr and TPA-induced free carriers) depends on the effective intensity in the waveguide, which in turn scales with the slow-down factor S as described above.

In order to examine which physical mechanism is dominant we compute ratios of the key effects at the wavelengths under investigation. Figure 3 shows the scaling of these ratios as a function of power for the 1543 nm case. Similar results occur for the other wavelengths. We observe that the first ratio to exceed the threshold is L/L_{FCD}. The ratio L/L_{FCD} indicates

the relative importance of nonlinear FCD over the propagation length L with pulse conditions of $L/L_{FCD} > 1$ exhibiting significant FCD effects such as frequency blue shift [15].

The next ratio to come into play is L_{NL}/L_{FCD}, which represents the importance of SPM in relation to FCD. When $L_{NL}/L_{FCD} > 1$, the instantaneous phase shift induced by the free carriers is larger than the Kerr-induced phase shift. Note that L_{FCD} scales inversely with P_o^2 for free carriers generated by TPA, while L_{NL} scales with P_o. We expect SPM to be the dominant nonlinearity at lower powers, while FCD will dominate at high powers due to its power-squared dependence as shown in the plot. As dispersion is quite strong in this system from both the large β_2 and short pulse duration, dispersion is the last effect overcome by nonlinear FCD. This is shown by the ratio $L_D/L_{FCD} > 1$, which indicates the importance of FCD compared to GVD. The temporal broadening mechanism is tied directly to this ratio as we describe below. It is clear that the nonlinear FCD effect ultimately dominates in the system as we increase the input power.

Table 1 summarizes these values for the other wavelengths we investigated. To illustrate the dynamics, we choose an intermediate power point (3 W), as higher power levels are all dominated by FCD. Here we see that L/L_{FCD} is well above a value of 1 in all cases, showing that FCD effects are quite strong even at these modest power levels. Notice that at this intermediate power, the free-carrier effects (L_{FCD}) are stronger than SPM (L_{NL}) and on the order of L_D for all wavelengths. The last ratio in the table, L_D/L'_D, reveals the significance of the second- and third-order dispersion terms over the pulse propagation. Despite being relatively small compared to L_D, later we show that L'_D plays a role in the temporal dynamics.

The largest point of difference between the photonic crystal employed here and nanowire (channel) waveguides is the relative strength of the dispersive and nonlinear effects. More specifically, the dispersion and nonlinear values in nanowire waveguides are smaller than in PhC-wgs [4,33]. Despite these differences, all of the ratios will eventually be dominated by FCD, similar to the PhC-wg. The main difference is the order in which the phenomena are overcome and the required pulse durations and powers. Detailed analysis can be found in Supplement 1. For the case in [33], we expect that significant FCD temporal dynamics will be visible at peak powers slightly

beyond those reported there, which could be achieved with improved insertion loss. Given that shorter pulse durations of hundreds of femtoseconds are often used in nanowires, the pulse energies are the same order of magnitude as those used here for PhC-wgs.

With the physical length scales in mind, we return to Fig. 2(b) and elucidate the dominant mechanism in each region. In the linear regime shaded red in Fig. 2(b), the GVD dominates and the pulse experiences dispersive broadening from its initial pulse duration of 1.3 ps to an output duration scaling with β_2. This significant broadening is due to the fact that the dispersion lengths, L_D (65, 62, and 86 µm for each of the three wavelengths, respectively), are well below the length of the 396 µm PhC-wg. Coherently with the dispersion curve shown in Fig. 1(a), the wavelength with the largest GVD parameter, i.e., 1543 nm with $\beta_2 = -10.1$ ps^2/mm, broadens the most, while 1545 nm, with $\beta_2 = -8.4$ ps^2/mm, broadens the least in the linear regime.

As the peak power coupled into the PhC-wg increases, the pulse tends to narrow in time from its initially dispersion-broadened state, as indicated by the yellow-shaded region in Fig. 2(b). The temporal narrowing in this region is governed by SPM-induced chirp interplaying with the anomalous GVD-induced chirp. Note, however, that the observations here are not higher-order soliton compression, as opposed to our previous work [3]. In this case, the SPM is only beginning to cancel the dispersive chirp.

For all wavelengths, there is a certain peak power threshold from which the pulse experiences a significant temporal broadening, as shown by the blue-shaded region of Fig. 2(b). The power threshold relates to the relative significance of the free carriers with respect to the GVD and sample length and occurs at the point where both $L_D/L_{FCD} > 1$ and $L/L_{FCD} > 1$. The power threshold is different with each wavelength due to the different sample parameters. Physically this nonlinear effect is a direct consequence of the interplay of the anomalous GVD and new blue components generated by FCD, as we will discuss in detail in the next section.

5. TEMPORAL PULSE DYNAMICS DOMINATED BY FREE-CARRIER NONLINEARITY IN SILICON

Figures 4(a) and 4(b) show the normalized intensity for several input power levels in both the time and the frequency domains for the 1543 nm case and the 1545 nm case. The pulse retrieved from the input spectrogram in Fig. 2(a) is used as the simulation input. The red lines represent the retrieved experimental FREG pulses (time) or OSA traces (frequency). Our GNLSE model, indicated by the blue lines, shows excellent agreement with the spectral and temporal profiles of the optical pulses. For all the wavelengths we examined, the pulse consistently experiences a spectral blue shift and accelerates, i.e., diminishes its time of flight, with increasing powers, as clearly indicated in Figs. 4(a) and 4(b). The three previously identified regimes of temporal propagation: dispersive broadening, Kerr-effect narrowing, and free-carrier broadening are noticeable in Figs. 4(a) and 4(b) using the same color code as in Fig. 2(b).
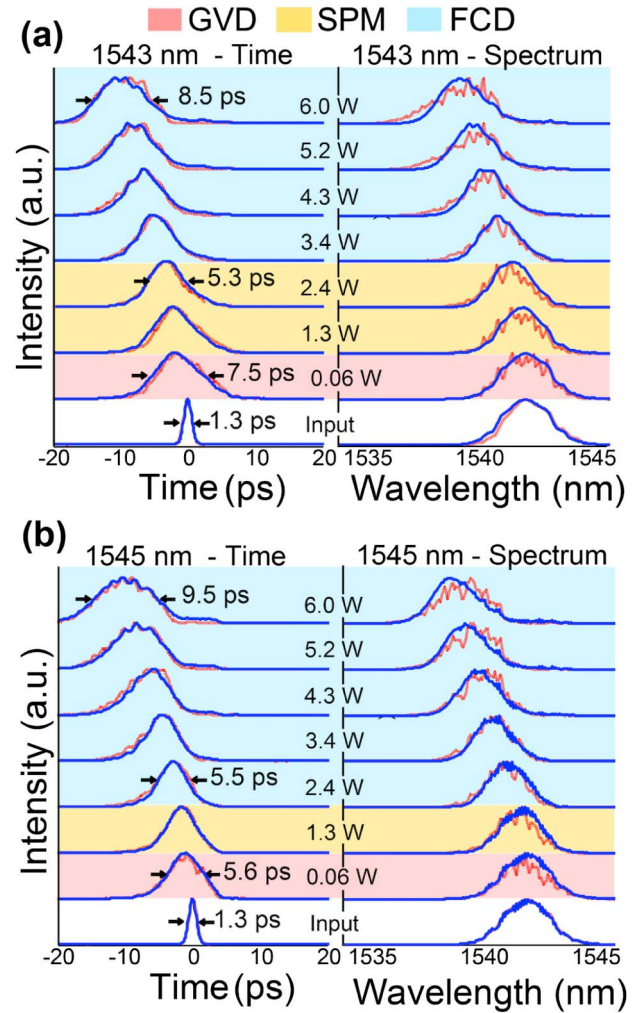
Fig. 4. Temporal and spectral pulse profiles: experiment and model. (a),(b) Normalized intensity in the time and frequency domains for (a) 1543 nm and (b) 1545 nm. The red lines represent the experiment and the solid blue lines the GNLSE simulations. Color-shaded regions indicate the dominant effect: dispersive broadening (GVD, red), Kerr-induced narrowing (SPM, yellow), and free-carrier dispersion broadening (FCD, blue).

As is known from past experiments, the spectral blue shift is a direct consequence of FCD alone [15–17]. This results from the time-dependent phase modulation induced by TPA-generated free carriers: $\delta\omega_{FC} = -\frac{d\phi_{FC}}{dt}$, where $\phi_{FC} = k_o n_{FC} N_c(z, t)$. The inclusion of GVD induces only a small perturbation to this trend in the frequency domain. In contrast, the temporal properties are dominated by the dynamic interaction of FCD with dispersion. For example, the acceleration of the pulse stems from the free-carrier generated blue components traveling faster in time due to the strong anomalous dispersion of the waveguide [3]. In this work we demonstrate pulse temporal advances up to more than six times the initial pulse duration T_{FWHM}, notably larger than any prior reported acceleration [34,35]. Apart from those known effects, here we report a significant nonlinear pulse broadening associated with the FCD-GVD interaction, which we now examine in detail.

Figures [5(a)](5(a))–[5(c)](5(c)) depict the experimental and GNLSE modeled output values of T_{FWHM} as a function of the coupled peak power for the three different wavelengths. The pulse broadens in time at least six times the initial T_{FWHM} for all cases. The strong agreement between the full model (black solid lines) and experiments (markers) across the three cases allows us to switch on and off each effect independently to explain the origins of the observed pulse propagation behavior. We focus on the 1545 nm case in Fig. [5(a)](5(a)), as it gives the clearest presentation of these effects.

First, we focus our attention to the origin of temporal broadening. When we turn the free-carrier effects off in the model there is no broadening, but rather a continued narrowing as shown by the black dashed lines. This is the expected interaction for a pulse undergoing SPM with anomalous GVD. Importantly, we confirm that temporal broadening requires both FCD and GVD. We confirm this by turning off only the GVD and the TOD (red dotted–dashed line) and observing that the pulse does not experience significant broadening at high powers. The marginal change in T_{FWHM} is due to TPA. We further verified that FCA has only a marginal impact for our conditions by turning this off in the model. As this effect is

negligible we exclude this case on the plot for clarity. Switching off TPA (not shown here for simplicity) would result in a narrower pulse, since the SPM-induced chirp would not be capped by this nonlinear absorption mechanism [17,19]. Turning off all effects except SPM, we recover the initial pulse with no temporal changes (blue dotted line).

Examining these results in further detail, we observed physics particular to free carriers interacting with the TOD β_3. To our knowledge, this process has not been reported in the literature. The purple dotted lines in Figs. [5(a)](5(a))–[5(c)](5(c)) represent the results of the pulse duration using our GNLSE model neglecting the effect of TOD ($\beta_3 = 0$). For positive β_3 (+1.1 ps^3/mm) in the case of 1541 nm, the absence of TOD broadens the output pulse. Stated equivalently, the positive β_3 acts counter to the anomalous FCD-GVD-induced broadening. In the case of a large negative β_3 (–2.57 ps^3/mm), as in the 1545 nm case, the absence of TOD results in a narrower pulse, thereby demonstrating negative β_3 reinforces the FCD-GVD broadening. The pulse shape is relatively unchanged for the 1543 nm case.

We have also verified that β_3 has a non-negligible impact on the pulse temporal acceleration. Figure [6](6) shows the measured (green dots) and simulated acceleration for 1545 nm. Notice that the pulse acceleration is stronger with (solid black line) than without TOD (dotted purpled line), from which we conclude that negative β_3 causes larger values of free-carrier-induced acceleration, once again supporting the combined effect of FCD and negative β_2. Two effects can potentially contribute to this: intrapulse TOD broadening and the effective dispersion at the blue-shifted frequency. Intrapulse TOD broadening plays a minor role here due to the relatively long pulses. The effective dispersion β_2' can be understood by recognizing that TOD corresponds to the dispersion slope. The
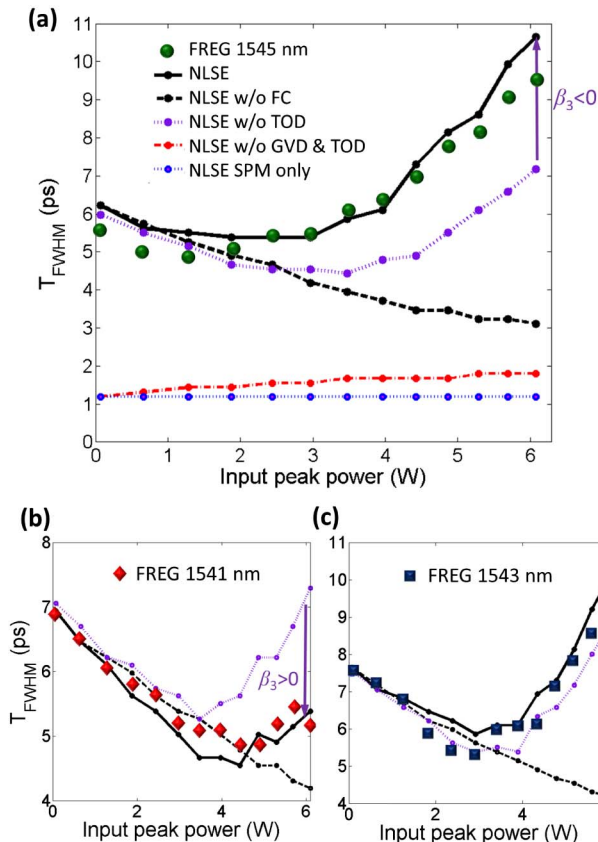
Fig. 5. Nonlinear temporal dynamics in the silicon waveguide FCD-GVD regime. (a)–(c) Pulse duration as a function of coupled peak power for (a) 1545 nm, (b) 1541 nm, and (c) 1543 nm cases. The color markers represent the experimental FREG measurements, the solid black lines represent the full GNLSE simulation, the dashed black lines neglect the free-carrier effects, the purple dotted lines neglect TOD, the red dotted–dashed line neglects GVD and TOD, and the blue dotted line neglects all effects except for SPM.
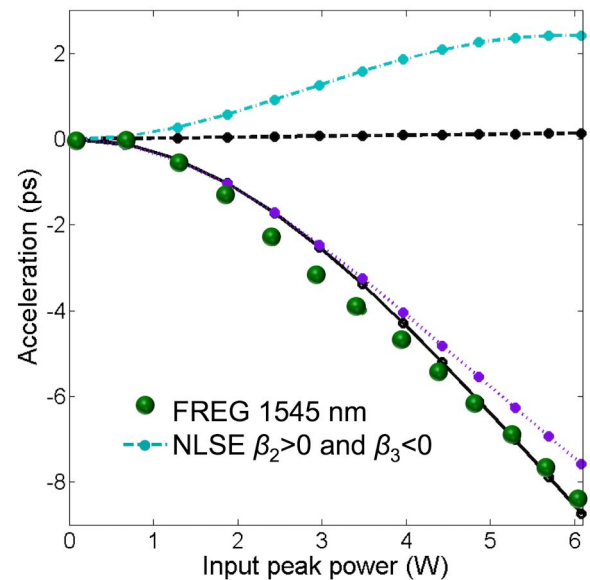
Fig. 6. Pulse acceleration for the 1545 nm case. We show the experimental FREG measurements (colored markers), the full GNLSE simulation (solid black line), free-carrier effects off (dashed black line), TOD off (purple dotted line), and positive β_2 with the remaining parameters from the full simulation (turquoise dot-dashed line).

blue-shifted pulses thus experience the effective dispersion $\beta_2' = \beta_2 + \beta_3 \Delta\omega_{FC}$ [32]. At 1545 nm and $P_0 = 6$ W, the $\beta_3 \Delta\omega_{FC}$ product increases by up to –5.5 ps^2/mm for the maximum blue shift of 0.34 THz. This effect contributes additional pulse acceleration as it is the same order and sign as β_2. It can be seen from β_2' that if the sign of TOD was opposite to GVD, it would instead reduce the effective dispersion and thus acceleration.

Though not experimentally demonstrated here, FCD coupled with normal dispersion ($\beta_2 > 0$) would yield pulse delay and pure temporal broadening of T_{FWHM} while retaining a spectral blue shift. This case (still with negative β_3) is shown as the turquoise dot-dashed line in Fig. 6 with evident pulse delay.

6. FUTURE DIRECTIONS

In this section, we consider the implications of these results from a practical perspective. Silicon waveguides are expected to play a key role as optical interconnects in future integrated opto-electronic chips [36]. Concretely, signal processing of dense optical channels confined to subwavelength waveguides will inevitably trigger nonlinear effects and require mitigation akin to the nonlinear Shannon limit in fiber optic telecommunications networks [37]. The nonlinear temporal broadening mechanism due to FCD-GVD presented here will certainly need to be taken into account in future on-chip photonic networks.

While TPA is intrinsically linked to the band gap of silicon ($E_g = 1.1$ eV), and therefore unavoidable, there are a number of proposed strategies for controlling the free carriers. Some examples include the use of reversed p-i-n junctions to sweep the carriers out of the waveguide [38], the modification of the waveguide fabrication process to minimize the carrier lifetime [39], or the use of short (femtosecond) pulses [40]. Notably, other demonstrations harness p-i-n junctions to inject carriers into the optical mode for modulation [36,41,42], regeneration [43], and detection [44].

These experiments reveal a new approach to control the free-carrier effects with dispersion engineering. In particular the combination of the group index (n_g) and the GVD parameter (β_2) determines the power threshold at which the FC effects start dominating the temporal dynamics. Further, TOD (β_3) becomes an instrument to counteract or support these FC effects in silicon waveguides. This is in analogy with the work presented in [45], where dispersive radiation was used to cancel the most significant higher-order nonlinearity in glass, the Raman effect. Here we control the most significant higher-order nonlinearity in semiconductors, the free-carrier effects. More complex temporal dynamics (T_{FWHM} and acceleration) are possible when dispersion profiles with similar amplitudes of β_2 and β_3 ($L_D/L_D' \sim 1$) and mixed signs are considered. The new insight presented here provides a powerful control mechanism for free-carrier temporal effects in silicon devices simply by designing the waveguide.

7. CONCLUSION

By making use of an ultrasensitive FREG technique we examined the nonlinear pulse dynamics of subpicojoule pulses in nanostructured silicon waveguides directly in the time domain. Importantly, the unique ability to independently tune the dispersion and nonlinearity in our PhC-wg enabled our systematic investigation into different strengths of linear and nonlinear effects, which would be challenging in other media. In particular, we experimentally demonstrated free-carrier-induced temporal broadening of picosecond pulses. The temporal broadening stems from the combination of nonlinear-induced FCD combined with GVD. We further examined the role of β_3 with the conclusion that positive values of the TOD parameter, $\beta_3 > 0$, counteract the effects of free carriers in anomalous dispersion media, whereas $\beta_3 < 0$ reinforces them. These results were supported by strong agreement with a numerical GNLSE model. The physics unveiled in this paper provide further insight into the role of free carriers in nonlinear pulse propagation in silicon and means to control their effects. These realizations could be key to the development of optical interconnects and data processing in integrated CMOS opto-electronic chips.

See Supplement 1 for supporting content.

REFERENCES

1. J. Leuthold, C. Koos, and W. Freude, "Nonlinear silicon photonics," Nat. Photonics **4**, 535–544 (2010).
2. D. T. H. Tan, P. C. Sun, and Y. Fainman, "Monolithic nonlinear pulse compressor on a silicon chip," Nat. Commun. **1**, 116 (2010).
3. A. Blanco-Redondo, C. Husko, D. Eades, Y. Zhang, J. Li, T. F. Krauss, and B. J. Eggleton, "Observation of soliton compression in silicon photonic crystals," Nat. Commun. **5**, 3160 (2014).
4. I.-W. Hsieh, X. Chen, X. Liu, J. I. Dadap, N. C. Panoiu, C.-Y. Chou, F. Xia, W. M. Green, Y. A. Vlasov, and R. M. Osgood, "Supercontinuum generation in silicon photonic wires," Opt. Express **15**, 15242–15249 (2007).
5. S. Clemmen, K. P. Huy, W. Bogaerts, R. G. Baets, P. Emplit, and S. Massar, "Continuous wave photon pair generation in silicon-on-insulator waveguides and ring resonators," Opt. Express **17**, 16558–16570 (2009).
6. Y. Takahashi, Y. Inui, M. Chihara, T. Asano, R. Terawaki, and S. Noda, "A micrometre-scale Raman silicon laser with a microwatt threshold," Nature **498**, 470–474 (2013).
7. C. Monat, C. Grillet, M. Collins, A. Clark, J. Schroeder, C. Xiong, J. Li, L. O'Faolain, T. F. Krauss, B. J. Eggleton, and D. J. Moss, "Integrated optical auto-correlator based on third harmonic generation in a silicon photonic crystal waveguide," Nat. Commun. **5**, 3246 (2014).

8. T. Baehr-Jones, T. Pinguet, P. L. Guo-Qiang, S. Danziger, D. Prather, and M. Hochberg, "Myths and rumours of silicon photonics," Nat. Photonics **6**, 206–208 (2012).

9. M. A. Foster, A. C. Turner, J. E. Sharping, B. S. Schmidt, M. Lipson, and A. L. Gaeta, "Broad-band optical parametric gain on a silicon photonic chip," Nature **441**, 960–963 (2006).

10. V. Raghunathan, R. Claps, D. Dimitropoulos, and B. Jalali, "Wavelength conversion in silicon using Raman induced four-wave mixing," Appl. Phys. Lett. **85**, 34–36 (2004).

11. F. Leo, S. Coen, P. Kockaert, S.-P. Gorza, P. Emplit, and M. Haelterman, "Temporal cavity solitons in one-dimensional Kerr media as bits in an all-optical buffer," Nat. Photonics **4**, 471–476 (2010).

12. T. D. Vo, B. Corcoran, J. Schröder, M. D. Pelusi, D.-X. Xu, A. Densmore, R. Ma, S. Janz, D. J. Moss, and B. Eggleton, "Silicon-chip-based real-time dispersion monitoring for 640 Gbit/s DPSK signals," J. Lightwave Technol. **29**, 1790–1796 (2011).

13. D. Vukovic, Y. Ding, H. Hu, H. Ou, L. K. Oxenlø we, and C. Peucheret, "Polarization-insensitive wavelength conversion of 40 Gb/s NRZ-DPSK signals in a silicon polarization diversity circuit," Opt. Express **22**, 12467–12474 (2014).

14. P. Chaisakul, D. Marris-Morini, J. Frigerio, D. Chrastina, M.-S. Rouifed, S. Cecchi, P. Crozat, G. Isella, and L. Vivien, "Integrated germanium optical interconnects on silicon substrates," Nat. Photonics **8**, 482–488 (2014).

15. C. Monat, B. Corcoran, M. Ebnali-Heidari, C. Grillet, B. J. Eggleton, T. P. White, L. O'Faolain, and T. F. Krauss, "Slow light enhancement of nonlinear effects in silicon engineered photonic crystal waveguides," Opt. Express **17**, 2944–2953 (2009).

16. C. A. Husko, A. S. Clark, M. J. Collins, A. De Rossi, S. Combrié, G. Lehoucq, I. H. Rey, T. F. Krauss, C. Xiong, and B. J. Eggleton, "Multi-photon absorption limits to heralded single photon sources," Sci. Rep. **3**, 3087 (2013).

17. L. Yin and G. P. Agrawal, "Impact of two-photon absorption on self-phase modulation in silicon waveguides," Opt. Lett. **32**, 2031–2033 (2007).

18. R. A. Soref and B. R. Bennett, "Electrooptical effects in silicon," IEEE J. Quantum Electron. **23**, 123–129 (1987).

19. C. A. Husko, S. Combrié, P. Colman, J. Zheng, A. De Rossi, and C. W. Wong, "Soliton dynamics in the multiphoton plasma regime," Sci. Rep. **3**, 1100 (2013).

20. P. Colman, C. Husko, S. Combrie, I. Sagnes, C. W. Wong, and A. De Rossi, "Temporal solitons and pulse compression in photonic crystal waveguides," Nat. Photonics **4**, 862–868 (2010).

21. J. Zhang, Q. Lin, G. Piredda, R. W. Boyd, G. P. Agrawal, and P. M. Fauchet, "Optical solitons in a silicon waveguide," Opt. Express **15**, 7682–7688 (2007).

22. C. Dorrer and I. Kang, "Simultaneous temporal characterization of telecommunication optical pulses and modulators by use of spectrograms," Opt. Lett. **27**, 1315–1317 (2002).

23. D. A. Miller, "Device requirements for optical interconnects to silicon chips," Proc. IEEE **97**, 1166–1185 (2009).

24. J. Li, L. O'Faolain, I. H. Rey, and T. F. Krauss, "Four-wave mixing in photonic crystal waveguides: slow light enhancement and limitations," Opt. Express **19**, 4458–4463 (2011).

25. N. A. R. Bhat and J. E. Sipe, "Optical pulse propagation in nonlinear photonic crystals," Phys. Rev. E **64**, 056604 (2001).

26. R. W. Boyd, "Material slow light and structural slow light: similarities and differences for nonlinear optics [invited]," J. Opt. Soc. Am. B **28**, A38–A44 (2011).

27. R. Trebino, K. W. DeLong, D. N. Fittinghoff, J. N. Sweetser, M. A. Krumbügel, B. A. Richman, and D. J. Kane, "Measuring ultrashort laser pulses in the time-frequency domain using frequency-resolved optical gating," Rev. Sci. Instrum. **68**, 3277–3295 (1997).

28. B. C. Thomsen, M. A. F. Roelens, R. T. Watts, and D. J. Richardson, "Comparison between nonlinear and linear spectrographic techniques for the complete characterization of high bit-rate pulses used in optical communications," IEEE Photon. Technol. Lett. **17**, 1914–1916 (2005).

29. A. D. Bristow, N. Rotenberg, and H. M. van Driel, "Two-photon absorption and Kerr coefficients of silicon for 850–2200 nm," Appl. Phys. Lett. **90**, 191104 (2007).

30. S. Johnson and J. Joannopoulos, "Block-iterative frequency-domain methods for Maxwell's equations in a planewave basis," Opt. Express **8**, 173–190 (2001).

31. M. Soljacic and J. D. Joannopoulos, "Enhancement of nonlinear effects using photonic crystals," Nat. Mater. **3**, 211–219 (2004).

32. G. P. Agrawal, *Nonlinear Fiber Optics*, 5th ed. (Academic, 2013).

33. W. Ding, A. V. Gorbach, W. J. Wadsworth, J. C. Knight, D. V. Skryabin, M. J. Strain, M. Sorel, and R. M. D. L. Rue, "Time and frequency domain measurements of solitons in subwavelength silicon waveguides using a cross-correlation technique," Opt. Express **18**, 26625–26630 (2010).

34. J. Liao, M. Marko, X. Li, H. Jia, J. Liu, Y. Tan, J. Yang, Y. Zhang, W. Tang, M. Yu, G.-Q. Lo, D.-L. Kwong, and C. W. Wong, "Cross-correlation frequency-resolved optical gating and dynamics of temporal solitons in silicon nanowire waveguides," Opt. Lett. **38**, 4401–4404 (2013).

35. F. Raineri, T. J. Karle, V. Roppo, P. Monnier, and R. Raj, "Time-domain mapping of nonlinear pulse propagation in photonic-crystal slow-light waveguides," Phys. Rev. A **87**, 041802 (2013).

36. G. T. Reed, G. Mashanovich, F. Gardes, and D. Thomson, "Silicon optical modulators," Nat. Photonics **4**, 518–526 (2010).

37. A. D. Ellis, J. Zhao, and D. Cotter, "Approaching the non-linear Shannon limit," J. Lightwave Technol. **28**, 423–433 (2010).

38. R. Jones, H. Rong, A. Liu, A. Fang, M. Paniccia, D. Hak, and O. Cohen, "Net continuous wave optical gain in a low loss silicon-on-insulator waveguide by stimulated Raman scattering," Opt. Express **13**, 519–525 (2005).

39. M. Waldow, T. Plötzing, M. Gottheil, M. Först, J. Bolten, T. Wahlbrink, and H. Kurz, "25 ps all-optical switching in oxygen implanted silicon-on-insulator microring resonator," Opt. Express **16**, 7693–7702 (2008).

40. L. Yin, Q. Lin, and G. P. Agrawal, "Soliton fission and supercontinuum generation in silicon waveguides," Opt. Lett. **32**, 391–393 (2007).

41. Q. Xu, B. Schmidt, S. Pradhan, and M. Lipson, "Micrometre-scale silicon electro-optic modulator," Nature **435**, 325–327 (2005).

42. H. C. Nguyen, Y. Sakai, M. Shinkawa, N. Ishikura, and T. Baba, "10 Gb/s operation of photonic crystal silicon optical modulators," Opt. Express **19**, 13000–13007 (2011).

43. F. D. Ros, D. Vukovic, A. Gajda, K. Dalgaard, L. Zimmermann, B. Tillack, M. Galili, K. Petermann, and C. Peucheret, "Phase regeneration of DPSK signals in a silicon waveguide with reverse-biased p-i-n junction," Opt. Express **22**, 5029–5036 (2014).

44. L. Chen, K. Preston, S. Manipatruni, and M. Lipson, "Integrated GHz silicon photonic interconnect with micrometer-scale modulators and detectors," Opt. Express **17**, 15248–15256 (2009).

45. D. V. Skryabin, F. Luan, J. C. Knight, and P. S. J. Russell, "Soliton self-frequency shift cancellation in photonic crystal fibers," Science **301**, 1705–1708 (2003).

optica

Platform for enhanced light–graphene interaction length and miniaturizing fiber stereo devices

Jun-long Kou,[1,†] Jin-hui Chen,[1,†] Ye Chen,[1] Fei Xu,[1,*] and Yan-qing Lu[1,2]

[1]*National Laboratory of Solid State Microstructures and College of Engineering and Applied Sciences, Nanjing University, Nanjing 210093, China*

[2]*e-mail: yqlu@nju.edu.cn*

*Corresponding author: feixu@nju.edu.cn*

Sufficient light–matter interactions are important for waveguide-coupled graphene optoelectronic devices. Subwavelength-diameter microfibers (MFs) with a strong evanescent field are attractive for graphene integration in fiber optics system, which can be realized by covering or wrapping a graphene sheet on a straight and thin MF. However, it is challenging to handle such a thin MF and graphene for sufficient length and strength of interaction. Using an MF-based lab-on-a-rod technique, we present a platform for ultralong light–graphene interaction and design graphene-integrated helical MF devices. Using this approach, we experimentally demonstrate polarization manipulation by wrapping an MF on a rod pretreated with a graphene sheet. The device can operate as not only a broadband polarizer but also a high-Q single-polarization resonator by tuning the geometry of MF coils. By specializing the rod surface and coil geometry, we believe the platform could contribute to advancing the research for more graphene–MF-integrated devices including modulators and photodetectors. © 2014 Optical Society of America

Since the discovery of graphene, the optical properties of two-dimensional Dirac fermions have been studied extensively [1,2]. By utilizing properties such as linear optical absorption, saturable absorption, and the tunability of chemical potential through doping or electrical gating, various broadband applications [3], such as modulators [4,5], photon detectors [6,7], polarizers [8], and mode-lock lasers [9,10], have been realized. Most practical applications require graphene to be integrated with existing photonic technology to attain sufficient interaction lengths between the graphene and optical field because the interaction length is limited by the thickness of graphene for normal incident light in conventional free-space optical systems. This integration can be readily achieved by transferring and laminating graphene on top of waveguides [11]. In fiber optics systems, side-polishing or flame-drawing techniques are employed to obtain D-shaped fibers or microfibers (MFs) [8,12], which provide an accessible evanescent field. In particular, MFs with a strong evanescent fields have attracted increasing attention. Hybrid graphene–microfiber (GMF) devices can be fabricated by covering or wrapping a graphene sheet on a straight, thin MF [13]. However, it is still challenging to handle such a thin MF–graphene structure for sufficient lengths and strengths of interaction. Here, relying on the MF-based lab-on-a-rod technique, we present an alternative approach to integrate GMF devices by wrapping an MF on a graphene-coated rod, schematically shown in Fig. 1. Implementation of the approach is simple and efficient because the process only involves coating a small piece of graphene onto a rod. While maintaining a strong evanescent field, the GMF interaction length can, in theory, be increased arbitrarily with a helical structure of multicoils. Another unique advantage is the possible formation of resonators with strong coupling between adjacent coils through adjustment of the spring pitches. The approach provides new opportunities for elaboration of stereo GMF-integrated devices. Various all-fiber graphene devices are expected to be developed by employing such a flexible platform; such devices include electrical or optical modulators, photon detectors, and polarization controlling components (PCCs). In this work, we show the platform's application to broadband polarization manipulation.
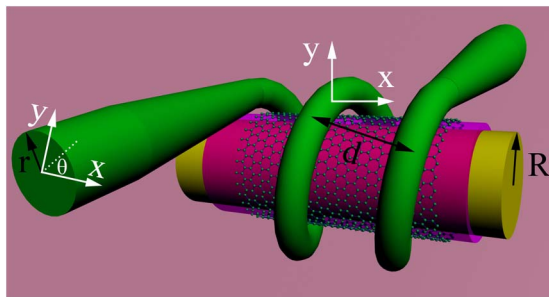
Fig. 1. Schematic of a graphene-based MF in-line polarizer with a two-coil structure. The rod's diameter is hundreds of times larger than that of the MF. The GMF interaction length can be extended nearly indefinitely on a small piece of graphene by increasing the number of helical turns. R, radius of the rod; r, radius of the MF; θ, angle between the incident polarization direction and the x axis. Two sets of local coordinates are shown, one at the input and the other in the middle. The dominant component of the electric field for the even and odd modes is polarized in the x and y directions, respectively.

Polarization behavior has a profound impact on the performance of optical-fiber devices and systems [8,14]. To implement optical-fiber devices in practical applications, control and manipulation of the polarization state of light is highly desirable. All-fiber PCCs are more attractive because manipulating free-space PCCs during collimating, aligning, and (re) focusing is time consuming and labor intensive. However, conventional-fiber PCCs have to be carefully kept as straight as possible to prevent additional birefringence. This requires splicing or connecting and careful assembly as well as alignment to achieve the desired optical performance. It is also difficult to coil conventional-fiber PCCs well and form a single-polarization microresonator. Moreover, miniaturization of devices is important for large scale. One of the apparent advantages of our device is the compact footprint attributed to its coil configuration, which employs the stereo structure. Recently, we demonstrated a broadband single-polarization resonator based on a silver-film configuration [15]. Here, we take one step forward by mating MF with a 2D graphene sheet, which interacts strongly with an in-plane lightwave. Meanwhile, due to the unique dispersion property of graphene, the stereo device in this Letter exhibits intriguing results that are not likely to be expected in the silver-film devices due to the tremendous difference in the fabrication method and polarization behavior. In particular, the extinction ratio (ER) is intensity dependent because of the special absorption properties of graphene.

In this study, a stereo GMF-integrated platform and the so-called wrap-on-a-rod technique are used to enable the integration and miniaturization of multifunctional GMF PCCs. The key to the technique lies in the graphene specialization of the rod's surface, which interacts strongly with the evanescent field propagating outside the MF. By adjusting the neighboring distance of the coils, a compact in-line polarizer or high-Q single-polarization resonator can be obtained. This stereo graphene-integrated resonator with unique 3D geometry eliminates the requirement of separate couplers, which makes the resonator especially attractive for special applications, such as

gyroscopes and current sensors. This preliminary work could lay the foundation for future lab-on-a-rod GMF devices.

Figure 1 is a schematic of the GMF in-line polarizer (GMF-IP) or GMF single-polarization resonator (GMF-SR). The only difference between these lies in the distance (d, as labeled in Fig. 1) between neighboring coils. To prevent the loss induced by the relatively high-index rod (polymethyl methacrylate or PMMA, diameter is ~2 mm), a thin layer of low-index Teflon (Teflon AF 601S1-100-6, DuPont, tens of micrometers in thickness, index is ~1.31) was initially dip-coated on the rod surface. A monolayer graphene sheet (ACS Material) grown by chemical vapor deposition (CVD) was then mechanically transferred onto the surface of the Teflon coating. The length of the graphene sheet was carefully tailored so that it could be wrapped around the rod such that the opposite edges meet at the same line and do not overlap. Finally, an MF (~3 μm in diameter) was tightly wrapped on the graphene sheet supported by the rod.

The broken symmetry with respect to the local $y = 0$ plane causes the nondegeneracy of the two fundamental modes in this hybrid structure. Here, we define the mode with the dominant electric field component in the x direction (E_x) as an even mode because E_x is symmetric to the mirror plane ($x = 0$ plane, perpendicular to the local graphene plane). The other mode, mainly polarized in the y direction, is considered an odd mode. Because of the large evanescent field of the MF, a fraction of the light field penetrates the ambient environment, including the graphene sheet. For intrinsic or slightly doped graphene ($|\mu| < h\omega/4\pi$), an inter band transition dominates the high-frequency dynamic conductivity within the range from visible to infrared (IR) [3]. Thus, the existence of the graphene sheet contributes to the losses in different modes, causing the device to exhibit a contrasting ER.

We first studied the optical transmission properties of the GMF-IP, in which a distance (tens of micrometers) was maintained between different coils of the MF to prevent mutual coupling [16]. The ER was experimentally measured in the near IR (NIR) range, from 1200 to 1650 nm. We chose this range because many high-order modes appear below 1200 nm, and the broadband light source (SuperK Versa, NKT) terminates near 1650 nm. By incorporating a linear polarizer followed by a half-wave plate between the source and the device, the polarization state of the incident light can be controlled by rotating the plate. As clearly shown in Fig. 2, maximum transmission is achieved at $\theta = 90°$, in which case the odd mode is excited, whereas minimum transmission occurs at $\theta = 0°$. The device with a one-coil structure (meaning that the MF is in contact with the graphene sheet over ~6.3 mm) gives an ER of ~5 dB at 1310 nm and ~8 dB at 1550 nm. As the operating wavelength increases, the ER increases; this phenomenon will be explained below. To further increase ER, a longer MF was employed to form a two-coil [Fig. 3(a)] or multicoil structure. As expected, ER nearly doubled when the contact between the MF and graphene was lengthened to ~12.6 mm. We note a dip in the output spectrum around 1380 nm, which is possibly caused by the absorption loss of the extra OH groups released during hydrogen flame heating [17]. A control experiment was also performed on an MF
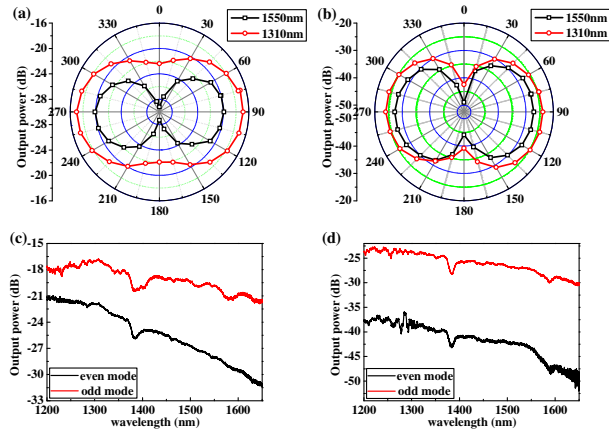
Fig. 2. Output power as a function of θ at 1310 and 1550 nm for (a) a one-coil structure and (b) a two-coil structure. The data were recorded by rotating the half-wave plate in 7.5° increments. Wavelength-dependent output power for (c) one-coil structure and (d) a two-coil structure. The black (red) line represents the data at $\theta = 0°$ (90°).

wrapped on a rod pretreated only with Teflon coating, without a graphene sheet. The results show no evident polarizing effect.

When adjacent coils of the MF are sufficiently close, they form a high-Q resonator [18]. We carefully wrapped two MF coils onto the graphene-coated rod with the help of a microscope to ensure that the coils were close to each other, as illustrated in Fig. 3(b). The transmission spectra of GMF-SR for two orthogonal modes (even and odd) are shown in Fig. 4. They clearly differ in output power because the modes suffer from different propagation losses. From Fig. 4(b), we find that around the telecommunication wavelength of 1550 nm, the free spectral range (FSR) and full width at half-maximum (FWHM) are approximately 0.23 nm and 0.08 nm, respectively, indicating that the Q-factor approaches 2×10^4. The difference in output power between the dips of the two modes is ~11 dB, from which we conclude that the device could work as a single-polarization resonator. In this manner, mutual coupling between different modes could be well suppressed, which is especially attractive for certain specialized applications such as gyroscopes and current sensors. This functionality cannot be realized in a one-dimensional fiber system. The ER could be further improved if the MFs are drawn into even thinner structures.

To confirm the experimental results, we theoretically analyzed the mode losses. In our simulations, the ultrathin graphene sheet was treated as a 1-nm-thick dielectric layer. The relative permittivity of graphene was obtained using the
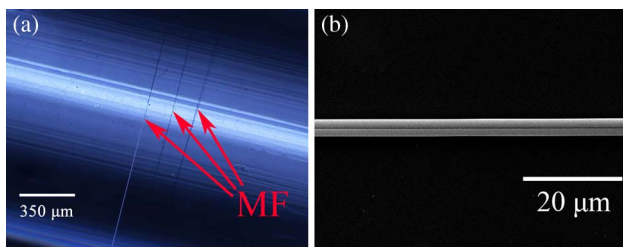

Fig. 3. (a) Optical microscope image of a two-coil MF wrapped on a rod pretreated with Teflon coating and a graphene sheet. (b) Scanning electron microscope image of two coils close to each other.
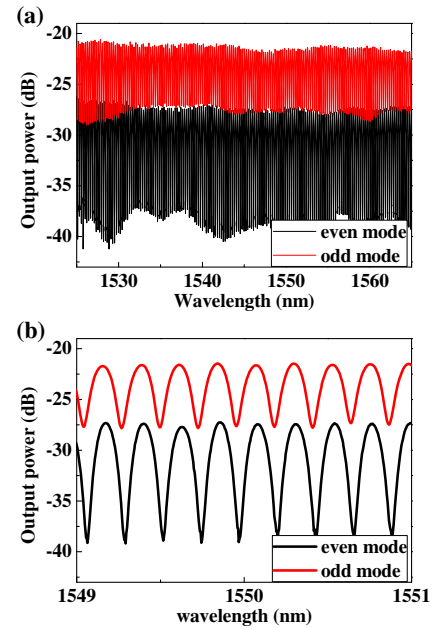

Fig. 4. (a) Transmission spectrum of the graphene-based resonator for two orthogonal modes. (b) Detailed expansion of the spectrum at around 1550 nm.

relation $\varepsilon = 1 + i\sigma/\varepsilon_0\omega d$, where σ is the dynamical conductivity determined from the Kubo formula, ε_0 is the permittivity of vacuum, and ω is the operating frequency [3]. The theoretical ER was obtained via $(\alpha_{\mathrm{even}} - \alpha_{\mathrm{odd}})L_{\mathrm{MF}}$, with α_i ($i =$ even or odd) being the attenuation constant of each mode and L_{MF} being the length of the MF in contact with the graphene sheet. α_i can be readily obtained from the imaginary part of the propagation constants solved by the finite element method. Figure 5(a) displays the results of ER versus operating wavelength for GMF-IP. The trend of the experimental results
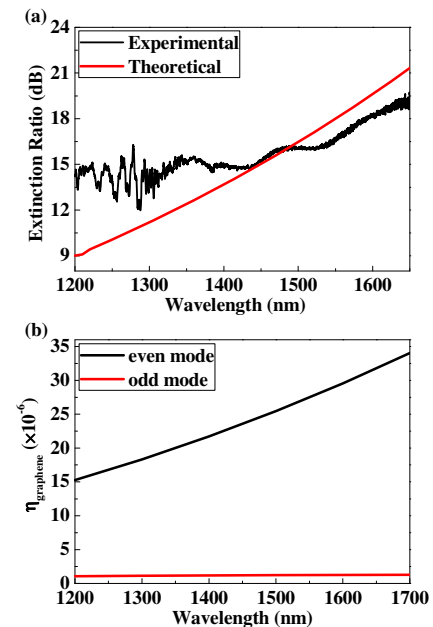
Fig. 5. (a) Experimental and theoretical results of ER for GMF-IP. (b) Calculated time-averaged power flow ratio for power carried by the graphene sheet as a function of wavelength.
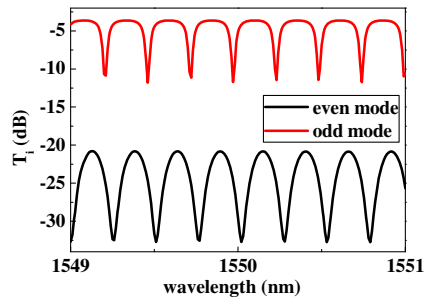
Fig. 6. Calculated transmission of the GMF-SR based on a semi-theoretical method. Insertion loss resulting from coupling, connection, scattering, and bending was not taken into account here.

follows that of the theory at high frequencies. However, mismatch appears at wavelengths below 1300 nm. This mismatch can be attributed to the contribution of high-order modes and the nonuniformity of MFs, both of which are neglected in our calculation. Moreover, ER increases with the wavelength, which is also observed in Ref. [8]. Another calculation was performed to obtain the time-averaged power flow ratio in the graphene layer (η_{graphene}), shown in Fig. 5(b). For the even mode, we clearly see that as the wavelength increases, η_{graphene} increases. For the odd mode, however, η_{graphene} remains constant over the 450 nm wavelength range. Because the graphene sheet is a lossy medium, more energy will be attenuated when η_{graphene} is high. This explains the increasing tendency of ER in Fig. 5(a).

For GMF-SR, the transmission spectrum of each mode can be obtained (Fig. 6) through the following equation, which incorporates loss [19]:

$$T_i = \frac{e^{-4\pi R\beta_{2,i}} + \sin^2(2\pi R\kappa_i) - 2\sin(2\pi R\beta_{1,i})\sin(2\pi R\kappa_i)e^{-2\pi R\beta_{2,i}}}{e^{4\pi R\beta_{2,i}} + \sin^2(2\pi R\kappa_i) - 2\sin(2\pi R\beta_{1,i})\sin(2\pi R\kappa_i)e^{2\pi R\beta_{2,i}}},$$

(1)

where $\beta_{1,i}$ and $\beta_{2,i}$ are the real and imaginary parts of the complex propagation constant, respectively, R is the radius of the rod, and κ_i is the coupling coefficient for the corresponding mode. Here, a semi-theoretical method was employed. $\beta_{1,i}$ and $\beta_{2,i}$ were calculated by the finite element method, while $2\pi R\kappa_{\text{even}} = 0.15$ and $2\pi R\kappa_{\text{odd}} = 1.0$ were chosen to fit the experimental results. These values of κ_i were selected on the basis of two aspects. On one hand, κ_i is dependent on polarization. On the other hand, κ_i is difficult to predict because it is sensitive to both the distance between neighboring coils and the MF radius. In the fitting, the insertion loss (I_i) of different modes resulting from coupling, connection, scattering, and bending was not included. The calculated FSR was ~0.25 nm, which is close to the experimentally observed value (~0.23 nm). The even mode exhibits a lower transmission than the odd mode because, in the even mode, the electric field, mainly polarized in the x direction, interacts more with the graphene sheet.

In conclusion, we have presented a new platform for miniaturizing GMF-integrated stereo devices. The unique geometry practically enables multiple light–graphene interaction lengths on a small piece of graphene, and the realization of a number of GMF broadband devices, including microresonators. As an

example, we demonstrated the in-line manipulation of polarization with GMF-integrated devices. First, a GMF-IP was shown to achieve an ER of 8 dB/coil. By employing a two-coil structure, an ER as high as ~16 dB was obtained over a 450 nm bandwidth in the telecommunication wavelength range. Second, we took a step toward the realization of a high-Q graphene-based SR with excellent suppression of polarization noise and used a semi-empirical model to explain the results. Similar results are expected with the use of RGB fibers in the visible range and endless single-mode photonic crystal fibers over the visible to NIR range. Moreover, our design also gives insights into the realization of future lab-on-a-rod devices and provides the general recipe for optoelectrical applications on the integration of MFs with the fast rising 2D materials, including graphene and transition metal dichalcogenide.

REFERENCES

1. F. Bonaccorso, Z. Sun, T. Hasan, and A. C. Ferrari, Nat. Photonics **4**, 611 (2010).
2. P. Avouris, Nano Lett. **10**, 4285 (2010).
3. Q. Bao and K. P. Loh, ACS Nano **6**, 3677 (2012).
4. M. Liu, X. Yin, E. Ulin-Avila, B. Geng, T. Zentgraf, L. Ju, F. Wang, and X. Zhang, Nature **474**, 64 (2011).
5. M. Liu, X. Yin, and X. Zhang, Nano Lett. **12**, 1482 (2012).
6. F. Xia, T. Mueller, Y.-M. Lin, A. Valdes-Garcia, and P. Avouris, Nat. Nanotechnol. **4**, 839 (2009).
7. T. Mueller, F. Xia, and P. Avouris, Nat. Photonics **4**, 297 (2010).
8. Q. Bao, H. Zhang, B. Wang, Z. Ni, C. H. Y. X. Lim, Y. Wang, D. Y. Tang, and K. P. Loh, Nat. Photonics **5**, 411 (2011).
9. H. Zhang, Q. Bao, D. Tang, L. Zhao, and K. Loh, Appl. Phys. Lett. **95**, 141103 (2009).
10. Z. Sun, T. Hasan, F. Torrisi, D. Popa, G. Privitera, F. Wang, F. Bonaccorso, D. M. Basko, and A. C. Ferrari, ACS Nano **4**, 803 (2010).
11. S. J. Koester and L. Mo, IEEE J. Sel. Top. Quantum Electron. **20**, 84 (2014).
12. W. Li, B. Chen, C. Meng, W. Fang, Y. Xiao, X. Li, Z. Hu, Y. Xu, L. Tong, H. Wang, W. Liu, J. Bao, and Y. R. Shen, Nano Lett. **14**, 955 (2014).
13. Z.-B. Liu, M. Feng, W.-S. Jiang, W. Xin, P. Wang, Q.-W. Sheng, Y.-G. Liu, D. N. Wang, W.-Y. Zhou, and J.-G. Tian, Laser Phys. Lett. **10**, 065901 (2013).
14. V. I. Kopp, V. M. Churikov, J. Singer, N. Chao, D. Neugroschl, and A. Z. Genack, Science **305**, 74 (2004).
15. J.-H. Chen, Y. Chen, W. Luo, J.-L. Kou, F. Xu, and Y.-Q. Lu, Opt. Express **22**, 17890 (2014).
16. J.-L. Kou, Y. Chen, F. Xu, and Y.-Q. Lu, Opt. Express **20**, 28431 (2012).
17. H. Osanai, T. Shioda, T. Moriyama, S. Araki, M. Horiguchi, T. Izawa, and H. Takata, Electron. Lett. **12**, 549 (1976).
18. G. Brambilla, J. Opt. **12**, 043001 (2010).
19. M. Sumetsky, Opt. Express **12**, 2303 (2004).

Phase-locked, chip-based, cascaded stimulated Brillouin scattering

Thomas F. S. Büttner,[1,*] Moritz Merklein,[1] Irina V. Kabakova,[1] Darren D. Hudson,[1] Duk-Yong Choi,[2] Barry Luther-Davies,[2] Stephen J. Madden,[2] and Benjamin J. Eggleton[1]

[1]*CUDOS, Institute of Photonics and Optical Science (IPOS), School of Physics, University of Sydney, NSW 2006, Australia*

[2]*CUDOS, Laser Physics Centre, Australian National University, Canberra, ACT 0200, Australia*

*Corresponding author: thomasb@physics.usyd.edu.au

Compact optical frequency comb sources with gigahertz repetition rates are desirable for a number of important applications including arbitrary optical waveform generation and direct comb spectroscopy. We report the generation of phase-locked, gigahertz repetition rate optical frequency combs in a chalcogenide photonic chip. The combs are formed via the interplay of stimulated Brillouin scattering and Kerr-nonlinear four-wave mixing in an on-chip Fabry–Perot waveguide resonator incorporating a Bragg grating. Phase-locking of the comb is confirmed with real-time measurements, and a chirp of the comb repetition rate within the pump pulse was observed. These results represent a significant step towards the realization of integrated optical frequency comb sources with gigahertz repetition rates. © 2014 Optical Society of America

Compact optical frequency comb sources with gigahertz repetition rates have applications ranging from arbitrary optical waveform generation [1] and direct comb spectroscopy [2] to advanced telecommunications. In practice, however, such sources are difficult to achieve: conventional passively mode-locked lasers have repetition rates on the order of 10–100 MHz [3], whereas most Kerr combs generated in microresonators have repetition rates on the order of terahertz [1,4]. The nonlinear optical process of stimulated Brillouin scattering (SBS) enables the generation of highly coherent gigahertz-frequency shifted waves [5]. It is based on inelastic scattering on acoustic phonons, leading to the generation of Stokes waves, which are Doppler shifted by the acoustic resonance frequency ($\nu_B \sim 7\text{–}11$ GHz for most glasses).

In the presence of cavity feedback, the threshold of SBS is reduced and SBS can be cascaded, leading to the formation of Brillouin frequency combs (BFCs) with a comb line spacing equal to the Brillouin frequency shift ν_B [6–11]. In contrast to both passively mode-locked lasers and Kerr combs generated in microresonators, the frequency spacing of BFCs is determined by the acoustic properties of the medium and is independent of the resonator dimensions.

Phase-locking of the spectral components of BFCs is required for most applications. The SBS process, however, does not provide a mechanism for phase-locking. Recently, phase-locked generation of BFCs in a Fabry–Perot (FP) fiber resonator was reported [12]. The phase-locking mechanism was attributed to Kerr-nonlinear four-wave mixing (FWM). Due to the long resonator length (38 cm), however, the demonstrated device was very sensitive to environmental fluctuation, limiting its performance. Furthermore, the fiber-based resonator is not compatible with integration of other functionalities such as on-chip lasers [13].

Here, we report for the first time to our knowledge chip-based generation of phase-locked BFCs. The BFCs were generated in a novel configuration consisting of a low-finesse FP resonator incorporating an on-chip Bragg grating. The FP resonator was formed by the facet reflections of a 6.5 cm long As_2S_3 chalcogenide glass [14] rib waveguide. Enhancement of nonlinear interactions by the Bragg grating was essential for the comb generation, due to the small feedback from the facets. Phase-locking of the comb was confirmed by real-time measurements. The RF spectrum of the BFC was analyzed, revealing a chirp (130 kHz/ns) of the comb repetition rate within the pump pulse without loss of phase-locking.

Figure 1(a) illustrates the generation of phase-locked BFCs in FP resonators. The frequency combs are generated via the

interplay of SBS of counterpropagating and FWM of copropagating comb components. Initially, a narrow band optical pump with frequency ν_0 is coupled into the resonator. If the pump power is above a certain threshold value, it can excite the first-order Stokes wave via SBS at frequency $\nu_{-1} = \nu_0 - \nu_B$ (at longer wavelength). This initial frequency shift determines the repetition rate of the comb. Copropagating pump and first-order Stokes waves can then generate anti-Stokes waves ($j > 0$) and higher-order Stokes waves ($j < -1$) via FWM at frequencies $\nu_j = \nu_0 + j\nu_B$, where j is an integer [6]. These newly generated frequencies are also coupled by SBS since they inherit the initial frequency shift of the Stokes wave ν_B.

SBS by itself would not lead to phase-locking of BFCs as it only couples adjacent comb components and is independent of the spectral phase [12,15]. Unequally spaced frequency components would also be expected in the absence of an additional nonlinear effect than SBS. The comb frequency components have a linewidth much narrower than the Brillouin gain bandwidth [16] $\Delta\nu_B \sim 15$–80 MHz due to cavity feedback [17], and their exact frequencies are individually subject to frequency pulling arising from the interplay of gain, cavity resonances, and nonlinear phase shifts [12,15]. On the other hand, FWM is sensitive to the spectral phase [1,18], and the contribution of FWM can lead to equally spaced, phase-locked BFCs with deterministic spectral phases [12].

A schematic of the configuration used to generate and characterize chip-based BFCs is shown in Fig. 1(b). Polarized, quasi-continuous-wave (quasi-CW) pump light at $\lambda = 1551$ nm consisting of 300 ns long square pulses at 20 kHz repetition rate was used. A trace of one input pulse observed with an oscilloscope is shown in Fig. 1(b). The linewidth of the input light was estimated to be ~ 3 MHz determined by the temporal pulse length. The FP waveguide resonator used as a BFC resonator was a $L = 6.5$ cm long As_2S_3 chalcogenide rib waveguide [10,17,19] with cross-sectional dimensions of 3 μm × 850 nm and an effective optical mode area of 1.725 μm². The waveguide was fabricated as described in [19] with the exception that the upper cladding was made out of polytetrafluoroethylene. The propagation loss of the waveguide was estimated to be about 0.3 dB/cm [19]. A low-Q resonator with free spectral range (FSR) of 886 MHz was formed due to the refractive index step from As_2S_3 ($n = 2.4$) to air. The waveguide facets provided a reflectivity of $\sim 17\%$. In As_2S_3, the Kerr nonlinearity and SBS
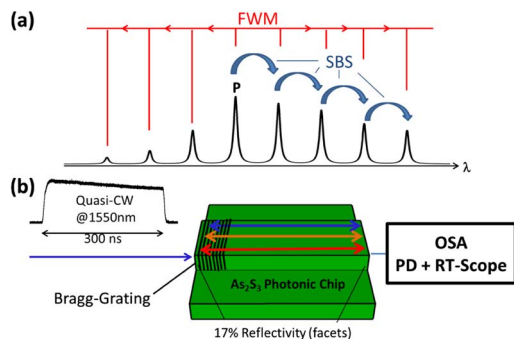
are strong due to a large nonlinear index [14] $n_2 = 3.0 \times 10^{-18}$ m²/W and a large Brillouin gain [16] $g_B = 0.715 \times 10^{-9}$ m/W. The light was coupled in and out of the waveguide using lensed silica fibers.

A polarization controller before the chip was used to ensure the excitation of only one polarization mode of the waveguide. The output light was characterized in the spectral domain with an optical spectrum analyzer (OSA) and in the time domain with a photodiode connected to an oscilloscope, which allowed real-time analysis of the output signal.

The cascaded SBS process was additionally enhanced by a "Hill-type" Bragg grating written into the waveguide prior to the experiment [20,21]. The grating was located close to the input facet and had an estimated length of 6 mm. The pump wavelength was tuned such that the first- and second-order Stokes waves coincided with a band edge and a grating resonance, respectively. Higher-order Stokes, pump, and anti-Stokes waves did not experience feedback from the grating.

The spectrum of the input light shown in Fig. 2(a) consisted of a single line at the pump wavelength. The observed linewidth in Fig. 2(a) is determined by the resolution of the OSA. Figure 2(b) shows the normalized transmission spectrum of the Bragg grating. Figure 2(c) presents optical output spectra for ~ 2 W coupled peak power. The solid blue line shows the BFC obtained with the grating enhancement. It exhibits four orders of Stokes waves (1S–4S) at longer wavelengths and three orders of anti-Stokes waves at shorter wavelengths (1AS–3AS). The wavelength spacing between the waves is $\Delta\lambda = 60$ pm, which corresponds to a Brillouin frequency shift of $\nu_B = c\Delta\lambda/\lambda^2 = 7.5$ GHz, where c is the vacuum speed of light. For comparison, the red dotted line in Fig. 2(c) shows the output spectrum observed for the same input power but without the Bragg grating. In this case, only weak first-order Stokes and first-order anti-Stokes waves were generated.

The grating-enhanced BFC generated in the resonator was characterized by recording the traces of 110 consecutive quasi-CW output pulses in real time within a time interval of 5 ms. Figure 3(a) shows every tenth trace of this measurement. Each

Fig. 1. (a) Illustration of BFC generation via the interplay of SBS and Kerr-nonlinear FWM (P, pump laser). (b) Schematic of the experiment. OSA, optical spectrum analyzer; PD, photodiode; RT-Scope, real-time oscilloscope.
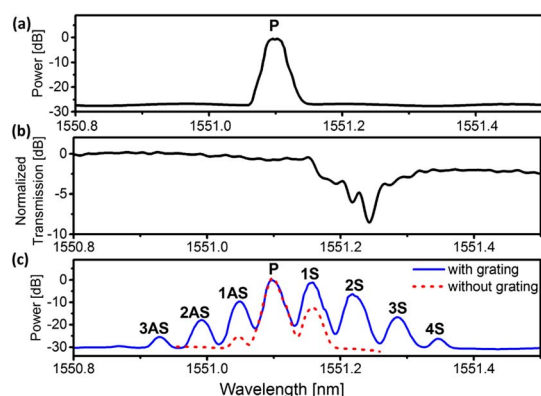

Fig. 2. Spectral measurements. (a) Input pump light (P) coupled into the resonator. (b) Normalized transmission spectrum of the Bragg grating. (c) Output spectra: with grating enhancement (solid blue line) revealing several Stokes waves (1S–4S) and anti-Stokes waves (1AS–3AS), and without grating enhancement (red dotted line). (a) and (c) were measured with an OSA (resolution ~ 10 pm), and (b) was measured with a swept wavelength system (resolution ~ 1.3 pm).

of the traces exhibited very similar temporal behavior: after about 20 ns, a rapidly oscillating interference signal was observed, which was not resolved in Fig. 3(a). This oscillation arises from the interference between the pump and the generated Stokes and anti-Stokes waves. After about 35 ns the dynamic interaction between the comb components seems to reach a steady state, resulting in an interference signal with a constant envelope. Figures 3(b)I and 3(b)II show 1 ns long zoomed-in sections of the interference at 70 and 280 ns, respectively. In Figs. 3(b)I and 3(b)II the traces of all 11 measurements presented in Fig. 3(a) are shown in the same plot in order to illustrate their similarity. We can see that the 11 independent measurements exhibit the same interference pattern, which is stable over the quasi-CW pulse length.
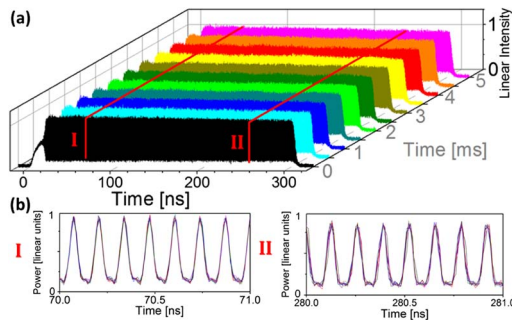
To understand the implications of this result we consider the spectral phase of the BFC. The complex electric fields of the individual comb components can be written in the form $E_j(t) \propto \exp[i(\phi_j(t) - 2\pi\nu_j t)]$, where ϕ_j are phase offsets of the spectral components. The measured interference signal is independent of a constant offset of all phases ϕ_j. A linear change of the spectral phase corresponds to the shift in time [1,18]. The shape of the interference signal is determined by the phase dispersion $\Delta\Delta\phi_j(t) = \phi_{j-1} + \phi_{j+1} - 2\phi_j$.

A stable interference pattern in the time domain requires phase-locking of the spectral components, i.e.,

$$\frac{d}{dt}\Delta\Delta\phi_j(t) = 0. \tag{1}$$

The stable and deterministic interference signal of the BFC shown in Figs. 3(a) and 3(b) indicates that the pump, Stokes, and anti-Stokes waves attained the same phase-locked steady state with identical spectral phases (same values of $\Delta\Delta\phi_j$) for all independent measurements. Coherent coupling of more than two adjacent comb components to a single acoustic wave is expected to be negligible since the corresponding interactions are not phase-matched and have coherence lengths <1 cm [12]. We therefore believe that FWM of copropagating waves provides the phase-locking mechanism.

Recording the interference signal with real-time measurements allows the analysis of its RF spectrum via fast Fourier transform (FFT). Figure 4(a) shows the RF power spectrum (squared FFT magnitude) of one of the traces shown in

Fig. 3(a). We can identify the beat notes of the comb components at multiple integer values of the Brillouin frequency shift $n\nu_B$ ($n = 1\ldots4$). A phase-locked frequency comb has narrow linewidth RF-beat notes that are equally spaced. The resolution bandwidth of the measurement in our case is limited by the length of the 300 ns pulses, i.e., ∼3 MHz. Equally spaced RF-beat notes of ∼3 MHz bandwidth would therefore be expected. However, we observed beat notes in the experiment [Fig. 4(a)] that were much broader. For example, the beat note at the frequency $\nu_B = 7.5$ GHz has a linewidth of ∼40 MHz.

To understand the origin of this broadening we performed a FFT of four consecutive, 70 ns long, time intervals of one 300 ns long pulse shown in Fig. 3(a). Figure 4(b) shows zoomed-in sections of the RF spectra around ν_B and $2\nu_B$. The four traces shown in both plots correspond to the RF spectra obtained for the consecutive 70 ns long time intervals centered around 55 ns, 125 ns, 195 ns, and 265 ns, respectively. Figure 4(b) explains why the phase-locked BFC exhibits broad beat notes in the RF spectrum [Fig. 4(a)]. The bandwidths of the beat notes within the consecutive intervals in Fig. 4(b) are resolution limited; however, the beat frequency at ν_B drifts within the 300 ns pulses by about 40 MHz towards higher frequency. At the same time the beat notes at $n\nu_B$ experience n times the frequency shift, which is shown for the RF frequency $2\nu_B$ in Fig. 4(b). In other words, the RF-beat notes are narrow and equally spaced, but the repetition rate of the comb is chirped by about 130 kHz/ns. The observation of a single beat at 7.5 GHz and the fact that the RF-beat notes at ν_B, $2\nu_B$, $3\nu_B$, and $4\nu_B$ remain exactly equally spaced despite the chirp additionally demonstrate phase-locking of the comb, i.e., that Eq. (1) is fulfilled. We observed the same drift of the repetition rate for all 110 recorded traces with the same initial and final repetition rates of the comb.

We believe that the increase of repetition rate is caused by a red-shift of the FP resonances, which leads to an increase in the Stokes wavelength due to frequency pulling [15]. A red-shift of the FP resonances is caused by an increase of the optical round-trip path length ($\Delta(2nL) > 0$). We exclude the Kerr effect as the possible cause since the total power in the cavity is not increasing. The effect causing the shift seems to be accumulative
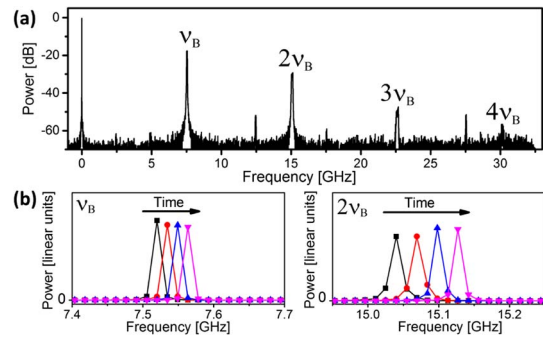

Fig. 3. Temporal measurements of the BFC (sampling rate, 80 GSa/s; bandwidth, 33 GHz). (a) Eleven output pulses generated by coupling eleven 300 ns input pump pulses into the waveguide with 0.5 ms delay. (b) 1 ns long zoomed-in section at 70 and 280 ns of all 11 traces shown in (a) (the traces have been shifted in time for better visibility).

Fig. 4. RF spectra of the BFC obtained via FFT of the temporal measurement shown Fig. 3. (a) RF spectrum of one entire quasi-CW output pulse. (b) Zoomed-in sections at ν_B and $2\nu_B$ of RF spectra of 70 ns long intervals of one quasi-CW output pulse centered around 55 ns (black, squares), 125 ns (red, dots), 195 ns (blue, triangles pointing up), and 265 ns (magenta, triangles pointing down), illustrating the increase of the comb repetition rate on a nanosecond time scale.

within the 300 ns pulses and reversible within 50 μs, which is the time separation between consecutive pulses.

Local heating of the waveguide is one possible explanation for an increase of the optical path length. Neglecting heat dissipation, the heating of the waveguide by one quasi-CW pulse can be estimated with

$$\Delta T = \frac{P(1 - e^{-\alpha L})\Delta t}{V \rho c_m} = 0.16 \text{ K}, \qquad (2)$$

where $P = 2$ W is the coupled power, $\Delta t = 300$ ns is the pulse duration, and V is the volume of the waveguide. The parameters $\rho = 3.2$ g/cm^3, $c_m = 0.456$ J/(gK), and $\alpha = 0.01$ cm^{-1} are the density, the specific heat, and the bulk material absorption coefficient of As$_2$S$_3$, respectively [22]. This leads to a change of the accumulated roundtrip phase of

$$\Delta\phi = \frac{2\pi}{\lambda} \times 2\left(n\frac{\partial L}{\partial T} + L\frac{\partial n}{\partial T}\right)\Delta T = 1.7\pi, \qquad (3)$$

where $\partial L/\partial T = L\alpha_L$ is the temperature-dependent expansion of the waveguide, $\alpha_L = 21.49 \times 10^{-6}$ K^{-1} is the expansion coefficient, and $\partial n/\partial T = 9 \times 10^{-6}$ is the refractive index change with temperature at 1550 nm [22,23]. A phase shift $\Delta\phi$ of 2π corresponds to a shift of the FP resonances by one FSR. The calculated estimate of the phase shift $\Delta\phi = 1.7\pi$ shows that local heating could lead to a significant shift of the FP resonances and therefore the comb repetition rate. Another possible explanation for the frequency drift is a photosensitive refractive index change on a nanosecond time scale, which is reversed between the quasi-CW pulses [24].

In a previous experiment that demonstrated the generation of phase-locked BFCs in a 38 cm long FP chalcogenide fiber resonator, a change of the repetition rate within 500 ns long quasi-CW pulses was not observed [12]. In the fiber experiment, the effects of local heating are expected to be much smaller compared to the chip, and the maximum phase drift is estimated to be $\Delta\phi = 0.4\pi$ [using the parameters from [12] with Eqs. (2) and (3)]. The smaller FSR of the fiber cavity additionally reduces the frequency pulling [15]. Photosensitivity is also less pronounced in drawn chalcogenide fibers compared to thin films made with vapor deposition as used for the chips.

In summary, we temporally characterized a quasi-CW BFC generated by cascaded SBS. The BFC was generated in a FP waveguide resonator on a photonic chip. Real-time measurements demonstrate phase-locking of the comb components. In contrast to previous fiber-based work, the comb generation was enabled by an on-chip Bragg grating, which enhanced the nonlinear interactions between the comb components. Furthermore, we utilized the real-time measurements to study the RF spectrum of the BFC, which revealed a novel phenomenon for frequency combs generated by quasi-CW pumping: a chirp (130 kHz/ns) of the comb repetition rate without the loss of phase-locking.

In the future, we will investigate generation of BFCs in on-chip high-finesse resonators. In CW configurations the observed frequency drift is expected to stabilize. Besides being more compact than a fiber cavity [12], generating BFCs on chip has also proven to be much more robust to environmental fluctuations due to the much shorter resonator length. Photolithographic fabrication will allow construction of a large number of waveguides with precise control over the resonator length, which is crucial in the case of high-finesse resonators. Furthermore, by combining these nonlinear waveguide resonators with the rapidly developing technology of on-chip lasers [13], a gigahertz repetition rate source could be realized in a completely integrated package. Due to the transparency of chalcogenide glasses, this technology could also be used to generate high repetition rate optical frequency comb sources at mid-infrared wavelengths (3–10 μm) relevant for direct comb spectroscopy and sensing.

REFERENCES

1. F. Ferdous, H. Miao, D. E. Leaird, K. Srinivasan, J. Wang, L. Chen, L. T. Varghese, and A. M. Weiner, Nat. Photonics **5**, 770 (2011).
2. S. A. Diddams, L. Hollberg, and V. Mbele, Nature **445**, 627 (2007).
3. S. T. Cundiff and J. Ye, Rev. Mod. Phys. **75**, 325 (2003).
4. P. Del'Haye, A. Schliesser, O. Arcizet, T. Wilken, R. Holzwarth, and T. J. Kippenberg, Nature **450**, 1214 (2007).
5. E. P. Ippen and R. H. Stolen, Appl. Phys. Lett. **21**, 539 (1972).
6. K. O. Hill, D. C. Johnson, and B. S. Kawasaki, Appl. Phys. Lett. **29**, 185 (1976).
7. M. Tomes and T. Carmon, Phys. Rev. Lett. **102**, 113601 (2009).
8. I. S. Grudinin, A. B. Matsko, and L. Maleki, Phys. Rev. Lett. **102**, 043902 (2009).
9. D. Braje, L. Hollberg, and S. Diddams, Phys. Rev. Lett. **102**, 193902 (2009).
10. R. Pant, E. Li, D.-Y. Choi, C. G. Poulton, S. J. Madden, B. Luther-Davies, and B. J. Eggleton, Opt. Lett. **36**, 3687 (2011).
11. J. Li, H. Lee, T. Chen, and K. J. Vahala, Opt. Express **20**, 369 (2012).
12. T. F. S. Büttner, I. V. Kabakova, D. D. Hudson, R. Pant, C. G. Poulton, A. C. Judge, and B. J. Eggleton, Sci. Rep. **4**, 1 (2014).
13. D. Van Thourhout, T. Spuesens, S. Kumar, S. Member, L. Liu, R. Kumar, G. Morthier, S. Member, P. Rojo-Romeo, F. Mandorlo, P. Regreny, O. Raz, C. Kopp, and L. Grenouillet, IEEE J. Sel. Top. Quantum Electron. **16**, 1363 (2010).
14. B. J. Eggleton, B. Luther-Davies, and K. Richardson, Nat. Photonics **5**, 141 (2011).
15. V. Lecoeuche, S. Randoux, B. Ségard, and J. Zemmouri, Quantum Semiclassical Opt. **8**, 1109 (1996).
16. R. Pant, C. G. Poulton, D.-Y. Choi, H. Mcfarlane, S. Hile, E. Li, L. Thevenaz, B. Luther-Davies, S. J. Madden, and B. J. Eggleton, Opt. Express **19**, 8285 (2011).
17. I. V. Kabakova, R. Pant, D.-Y. Choi, S. Debbarma, B. Luther-Davies, S. J. Madden, and B. J. Eggleton, Opt. Lett. **38**, 3208 (2013).
18. P. Del'Haye, K. Beha, S. B. Papp, and S. A. Diddams, Phys. Rev. Lett. **112**, 043905 (2014).
19. T. Han, S. Madden, D. Bulla, and B. Luther-Davies, Opt. Express **18**, 19286 (2010).
20. K. O. Hill, Y. Fujii, D. C. Johnson, and B. S. Kawasaki, Appl. Phys. Lett. **32**, 647 (1978).
21. T. F. S. Büttner, I. V. Kabakova, D. D. Hudson, R. Pant, E. Li, and B. J. Eggleton, Opt. Express **20**, 26434 (2012).
22. Amorphous Materials, Inc., "AMTIR-6 (As2S3)," http://www.amorphousmaterials.com/app/download/6552919404/AMTIR-6+Information.pdf.
23. W. S. Rodney, I. H. Malitson, and T. A. King, J. Opt. Soc. Am. **48**, 633 (1958).
24. Y. Sakaguchi and K. Tamura, J. Phys. Condens. Matter **18**, L331 (2006).

optica

Two-octave-spanning dispersion-controlled precision optics for sub-optical-cycle waveform synthesizers

SHIH-HSUAN CHIA,[1,2,3] GIOVANNI CIRMI,[1,3] SHAOBO FANG,[1,3] GIULIO M. ROSSI,[1,3] OLIVER D. MÜCKE,[1,3] AND FRANZ X. KÄRTNER[1,2,3,4,*]

[1]Center for Free-Electron Laser Science, Deutsches Elektronen-Synchrotron DESY, Notkestraße 85, 22607 Hamburg, Germany

[2]Physics Department, University of Hamburg, Luruper Chaussee 149, 22761 Hamburg, Germany

[3]The Hamburg Center for Ultrafast Imaging, Luruper Chaussee 149, 22761 Hamburg, Germany

[4]Department of Electrical Engineering and Computer Science and Research Laboratory of Electronics, Massachusetts Institute of Technology, Cambridge, Massachusetts 02139, USA

*Corresponding author: franz.kaertner@desy.de

Two-octave-spanning precision dispersive mirror systems are demonstrated, providing a new enabling technology for pulse-energy and bandwidth scaling of sub-cycle optical waveform synthesizers. We propose and characterize new dispersion management schemes with advanced dielectric coating designs. Based on an analytic dual adiabatic matching structure, we implement a chirped dichroic mirror, to efficiently optimize the beam combining from different spectra, and a double-chirped mirror pair, to avoid unwanted nonlinearity during beam propagation, with custom-tailored dispersion and reflectivity over more than two octaves of bandwidth ranging from 0.49 to 2.3 μm, supporting 1.9-fs-short sub-optical-cycle pulses. The multilayer coating structures can also be applied to the design of chirped-fiber Bragg gratings and general optical filters. The proposed designs and schemes will benefit ultrabroadband applications requiring precise dispersion management, especially enabling the generation of intense sub-optical-cycle light transients.   © 2014 Optical Society of America

OCIS codes: (320.7160) Ultrafast technology; (310.4165) Multilayer design; (190.4970) Parametric oscillators and amplifiers.

http://dx.doi.org/10.1364/OPTICA.1.000315

1. INTRODUCTION

The generation of extremely short and ultrabroadband optical waveforms, which are custom-tailored within a single cycle of light, opens up unprecedented opportunities for the emerging field of *waveform nonlinear optics*, which is of primary importance, e.g., for the generation of intense isolated attosecond extreme-UV pulses [1,2], launching valence-electron wave-packet dynamics in atoms and molecules [3–5], relativistic laser–plasma interactions and laser-driven electron acceleration [6–9], and control of sub-cycle electron transport in solids [10]. However, the feasibility of studying nonlinear interactions of matter with intense sub-cycle waveforms critically

depends on the availability of high-energy multi-octave-spanning carrier-envelope-phase-controlled optical pulses. In addition, the realization of the energy and bandwidth scalability of ultrashort optical transients provides a new enabling technology for the demonstration of bright coherent tabletop high-harmonic sources, especially in the water window and keV x-ray region [11,12]. Therefore, the generation and precise dispersion control of ever broader optical bandwidth is in high demand, in order to tailor the shortest light bursts in the time domain.

Recent progress in broadband waveform generation has produced coherent optical spectra with >1-octave bandwidth

by sub-cycle waveform synthesis [13] and supercontinuum generation [3–5]. However, it is difficult to obtain sub-optical-cycle pulses with high pulse energy [i.e., at the millijoule (mJ) level], limited by the trade-off between the required high non-linearity for the generation of ultrabroad bandwidth and the output beam quality in terms of the beam stability and beam profile distortion. The dispersion management of intense multi-octave spectra is extremely delicate and challenging, especially requiring ultrabroadband precision dispersive optics with high damage threshold. Active compression systems based on spatial light modulators with >1-octave bandwidths have been demonstrated [14,15]. However, they are hampered by the bandwidth and diffraction efficiency of the gratings used in 4-f systems. Therefore, they have not directly been applied to multi-octave-spanning high-intensity sources. Multilayer dielectric coatings, such as the ones used for chirped mirrors [16,17] and complementary mirror pairs [18–20], although not adaptable, have the advantage of potentially supporting multi-octave bandwidth with high reflectivity. Therefore, multilayer mirror designs are widely employed as robust solutions. 1.5-octave-wide chirped-mirror pairs [19] for pulse compression have been developed, and optical synthesizers based on hollow-core-fiber compressors with up to four channels have been realized with separate chirped-mirror designs [3–5]. The pulses covering different spectral ranges are individually recompressed before pulse recombination. While hollow-core-fiber compressors are limited in energy handling, a pulse synthesizer based on parametric amplifiers can further scale the energy to the multi-mJ range [13,21–24]. Then the maximum pulse energy reachable is ultimately limited by the peak power of the combined intense ultrashort pulse, which induces detrimental nonlinearities (i.e., B-integral) in the following optical beam path and particularly in the beam combiner optics and the window of vacuum chambers housing the experiment. In

addition, the dispersion of the beam combiner around the edge of the high-reflection band is difficult to control. As a result, synthesized electric-field transients without spectral gaps are hard to achieve with dichroic mirrors (DMs): spectral gaps cannot be avoided in between the channels [3–5]. Therefore, to efficiently synthesize ultrabroad optical waveforms, precise dispersion matching between the transmission and reflection ports of the beam combiner is required. Broadband DMs with exquisite dispersion control are necessary but are not available yet, to the best of our knowledge. In this work, novel mirror designs for >2-octave-spanning waveform synthesizers delivering multi-mJ pulse energy [21–23] are introduced. We design, fabricate, and characterize the required laser optics [25], chirped dichroic mirrors (CDMs) for efficient splitting and coherent combining of pulses, and ultrabroadband double-chirped mirror (DCM) pairs for final compression. To avoid B-integral problems, we recombine the still slightly chirped pulses first on the CDMs and then use an ultrabroadband DCM pair as a final compressor unit. Figure 1 shows the use of these optics in an actual >2-octave-wide three-channel parametric synthesizer, which was recently demonstrated [21–23].

2. DUAL-ADIABATIC-MATCHING STRUCTURE

In principle, chirped mirrors are designed as dispersive optical interference coatings with low-/high-index dielectric layer pairs to achieve dispersion management [16–20,26]. In chirped mirrors, the Bragg wavelength is chirped so that different wavelengths penetrate different depths into the mirror until Bragg reflection, giving rise to a wavelength-dependent group delay (GD). Figure 2(a) shows the simple-chirped (SC) structure, where the Bragg wavelength is monotonically increased with each quarter-wave layer pair to provide negative dispersion, as well as a broader high-reflection bandwidth than
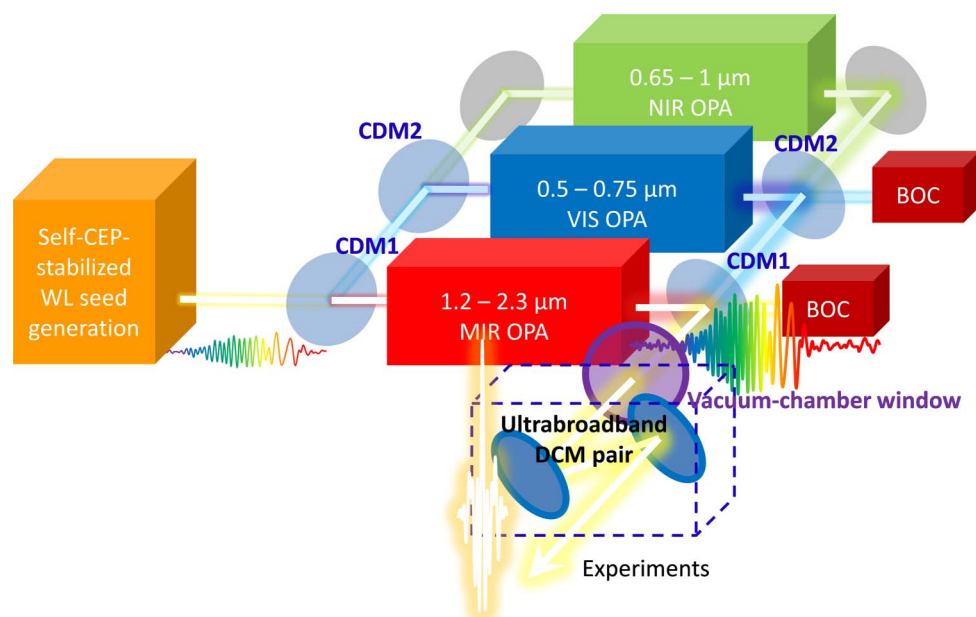
Fig. 1. Schematic of a >2-octave-wide three-channel parametric synthesizer [21–23]. CEP, carrier-envelope phase; WL, white light; CDM, chirped dichroic mirror; OPA, optical parametric amplifier; DCM, double-chirped mirror; BOC, balanced optical cross correlator.

the Fresnel reflection bandwidth of a fixed layer pair [26,27]. However, pronounced GD ripples are usually observed, as shown in Fig. 2(d). These ripples are due to the impedance mismatch between free space and the multilayer grating, which acts as a Gires–Tournois interferometer. Since the period of the oscillations in the spectral domain determines the position of a satellite in the time domain upon reflection, the suppression of the adverse GD ripples by achieving impedance matching to avoid internal resonances is of great importance especially in few-cycle pulse generation. The double-chirped (DC) structure [16], as shown in Fig. 2(b), has been proposed to achieve impedance matching by adiabatically tapering the impedance in the front layer pairs, which is shown to be equivalent to an adiabatic chirp in the thickness of the high-index layer in addition to the chirp of the center wavelength of the Bragg mirror. However, a multilayer mirror design covering more than 2 octaves in bandwidth, which requires multi-octave impedance matching, has not been achieved so far. Here, we introduce a dual-adiabatic-matching (DAM) structure [25], as shown in Fig. 2(c), that generates also a double chirp in the back section of the mirror approaching the substrate, adiabatically tapering the impedance again to provide high transmission for long wavelengths. The front and back chirped high-index layers perform dual adiabatic impedance matching, providing (1) high reflectivity and smooth GD over the high-reflectivity range of the mirror and (2) high transmission with sidelobe suppression outside the high-reflectivity range, respectively.

Because of the smooth transmittance with smooth GD behavior as shown in Fig. 2(d), the DAM structure can be used as a >2-octave-spanning dispersive CDM. With the impedance-matching features shown in Fig. 2(d), we implement the DAM structure to design a CDM. To realize the idea experimentally, the analytical DAM structure is employed as an initial design, which provides a high-reflection window for the spectral range of 0.45–1 μm and transmission in the range of 1.1–2.5 μm for p-polarized laser beams with an incidence angle of 45°. The numerically optimized result using a fast algorithm [28] is shown in Fig. 3(a). With an antireflection (AR) coating in the initial few layers to provide impedance matching from air to the low-index coating material, the following structure preserves the DAM structure. The GD in reflection is designed to compensate a 0.52 mm optical path in fused silica over the spectral range from 0.45–1.3 μm, which is even broader than the high-reflectivity range of 0.45–1.1 μm, as shown in Fig. 3(b).

To combine spectra with a spectral overlap, the simultaneous dispersion management in both reflection and transmission, especially around the edge of the high-reflection band, is very important. The GD oscillations in reflection of a DM in this range are usually rather large due to the strong resonant interferences originating from internal Fabry–Pérot effects. The backside impedance-matching section in the DAM structure reduces these typically observed GD oscillations. Since the reflection from the back impedance-matching region is suppressed, the etalon resonance is reduced between the quarter-wave Bragg stacks and the back impedance-matching section. On the other hand, the GD in transmission is subject to the Kramers–Kronig relation [29]:

$$\phi_t = \frac{-1}{\pi} P \int_{\infty}^{-\infty} \frac{\ln |T(\omega')|}{\omega - \omega'} d\omega', \tag{1}$$
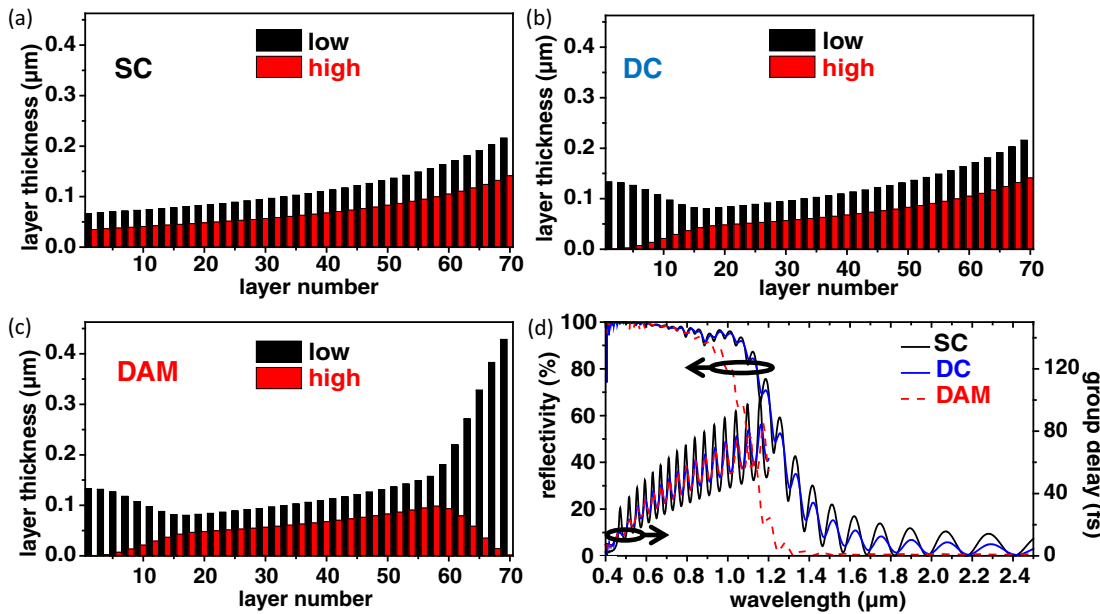
Fig. 2. (a)–(c) Structures and (d) reflectivity/GD of different chirped mirror structures: (a) a design of the SC structure monotonically increases the Bragg wavelength with quarter-wave layer pairs to provide negative dispersion; (b) the DC design tapering the impedance in the front section based on the SC layers features reduced GD ripples in the high-reflectivity range; (c) the proposed DAM structure further introduces another impedance-matching section in the back layers, resulting in high transmittance for longer wavelengths; low, low-index material (e.g., SiO₂); high, high-index material (e.g., TiO₂).
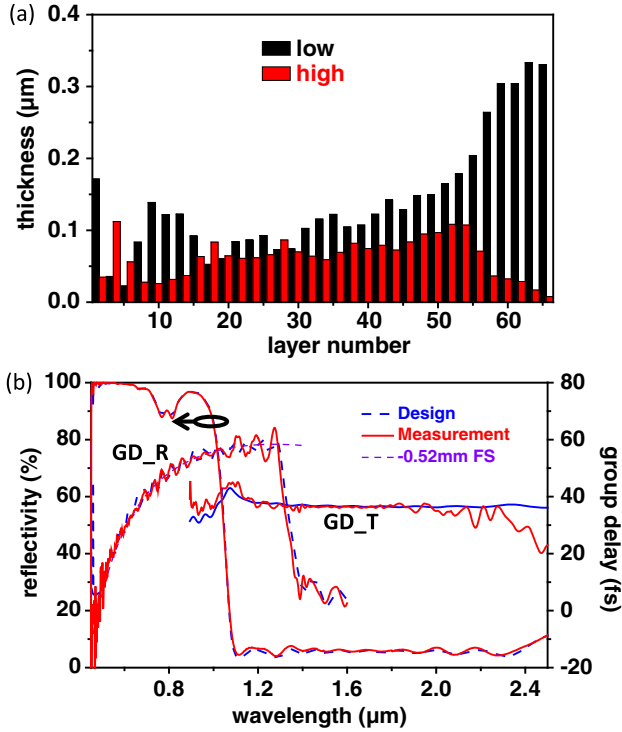
Fig. 3. (a) Structure and (b) the designed/measured reflectivity/GD of the CDM, as well as the corresponding GD design goals. The imperfect transmittance around 0.8 μm and the 5% reflection above 1.1 μm are intentionally created to supply a BOC for waveform synthesis; low, low-index material, SiO$_2$; high, high-index material, TiO$_2$; GD_R, designed/measured GD in reflection; GD_T, the transmitted designed/measured GD; FS, fused silica.

where ϕ_t and $T(\omega)$ are the transmission phase and transmittance, respectively. By taking the derivatives on both sides and integration by parts on the right-hand side, one can obtain

$$\text{GD} = \frac{d\phi}{d\omega} = \frac{1}{\pi} P \int_{\infty}^{-\infty} \frac{T'}{\omega - \omega'} d\omega',$$

$$\text{where } T' = \frac{dT(\omega')/d\omega'}{|T(\omega')|}. \tag{2}$$

Therefore, GD in transmission is the Hilbert transform of T', mathematically analogous to the relation between absorption coefficient and reflection in electron spectroscopy [30,31]. As a result, the variations of GD in transmission [i.e., group-delay dispersion (GDD)] are related to the changes of the transmittance curves, especially in the spectral range close to the edge of the high-reflection band: if the transmittance of the CDM is slowly varying in the transition region, the corresponding GD curve is also slowly varying. With the designed CDM, the variation of the transmission GD in the transition range between high-transmission band and high-reflection band, 1.0–1.1 μm, is <10 fs, as shown in Fig. 3(b). The nature of the Hilbert transform in Eq. (2) suggests that even lower GD variation is possible based on a mirror with a smoother transmittance curve and a wider transition region.

3. DISPERSION-MATCHED SCHEME FOR COHERENT BEAM COMBINING

To match the beam dispersion between the reflection port and the transmission port, the dispersion for the two combined beam paths in the spectrally overlapping region should be the same after the CDM, which is similar to a previous scheme based on a dispersion-matched neutral beam splitter [32]. A proposed scheme with a CDM and a dielectric plate in port 1 is shown in Fig. 4(a). Let us denote the GDD of the coating between the air and the substrate interfaces with reflection R1, transmission T1, reflection R2, and transmission T2 by GDD$_{R1}$, GDD$_{T1}$, GDD$_{R2}$, and GDD$_{T2}$, respectively. Also, the GDD for a single pass through the substrate of the CDM and the dielectric plate are denoted as GDD$_S$ and GDD$_P$, respectively. In the design, we will match the GDD of the substrate with the GDD of the plate and GDD$_{R1}$ (i.e., GDD$_S$ = GDD$_{R1}$ + GDD$_P$). The GDD for each optical path is then given by

$$\text{GDD}(1 \rightarrow 4) = \text{GDD}_P + \text{GDD}_{R1} = \text{GDD}_S,$$
$$\text{GDD}(2 \rightarrow 4) = \text{GDD}_S + \text{GDD}_{T2},$$
$$\text{GDD}(1 \rightarrow 3) = \text{GDD}_P + \text{GDD}_{T1} + \text{GDD}_S,$$
$$\text{GDD}(2 \rightarrow 3) = 2\text{GDD}_S + \text{GDD}_{R2}. \tag{3}$$
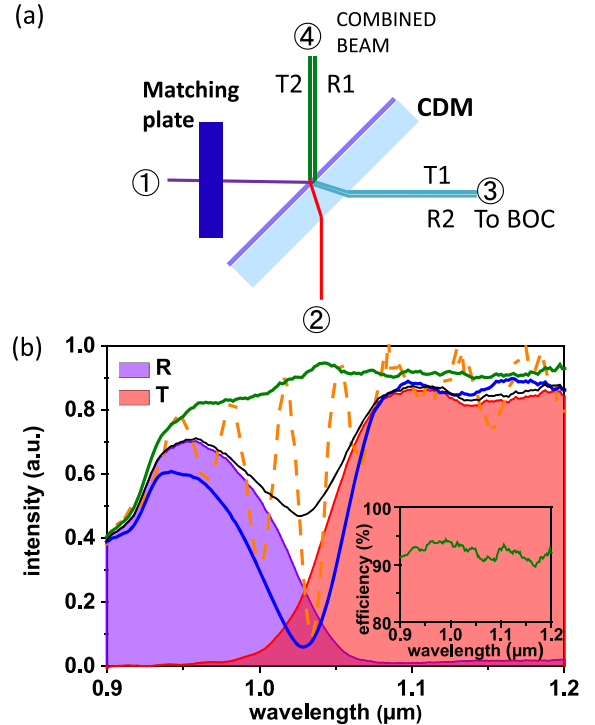
Fig. 4. (a) Schematic diagram of a dispersion-matched system based on the CDM. (b) The reflection (purple), transmission (red), and the combined spectra (green, blue, and orange dashed) in port 4 with different delays between port 1 and port 2 in (a), as well as the incoherently combined spectrum (black). Constructively/destructively interfered spectrum over the whole transition range (1.0–1.1 μm) can be obtained as the green/blue curve. (Inset) The optimized beam combining efficiency is >90%, even including the ~8% total interface reflection losses of the matching plate in port 1.

For a lossless coating of the CDM, the following relationships are generally valid [27,32]: $GDD_{T1} = GDD_{T2}$ and $GDD_{R1} + GDD_{R2} = GDD_{T1} + GDD_{T2}$. Assuming the transmittance of the CDM in the transition region is smooth enough, the corresponding GDD is negligible (i.e., $GDD_{T1} \approx 0$). With these additional conditions for a lossless and slowly varying transmission coating in the transition region, the GDD for each beam path to port 4 becomes identical:

$$GDD(1 \rightarrow 4) = GDD_P + GDD_{R1} = GDD_S,$$
$$GDD(2 \rightarrow 4) = GDD_S + GDD_{T2} = GDD_S. \quad (4)$$

The GDD for each beam path to port 3 is also identical:

$$GDD(1 \rightarrow 3) = GDD_P + GDD_{T1} + GDD_S$$
$$= GDD_P + GDD_S,$$
$$GDD(2 \rightarrow 3) = 2GDD_S + GDD_{R2}$$
$$= GDD_P + GDD_S. \quad (5)$$

Furthermore, if we additionally place an identical plate in port 4 or have a coating design that $GDD_{R1} = GDD_S$, the GDD of all input and output ports are matched. In our case, GDD_{R1} and GDD_S are equivalent to the GDD of –0.52 mm and 3.21 mm optical path of fused silica, respectively. Therefore, the matched optical path of the fused silica plate is 3.73 mm. In the waveform synthesizer, as shown in the scheme depicted in Fig. 1, the combined 5% of light in port 3 will supply a balanced optical cross correlator (BOC) for active feedback stabilization of the relative time delay of the individual pulses [13].

Since the dispersion is matched, the spectrum in the spectrally overlapping region in port 4 can constructively be combined with matched spectral phase over the overlapping region, which further boosts the combination efficiency. The purple/red curves in Fig. 4(b) show the reflected/transmitted spectra measured using a white-light source from port 1 and port 2, respectively. The combined spectra are also shown as the green, blue, and orange dashed curves in Fig. 4(b), as well as the incoherently combined spectrum as a reference: interference fringes (orange dashed curve) are observed due to the optical delay between the beams from the two input ports. By fine-tuning the optical delay, constructively/destructively interfered spectra over the spectrally overlapping region can be obtained as the green/blue curves, respectively. The beam combining efficiency with the green spectrum is >90% over the transition range, even including the ~8% total interface reflection losses of the silica plate in port 1.

The interfered fringes in the spectrally overlapping region are extremely sensitive to the delay between the pulses from the two input ports, which benefit the precise active stabilization of the relative timing.

4. >2-OCTAVE-WIDE HIGH-REFLECTION DCM PAIRS

The DAM structure lends itself to the design of an ultrabroadband DCM pair as the final compression unit, which is key

enabling technology to realize >2-octave multi-mJ sub-cycle waveforms without running into *B*-integral problems that destroy the pulse quality. The proposed structure particularly reflects the light within its Bragg wavelength and provides smooth transmittance for the longer wavelengths, which is a proper impedance-matching section to reduce the Gires–Tournois effect in the chirped mirror design. As a result, cascading the DAM structure in the front layers, as an ultrabroadband impedance-matching section, makes it possible to achieve >2-octave bandwidth DCMs, as shown in Fig. 5. The ultrabroadband DCM pair is designed and optimized for compensating 1.44 mm optical path in fused silica in the spectral range from 0.49 to 1.05 μm, the high-reflectivity range of the CDM, and 0.32 mm optical path in ZnSe in the range of 1.05–2.3 μm, the transmission range of the CDM. For >1-octave-wide chirped mirrors, mirrors providing negative chirp are advantageous, because short-wavelength light is reflected by the top layers, whereas long-wavelength light penetrates deeper and mostly sees an average index of the thinner top layers. To demonstrate the broadband impedance matching of the cascaded-DAM-like structures, Figs. 5(c) and 5(d) show the reflectivity of the structures from the ambient air to the specific layers pointed at by the arrows in Figs. 5(a) and 5(b), respectively. As the number of front layers increases, starting from the air, the high-reflectivity band expands to longer wavelengths, which is determined by the Bragg wavelength of the layer pairs. The arrows in Figs. 5(a) and 5(b) point to the end layer of each DAM-like structure, providing broadband AR coating (impedance matching) with <5% reflection to the design wavelength of 2.3 μm. The designed/measured reflectivity and GD of the pair are shown in Fig. 6. The average reflectivity of the ultrabroadband DCM pair is >90% and the calculated peak-to-peak values of the averaged residual GD ripples are controlled to <5 fs over >2-octave bandwidth. In Fig. 6, the dispersion and reflectivity measurements using a home-built white-light interferometer and a photospectrometer, respectively, show excellent agreement with the design targets.

Even broader design bandwidth of DCM pairs is possible but, depending on the applications, limited by the required reflectivity and dispersion control. For example, it is difficult to design chirped mirrors with >99.5% reflection over >2-octave-wide bandwidth used as intracavity mirrors for precise dispersion compensation in a broadband laser oscillator. The laser-induced damage threshold of the lower bandgap dielectric coating material, TiO_2 in our case, would hamper the energy scalability of the ultrabroadband source based on the DCMs. The threshold fluence of ion-beam sputtering TiO_2 films is measured to be >0.1 J/cm² using a 25 fs Ti:sapphire amplifier [33]. Although the repetition rate [34], pulse duration, and center wavelength of the optical source, as well as the coating structures of the DCMs, would affect the breakdown fluence, sub-cycle optical waveform synthesizers supporting up to several tens of mJ of pulse energy with a >1 cm² beam size should be possible based on the multilayer chirped mirrors.

We evaluate the expected pulse distortions introduced by the demonstrated ultrabroadband DCM pair on the waveform synthesizer output using the experimental combined
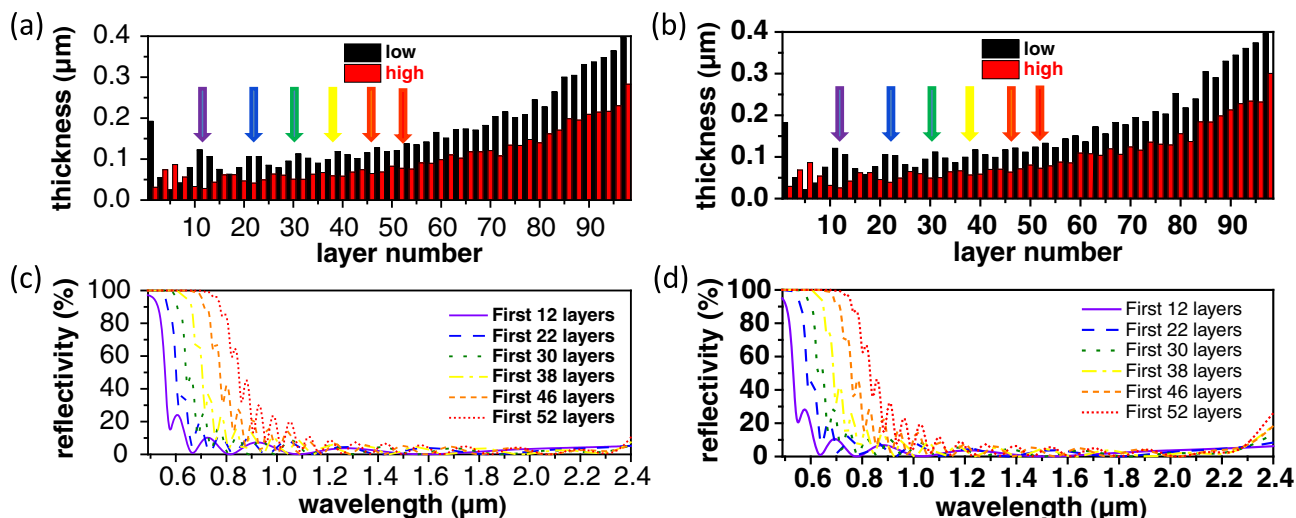
Fig. 5. (a) and (b) Structure of the mirror pair of the optimized DAM DCM pair. (c) and (d) AR behavior for the longer wavelengths in the cascaded DAM sections indicated by the arrows in the mirror structure in (a) and (b), respectively; low, low-index material, SiO_2; high, high-index material, TiO_2.

second-stage optical parametric amplifier (OPA) output spectra of Ref. [22]. As the scheme shows in Fig. 1, the spectrum below 1 µm is reflected by the CDM, and the spectrum above 1.1 µm is transmitted. The combined pulse, with 1.88 fs FWHM transform-limited pulse duration, is still chirped when passing through the combiner substrate and the vacuum-chamber window to decrease the peak intensity and thus reduce the B-integral, and the ultrabroadband DCM pair can compensate the dispersion of the combined waveform afterward. The pulse distortions were examined by considering the measured reflectivity and residual GD errors of the mirrors (i.e., starting from the flat-phase waveform and accounting for the measured GD deviation of the mirrors from the design goal, the GD of 1.44 mm optical path in fused silica or of 0.32 mm optical path in ZnSe), as shown in Fig. 7. Figure 7(b) shows the synthesized waveform after final compression by the ultrabroadband DCM pair according to Figs. 5 and 6. The measured residual phase error of the DCM pair,
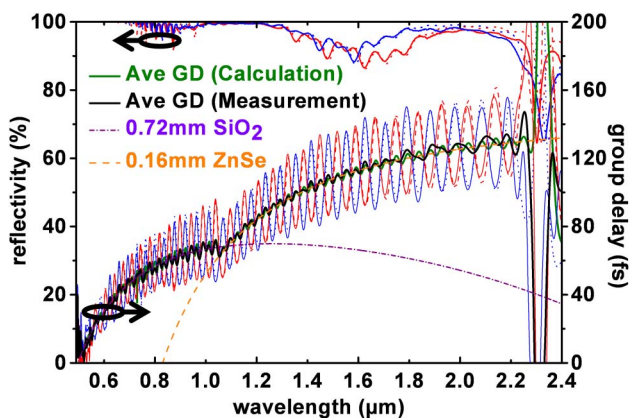
Fig. 6. Reflectivity and GD of the ultrabroadband DCM pair: the calculation shown as the blue/red dashed lines and the solid lines show the measurement results. The dispersion of the DCM pair compensates a 1.44-mm optical path in fused silica and a 0.32-mm optical path in ZnSe for ranges of 0.49–1.05 µm and 1.05–2.3 µm, respectively.
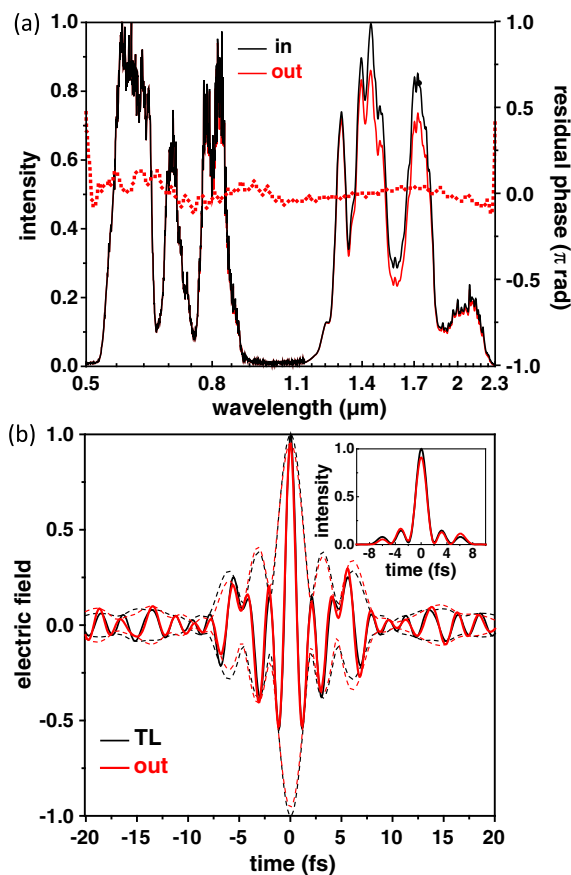
Fig. 7. Evaluated pulse characteristics in (a) frequency domain and (b) time domain after the ultrabroadband DCM pair. The black curve in (a) is the measured combined OPA spectra, as well as the transform-limited electric-field waveform (TL) in (b). The red curves show the pulse after the mirror pair, as well as the residual phase shown as dotted line in (a). The duration of the pulses depicted in the inset as the black and red lines are 1.88 and 1.93 fs, respectively.

is $<0.1\pi$ rad (i.e., $<\lambda/20$), as the red dotted curve in Fig. 7(a) shows, enabling pulse compression very close to its transform limit. Pulse compression over >2-octave-bandwidth can thus be achieved for the first time, to the best of our knowledge.

5. CONCLUSIONS

We proposed a DAM structure that enables >2-octave-wide dispersion control. The proposed structure is similar to refractive-index apodization in fiber Bragg gratings [35,36]: the DAM structure adiabatically matches the impedance of both the Bragg stacks and low-index material, providing not only high reflectivity with smooth GD in reflection at the Bragg wavelength, but also a broadband AR coating for the longer wavelengths with smooth GD in transmission. Dispersive CDMs based on the DAM structure can thus be designed and fabricated to achieve both beam combination and dispersion compensation with >2-octave bandwidth. With the demonstrated CDM and the dispersion-matched scheme, the combined spectrum from different input ports can be optimized. In principle, near-100%-constructive-interfered beam combining over the whole spectrally overlapping region can be achieved; here, >90% of beam combining efficiency was demonstrated experimentally, taking Fresnel losses of interfaces into account. In chirped-mirror designs, a broadband AR coating as an impedance-matching section is critical to reduce the amplitude of GD ripples induced by the Gires–Tournois effect. As a result, cascades of DAM structures in the front section of a chirped-mirror design for an ultrabroadband DCM pair are demonstrated, resulting in the most broadband chirped mirror designed so far. The designed CDM and DCM pairs are key enabling technology for a >2-octave multi-mJ parametric synthesizer supporting 1.9 fs FWHM waveforms without running into *B*-integral problems that destroy the pulse quality. No temporal pulse broadening is found due to the use of CDM and DCM pairs. The results indicate that the proposed designs will pave the way for the development of intense ultrabroadband parametric synthesizers and in general dispersion control of multi-octave-bandwidth coherent optical sources [37].

REFERENCES

1. E. J. Takahashi, P. Lan, O. D. Mücke, Y. Nabekawa, and K. Midorikawa, "Attosecond nonlinear optics using gigawatt-scale isolated attosecond pulses," Nat. Commun. **4**, 2691 (2013).

2. E. J. Takahashi, P. Lan, O. D. Mücke, Y. Nabekawa, and K. Midorikawa, "Infrared two-color multicycle laser field synthesis for generating an intense attosecond pulse," Phys. Rev. Lett. **104**, 233901 (2010).

3. A. Wirth, M. T. Hassan, I. Grguraš, J. Gagnon, A. Moulet, T. T. Luu, S. Pabst, R. Santra, Z. A. Alahmed, A. M. Azzeer, V. S. Yakovlev, V. Pervak, F. Krausz, and E. Goulielmakis, "Synthesized light transients," Science **334**, 195–200 (2011).

4. M. T. Hassan, A. Wirth, I. Grguraš, A. Moulet, T. T. Luu, J. Gagnon, V. Pervak, and E. Goulielmakis, "Attosecond photonics: synthesis and control of light transients," Rev. Sci. Instrum. **83**, 111301 (2012).

5. T. T. Luu, M. T. Hassan, A. Moulet, O. Razskazovskaya, N. Kaprowicz, V. Pervak, F. Krausz, and E. Goulielmakis, in *Conference on Lasers and Electro-Optics* (2013), paper QF1C.6.

6. A. Buck, M. Nicolai, K. Schmid, C. M. S. Sears, A. Sävert, J. M. Mikhailova, F. Krausz, M. C. Kaluza, and L. Veisz, "Real-time observation of laser-driven electron acceleration," Nat. Phys. **7**, 543–548 (2011).

7. L. Veisz, D. Rivas, G. Marcus, X. Gu, D. Cardenas, J. Mikhailova, A. Buck, T. Wittmann, C. M. S. Sears, S.-W. Chou, J. Xu, G. Ma, D. Herrmann, O. Razskazovskaya, V. Pervak, and F. Krausz, "Generation and applications of sub-5-fs multi-10-TW light pulses," in *Conference on Lasers and Electro-Optics: Pacific Rim* (2013), paper TuD2-3.

8. S. Payeur, S. Fourmaux, B. E. Schmidt, J.-P. MacLean, C. Tchervenkov, F. Légaré, M. Piché, and J.-C. Kieffer, "Generation of a beam of fast electrons by tightly focusing a radially polarized ultrashort laser pulse," Appl. Phys. Lett. **101**, 041105 (2012).

9. V. Marceau, C. Varin, T. Brabec, and M. Piché, "Femtosecond 240-keV electron pulses from direct laser acceleration in a low-density gas," Phys. Rev. Lett. **111**, 224801 (2013).

10. O. D. Mücke, "Isolated high-order harmonics pulse from two-color-driven Bloch oscillations in bulk semiconductors," Phys. Rev. B **84**, 081202(R) (2011).

11. E. J. Takahashi, T. Kanai, K. L. Ishikawa, Y. Nabekawa, and K. Midorikawa, "Coherent water window x ray by phase-matched high-order harmonic generation in neutral media," Phys. Rev. Lett. **101**, 253901 (2008).

12. T. Popmintchev, M.-C. Chen, D. Popmintchev, P. Arpin, S. Brown, S. Ališauskas, G. Andriukaitis, T. Balčiunas, O. D. Mücke, A. Pugzlys, A. Baltuška, B. Shim, S. E. Schrauth, A. Gaeta, C. Hernández-García, L. Plaja, A. Becker, A. Jaron-Becker, M. M. Murnane, and H. C. Kapteyn, "Bright coherent ultrahigh harmonics in the keV x-ray regime from mid-infrared femtosecond lasers," Science **336**, 1287–1291 (2012).

13. S.-W. Huang, G. Cirmi, J. Moses, K.-H. Hong, S. Bhardwaj, J. R. Birge, L.-J. Chen, E. Li, B. J. Eggleton, G. Cerullo, and F. X. Kärtner, "High-energy pulse synthesis with sub-cycle waveform control for strong-field physics," Nat. Photonics **5**, 475–479 (2011).

14. E. Matsubara, K. Yamane, T. Sekikawa, and M. Yamashita, "Generation of 2.6 fs optical pulses using induced-phase modulation in a gas-filled hollow fiber," J. Opt. Soc. Am. B **24**, 985–989 (2007).

15. T. Tanigawa, Y. Sakakibara, S. Fang, T. Sekikawa, and M. Yamashita, "Spatial light modulator of 648 pixels with liquid crystal transparent from ultraviolet to near-infrared and its chirp compensation application," Opt. Lett. **34**, 1696–1698 (2009).

16. F. X. Kärtner, N. Matuschek, T. Schibli, U. Keller, H. A. Haus, C. Heine, R. Morf, V. Scheuer, M. Tilsch, and T. Tschudi, "Design and fabrication of double-chirped mirrors," Opt. Lett. **22**, 831–833 (1997).

17. G. Steinmeyer, "Brewster-angled chirped mirrors for high-fidelity dispersion compensation and bandwidths exceeding one optical octave," Opt. Express **11**, 2385–2396 (2003).

18. F. X. Kärtner, U. Morgner, R. Ell, T. Schibli, J. G. Fujimoto, E. P. Ippen, V. Scheuer, G. Angelow, and T. Tschudi, "Ultrabroadband double-chirped mirror pairs for generation of octave spectra," J. Opt. Soc. Am. B **18**, 882–885 (2001).

19. V. Pervak, A. V. Tikhonravov, M. K. Trubetskov, S. Naumov, F. Krausz, and A. Apolonski, "1.5-octave chirped mirror for pulse compression down to sub-3 fs," Appl. Phys. B **87**, 5–12 (2007).

20. V. Pervak, I. Ahmad, M. K. Trubetskov, A. V. Tikhonravov, and F. Krausz, "Double-angle multilayer mirrors with smooth dispersion characteristics," Opt. Express **17**, 7943–7951 (2009).
21. G. Cirmi, S. Fang, S.-H. Chia, O. D. Mücke, C. Manzoni, P. Farinello, G. Cerullo, and F. X. Kärtner, "Towards parametric synthesis of millijoule-level two-octave-wide optical waveforms for strong-field experiments," in *Ultrafast Optics (UFO IX)* (2013), paper We3.3.
22. S. Fang, G. Cirmi, S.-H. Chia, O. D. Mücke, F. X. Kärtner, C. Manzoni, P. Farinello, and G. Cerullo, "Multi-mJ parametric synthesizer generating two-octave-wide optical waveforms," in *Conference on Lasers and Electro-Optics: Pacific Rim* (2013), paper WB3-1.
23. G. M. Rossi, G. Cirmi, S. Fang, S.-H. Chia, O. D. Mücke, F. X. Kärtner, C. Manzoni, P. Farinello, and G. Cerullo, "Spectro-temporal characterization of all channels in a sub-optical-cycle parametric waveform synthesizer," in *Conference on Lasers and Electro-Optics* (2014), paper SF1E.3.
24. B. E. Schmidt, N. Thiré, M. Boivin, A. Laramée, F. Poitras, G. Lebrun, T. Ozaki, H. Ibrahim, and F. Légaré, "Frequency domain optical parametric amplification," Nat. Commun. **5**, 3643 (2014).
25. S.-H. Chia and F. X. Kärtner, "Chirped dichroic mirror and a source for broadband light pulses," European patent application EP14155053 (February 13, 2014).
26. R. Szipöcs, K. Ferencz, C. Spielmann, and F. Krausz, "Chirped multilayer coatings for broadband dispersion control in femtosecond lasers," Opt. Lett. **19**, 201–203 (1994).
27. H. A. Haus, *Waves and Fields in Optoelectronics* (Prentice-Hall, 1984).
28. J. R. Birge and F. X. Kärtner, "Efficient optimization of multilayer coatings for ultrafast optics using analytic gradients of dispersion," Appl. Opt. **46**, 2656–2662 (2007).
29. R. H. J. Kop, P. de Vries, R. Sprik, and A. Lagendijk, "Kramers-Kronig relations for an interferometer," Opt. Commun. **138**, 118–126 (1997).
30. R. F. Egerton, *Electron Energy Loss Spectroscopy in the Electron Microscope* (Springer, 2011).
31. A. Damascelli, Z. Hussain, and Z.-X. Shen, "Angle-resolved photoemission studies of the cuprate superconductors," Rev. Mod. Phys. **75**, 473–541 (2003).
32. J. Kim, J. R. Birge, V. Sharma, J. G. Fujimoto, F. X. Kärtner, V. Scheuer, and G. Angelow, "Ultrabroadband beam splitter with matched group-delay dispersion," Opt. Lett. **30**, 1569–1571 (2005).
33. M. Mero, J. Liu, W. Rudolph, D. Ristau, and K. Starke, "Scaling laws of femtosecond laser pulse induced breakdown in oxide films," Phys. Rev. B **71**, 115109 (2005).
34. M. Mero, B. Clapp, J. C. Jasapara, W. Rudolph, D. Ristau, K. Starke, J. Krüger, S. Martin, and W. Kautek, "On the damage behavior of dielectric films when illuminated with multiple femtosecond laser pulses," Opt. Eng. **44**, 051107 (2005).
35. M. Matsuhara and K. O. Hill, "Optical-waveguide band-rejection filters: design," Appl. Opt. **13**, 2886–2888 (1974).
36. B. Malo, S. Thériault, D. C. Johnson, F. Bilodeau, J. Albert, and K. O. Hill, "Apodised in-fiber Bragg grating reflectors photoimprinted using a phase mask," Electron. Lett. **31**, 223–225 (1995).
37. S.-H. Chia, T.-M. Liu, A. A. Ivanov, A. B. Fedotov, A. M. Zheltikov, M.-R. Tsai, M.-C. Chan, C.-H. Yu, and C.-K. Sun, "A sub-100 fs self-starting Cr:forsterite laser generating 1.4 W output power," Opt. Express **18**, 24085–24091 (2010).

optica

Metastable electronic states and nonlinear response for high-intensity optical pulses

M. Kolesik,[1,2,3,*] J. M. Brown,[2] A. Teleki,[3] P. Jakobsen,[4] J. V. Moloney,[1,2] and E. M. Wright[2]

[1]*Arizona Center for Mathematical Sciences, University of Arizona, Tucson, Arizona 85721, USA*

[2]*College of Optical Sciences, University of Arizona, Tucson, Arizona 85721, USA*

[3]*Constantine the Philosopher University, Nitra, Slovakia*

[4]*Department of Mathematics and Statistics, University of Tromsø, Tromsø, Norway*

Corresponding author: kolesik@acms.arizona.edu

In this paper we propose and demonstrate that the ultrafast nonlinear optical response of atoms may be accurately calculated in terms of metastable states obtained as solutions of the stationary Schrödinger equation including the quasi-static applied electric field. We first develop the approach in the context of an exactly soluble one-dimensional atomic model with delta-function potential, as this allows comparison between the exact ultrafast nonlinear optical response and our approximate approach, both in adiabatic approximation and beyond. These ideas are then applied to a three-dimensional hydrogen-like atom and yield similar excellent agreement between the metastable state approach and simulations of the Schrödinger equation for off-resonant excitation. Finally, our approach yields a model for the ultrafast nonlinear optical response with no free parameters. It can potentially replace the light–matter interaction treatment currently used in optical filamentation, and we present a numerical example of application to femtosecond pulse propagation.   © 2014 Optical Society of America

OCIS codes: (020.1335) Atom optics; (020.2649) Strong field laser physics; (190.7110) Ultrafast nonlinear optics.

http://dx.doi.org/10.1364/OPTICA.1.000323

1. INTRODUCTION

Propagation of ultrashort, off-resonant optical pulses in atomic gases produces a broad range of extreme nonlinear optical effects including high-harmonic generation [1], synthesis of attosecond pulse forms [2], and optical filamentation [3,4]. While it is generally accepted that the origin of the first two examples resides in the quantum mechanical nature of the light–matter interaction, the standard model of the nonlinearity underlying filamentation, comprising third-order nonlinearity for bound electrons plus a Drude model for freed electrons, has met with some success. However, numerical calculations of the nonlinear optical response of atoms using the time-dependent Schrödinger equation (TDSE) [5–10] make it abundantly clear that the quantum mechanical nature of the extreme nonlinearity involved is also required for a more complete and deeper understanding of filamentation. In particular, for off-resonant pulse excitation the quantum coherent nature of the light–matter interaction becomes key, and the distinction between bound and freed electrons employed in the standard model becomes problematic. In addition to the numerical simulations based on the TDSE, some model systems have been explored to gain insight. For example, some of the present authors have studied the nonlinear optical response via an exactly soluble one-dimensional (1D) atomic model with delta-function potential [11], and Richter *et al.* studied the role of the Kramers–Hennenberger atom, which displays bound states of a free electron, to elucidate the higher order Kerr effect. Models employing separable interactions [12] have also been studied in this context.

The above discussion highlights the urgent need for microscopically based and computationally economical descriptions

of extreme nonlinear interactions that lend themselves to incorporation into full space–time field simulations. In particular, numerical solution of the TDSE coupled to the field propagation equations over the space and time scales relevant to filamentation in gases poses a formidable computational task that will not be realistic in the foreseeable future, although forefront simulations over restricted spatial domains have appeared [13,14]. The standard model is easily incorporated into existing propagation schemes but the third-order nonlinear and plasma contributions to the model are not self-consistently and microscopically linked as they are in the present unified approach.

In this paper we propose and demonstrate that the ultrafast, off-resonant nonlinear optical response of atoms may be accurately calculated in terms of metastable states as opposed to the more common bound and continuum states of the free atom. In particular, we consider solutions of the atomic time-independent Schrödinger equation including the quasi-static applied electric field, these states having complex energies, the imaginary parts being related to the metastable state lifetime. Meta-stability refers to the fact that while these states ionize and thus "decay" over relatively long times, when observed on shorter time-scales in the vicinity of the atom, they are difficult to distinguish from the normal (i.e., field-free) electronic states. These metastable states, also termed resonance, Siegert, or Gamow states, encapsulate the quantum coherent coupling between the bound and continuum states of the free atom, and provide a natural time-domain description of an atom exposed to strong fields [15]. More specifically, although the single atom represents a closed system, we consider that the atomic wave function may be split into two components, $\psi = \psi_M + \psi_F$, in which ψ_M is expressed as a superposition of metastable states that is used to calculate the nonlinear optical response arising from the quantum coherent light–matter interaction. In contrast, ψ_F accounts for electrons that are to all intents and purposes freed from their parent ion and contribute a classical current density. This portion of the wavefunction is populated by the losses from the metastable states, and is subsequently driven by the applied electric field according to Ehrenfest's theorem. The metastable portion of the wavefunction, ψ_M, gives rise to a complex, nonperturbative nonlinear response, which only reduces to the usual optical Kerr effect in the limit of a weak field. Using examples we demonstrate that our approach, which we term "the Metastable Electronic State Approach" or simply MESA, provides an extremely economical computational method of calculating the nonlinear optical response: already retaining only the ground metastable state in adiabatic approximation can provide a quantitative model for the nonlinear optical response and strong-field ionization, and further improvement is shown to result from retaining post-adiabatic corrections.

The remainder of this paper is organized as follows. We develop MESA in the context of an exactly soluble 1D atomic model with delta-function potential as a test bed as this allows for comparison between the exact ultrafast nonlinear optical response and our approximate approach, both in the adiabatic approximation and beyond. The method is then applied to a three-dimensional (3D) hydrogen-like atom, and this is key to

showing that the approach can be employed for more realistic systems. We employ results for the nonlinear optical response from MESA to an example of optical filamentation as a demonstration of the computational economy and feasibility of the approach. Finally, a summary with conclusions and future research directions are given in Section 9.

2. EXACTLY SOLVABLE QUANTUM SYSTEM

An exactly solvable system proves to be of great utility for testing the method we propose. It also makes it easier to appreciate the structure of the theory, since all quantities we need can be evaluated analytically. We use a 1D, single-particle model with a Dirac-delta potential. Its time-domain Schrödinger equation can be written as

$$\left[i\partial_t + \frac{1}{2}\partial_x^2 + B\delta(x) + xF(t) \right]\psi(x,t) = 0, \qquad (1)$$

with B controlling the ionization potential of the single bound state this model has, and $F(t)$ being the time-dependent field strength of the optical pulse. An exact solution for the induced dipole moment and/or current has been recently derived [11], and this we use to test our approximate solutions. The metastable states (Stark resonances) can also be obtained exactly:

$$\psi(\lambda, x) = \begin{cases} Ci(\xi_0)Ai(\xi) & x < 0 \\ Ai(\xi_0)Ci(\xi) & x > 0 \end{cases}, \qquad (2)$$

where we define $Ci(z) = Bi(z) + iAi(z)$, with $\xi = -(2F)^{1/3}(x + \lambda/F)$ and $\xi_0 = -(2F)^{1/3}(\lambda/F)$. The spectral parameter λ must solve the eigenvalue equation for a given F:

$$1 = \frac{2\pi B}{(2F)^{1/3}}Ai\left(\frac{-2\lambda}{(2F)^{2/3}}\right)\left[iAi\left(\frac{-2\lambda}{(2F)^{2/3}}\right) + Bi\left(\frac{-2\lambda}{(2F)^{2/3}}\right)\right]. \qquad (3)$$

The infinitely many solutions to this equation, denoted by $E_n(F)$, $n = 0, 1, 2, \ldots$, represent the complex-valued metastable energies. The most important resonance, $\psi_0 = \psi(\lambda = E_0(F), x)$, converges to the ground state when $F \to 0$. Besides ψ_0, there are two distinct families of resonances. Energies of the first are located just below the positive real axis, while family-two energies extend along the ray with the complex argument of $-2\pi/3$ [16]. Meta-stable states constitute a bi-orthogonal system:

$$\langle \psi_i | \psi_j \rangle = \int_C \psi_i(z)\psi_j(z)\mathrm{d}z = N_i^2(F)\delta_{ij}, \qquad (4)$$

where $N_i^2(F) = -(2F)^{-1/3}\pi^{-1}[Ci(\xi_0)Ai'(\xi_0) + Ci'(\xi_0)Ai(\xi_0)]$. The integration proceeds along a contour in the complex plane that follows the real axis and deviates into the upper half-plane for large positive real part of z (assuming $F > 0$). Because far from the center the resonances are outgoing waves, the contour deformation ensures convergence of the integral.

The bi-orthogonality relations of Eq. (4) allow one to define a "norm," and to generalize observables [17]. In particular, we
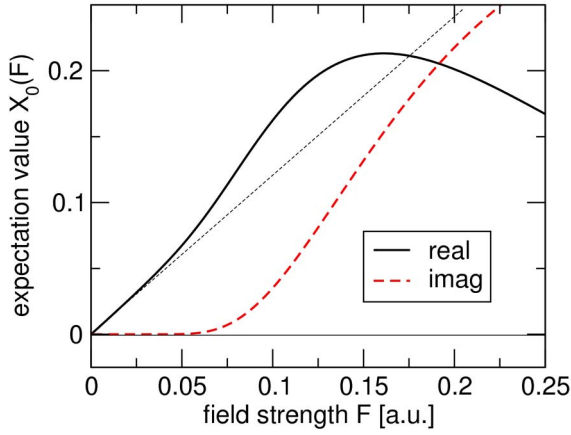
Fig. 1. Complex-valued expectation value of the dipole moment in the metastable ground state as a function of the external field strength. The fine dashed line indicates the linear susceptibility. The gap between the thin dashed and the thick black line represents the nonlinear response Eq. (11).

use the dipole-moment expectation value in the metastable ground-state:

$$X_0(F) = N_0^{-2}(F) \int_C \psi_0(z) z \psi_0(z) \mathrm{d}z. \qquad (5)$$

This quantity is shown in Fig. 1 as a function of F. Its real part is superlinear for weak fields (Kerr effect), and it saturates and decays in very strong fields, whereas the imaginary part is intimately related to the ionization losses. As noted in our previous work, the saturation and decay of the real part is accompanied by rapid growth of the freed electron population, which produces a defocusing nonlinear response. This generic behavior turns out to be the same for more realistic 3D quantum systems.

3. GENERAL SCHEME

The central idea of the method we put forward, namely, MESA, is to abandon the traditional description of the quantum evolution in terms of Hamiltonian eigenstates. Instead, we argue that for a system exposed to a strong external field, such as due to a high-intensity optical pulse, it is more natural to utilize metastable states. They are superpositions of the (field-free) bound and free electronic states, reflecting the current strength of the field and the probability density "leakage" due to ionization [18].

We assume that it is possible to represent the wavefunction split into "metastable" and "free" components, $\psi = \psi_M + \psi_F$, as described in the introduction. Our method is motivated by Berggren's completeness relations [19] employed in nuclear scattering theory:

$$1 = \sum_n |\psi_n\rangle\langle\psi_n| + \int_L \mathrm{d}\lambda |\phi_\lambda\rangle\langle\phi_\lambda|, \qquad (6)$$

where the sum projects onto several resonant states, and the integral involving scattering states ϕ proceeds along a contour

L that deviates from the real axis in order to include the poles corresponding to the complex energies of the resonances included in the first term. In our method, one or more resonant states represent ψ_M, which we assume to be the part of the wave function interacting strongly with the atomic potential. The "remainder" of the wavefunction, ψ_F, is projected from the full state via the continuum component of the above completeness relation. Note that our approximation does not rely on completeness of the resonant states. Rather the key assumption is that the continuum part of the wavefunction, ψ_F, is so spread out in space that its interaction with the atom may be neglected. If it is, we do not need to know any specific properties of ψ_F, because the quantity of interest, namely, the current, can be obtained from the Ehrenfest theorem. Validity of this approximation obviously depends on the initial state, and it is not *a priori* obvious that a small number of resonant states can capture the "interacting part" of the wave function with sufficient accuracy. However, our numerical examples below demonstrate that even a single ground-state resonance provides an extremely good approximation.

We are specifically interested in the case of off-resonant excitation, meaning that the instantaneous frequency $\omega_{\mathrm{eff}}(t) = \frac{\partial \Phi}{\partial t}$ of the applied field $F(t) = A(t)\cos(\Phi(t))$ should remain well below the ionization frequency $I/\hbar$ for all times, I being the ionization energy. Our method should therefore be more accurate for longer wavelengths, and we find this to be the case. Moreover, for the case of the exactly solvable 1D model there is an analytic result that states that the lowest Siegert state exactly captures the quantum atomic dynamics in the adiabatic or quasi-static approximation for which $\hbar\omega_{\mathrm{eff}}(t)/I \ll 1$ [15].

Concentrating on the "metastable" component, we deal with an effectively open system. We write its evolution equation as an expansion into the system of metastable states slaved to the time-dependent field:

$$i\partial_t \psi_M = \hat{H}(F(t))\psi_M(x, t),$$
$$\psi_M = \sum_i c_i(t)\psi_i(F(t), x), \qquad (7)$$

where for any instantaneous value of F, $\psi_i(F, x)$ solves the same differential equation as the proper Hamiltonian eigenstates,

$$\hat{H}(F)\psi_i(F, x) = E_i(F)\psi_i(F, x), \qquad (8)$$

but these metastable states must behave as outgoing waves at infinity. One way to "select" such waves is to modify the domain of the differential operator representing the action of the Hamiltonian. We achieve this by replacing the real coordinate axis by a contour in the complex plane. The contour is chosen to follow the real axis in the inner domain, while in the positive (negative) "outside regions" it deviates into the upper (lower) half planes. While the outgoing waves decay exponentially at infinity along this "complexified" domain axis, they still represent the same solutions (see Ref. [20] for details of implementation). Such boundary conditions make this operator non-Hermitian, and the complex-valued metastable energies

$E_i(F)$ reflect the decaying nature of the resonant states. It can be shown that the adjoint H^+ has eigenfunctions which are just complex-conjugates of ψ_i and that pairing Eq. (4) is nothing but a bi-orthogonality relation [21].

We use Eq. (4) to project out the evolution equations, normalizing all ψ_i to unity for all times t for simplicity of notation. The resulting evolution equations reflect the fact that $\psi_j(F(t))$ are effectively time dependent and, therefore, contain matrix elements that show the change of metastable states with field strength F:

$$c_{n'}(t) = -ic_n E_n(F(t)) - \sum_k c_k(t) F'(t) \langle \psi_n | \partial_F \psi_k(F(t), x) \rangle.$$

$$(9)$$

We will first concentrate on the adiabatic approximation. For the initial condition in the ground state, the adiabatic wavefunction [15] becomes dominated by the ground-state resonance and the solution is

$$c_0^{(a)}(t) = \exp\left\{ -iE_G t - i \int_{-\infty}^{t} [E_0(F(\tau)) - E_G] d\tau \right\}, \quad (10)$$

where E_G is the field-free ground-state energy. If the field is not too strong, the ground-state resonance dominates at all times, and then the generalized dipole-moment expectation of Eq. (5) is the main contribution to the induced polarization [17], $P(F(t)) = |c_0(t)|^2 X_0(F(t))$. In pulse propagation simulations the linear medium properties are captured exactly by a spectral solver. To avoid double counting, only the nonlinear part of the atom polarization is used and coupled to the Maxwell equations. This we obtain as

$$P^{(nl)}(F(t)) = P(F(t)) - \lim_{\epsilon \to 0} \frac{1}{\epsilon} P(\epsilon F(t)), \quad (11)$$

where the second term tends to the linear part of the response as the auxiliary parameter ϵ gets small. The polarization Eq. (11) is our first contribution to the nonlinear medium response. The second comes from ψ_F, in the form of a classical current, because we assume that this is the "distant part" of the wave function that is no longer interacting with the atom. Its norm grows as a result of the metastable decay, so that the total probability is conserved as it should be in a closed system. Thus, the ionization rate is given by the imaginary part of the ground-state resonance complex energy, and the ionized fraction of atoms obey

$$\partial_t \rho(t) = [1 - \rho(t)] \Im\{2E_0(F(t))\}. \quad (12)$$

The current induced by freed electrons is obtained from the Ehrenfest theorem, and is evaluated by integrating

$$\partial_t J(t) = \rho(t) F(t). \quad (13)$$

Note that this induced current arises only after ionization, which is a highly nonlinear process, and it therefore does not contain a component linear in the field strength. Thus,

the two functions $X_0(F)$ and $E_0(F)$ are needed to characterize the nonlinear optical response of the system. The proposed model has structure similar to the one used in filamentation simulations, with $P^{(nl)}(t)$ and $J(t)$ coupled into pulse propagation equations. However, the meaning of its components is new: Kerr response is now contained within the nonlinear polarization of the metastable state, which now also includes contribution from the continuum states. Moreover, what used to be the Drude current is now solely due to electrons NOT in the resonant state(s) included in our treatment. Thus, the wavefunction split, and with it the relative contributions of polarization and current density, will depend on how many metastable states we can explicitly account for. As of now we include only the ground-state resonance, and next we look at how the higher order states can be accounted for in an approximate fashion.

4. POST-ADIABATIC CORRECTIONS

The purpose of this section is to describe three kinds of corrections that take MESA beyond the adiabatic approximation outlined above. In doing so, we will strive to formulate our theory in such a way that it will require the knowledge of only a *single* metastable state, namely, the one related to the ground state. This will greatly simplify practical applications, because it is relatively simple to characterize the ground-state resonance, while it may be more difficult to calculate properties of higher metastable states. The assumption underlying the following consideration is one of a weak field $F(t)$, which is changing slowly. This is the case for many regimes in extreme nonlinear optics, where typical intensities attained in hot spots are still 2 orders of magnitude weaker than atomic fields. Moreover, the propagation dynamics dynamically adjusts the evolving pulse such that the peak intensity is clamped. As a result the quantum state is strongly dominated by the contribution from the metastable ground state, and we construct the post-adiabatic corrections under this assumption.

The first correction of the adiabatic solution is obtained by solving Eq. (9) for the expansion coefficients c_n driven by the dominant c_0. Feeding that intermediate result back into the equation for the ground-state resonance, $c_0^{(1)}(t)$ is obtained in the same form as $c_0^{(a)}(t)$, only with the resonant energy E_0 replaced by the corrected one:

$$E_0^{(R)}(F(t)) = E_0(F(t)) - \sum_{n \neq 0} \frac{(F'(t))^2 (\langle \psi_0 | \partial_F \psi_n(F(t)) \rangle)^2}{[E_n(F(t)) - E_0(F(t))]}.$$

$$(14)$$

Evaluation of this quantity requires the knowledge of higher order resonant states. Fortunately, an approximation in terms solely of ψ_0 can be obtained as follows. First, since $E_n(F)$ accumulate close to zero, at least in relatively weak fields, they are dominated by E_0, which can approximate the denominator in Eq. (14). Next, because normalization to unity for all F ensures that $\langle \psi_0 | \partial_F \psi_n \rangle = -\langle \partial_F \psi_0 | \psi_n \rangle$, the numerator in Eq. (14) can be rewritten, moving the action of ∂_F onto ψ_0 and thus giving rise to $\sum_{n \neq 0} \ldots |\psi_n\rangle\langle\psi_n|\ldots$. Our second assumption is that, at least within the space of the solutions

that evolve from the ground state, the system of $\{\psi_n\}$ is complete, and this projection can be approximated by $1 - |\psi_0\rangle\langle\psi_0|$. Then we can simplify the above correction to

$$E_0^{(R)}(F(t)) = E_0(F(t)) + \frac{(F'(t))^2}{E_0(F(t))}\langle\partial_F\psi_0(F(t))|\partial_F\psi_0(F(t))\rangle.$$
(15)

This modifies both the real and imaginary parts of the complex metastable energy. It is the imaginary part that is more important for our purposes because it increases the ionization yield. Figure 2 illustrates this effect, and shows ionization yields caused by a driving pulse in the adiabatic and post-adiabatic [i.e., with Correction (15)] approximations, compared to the exact solution. It is evident that the correction becomes negligible for longer wavelengths. At shorter wavelengths, it significantly decreases the gap between the adiabatic and exact solutions, thus justifying the approximations adopted in the derivation. Perhaps the most important observation to be made here is that even the uncorrected adiabatic solution provides rather accurate ionization rates. For practical purposes in the field of optical filamentation, especially in the

Fig. 2. Ionization yield as a function of the intensity of the driving pulse. Exact, adiabatic, and corrected solutions are compared. The top and bottom panels correspond to wavelengths of $\lambda = 2400$ nm and $\lambda = 800$ nm, respectively.

near and mid-infrared, the adiabatic treatment should therefore be sufficient.

However, there is one post-adiabatic correction that should be included in such simulations; because it captures the losses, the optical field must suffer due to ionization. Interestingly, this correction is connected to the *imaginary part* of the metastable expectation value of the dipole moment. To derive the corresponding nonlinear polarization term, one has to include the first corrections $c_n^{(1)}$ of the wavefunctions when evaluating the expectation value of the dipole moment. Then, under the same approximation as in the derivation of the corrected resonant energy in Eq. (15), one obtains the following estimate:

$$P_{\mathrm{NL}}^{(\mathrm{corr})}(t) \sim \frac{1}{E_G}\Im\left\{\frac{\partial}{\partial t}\langle\psi_0(F(t))|X|\psi_0(F(t))\rangle\right\}.$$
(16)

This component of the nonlinear polarization turns out to be responsible for a major part of nonlinear losses. It is a microscopically motivated replacement for the purely phenomenological current, which is routinely introduced into the standard filamentation model [3] in order to salvage energy conservation. Our comparative simulations show that the amount of loss caused by $P^{(\mathrm{corr})}$ is actually quite similar to that obtained in the phenomenological treatment. It is fair to say that Eq. (16) is an approximation, yet it is a first step beyond the current method. Naturally, it could be improved provided one can calculate higher resonant states.

Finally, the third correction originates in the split between ψ_M and ψ_F, and the fact that the response of the latter is approximated by a Drude-like classical current as if this portion of the wavefunction was completely free. A generalized version of Eq. (13) should contain an additional term,

$$\partial_t J(t) = \rho(t)F(t) + v_i\partial_t\rho(t),$$
(17)

where v_i stands for the initial velocity of freed electrons, which "disappear" from ψ_M and are "injected" into ψ_F. This correction can give rise to an important contribution to terahertz (THz) generation, and will be discussed in detail elsewhere. However, because it generates only a DC-like, low-frequency current, it has a negligible influence on the propagation of the driving pulse and can be safely ignored for that purpose.

5. COMPARISON WITH EXACT SOLUTIONS

The exactly solvable Dirac-delta system is an ideal test bed to assess accuracy of the proposed light–matter interaction description. We utilize the time-dependent exact solution for the nonlinear response given in Ref. [11]. This is then compared with the nonlinear response calculated as described in the previous sections.

The sole adjustment we make before comparing these results concerns the low-frequency part of the response described above. It shows up as a constant current after the driving pulse vanishes, reflecting the net average velocity imparted on the ionized electrons. While it is possible to capture this effect in the resonance-response model, at present an estimate of
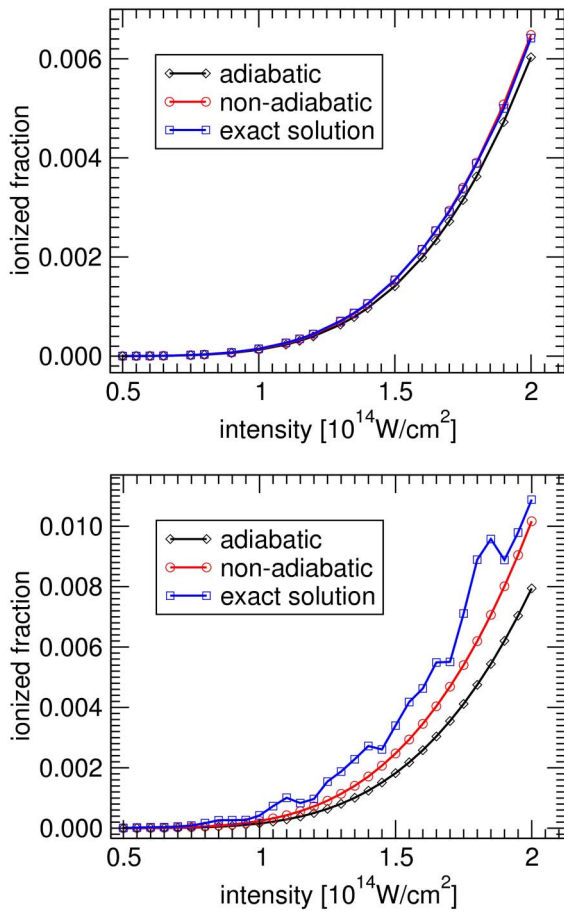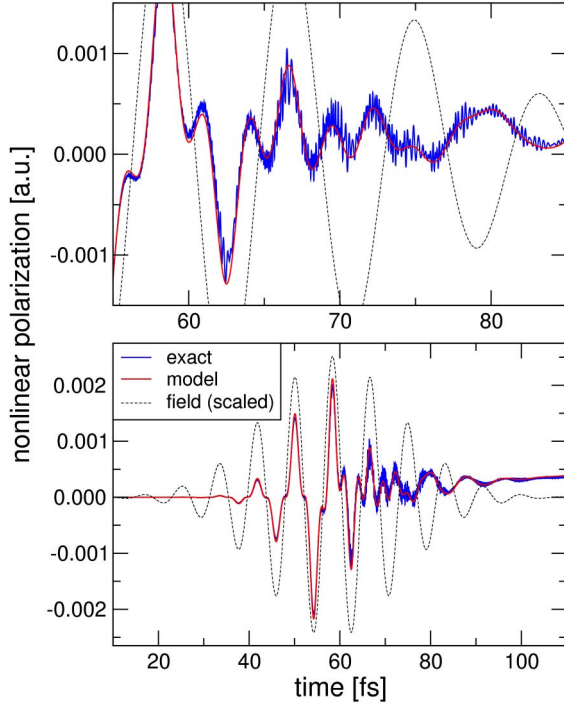
Fig. 3.　Nonlinear response of the Dirac-delta system to a $\lambda = 2.5 \ \mu m$ driving pulse indicated by the thin dashed line. The exact response is shown as a blue solid line, and the resonant-response model result is shown in thick red. The top panel zooms in to highlight that our response model "filters out" very-high-frequency components. The bottom panel demonstrates accurate overall agreement between approximate and exact solutions.

v_i requires one adjustable parameter. We therefore filter out the very low-frequency part of the exact response and add this to the MESA result to compare the nonlinear response.

Figure 3 illustrates that very good agreement can be achieved between the exact and approximated nonlinear response for a 2.5 μm wavelength driving pulse. One can see that the approximate solution follows the exact one while it filters out the very-high-frequency components. These are due to higher order resonances and are therefore absent in our post-adiabatic approximation.

The top panel shows that these response oscillations are too fast to affect the optical-frequency components of the driving pulse. For simulation of pulse propagation, it is therefore quite convenient that the model response does not follow them.

We thus can conclude that the proposed method captures precisely that frequency part of the total nonlinear response that is responsible for the back-reaction of the medium on the driving pulse. At the same time, even small-scale details in the nonlinear response shape are reproduced quite well.

6. 3D HYDROGEN-LIKE MODEL ATOM

Having seen that the nonlinear response of the exactly solvable model can be reproduced by the metastable-state response model quite accurately, the important question is if it still works for more realistic systems. The crucial difference is that one has to resort to approximate methods to find, and

"measure," properties of the ground-state resonance. In the following we describe the procedure that allows one to obtain parameterized nonlinear response from a series of TDSE simulations of a given system. The Hamiltonian represents a single-electron, hydrogen-like system,

$$H = -\frac{1}{2}\Delta - \frac{1}{\sqrt{a^2 + x^2 + y^2 + z^2}} - xF(t), \qquad (18)$$

with a "soft" Coulomb potential and a time-dependent external field (of the optical pulse) $F(t)$.

To obtain the ground-state resonance as a function of the static-field strength F, we start a TDSE simulation in the numerical ground state, and add transparent boundary conditions realized as a perfectly matched layer (PML) to the computational domain. Because the ground-state resonance is the longest living state, the initial wavefunction is driven toward it during the simulated real-time evolution, while the "unwanted" states decay as they leak through the PML layers. Once the solution stabilizes, we characterize this ground-state resonance by calculating the metastable expectation value for its dipole moment. We also extract its complex-valued resonance energy. This process is repeated for a range of field strengths, and the relevant data are tabulated. We envision that this kind of procedure will be applied when working with realistic (single-active-electron) models of atoms and perhaps even molecules.

Figure 4 shows the real and imaginary parts of metastable dipole moment $X_0(F)$. We have determined this quantity as a function of the field strength on different-size grids, and with three different implementations of the PML boundary. Two data sets, obtained for grid sizes of $L = 100$ a.u. and $L = 150$ a.u., are shown in the figure to match closely, thus indicating that convergence is already achieved on relatively small computational domains. It should be noted that, if one attempts to determine the standard quantum-mechanical expectation value of the dipole moment, no convergence can be reached because metastable wavefunctions diverge at
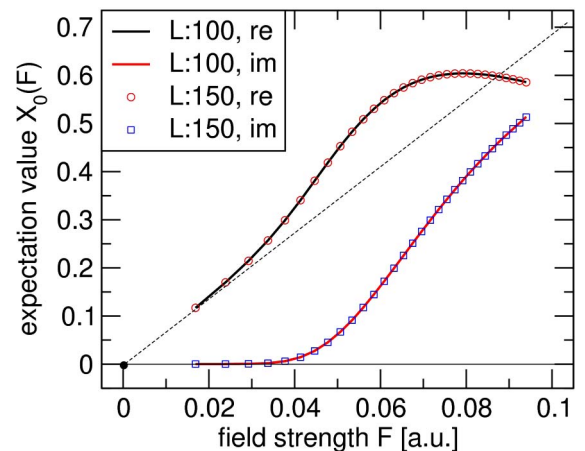
Fig. 4.　Complex-valued dipole moment of a 3D hydrogen-like model atom, measured in the metastable state born from the ground-state as a function of the external field strength. Data obtained for two computational domain size L are shown, indicating fast convergence.

infinity. It is thus crucial that our method works with the metastable generalization of the dipole moment [Eq. (5)].

Importantly, comparing Fig. 4 to Fig. 1, one can see that the behavior of the field-induced dipole is qualitatively the same in the 3D system as in the exactly solvable 1D model. This makes us believe that features of $X_0(F)$ are quite generic.

Together with the field-dependent metastable ground-state energy $E_0(F)$, tabulation of the nonlinear of the dipole moment $X_0(F)$ shown in Fig. 4 constitutes the core data that characterize the quantum system, and makes it possible to calculate its response to arbitrary pulsed excitation. Note that the TDSE simulations to obtain these data sets require significant, but only a one-time, numerical effort.

7. COMPARISON WITH TDSE SOLUTIONS

To demonstrate that the nonlinear response can be calculated the same way also for a more realistic system, we have generated time-dependent solutions of the Schrödinger equation for our hydrogen-like system, exposed to a near-infrared frequency pulse. For comparison purposes, we remove the linear polarization from our numerical solutions. We also remove a low-frequency background, which contributes only to the THz generation that would not affect dynamics of the driving infrared pulse.

Figure 5 shows an example in which both Kerr-like and plasma-like responses show up in the leading and trailing edge of the pulse, respectively. Regimes like this one, when counteracting components of the nonlinear response manifest themselves on similar scales, are of utmost importance for extreme nonlinear optics, since the filamentation physics is naturally influenced by this kind of dynamic balance.

We have chosen the shape of the excitation pulse to have a flat middle portion in order to better visualize different processes that would control the dynamics of the propagating pulse. In the leading edge of the pulse, the polarization is in phase with the optical field. During this time, the self-focusing response dominates. In the trailing edge, in contrast, we see the response being out of phase, which is a sign that it acts mainly as a defocusing mechanism. In the temporal middle
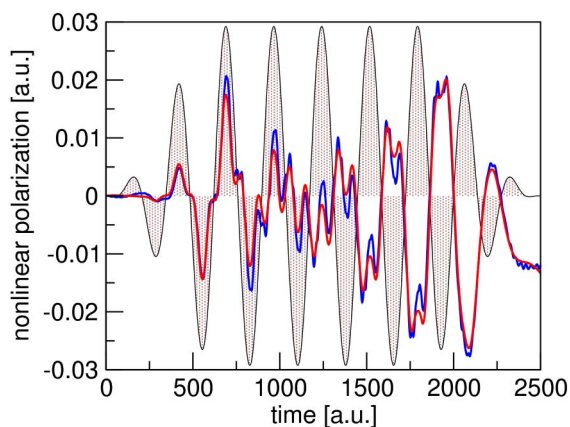
of the pulse one can see that the two compete. Importantly, the agreement between the numerically exact and the response calculated with the proposed model is rather good.

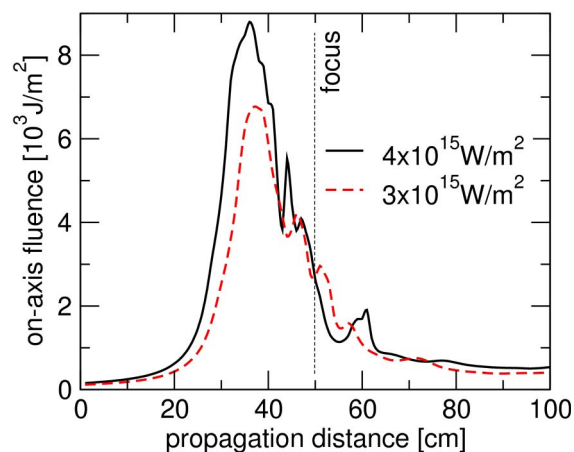## 8. APPLICATION EXAMPLE: FEMTOSECOND FILAMENTATION

As an illustrative example of the utility of MESA, we consider a femtosecond filament created by a 30 fs optical pulse propagating in a model gaseous medium. The medium consists of atoms at atmospheric pressure, each responding to the optical field as described above. Besides the nonlinear atomic response, the medium has a linear susceptibility, which we choose to be the same as that of air. This is implemented as a part of the linear optical propagator [22]. To execute the simulation, we utilize the generalized unidirectional pulse propagation equations framework (gUPPEcore) [23] with a medium module that implements the MESA response.

The parameters of our illustration are chosen to create a situation in which several processes affecting the dynamics act simultaneously. In particular, we choose the wavelength $\lambda = 2$ μm, for which the generation of new harmonics, along with their subsequent "temporal walk-off," are more relevant than for 800 nm pulses.

Furthermore, we assume relatively tight focusing geometry, with $f = 50$ cm. This is to verify that the defocusing properties of the model are sufficient to arrest the self-focusing collapse, which is made more severe by the external focusing. Figure 6, showing the on-axis energy fluence versus propagation distance for two different initial pulse intensities, demonstrates that it is indeed the case.

The defocusing effects are mainly due to free electrons. Figure 7 shows the linear density of generated freed electrons are versus propagation distance. The model accounts for the corresponding energy losses via the imaginary part of the induced dipole moment.

Figure 8 shows the spectrum for propagation distances just before and after the filament. Well-defined harmonic orders are obvious before the collapse: they give rise to an additional collapse regularization that is much stronger than for

Fig. 5. Nonlinear response of a hydrogen-like system to a $\lambda = 2$ μm driving pulse indicated by the shaded area(s). The exact TDSE response is shown by the blue dashed line, and the resonant-response model result is shown in red.

Fig. 6. On-axis energy fluence in a filament created by a 30 fs, $\lambda = 2.0$ μm pulse. The two curves represent simulations with the indicated initial intensity.
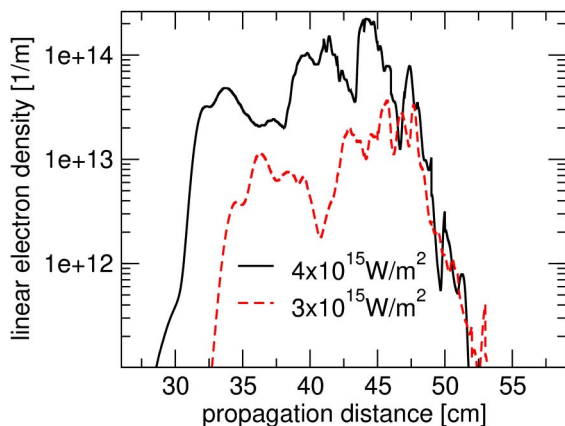
Fig. 7. Free electrons generated per unit of propagation length.
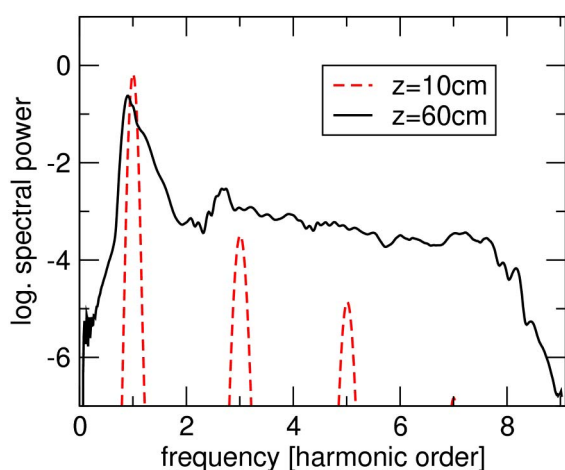
Fig. 8. Supercontinuum generation in a femtosecond filament. The spectrum before the collapse exhibits well-separated harmonic orders.

$\lambda \sim 800$ nm. Eventually, an extremely broad supercontinuum is generated in the filament (full line). In contrast to the more studied near-infrared regime, at this and still longer wavelengths the spectral dynamics coupled with the dispersion properties of the medium become the most important physical mechanism controlling filamentation. It thus becomes crucial that properties of third- and fifth-harmonic generation, together with free-electron generation and accompanying energy losses, are all modeled in a unified manner, so that, as the wavelength is varied, all processes are included in correct proportion.

Importantly for our demonstration, all relevant effects are captured in a self-consistent way, without the necessity and even possibility of parameter tuning. To our knowledge, this is the first demonstration of a filament simulation *on an experimentally relevant scale* in which the light–matter interaction description relies on first principles.

9. CONCLUSION

In summary, we have introduced the metastable state approach for calculating the ultrafast, off-resonant nonlinear

optical response of gases, and demonstrated its accuracy and computational economy. As a test bed, we employed a 1D atomic model that allows for comparison of MESA against exact solutions, and excellent agreement between the exact and approximate results were obtained for the nonlinear optical response even using only a single metastable state in adiabatic approximation. We have also identified post-adiabatic corrections that are responsible for the slight increase of ionization rate and for losses that the optical field suffers as a consequence of ionization. The approach was also applied to a 3D hydrogen-like model with similarly good agreement between MESA and TDSE simulations. As a demonstration of the computational economy of MESA, an example of optical filamentation was presented.

In the present work, we required knowledge of the properties of only a single metastable state, namely, the one that arises from the system's ground state. Higher order metastable states were included only indirectly with the help of additional approximations. It will be interesting to explore the feasibility of inclusion of several states in ψ_M. This should make it possible to capture even more noninstantaneous effects, and help to understand how a driven quantum system starts to exhibit behavior dependent on its own history.

In future work we plan to apply MESA to simulation of optical filamentation in current experiments, with argon, for example, and also to explore the application to molecules to allow simulation of air. While the initial TDSE-based characterization of the given model atom or molecule becomes much more demanding, the application of the method to such realistic systems remains conceptually the same. Recent progress in direct experimental characterization of optical nonlinearities at ultrafast time scales brought quantitative results concerning the self-focusing nonlinearity [24] as well as free-electron generation [25] in various gases. Importantly, spatiotemporal profiles of the nonlinear responses can now be obtained essentially free of propagation effects, which complicate interpretation of dynamics in other, for example, filamentation regimes. Comparison with these and similar future experiments should provide a practical way to validate and benchmark the nonlinear response models based on the approach proposed here.

To finish, we note that MESA yields a model for the ultrafast nonlinear optical response with no free parameters for a given gas. Importantly, from a practical simulation point of view, the approach has a computational complexity comparable to that of the standard light–matter interaction model used in optical filamentation. In this sense, the method provides a microscopically founded replacement.

REFERENCES

1. T. Popmintchev, M.-C. Chen, P. Arpin, M. M. Murnane, and H. C. Kapteyn, "The attosecond nonlinear optics of bright coherent x-ray generation," Nat. Photonics **4**, 822–832 (2010).

2. F. Krausz and M. Ivanov, "Attosecond physics," Rev. Mod. Phys. **81**, 163–234 (2009).

3. A. Couairon and A. Mysyrowicz, "Femtosecond filamentation in transparent media," Phys. Rep. **441**, 47–189 (2007).

4. L. Bergé, S. Skupin, R. Nuter, J. Kasparian, and J.-P. Wolf, "Ultrashort filaments of light in weakly ionized optically transparent media," Rep. Prog. Phys. **70**, 1633–1713 (2007).

5. M. Nurhuda, A. Suda, and K. Midorikawa, "Generalization of the Kerr effect for high intensity, ultrashort laser pulses," New J. Phys. **10**, 053006 (2008).

6. E. A. Volkova, A. M. Popov, and O. V. Tikhonova, "Nonlinear polarization response of an atomic gas medium in the field of a high-intensity femtosecond laser pulse," JETP Lett. **94**, 519–524 (2011).

7. E. A. Volkova, A. M. Popov, and O. V. Tikhonova, "Polarization response of a gas medium in the field of a high-intensity ultrashort laser pulse: high order Kerr nonlinearities or plasma electron component?" Quantum Electron. **42**, 680–686 (2012).

8. A. M. Popov, O. V. Tikhonova, and E. A. Volkova, "Polarization response of an atomic system in a strong mid-IR field," Laser Phys. Lett. **10**, 085303 (2013).

9. P. Béjot, E. Cormier, E. Hertz, B. Lavorel, J. Kasparian, J.-P. Wolf, and O. Faucher, "High-field quantum calculation reveals time-dependent negative Kerr contribution," Phys. Rev. Lett. **110**, 043902 (2013).

10. C. Köhler, R. Guichard, E. Lorin, S. Chelkowski, A. D. Bandrauk, L. Bergé, and S. Skupin, "Saturation of the nonlinear refractive index in atomic gases," Phys. Rev. A **87**, 043811 (2013).

11. J. M. Brown, A. Lotti, A. Teleki, and M. Kolesik, "Exactly solvable model for non-linear light-matter interaction in an arbitrary time-dependent field," Phys. Rev. A **84**, 063424 (2011).

12. T. C. Rensink, T. M. Antonsen, J. P. Palastro, and D. F. Gordon, "Model for atomic dielectric response in strong, time-dependent laser fields," Phys. Rev. A **89**, 033418 (2014).

13. E. Lorin, S. Chelkowski, and A. Bandrauk, "The WASP model: a micro–macro system of wave-Schrödinger-plasma equations for filamentation," Commun. Comput. Phys. **9**, 406–440 (2011).

14. E. Lorin, S. Chelkowski, and A. Bandrauk, "Maxwell-Schrödinger-Plasma (MASP) model for laser-molecule interactions: towards an understanding of filamentation with intense ultrashort pulses," Physica D **241**, 1059–1071 (2012).

15. O. I. Tolstikhin, T. Morishita, and S. Watanabe, "Adiabatic theory of ionization of atoms by intense laser pulses: one-dimensional zero-range-potential model," Phys. Rev. A **81**, 033415 (2010).

16. R. M. Cavalcanti, P. Giacconi, and R. Soldati, "Decay in a uniform field: an exactly solvable model," J. Phys. A **36**, 12065–12080 (2003).

17. T. Berggren, "Expectation value of an operator in a resonant state," Phys. Lett. B **373**, 1–4 (1996).

18. L. Hamonou, T. Morishita, O. I. Tolstikhin, and S. Watanabe, "Siegert-state method for ionization of molecules in strong field," J. Phys. Conf. Ser. **388**, 032030 (2012).

19. T. Berggren, "On the use of resonant states in eigenfunction expansions of scattering and reaction amplitudes," Nucl. Phys. A **109**, 265–287 (1968).

20. A. Bahl, A. Teleki, P. Jakobsen, E. M. Wright, and M. Kolesik, "Reflectionless beam propagation on a piecewise linear complex domain," J. Lightwave Technol. **32**, 3670–3676 (2014).

21. D. C. Brody, "Biorthogonal quantum mechanics," J. Phys. A **47**, 035305 (2014).

22. A. Couairon, E. Brambilla, T. Corti, D. Majus, O. J. Ramirez-Gongora, and M. Kolesik, "Practitioner's guide to laser pulse propagation models and simulation," Eur. J. Phys. Special Topics **199**, 5–76 (2011).

23. J. Andreasen and M. Kolesik, "Nonlinear propagation of light in structured media: generalized unidirectional pulse propagation equations," Phys. Rev. E **86**, 036706 (2012).

24. J. K. Wahlstrand, Y.-H. Cheng, and H. M. Milchberg, "Absolute measurement of the transient optical nonlinearity in N_2, O_2, N_2O, and Ar," Phys. Rev. A **85**, 043820 (2012).

25. Y.-H. Chen, S. Varma, T. M. Antonsen, and H. M. Milchberg, "Direct measurement of the electron density of extended femtosecond laser pulse-induced filaments," Phys. Rev. Lett. **105**, 215005 (2010).

optica

Three-dimensional integral imaging displays using a quick-response encoded elemental image array

ADAM MARKMAN, JINGANG WANG, AND BAHRAM JAVIDI*

Electrical & Computer Engineering Department, University of Connecticut, 371 Fairfield Road Unit 4157, Storrs, Connecticut 06269, USA

Corresponding author: bahram@engr.uconn.edu

Mobile devices are a ubiquitous technology, and many researchers are trying to implement three-dimensional (3D) displays on mobile devices for a variety of applications. We investigate a method to store compressed and encrypted elemental images (EIs) used for 3D integral imaging displays in multiple quick-response (QR) codes. This approach allows user friendly access, readout, and 3D display with mobile devices. We first compress the EIs and then use double-random-phase encryption to encrypt the compressed image and store this information in multiple QR codes. The QR codes are then scanned using a commercial Smartphone to reveal the encrypted information, which can be decrypted and decompressed. We also introduce an alternative scheme by applying photon counting to each color channel of the EIs prior to the aforementioned compression and encryption scheme to generate sparsity and nonlinearity for improved compression and security. Experimental results are presented to demonstrate both 3D computational reconstruction and optical 3D integral imaging display with a Smartphone using EIs from the QR codes. This work utilizing compressed QR encoded EIs for secure integral imaging displays using mobile devices may enable secure 3D displays with mobile devices. © 2014 Optical Society of America

Integral imaging, a promising three-dimensional (3D) imaging technique, has been extensively investigated in disciplines as diverse as entertainment, medical sciences, robotics, manufacturing, and defense [1–9]. Photon counting has been incorporated with integral imaging [6,7] to reconstruct a 3D image from a photon-starved environment. Recently, double-random-phase encryption (DRPE) with photon counting has been incorporated with integral imaging [7]. It was shown that integral imaging can provide better security performance along with the ability to secure 3D information. The DRPE technique [10–18] is able to encrypt and decrypt an image. There have been numerous improvements to the encryption system to enhance security [12–14] in the system. One encryption scheme involves applying a photon-counting technique to the amplitude of the encrypted image generating a photon-limited image [6,7,15,17]. This technique limits the number of photons arriving at a pixel. As a result, the decrypted image is sparse, noise-like, and difficult to visually authenticate. In [17], a binary image was encrypted and compressed using the full-phase DRPE with photon counting and an iterative Huffman coding technique, respectively, and stored in a quick-response (QR) code. The QR code was then scanned by a QR reader built in commercial Smartphones revealing the data. The scanned data were then decompressed and decrypted revealing a noise-like decrypted image that can be authenticated using nonlinear correlation filters [19–21]. In this Letter, we propose a method to securely store a RGB elemental image (EI) in a QR code by combining run-length encoding (RLE) [22] with the Huffman coding compression [23] scheme along with DRPE [10]. By storing data in a QR code [24–26], it is possible to reduce the amount of information needed to transfer the EI. We can store multiple EIs in QR codes that can be used in 3D integral imaging reconstruction [1–9]. In addition, we present an alternative scheme by first applying photon counting on the EI followed by RLE, Huffman coding, and encryption to generate sparsity and nonlinearity due to Poisson transformation for improved compression and security. Both computational and optical reconstruction of the EIs is presented.

Integral imaging [1–9] can produce a 3D image of a scene by recording multiple two-dimensional (2D) images
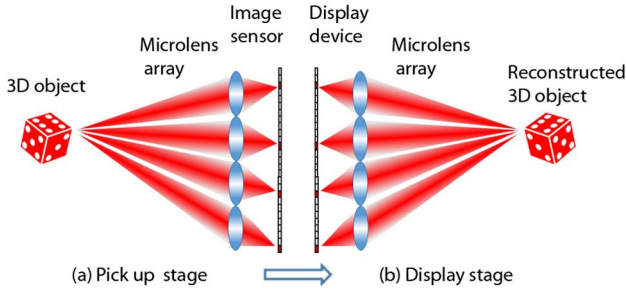
Fig. 1. (a) Pickup and (b) display stages of an integral imaging system.

of different perspectives of the scene, known as EIs. This is achieved by using various pickup methods such as an array of image sensors or a camera with a lenslet array, as shown in Fig. 1(a). Reconstruction of the 3D scene from the recorded EIs can be performed optically, as shown in Fig. 1(b), or computationally. Optical reconstruction is performed by projecting the EIs through a lenslet array to the image plane forming a 3D scene. Computational reconstruction uses a virtual pinhole array to inversely project the EIs to the image plane to obtain the reconstructed scene as follows [4,6,9]:

$$R(x,y,z) = \frac{1}{O(x,y)} \times \sum_{k=0}^{K-1} \sum_{l=0}^{L-1} E_{kl}\left(x - k\frac{N_x \times p}{c_x \times M}, y - l\frac{N_y \times p}{c_y \times M}\right),$$
$$(1)$$

where $R(x,y,z)$ is the intensity of the reconstructed 3D image at depth z, x and y are the index pixels, E_{kl} is the intensity of the kth column and the lth row of the EIs, K and L are the total numbers of EIs in the column and row, respectively, N_x and N_y are the total numbers of pixels for each EI, M is the magnification factor z/g, g is the focal length, p is the pitch between image sensors, c_x, c_y are the spatial sizes of the image sensor, and $O(x,y)$ is the overlapping number matrix.

DRPE is used to encrypt the input image [10]. One-dimensional (1D) notation will be used in explaining the encryption method. To implement the encryption scheme, let x and v denote the spatial and frequency domains, respectively, $f(x)$ be the primary input image, and $n(x)$ and $b(v)$ represent random noises that are uniformly distributed over the interval [0,1]. The encrypted image is

$$\psi(x) = \{f(x) \times \exp[i2\pi n(x)]\} * h(x),$$
$$(2)$$

where $*$ denotes convolution and $\times$ denotes multiplication, $\exp[i2\pi n(x)]$ is a phase mask, and $h(x)$ is a function whose Fourier transform is $\exp[i2\pi b(v)]$.

The decryption process is the reverse of the encryption process. The Fourier transform of the DRPE image, $\psi(x)$, is multiplied by the complex conjugate image of the phase mask, $\exp[-i2\pi b(v)]$. The Fourier transform is taken once more. The intensity of the image can then be recorded, which produces the decrypted image, $f_{decrypt}(x)$, if the primary input image is real and positive.

RLE [22] is a lossless compression technique that represents a series of repeated data by stating the number of times the data are repeated followed by the repeated integer. For example,

[8 8 8 8 8] is represented by [5 8]. Huffman coding [23] is a dictionary-based compression technique that can be combined with RLE to allow for sufficiently small images to be stored in a QR code. By combining the two compression methods, less information is stored in the QR code, improving the ability of a Smartphone to scan the QR code [24].

We compress each channel of the RGB image using RLE followed by Huffman coding. The DRPE [Eq. (2)] is used to encrypt each channel of the compressed image. Due to the ciphered images being complex, both the real and imaginary parts must be retained. As a result, both are stored in separate QR codes, which are generated using the ZXing project [25]. In addition, the encrypted images are rounded to one decimal place to minimize the amount of necessary information stored in the image. Each ciphered channel of the RGB image can then be stored in separate QR codes. Moreover, we can use the same encryption keys for each color channel. For a single RGB image, six QR codes are used in our experiments. The EI must be sufficiently small so that the compressed and encrypted data can be stored in a single QR code.

Once the QR code has been scanned, the data can be successfully decrypted if the decryption keys are known. In addition, the image can be decompressed if the dictionary associated with the Huffman code compression is known; no dictionary is required to decompress the RLE algorithm.

Figure 2(a) depicts a 19 × 19 pixel input RGB image. For brevity, the red channel of the RGB image is explained. The process can be repeated for the other channels. Figure 2(b) shows a QR code that stores the real part of the ciphered input image, while Fig. 2(c) shows the imaginary part of the ciphered input image. Figures 2(d) and 2(e) display the compressed and encrypted data stored in the QR codes using the iPhone SCAN application. After decompressing and decrypting the necessary data, the three color channels of the decrypted image are combined to form the decrypted RGB image as shown in Fig. 2(f).

To determine the degree of degradation (if any) due to DRPE combined with RLE and Huffman coding compression schemes, the mean squared error (MSE) is calculated as

$$MSE = \frac{1}{NM} \sum_{n=0}^{N-1} \sum_{m=0}^{M-1} [f_{decrypt}(x_n, y_m) - f(x_n, y_m)]^2, \quad (3)$$
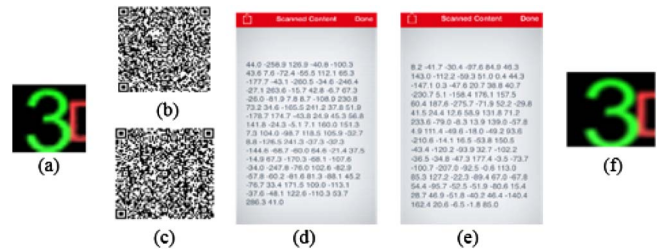
Fig. 2. (a) 19 × 19 pixel RGB image; (b) and (c) display the QR codes containing the real and imaginary information for the red color channel from the compressed and ciphered image shown in (a), respectively; (d) and (e) depict a scanned QR code using the iPhone SCAN application revealing the real and imaginary information from the compressed and ciphered image, respectively, for the red color channel of the image shown in (a); (f) shows the decrypted and decompressed image.
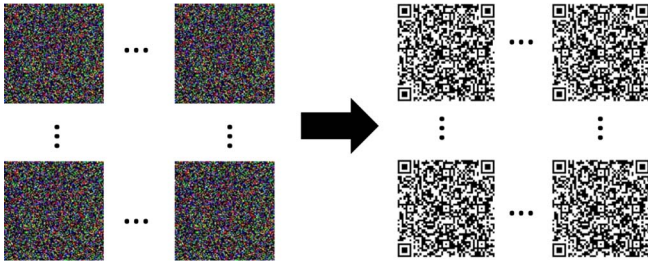
Fig. 3. Storing multiple RGB encrypted EIs inside of multiple QR codes.

where n and m are pixels in the x and y directions, respectively, N and M represent the total number of pixels in the x and y directions, respectively, $f_{\text{decrypt}}(x_n, y_m)$ is the decrypted and decompressed RGB image, and $f(x_n, y_m)$ is the original RGB image.

Since both Huffman coding and RLE are lossless, and no information is lost during DRPE, the MSE calculated between the images shown in Figs. 2(a) and 2(f) is 0.

It is possible to store multiple encrypted and compressed images in multiple QR codes as shown in Fig. 3. Each QR code can be scanned allowing for every EI to be recovered. Thus, this approach can have applications in integral imaging reconstruction by storing the EIs in QR codes.

A 3D integral imaging experiment was conducted for computational integral imaging reconstruction. Each EI used identical encryption and decryption keys. Moreover, identical encryption keys were used in the spatial and frequency domains. Four 19×19 pixel RGB EIs, shown in Fig. 4(a), were generated using 3Ds Max. The 3D scene consists of a green "3" and red letter "D" located 65 and 115 mm away from a lenslet array. These images were compressed using RLE followed by Huffman coding compression and then encrypted with DRPE. These EIs were decrypted and decompressed revealing the original EIs.

Computational reconstruction results using Eq. (1) were obtained. Figure 4(b) depicts the computational reconstruction at 65 mm focused on "3," while Fig. 4(c) depicts computational results at 115 mm focused on "D."

Storing a large quantity of EIs in multiple QR codes may prove burdensome and inconvenient. Regardless, with improving camera resolution and hardware of Smartphones, it will be possible in the future to store more information in QR codes. Thus, it may be feasible to store a prodigious number of encrypted and compressed EIs in QR codes. An optical experiment was carried out using the proposed compression and encryption scheme to secure EIs for 3D display. Using
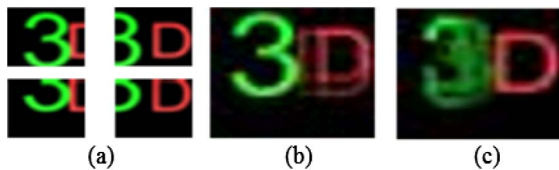
3Ds Max, 54×96 RGB EIs, similar to the EIs shown in Fig. 4(a), were used, which were each 19×19 pixels. As before, each EI used identical encryption and decryption keys. These images were then compressed using RLE followed by Huffman coding compression and encrypted with DRPE. Each EI had identical encryption keys for both the spatial and frequency domains. These EIs were then decrypted and decompressed revealing the EIs. An HTC One Smartphone was used to display the optical reconstruction. Figure 5 depicts the experimental setup for optical reconstruction using an HTC One Smartphone and a lenslet array. Table 1 presents the experimental parameters.

Figure 6(a) depicts the 3D optical reconstruction using the primary EIs, while Fig. 6(b) depicts the 3D optical reconstruction using the decompressed and decrypted EIs. The reconstruction results using our proposed method are as good as the conventional method. There is no visible loss of information due to compression, encryption, and QR encoding.

Storing data in QR codes holds many practical advantages due to not requiring any specialized hardware to scan the QR code. Moreover, Smartphones are a ubiquitous technology. The proposed technique of storing QR codes can potentially be modified by creating a video barcode as described in [26] to allow a faster user experience when scanning multiple QR codes.

We now introduce an alternative compression and security approach. We first apply photon counting [6,7,15,17] to each channel of an RGB EI, $f(x, y)$. Photon counting is described by a statistical method for a limited number of photons that arrive at a pixel. Thus, the lower the total number of photons in the image, the fewer the number of photons that arrive at a pixel. By reducing the number of photons, it is possible to have more sparsity, improving the RLE compression scheme used prior to Huffman coding. Also, the nonlinear transformation introduced by photon counting improves the security. Photon counting can be modeled as a Poisson distribution:

Fig. 5. Optical 3D integral imaging display setup using a Smartphone and a lenslet array.

Table 1. Specifications of 3D Display Setup

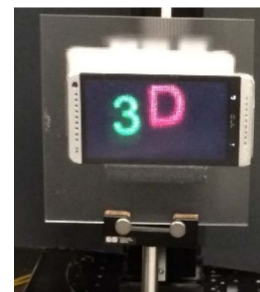| HTC One Smartphone Display Panel	Resolution	$1080(V) \times 1920(H)$
	Pixel Size	54.1 μm
Lenslet array	Pitch	0.985 mm
	Focal length	3.3 mm
	Numbers of lenses	$54(V) \times 96(H)$

Fig. 4. 19×19 pixel RGB: (a) EIs that were compressed using RLE and Huffman coding followed by encryption using DRPE; (b), (c) computational 3D integral imaging reconstructions with four EIs at a distance (range) of (b) 65 mm focused on "3" and (c) 115 mm focused on "D."
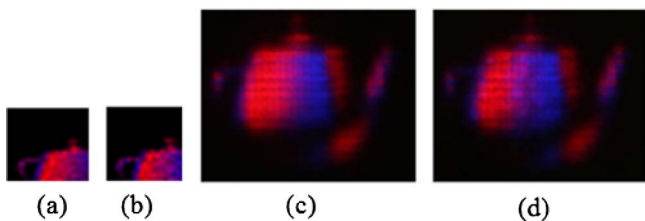
Fig. 6. 3D display results using Smartphone. (a) 3D optical reconstruction with integral imaging using the primary EIs. (b) Optical 3D reconstruction using the decrypted and decompressed EIs obtained from the compressed DRPE EIs in QR codes.

$$P(l_j; \lambda_j) = \frac{[\lambda_j]^{l_j} e^{-\lambda_j}}{l_j!}, \quad \text{for } \lambda_j > 0, \quad l_j \in \{0, 1, 2, \ldots\}, \quad \textbf{(4)}$$

where l_j is the number of photons detected at pixel j and λ_j is the Poisson parameter defined as $N_p x_j$, where N_p is the number of photons in the scene and x_j is the normalized irradiance at pixel j such that $\sum_{j=1}^{J} x_j = 1$ with J being the total number of pixels. Moreover, the normalized irradiance is defined as $|f(x_m, y_n)| / \sum_{m=1}^{M} \sum_{n=1}^{N} |f(x_m, y_n)|$, where m and n denote pixels in the x and y directions, respectively, and M and N represent the total numbers of pixels in the x and y directions, respectively.

A 54×96 RGB EI array with each EI being 19×19 pixels, similar to the EI depicted in Fig. 7(a), was used for 3D photon-counting imaging compression and security. The object chosen was a color gradient teapot generated by 3Ds Max.

Photon counting was applied to each channel of the RGB EI as shown in Fig. 7(b) using 3000 photons or about eight photons per pixel on each channel of the 19×19 RGB image. RLE is then applied, followed by Huffman coding and DRPE. The image was then decrypted and decompressed. Optical reconstruction using an HTC phone (see Table 1) was used to reconstruct the image [see Eq. (1)]. Figure 7(c) depicts the optical reconstruction showing the original EI, while Fig. 7(d) depicts the optical reconstruction using the photon-limited EI. The MSE [see Eq. (3)] was calculated to determine the degree of degradation for each individual color channel. For comparison, both images were normalized to [0,255]. The MSE for the red color channel was calculated as 62.94, the green channel was 1.07, and the blue channel was 19.73. Thus, there was some degree of degradation;

however, visually the 3D optical reconstruction of the photon-counted image can still be discerned.

A comparison of the compression with and without photon counting was conducted. It was found that for a sufficiently lower number of photons, the photon-counting method helped to improve the compression scheme. Using the EIs in Figs. 7(c) and 7(d), the total length of the Huffman code following RLE was compared. It was found that the red channel was 21.7% shorter and the blue channel was 18.53% shorter; there were no green channel components in the test image. These results show that photon counting may allow for larger EIs to be stored in QR codes after compression and encryption.

We have presented a method and experiments for secure integral imaging as a potential approach to store EIs in QR codes for 3D displays. The compressed and encrypted EIs using DRPE can be stored in multiple QR codes to be scanned by a commercial Smartphone revealing the encrypted and compressed EIs. This data can then be decrypted and decompressed to obtain the original EIs for secure 3D integral imaging displays. We also present an alternative compression and security scheme by applying photon counting to the input image followed by compression and encryption. By using photon counting, the compression and security system improve at the cost of diminished image quality. Future work may include alternative algorithms for encrypting the EIs, compressing the EIs, and video scanning the QR codes.

Fig. 7. 3D photon counting integral imaging compression and security experiments. A 54×96 EI array consisting of 19×19 pixel RGB EIs was used. (a) Shows an EI, while (b) depicts the corresponding photon-limited EI using about eight photons per pixel on each color channel of the EI. 3D optical reconstruction after decryption and decompression is shown (c) using original EIs and (d) when photon counting on the EIs was used.

REFERENCES

1. G. Lippmann, C. R. Acad. Sci. **146**, 446 (1908).
2. H. E. Ives, J. Opt. Soc. Am. **21**, 171 (1931).
3. F. Okano, H. Hoshino, J. Arai, and I. Yuyama, Appl. Opt. **36**, 1598 (1997).
4. S. Hong, J. Jang, and B. Javidi, Opt. Express **12**, 483 (2004).
5. F. Okano, J. Arai, K. Mitani, and M. Okui, Proc. IEEE **94**, 490 (2006).
6. B. Tavakoli, B. Javidi, and E. Watson, Opt. Express **16**, 4426 (2008).
7. M. Cho and B. Javidi, Opt. Lett. **38**, 3198 (2013).
8. L. Yang, M. McCormick, and N. Davies, Appl. Opt. **27**, 4529 (1988).
9. X. Xiao, B. Javidi, M. Martinez-Corral, and A. Stern, Appl. Opt. **52**, 546 (2013).
10. P. Réfrégier and B. Javidi, Opt. Lett. **20**, 767 (1995).
11. B. Javidi and J. L. Horner, Opt. Eng. **33**, 1752 (1994).
12. A. Carnicer, M. Montes-Usategui, S. Arcos, and I. Juvells, Opt. Lett. **30**, 1644 (2005).
13. Y. Frauel, A. Castro, T. J. Naughton, and B. Javidi, Opt. Express **15**, 10253 (2007).
14. O. Matoba and B. Javidi, Opt. Lett. **24**, 762 (1999).
15. E. Pérez-Cabré, M. Cho, and B. Javidi, Opt. Lett. **36**, 22 (2011).
16. J. F. Barrera, A. Mira, and R. Torroba, Opt. Express **21**, 5373 (2013).
17. A. Markman, B. Javidi, and M. Tehranipoor, IEEE J. Photonics **6**, 1 (2014).
18. J. F. Heanue, M. C. Bashaw, and L. Hesselink, Appl. Opt. **34**, 6012 (1995).
19. F. Sadjadi and B. Javidi, *Physics of Automatic Target Recognition* (Springer, 2007).
20. B. Javidi, Appl. Opt. **28**, 4518 (1989).
21. F. Dubois, Appl. Opt. **32**, 4365 (1993).
22. R. Bose, *Information Theory, Coding, and Cryptography* (Tata McGraw-Hill, 2002).
23. D. Huffman, Proc. IRE **40**, 1098 (1952).
24. "QR code minimum size," http://www.qrstuff.com.
25. http://zxing.appspot.com/generator.
26. X. Liu, D. Doermann, and H. Li, IEEE Trans. Multimedia **10**, 361 (2008).

optica

Adaptive multifrequency light collection by self-ordered mobile scatterers in optical resonators

Valentin Torggler and Helmut Ritsch*

Institute for Theoretical Physics, University of Innsbruck, Technikerstrasse 25/2, A-6020 Innsbruck, Austria

*Corresponding author: helmut.ritsch@uibk.ac.at

Photons carry momentum, and thus their scattering not only modifies light propagation but at the same time induces forces on particles. Confining mobile scatterers and light in a closed volume thus generates a complex coupled nonlinear dynamics. As a striking example, one finds a phase transition from random order to a crystalline structure if particles within a resonator are illuminated by a sufficiently strong laser. This phase transition can be simply understood as a minimization of the optical potential energy of the particles in concurrence with a maximization of light scattering into the resonator. Here, we generalize the self-ordering dynamics to several illumination colors and cavity modes. In this enlarged model, particles adapt dynamically to current illumination conditions to ensure maximal simultaneous scattering of all frequencies into the resonator as a sort of self-optimizing light collection system with built-in memory. Such adaptive self-ordering dynamics in optical resonators could be implemented in a wide range of systems from cold atoms and molecules to mobile nanoparticles in solution. In the quantum regime, it enables exploration of uncharted regions of multiparticle phases, allowing simulation of Hopfield networks, associative memories, or generalized Hamiltonian mean field models.   © 2014 Optical Society of America

OCIS codes: (270.0270) Quantum optics; (140.6630) Superradiance, superfluorescence; (020.7010) Laser trapping.

http://dx.doi.org/10.1364/OPTICA.1.000336

1. INTRODUCTION

Polarizable particles in an optical resonator which are coherently illuminated from the side at sufficient intensity will undergo a phase transition from homogeneous to crystalline order accompanied by super-radiant collective light scattering [1–3]. This transition can be understood from a simultaneous maximization of collective scattering of pump light into the cavity and the depth of the corresponding optical potential created via interference of pump and cavity light [4,5]. In a monochromatic plane wave geometry, the particles form a Bragg-like grating structure, which optimally couples cavity and pump wave so that the intensity of the scattered light grows with the square of the particle number. In a lossy cavity, the ordering process is dissipative and cools the particles, so that in the long time limit light is constantly collectively scattered into the cavity. For varying frequency and geometry of the

illumination, the particles continuously tend toward a configuration with maximal scattering, rendering the system an adaptive self-optimizing light collection device.

Here, we study a generalized model of these self-ordering dynamics with several light frequencies applied simultaneously, each of which tends to push the particles toward a competing order. As generic example, we study a spectral composition of laser light with several light frequencies tuned closely to different cavity modes. As the longitudinal cavity modes form an equidistant comb of distinct resonances, a corresponding illumination is implementable with standard comb technology at comparable technical complexity to the single-mode case. For sufficiently distinct pump frequencies, light scattering between different modes can be neglected. Hence, no precise phase locking is required and also the computational complexity of the model grows only linearly with the number

of modes. Besides studying the multitude of stationary solutions of the coupled particle-field dynamics, we also numerically compute the time evolution for larger particle ensembles and illumination frequencies, including friction and momentum-diffusion terms. Note that a more complex dynamics arises for cavities with degenerate mode families as, e.g., in a confocal cavity, which already exhibits a very rich structure for a single pump frequency [6,7]. Interestingly, even for particles in free space, collective light scattering can induce some spatial bunching and ordering via optical binding, which has been extensively studied in theory and experiments [8–15], and a rather complex motional dynamics via collective light scattering is also predicted for corresponding multifrequency configurations as, e.g., optical lattices [16].

After a short presentation of the semiclassical dynamical model in Section 2, we will study the forces and stationary states in generic two- and three-particle configurations in Section 3. Typical scenarios of dynamical evolution trajectories in the particle-field phase space of growing complexity are studied in Section 4, which is followed by long-term studies of many-particle dynamics including memory effects.

2. MODEL

We consider N identical polarizable point particles of mass m representing, e.g., individual atoms, molecules, or nanoparticles trapped within an optical resonator supporting a large number of modes of similar finesse with wave numbers $k_n := nk$ and frequencies ω_n (see Fig. 1). The particles are illuminated transversely by lasers with frequencies $\omega_{p,n}$, each closely tuned to one of the cavity modes but sufficiently detuned from internal optical excitations to ensure linear polarizability and negligible spontaneous emission. Each particle scatters light in and out of the nth cavity mode with phase and coupling strength $\eta_n \sin(k_n x_j)$ depending on its position x_j. For computational simplicity, we restrict the particles' motion along the cavity axis, but 2D and 3D traps should lead to essentially similar physics. Following standard adiabatic elimination procedures, the coherent dynamics of the system can be described by the effective Hamiltonian [5]

$$H = \sum_{j=1}^{N} \frac{p_j^2}{2m} + \hbar \sum_{n \in I} \left[-\left(\delta_{c,n} - U_{0,n} \sum_{j=1}^{N} \sin^2(k_n x_j) \right) a_n^\dagger a_n \right.$$
$$\left. + \eta_n \sum_{j=1}^{N} \sin(k_n x_j)(a_n + a_n^\dagger) \right]. \tag{1}$$
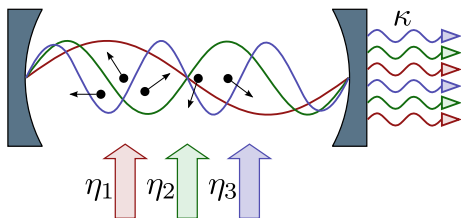
Fig. 1. Mobile particles inside a lossy multimode optical resonator with decay rate κ illuminated by various laser beams with pump strengths η_1, η_2, and η_3.

Here, η_n is the effective pump strength, $U_{0,n}$ is the light shift per photon, and $\delta_{c,n} := \omega_{p,n} - \omega_n$ is the detuning between laser and cavity mode frequency. For nanoparticles, $U_{0,n}$ is directly proportional to the particle's polarizability [17]. x_j and p_j denote position and momentum of the jth particle, while a_n and $a_n^\dagger$ are the bosonic annihilation and creation operators of the nth cavity mode field. The illumination pattern is specified by choosing a subset $I \subset \mathbb{N}$ of modes with pump amplitudes η_n. Including dissipation via cavity photon loss requires us to solve the master equation

$$\dot{\rho} = -\frac{i}{\hbar}[H, \rho] + \mathcal{L}\rho, \quad \text{with}$$
$$\mathcal{L}\rho := \sum_n \kappa_n (2a_n \rho a_n^\dagger - a_n^\dagger a_n \rho - \rho a_n^\dagger a_n) \tag{2}$$

being a Liouvillian damping operator $\mathcal{L}$.

While the full quantum model exhibits intriguing physical behavior as quantum phase transitions even for a single frequency [7,18], the enlarged case of two modes and few particles already touches the limits of current numerical computability [19]. Here, we focus on the essential physics of crystallization and collective light scattering for many particles and modes, which forces us to use simplifications. Hence, we treat particle motion classically and assume coherent states with complex amplitudes α_n for the cavity modes. Fortunately, this approximation works well in related treatments of cavity cooling [6] and self-ordering. The corresponding semiclassical equations for the coupled particle-mode dynamics can be written as [5]

$$\dot{x}_j = \frac{p_j}{m}, \tag{3a}$$

$$\dot{p}_j = -\hbar \sum_{n \in I} k_n (U_{0,n}|\alpha_n|^2 \sin(2k_n x_j)$$
$$+ \eta_n (\alpha_n + \alpha_n^*) \cos(k_n x_j)), \tag{3b}$$

$$\dot{\alpha}_n = i(\delta_{c,n} - U_{0,n} \sum_{j=1}^{N} \sin^2(k_n x_j))\alpha_n - \kappa_n \alpha_n$$
$$- i\eta_n \sum_{j=1}^{N} \sin(k_n x_j) + \xi_n. \tag{3c}$$

The Langevin noise term ξ_n and the weak frequency dependence of U_0, δ_c, and κ will be mostly neglected in the following. These equations, obtained in similar form previously [6,20], contain the essence of multicolor self-ordering. Generalizations to include spontaneous emission leading to extra momentum diffusion of the particles are straightforward to introduce in principle, but are much harder to analyze in practice.

3. SELF-ORDERED STATES AND LIGHT SCATTERING OF FEW PARTICLES IN A MULTICOLORED FIELD

Before starting a detailed and extensive numerical analysis, let us first examine a few simple but instructive few-particle cases where we look for stationary states. In the bad cavity limit, where cavity losses happen on a shorter timescale compared to particle motion, the field adiabatically follows the particle positions and can be expressed in the form

$$\alpha_n(x_1, \ldots, x_N) = \eta_n \frac{\sum_j \sin(k_n x_j)}{\delta_c - U_0 \sum_j \sin^2(k_n x_j) + i\kappa}, \quad (4)$$

where we neglect the n-dependence of U_0, δ_c, and κ. This immediately shows that a homogeneous particle distribution possesses a close to zero field as the sum in the numerator will vanish. Only an ordered configuration will show significant scattering with an amplitude proportional to the particle number in the best case, when all sines in the sum are of same sign and order 1. Such a configuration is connected to a particular wave vector k_n, but one can envisage particle distributions which are close to optimal for several distinct frequencies. Note that the denominator shows resonant scattering enhancement if δ_c is suitably shifted from the bare cavity resonance $\delta_c = 0$ to induce a deep optical potential and stable particle order.

In the bad cavity limit, the force on the jth particle [Eq. (3b)] thus is effectively a function $F_j(x_1, \ldots, x_N)$ of the particle positions. Hence, when we determine the points in configuration space where all F_j's are vanishing, we obtain the equilibrium points of the system. To determine their stability in a strongly damped case, where $\dot{x}_j \propto F_j(x_1, \ldots, x_N)$, a stability criterion which only involves checking the sign of the real part of the eigenvalues of the Jacobian of the vector containing the F_j's is employed.

A. Two Particles

As a first nontrivial example, we consider two particles subject to transverse red-detuned multicolor pumping, where we first choose low-order cavity modes to graphically better display the physics. Depending on their positions, they scatter a different fraction of the various pump fields into the cavity. For the known case of a single pump frequency as shown in Fig. 2 on the left, we find a periodic pattern of strong scattering configurations when both particles sit on field antinodes with the same phase. Adding extra pump lasers close to other longitudinal modes only slightly shifts the stable equilibrium points with respect to the single-pump frequency configuration and creates some extra equilibria (see Fig. 2 on the right). However, the total amount of scattered light $P_{tot} = \sum_n |\alpha_n|^2$ at each stable point now strongly varies, which implies different local trap depths. In a statistical equilibrium distribution, one will then find the particles more likely in deeper potential wells. As these are naturally associated with stronger light scattering, the system adapts toward optimal light collection. Note that strong scattering more likely occurs along the diagonal, where both particles occupy the same well and scatter with exactly the same phase.
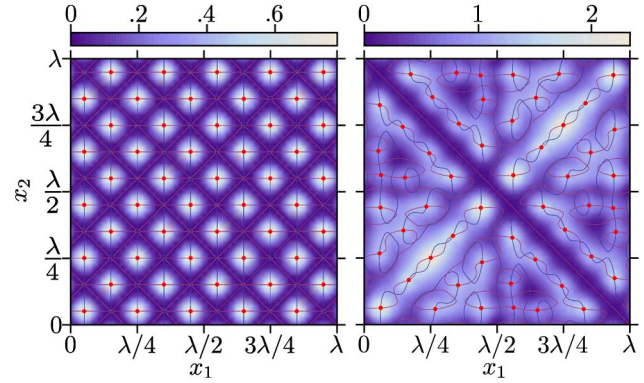
Fig. 2. Scattered light intensity and stable configurations (red dots) for two scatterers as function of position within one wavelength of the fundamental mode. The density plot shows the associated cavity light intensity P_{tot} and the contours give zero-force lines for each particle illuminated with frequencies near the five lowest-order modes ω_n, $n \in \{1, 2, 3, 4, 5\}$. On the left, we only pump at the fifth mode, i.e., $\eta_l/\eta = (0, 0, 0, 0, 1)$, while on the right four modes are pumped, i.e., $\eta_r/\eta = (1, 0, 1, 1, 1)$. Parameters are $\eta = 5\kappa/8$, $NU_0 = -\kappa/10$, $\delta_c = NU_0 - \kappa$.
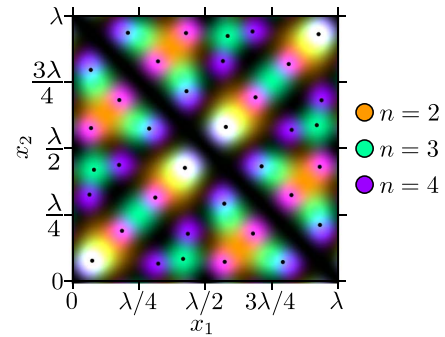

Fig. 3. Total scattered light intensity as in Fig. 2 for three pump frequencies $\eta_v/\eta = (0, 1, 1, 1, 0)$, with the different mode intensities color coded. In white areas, all three modes oscillate.

Clearly, the optimum scattering positions for the different frequencies do not coincide, as demonstrated in Fig. 3, where we color-code three different scattering intensities by different colors. For most particle positions one or two colors dominate, but there are a few spots with nearly equal intensity scattering, yielding "white" scattered light.

B. Three Particles

The more complex case of three particles and several frequencies invokes a configuration space of a cube of length $\lambda = 2\pi/k$. The distribution of the stable equilibrium points for two different illumination conditions is depicted in Fig. 4 by small spheres, where size and color of the spheres represent the total amount of scattered light at the corresponding stable point. Again, the points with maximum scattering are on the diagonal (i.e., all three particles are in the same well). Note that in the chosen example, the number of stable points is much larger than for two particles; it strongly increases with particle number as the number of possible distributions of particles
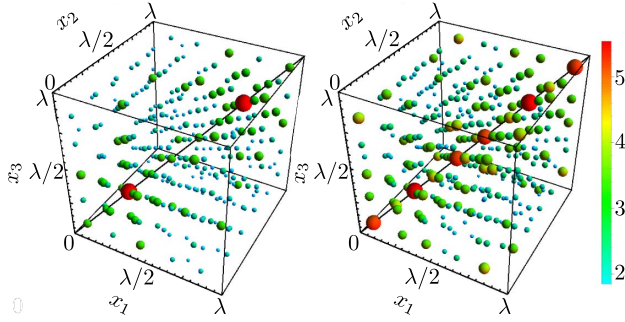
Fig. 4. Stable equilibrium configurations for three particles represented by spheres, whose size and color encode the amount of scattered light P_{tot} in this configuration. Illumination is set to $\eta_l/\eta = (1, 0, 1, 0, 1)$ on the left and $\eta_r/\eta = (1, 0, 1, 1, 1)$ on the right, with the other parameters fixed as in Fig. 2.
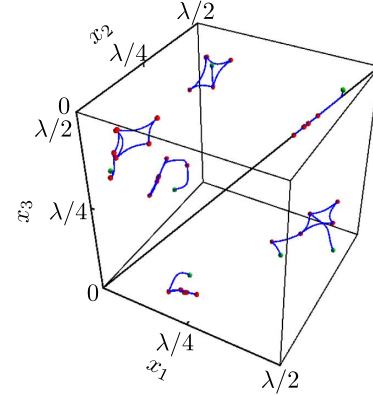

Fig. 5. Configuration space trajectories for three particles with periodically time-varying illumination starting at different initial positions. η_t/η periodically cycles through five different illumination conditions given by $(1, 0, 1, 0, 0, 0, 1)$, $(0, 1, 1, 0, 1, 1, 0)$, $(0, 0, 1, 0, 1, 0, 0)$, $(0, 1, 1, 1, 1, 1, 0)$, $(1, 1, 1, 1, 1, 0, 1, 0)$. The illumination changes after the system has reached a stable (zero force) point (red dots). Parameters are $\eta = \kappa/5$, $NU_0 = -\kappa$, and $\delta_c = NU_0/2 - 2\kappa$.

among the optical potential minima grows. Note, however, that the optical potential has to be self-consistently derived from the particle distribution, so that we were not able to find an explicit corresponding scaling law with particle number.

4. ADAPTIVE DYNAMICS OF THE COUPLED PARTICLE FIELD SYSTEM

So far, we have studied light fields and forces at fixed particle positions, where points of vanishing force give equilibrium positions. Equations (3), however, also describe dynamical properties of the system. As known from the single-mode case, the delayed field response during the self-ordering for negative detuning induces friction (cavity cooling) so that the system reaches a steady state [20]. To mimic cavity cooling as well as other possible damping, e.g., by a background gas in the system, in the following numerical simulations we simply add an effective linear friction force $f_\mu = -\mu \dot{p}_j$ to Eq. 3(b). This is only an approximation to the actual full dynamics, but will guide the system toward a stationary equilibrium state as desired.

A. Dynamics for Strongly Damped Particle Motion

Let us study the coupled particle-field dynamics in a simplified form first, where the friction force is large so that the particles quickly relax to a stationary velocity for a given light force (over damped case). The light fields in turn will continuously adapt to the current particle positions and the coupled system evolves to a close-by equilibrium configuration exhibiting a local light scattering maximum similar to the case of a self-consistent optical lattice [21]. When the illumination condition changes, the particles will evolve toward a new equilibrium point, which better adapts to the momentary pump field configuration. We visualize these dynamics by periodically repeating a series of different pump light patterns. In this case, after some initial position changes, the particles find a suitable closed loop in the configuration space and periodically follow the illumination sequence. In each step, they quickly arrange to a local optimum configuration to maximize combined light scattering. Due to the complexity of the optical potential landscape, for different initial conditions a multitude of such loops are

attained for the same illumination sequence. These can be distinguished by a characteristic corresponding output intensity sequence. Typical paths in the configuration space of three particles for a specific illumination sequence with different initial positions are shown in Fig. 5, nicely demonstrating this effect.

B. Dynamics with Noise Forces on the Particles

In any real system, damping is accompanied by noise forces on the particles, which in a simple form are modeled by random momentum kicks on individual particles as used for Brownian motion. Their effective strength relates to a temperature parameter. In the full dynamics [Eq. (1)], we also get white noise term ξ_n representing field fluctuations as derived in Ref. [20], which in the optical domain at room temperature just represent vacuum fluctuations of the cavity field. While in a quantitatively correct description, these and even more noise sources would have to be carefully modeled and scaled, we restrict ourselves here to their qualitatively most important effect, which is that they render the force-free stationary configurations of the particles metastable. Driven by fluctuations, the system will eventually leave any such equilibrium configuration and evolve toward a new metastable state. In Fig. 6, we show a typical simulated trajectory for two scatterers over an extended time. While the particles rapidly evolve in the dark areas between different equilibrium points, the trajectory concentrates close to bright areas of the background picture, denoting strong light scattering. The system thus explores a large volume of configuration space but preferentially stays at points of strong scattering, where trapping is efficient.

This effect of localization near scattering maxima is displayed more quantitatively in Fig. 7. On the left we see that often both particles stay in the same well, with $kx_{1,2}/\pi$ hopping between 0.5 and 1.5. These configurations correspond to points of maximal scattering as shown in the right picture. Because available phase space is rather limited for two particles in
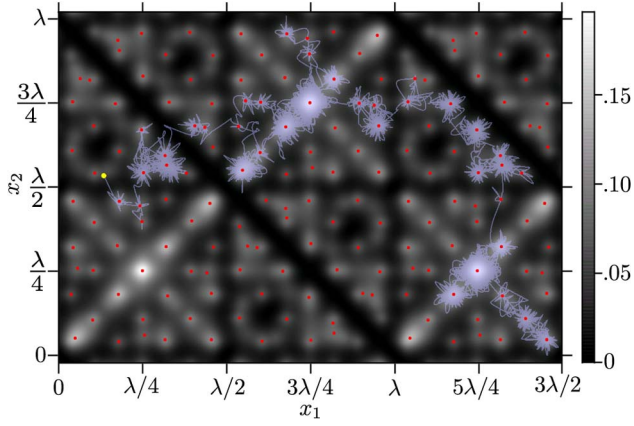
Fig. 6. Typical trajectory of two particles with static illumination $\eta_s/\eta = (1, 0, 1, 1, 1, 0, 1)$ and random momentum kicks at time intervals $\Delta t = 2/\kappa$ and friction $\mu = 2\kappa$, with the yellow dot indicating the initial position. As in Fig. 2, the background density shows the scattered intensity P_{tot} and red dots indicate equilibrium positions with zero average light force. Other parameters are $\eta = \kappa/5$, $U_0 = -\kappa/2$, and $\delta_c = NU_0/2 - 2\kappa$.

1D, they will eventually meet each other at the same position where collective scattering is strongest. As the trapping potential is deeper at such points, the time it takes the particles to diffuse out of the corresponding optical well is much larger than for shallow minima with low light scattering. Hence, adding noise finally helps the particles to find more stable equilibria with enhanced scattering rates, which is the basis of the system-inherent scattering optimization mechanism. This dynamic adaptation and optimization mechanism certainly requires and deserves a more in-depth and quantitatively accurate study. However, due to the large number of parameters and possible mode choices, a systematic investigation goes beyond the scope of this work and we will concentrate on a different aspect, namely the memory properties of the dynamics in the following.
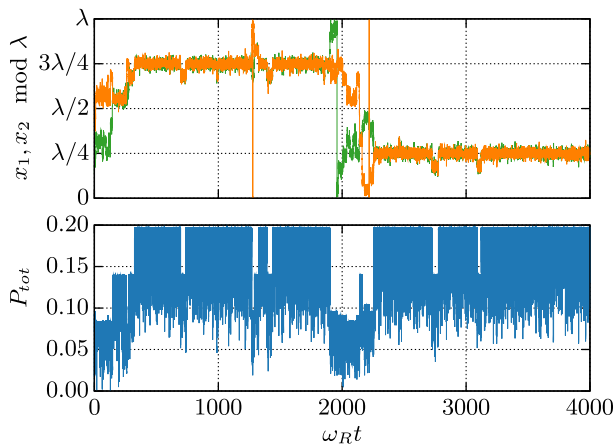
Fig. 7. Positions of the two particles' modulo 2 wavelengths (upper graph) and scattered light intensity P_{tot} (lower graph) for the trajectory of Fig. 6 with $\omega_R = \kappa\pi^2/10$. The particles spend most time at points of high scattering at $x_{12} \sim \lambda/4$ or $3\lambda/4$.

C. Time Evolution of Larger Ensembles with Randomly Varying Pump Light

While the previous examples nicely illustrate the basic physical mechanism of multicolor self-ordering, more interesting scenarios appear for many higher-order modes and larger particle numbers with smaller individual couplings. Since in the corresponding configuration space, a huge number of stationary states corresponding to local energy minima exist, it is far less likely for the system to come close to a global optimum, and many intermediate configurations appear. In the following, we consider many particles and tens of modes to study the extent to which we still get enhanced collective light scattering into several modes. Fortunately, in the classical regime of particle and field dynamics, this only requires a moderate increase in computing power. As particle phase space cannot be graphically depicted here, we show only important collective quantities as the total light intensity $P_{tot} = \sum_n |\alpha_n|^2$ scattered into all modes, and the sum of order parameters for all modes

$$\Theta_{tot} = \sum_n |\Theta_n|, \qquad \Theta_n = \frac{1}{N}\sum_j \sin(k_n x_j), \qquad (5)$$

where Θ_n quantifies how close the system is to perfect order with respect to the nth mode.

Of course, for large particle and mode numbers with numerous parameter choices, we can only discuss a few typical cases. As before, we assume high field-seeking particles and sufficiently red-detuned cavity pumping to avoid heating and nonlinear instabilities. Since we are interested in finding stationary configurations not so much in the precise time evolution toward them, we assume sufficiently strong friction again with negligible noise. We choose five illumination patterns consisting of about 50 distinct frequencies nk of equal pump strength η randomly chosen out of the set $\{n_1, n_1 + \Delta n, \ldots, n_1 + 99\Delta n\}$, with $n_1 = 1003$ and $\Delta n = 7$.

As in Section 4, we switch between the chosen illumination patterns after a prescribed time, when a stationary configuration is reached and the particles do not move anymore. In contrast to the periodic repetition considered previously, here we randomly choose one of the five patterns at every switch so that no closed loops are attained and the system will evolve nontrivially on a longer timescale.

One realization of these dynamics is shown in Fig. 8, where we plot the total scattered light intensity P_{tot} and the order parameter sum Θ_{tot}. We observe that P_{tot} and Θ_{tot} is roughly monotonically increasing, demonstrating that the system continuously improves its adaptation to the changing illumination. Due to the vast amount of possible configurations, this is a rather slow process, continuing at least to 8000 switches. After a sufficiently long time, the particles have found areas of configuration space with well-adapted positions to all five illumination patterns. Both the time needed to reach such a state and the resulting light intensity strongly vary for different realizations (i.e., different sequences of illumination patterns), but the qualitative behavior is generally similar. Interestingly we observed that if one particular mode is pumped in all of the applied illumination patterns, i.e., it is
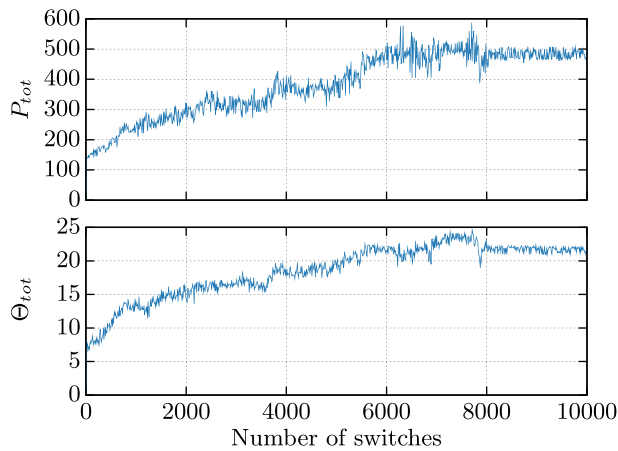
Fig. 8. Time evolution of 100 scatterers under aperiodically time-varying illumination with about 50 high-order modes. The illumination is switched randomly between five illumination patterns consisting of 50 randomly chosen modes after the particles have settled to a stationary state. The two graphs display the total scattered light P_{tot} (upper figure) and the sum of magnitudes of the order parameters Θ_{tot}, as defined in Eq. (5) (lower figure). Other parameters chosen are as in Fig. 5.

kept on continuously, the scatterers often preferentially adapt to scatter into this particular mode with much less light scattered to the others. Such a trapping gets more likely the higher the order of the mode is, as such a mode possesses more local minima. Overall, such a dominance of a particular mode results in a lower total scattering intensity summed over all modes. We also observe that the number of particles in clusters (i.e., with zero distance) grows with increasing Θ_{tot}. This mimics a lower effective particle number with higher individual coupling. In a more realistic model in 2D or 3D, such clusters can be expected to form much slower, and momentum diffusion will eventually split existing clusters and prevent lumping of the system.

Note that one can also interpret the adaptive ordering as acquisition of a memory of past illumination conditions. We see that when we apply any of the five illumination patterns after a long time evolution, more light will be scattered for each configuration than for the random particle distribution in the beginning. Hence, the system remembers that this illumination has been applied before, with the information stored in the order of the atoms.

5. CONCLUSIONS AND OUTLOOK

We have seen that the coupled particle-field evolution of mobile scatterers with multifrequency illumination in an optical resonator exhibits a wealth of intriguing phenomena beyond simple regular self-ordering. For a proper choice of the detunings and pump powers, the particles evolve toward a multitude of different spatial configurations, locally minimizing their optical potential energy and at the same time maximizing total light scattering into the cavity. For time-varying illumination conditions, the system continuously optimizes its light-scattering properties and acquires a memory of past conditions. This speeds up adaptation to a new equilibrium when similar conditions reappear, which increases overall scattering

efficiency with time. Adding noise and diffusion allows the system to explore larger volumes of configuration space, which results in a configuration diffusion dynamics toward close to optimum scattering conditions for many light frequencies simultaneously. This includes concurrent super-radiant scattering into several cavity modes. Hence, we can consider the system an adaptive and self-learning light collection system with built-in memory. While implementations with a cold gas in a high-Q cavity would give straightforward possibilities to experimentally study such dynamics, alternative setups using mobile nanoparticles in solutions provide equally interesting experimental platforms [22].

REFERENCES

1. P. Domokos and H. Ritsch, "Collective cooling and self-organization of atoms in a cavity," Phys. Rev. Lett. **89**, 253003 (2002).
2. A. T. Black, H. W. Chan, and V. Vuletić, "Observation of collective friction forces due to spatial self-organization of atoms: from Rayleigh to Bragg scattering," Phys. Rev. Lett. **91**, 203001 (2003).
3. K. Arnold, M. Baden, and M. Barrett, "Self-organization threshold scaling for thermal atoms coupled to a cavity," Phys. Rev. Lett. **109**, 153002 (2012).
4. T. Grießer, H. Ritsch, M. Hemmerling, and G. Robb, "A Vlasov approach to bunching and self-ordering of particles in optical resonators," Eur. Phys. J. D **58**, 349–368 (2010).
5. H. Ritsch, P. Domokos, F. Brennecke, and T. Esslinger, "Cold atoms in cavity-generated dynamical optical potentials," Rev. Mod. Phys. **85**, 553–601 (2013).
6. P. Domokos, T. Salzburger, and H. Ritsch, "Dissipative motion of an atom with transverse coherent driving in a cavity with many degenerate modes," Phys. Rev. A **66**, 043406 (2002).
7. S. Gopalakrishnan, B. L. Lev, and P. M. Goldbart, "Emergent crystallinity and frustration with Bose-Einstein condensates in multimode cavities," Nat. Phys. **5**, 845–850 (2009).
8. M. Burns, J. Fournier, and J. Golovchenko, "Optical matter: crystallization and binding in intense optical fields," Sci. Mag. **249**(4970), 749–754 (1990).
9. W. Singer, M. Frick, S. Bernet, and M. Ritsch-Marte, "Self-organized array of regularly spaced microbeads in a fiber-optical trap," J. Opt. Soc. Am. B **20**, 1568–1574 (2003).
10. K. Dholakia and P. Zemánek, "Colloquium: gripped by light: optical binding," Rev. Mod. Phys. **82**, 1767–1791 (2010).
11. P. Chaumet and M. Nieto-Vesperinas, "Optical binding of particles with or without the presence of a flat dielectric surface," Phys. Rev. B **64**, 035422 (2001).
12. R. W. Bowman and M. J. Padgett, "Optical trapping and binding," Rep. Prog. Phys. **76**, 026401 (2013).
13. B. Schmittberger, J. Greenberg, and D. Gauthier, "Free-space, multimode spatial self-organization of cold, thermal atoms," in *43rd Annual Meeting of the APS Division of Atomic, Molecular and Optical Physics* (American Physical Society, 2012), abstract ID BAPS.2012.DAMOP.H2.10.
14. D. E. Chang, J. I. Cirac, and H. J. Kimble, "Self-organization of atoms along a nanophotonic waveguide," Phys. Rev. Lett. **110**, 113606 (2013).
15. G. Labeyrie, E. Tesio, P. M. Gomes, G.-L. Oppo, W. J. Firth, G. R. Robb, A. S. Arnold, R. Kaiser, and T. Ackemann, "Optomechanical

self-structuring in a cold atomic gas," Nat. Photonics **8**, 321–325 (2014).

16. S. Ostermann, M. Sonnleitner, and H. Ritsch, "Scattering approach to two-colour light forces and self-ordering of polarizable particles," New J. Phys. **16**, 043017 (2014).

17. S. Nimmrichter, K. Hammerer, P. Asenbaum, H. Ritsch, and M. Arndt, "Master equation for the motion of a polarizable particle in a multimode cavity," New J. Phys. **12**, 083003 (2010).

18. K. Baumann, C. Guerlin, F. Brennecke, and T. Esslinger, "Dicke quantum phase transition with a superfluid gas in an optical cavity," Nature **464**, 1301–1306 (2010).

19. S. Krämer and H. Ritsch, "Self-ordering dynamics of ultracold atoms in multicolored cavity fields," arXiv:1404.5348 (2014).

20. W. Niedenzu, T. Grießer, and H. Ritsch, "Kinetic theory of cavity cooling and self-organisation of a cold gas," Eur. Phys. Lett. **96**, 43001 (2011).

21. I. H. Deutsch, R. J. C. Spreeuw, S. L. Rolston, and W. D. Phillips, "Photonic band gaps in optical lattices," Phys. Rev. A **52**, 1394 (1995).

22. K. M. Douglass, S. Sukhov, and A. Dogariu, "Superdiffusion in optically controlled active media," Nat. Photonics **6**, 834–837 (2012).

optica

Ultrafast resolution of tunneling delay time

Alexandra S. Landsman,[†],[*] Matthias Weger,[†] Jochen Maurer, Robert Boge,
André Ludwig, Sebastian Heuser, Claudio Cirelli, Lukas Gallmann, and Ursula Keller

Physics Department, ETH Zürich, CH-8093 Zürich, Switzerland

*Corresponding author: alexandra.landsman@phys.ethz.ch

The question of how long a tunneling particle spends inside the barrier region has remained unresolved since the early days of quantum mechanics. The main theoretical contenders, such as the Buttiker–Landauer, Eisenbud–Wigner, and Larmor time, give contradictory answers. On the other hand, recent attempts at reconstructing valence electron dynamics in atoms and molecules have entered a regime where the tunneling time genuinely matters. Here, we compare the main competing theories of tunneling time against experimental measurements using the attoclock in strong laser field ionization of helium atoms. The attoclock uses a close to circularly polarized femtosecond laser pulse, mapping the angle of rotation of the laser field vector to time similar to the hand of a watch. Refined attoclock measurements reveal a real (not instantaneous) tunneling delay time over a large intensity regime, using two independent experimental apparatus. Only two theoretical predictions are compatible within our experimental error: the Larmor time and the probability distribution of tunneling times constructed using a Feynman Path Integral formulation. The latter better matches the observed qualitative change in tunneling time over a wide intensity range, and predicts a broad tunneling time distribution with a long tail. The implication of such a probability distribution of tunneling times, as opposed to a distinct tunneling time, would imply that one must account for a significant, though bounded and measurable, uncertainty as to when the hole dynamics begin to evolve. We therefore expect our results to impact the reconstruction of attosecond electron dynamics following tunnel ionization.   © 2014 Optical Society of America

1. INTRODUCTION

The tunneling time problem is almost as old as quantum mechanics itself and is a highly debated subject [1]. Time is not a quantum observable, and therefore many conflicting theories have been developed over the decades [1–5], but definitive experiments were largely impossible and awareness of the controversy in the broader scientific world faded. More recently within the ultrafast science community, tunneling time is implicitly assumed to be deterministic and, in fact, very often posited to be instantaneous or imaginary [6,7]. Hence, even the best techniques for imaging valence electron dynamics in atoms and molecules are founded on a deterministic time at ionization [6,8–10]. On the other hand, it is widely accepted

in the tunneling-time community that the time is not instantaneous or even deterministic [1–3,5,11,12].

Our refined attoclock measurements using two independent measurement apparatus provide substantial advances in these key issues for both communities. Over a range of intensities, we show that only two prominent tunneling time theories are compatible with our experiments—and that the compatible probability distribution of times is broad enough to have significant impact on current experimental interpretation and reconstruction of hole dynamics.

2. ATTOCLOCK MEASUREMENTS

The attoclock definition of tunneling delay time relies on two independent measurements based on two observables.

Observable 1 is the polarization axis of the elliptically polarized light and observable 2 is the electron momentum vector. The angular orientation of the most probable momentum vector with respect to the polarization ellipse yields time delays as the hands of a watch indicate time (see [13] for further detail). Prior attoclock measurements [13] found an upper limit on tunneling time of around 40 as, but within a narrow intensity range, and hence observed no significant trends. More recent attoclock measurements in helium and argon covered high intensities, corresponding to very fast tunneling delay times, and therefore could not resolve tunneling time within experimental error [14]. Another recent experiment measured the time an electron involved in high harmonic generation (HHG) exits the barrier [6]. However, the absolute timing of ionization, and therefore the tunneling time, was not accessible [7].

Tunnel ionization occurs when a strong laser field bends the binding potential of an atom, creating a barrier [Fig. 3(c)] whereby electrons can tunnel out, be accelerated by the field, and eventually register their momenta at the detector (Fig. 1). An important parameter in strong field ionization is $\gamma = \omega \sqrt{2I_p}/F = \sqrt{I_p/2U_p}$ [15], where I_p is ionization potential, U_p is ponderomotive energy, ω is the central frequency of the laser, and F is the peak electric field, which divides the "vertical channel" of multiphoton ionization ($\gamma \gg 1$) from the "horizontal channel" of optical tunneling ($\gamma \ll 1$). Our experimental regime is in the $0.8 < \gamma < 2.5$ range, corresponding to "nonadiabatic tunnel ionization" [16]. In this regime, while the tunneling probability may be substantially modified from

the quasi-static rates [15,17], phase-independent contributions due to multiphoton absorption are small (approximately 3.3% of the total rate for $\gamma \sim 2$ [16]), and tunneling remains the dominant ionization mechanism [18], widely used to investigate molecular orbitals [8,19,20] and electron rearrangement [8–10,18] after ionization.

The momentum distributions were measured by two different instruments: a cold target recoil ion momentum spectrometer (COLTRIMS) [21] and a velocity map imaging spectrometer (VMIS) [22] (see Fig. 1). Figure 2 shows good overlap between COLTRIMS and VMIS, with error bars higher on COLTRIMS. The use of both apparatus gives access to a wide intensity range of $0.73–7.5 \times 10^{14}$ W/cm^2, corresponding to variation in the barrier width by about a factor of 3, from 7.5 to 24 au (0.4–1.27 nm), with width given approximately by I_p/F. Such large variation in barrier width resulted in a comparable variation of measured tunneling delay time (Fig. 3), allowing for a detailed comparison with theory. Tunneling delay time was extracted from measurements using attosecond angular streaking [13,23].

The experiment uses elliptically polarized laser light, with parameters given in Fig. 2. At lower intensities, attoclock [13,23] measurements were performed with VMIS with the gas nozzle integrated into the repeller plate [see Fig. 1(c)]. The integration of the gas nozzle allows one to achieve target gas densities that are significantly higher as compared to setups employing cold atomic beams. Two-dimensional projections of the photoelectron momentum distribution were recorded in steps of 2° covering 180°. The three-dimensional momenta
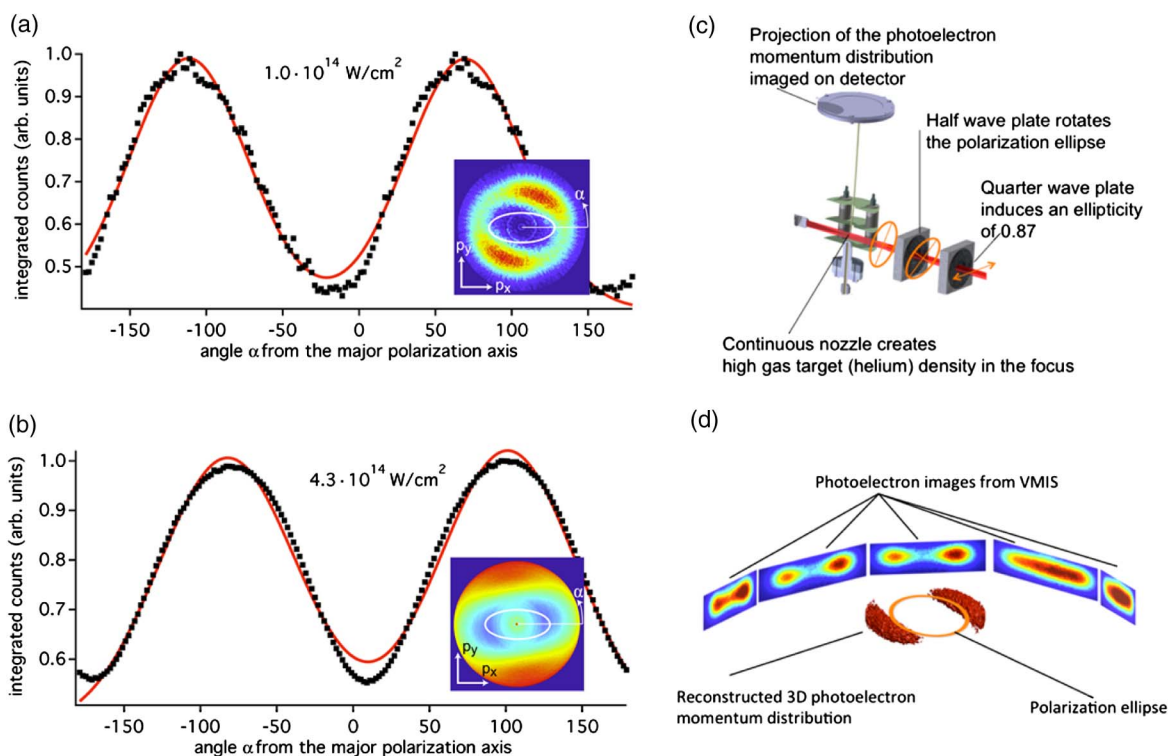
Fig. 1. Measuring electron momenta distributions using VMIS. (a) Fitting of peaks in electron momenta distribution with a Gaussian at lower intensity and clockwise polarization. (b) Higher-intensity and counterclockwise polarization. (c) Experimental setup. (d) Reconstruction of full 3D electron momenta distribution using projections in the momentum space.
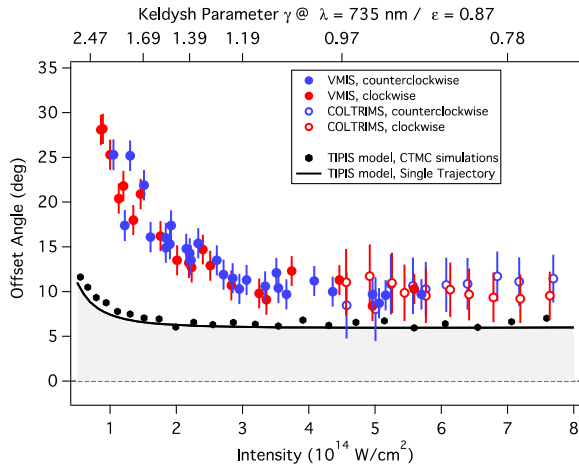
Fig. 2. Measured offset angle $\theta_m - \pi/2$, from which tunneling time is extracted. Black line and dots correspond to the Coulomb correction obtained using the TIPIS model [14] with single trajectory and classical trajectory Monte Carlo (CTMC) simulations, respectively (more in Section 2 of Supplement 1). The error bars are the result of a geometrical sum of the errors from the fit of the angular distribution of the electrons and the error of the polarization characterization. For the measurements performed with the COLTRIMS apparatus, an additional source of uncertainty comes from the thermal spread of the gas jet (more in Section 1 of Supplement 1).

distribution, and thus the electron momenta distribution in the polarization plane, was retrieved by tomographic reconstruction [24], shown in Fig. 1(d) (more detail in Supplement 1). The COLTRIMS measurements were performed in a similar way as described elsewhere [14].

3. EXPERIMENTAL EXTRACTION OF TUNNELING DELAY

The extraction of tunneling delay time follows the method first presented in [13]. The electron located at the peak of the momenta distribution, given by $|\langle \vec{k} | \Psi \rangle|^2$, corresponds to the most probable electron trajectory. To locate this peak from measurements, radial integration is used, combined with a double Gaussian fit (corresponding to two trajectories [25,26]) to extract the angle at which the maxima in the distribution occurs [see Figs. 1(a)–1(b)], corresponding to ionization at the peak of the laser field. This angle θ_m corresponds to the direction of the most probable electron momentum in the plane of polarization. The measured offset angle, $\theta_m - 90°$ shown in Fig. 2, is used to extract tunneling time after subtracting the Coulomb correction, θ_{Coul}, and the streaking angle, θ_{str}, which includes rotation due to the drift created by the vector potential of the electric field, resulting in the experimentally measured tunneling time, τ, given by $\omega\tau = \theta_i = \theta_m - \theta_{Coul} - \theta_{str}$. The semiclassical simulations that were compared with experiment
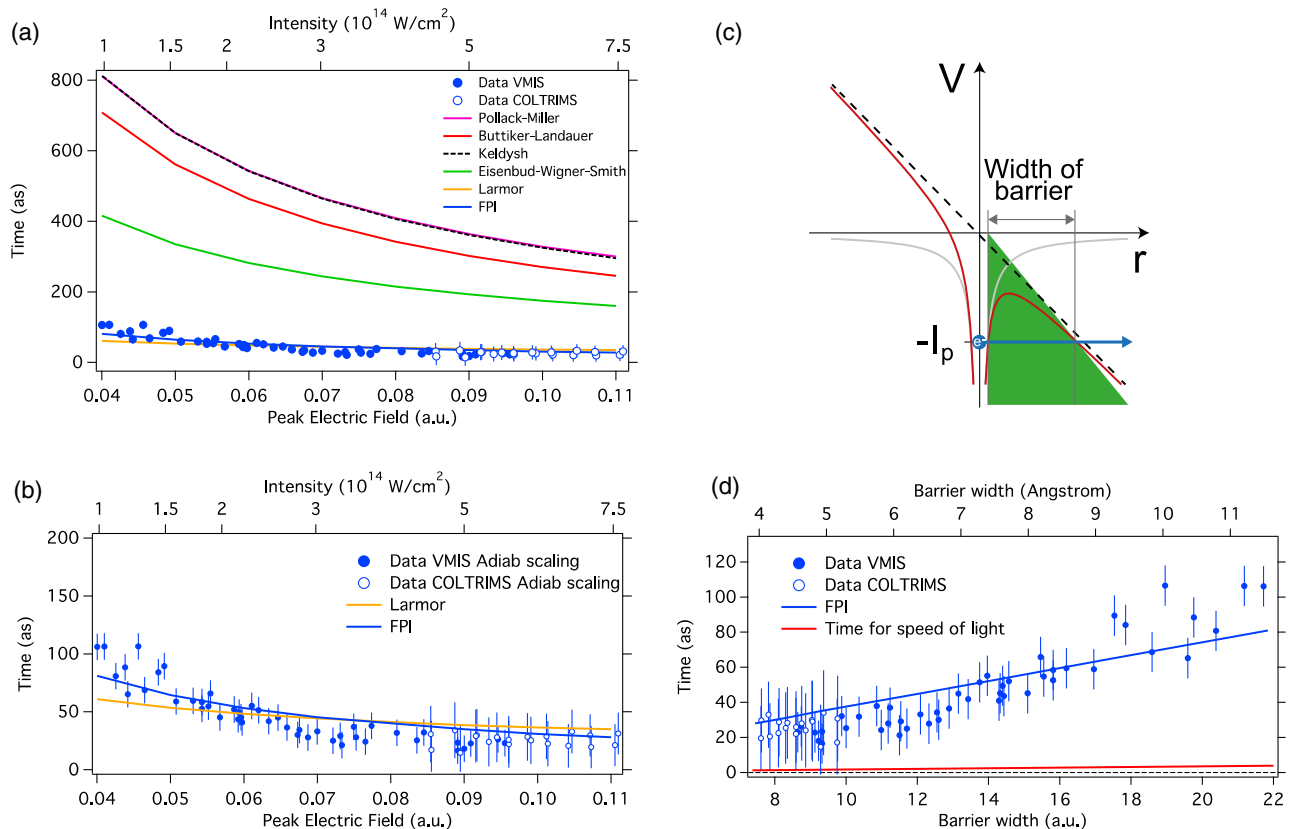
Fig. 3. Comparison of theory to experiment. (a) Five theoretical predictions of tunneling time compared to experiment. (b) Same as (a), but zoomed into the lower time delay. (c) Potential resulting from the combined Coulomb–laser field. (d) Tunneling time as a function of barrier width. The measured tunneling time is significantly smaller than the free propagation time for electrons with kinetic energies characteristic of electron motion in Helium: for example, around 40 as and 230 as for tunneling time and free propagation time, respectively, for barrier width of 13 au.

were based on the TIPIS model [14] (more detail in Section 2 of Supplement 1).

It was found in [27] that, for our experimental parameter range and ionization of Helium, TIPIS agrees within one degree (much less at higher intensities) with the semiclassical simulations based on the well-known nonadiabatic Perelomov, Popov, and Terentev model [28]. In calculating τ, nonadiabatic effects and an offset of the streaking angle from 90° were taken into account, resulting in a minor (less than 5 as and up to 15 as at the lowest intensity) correction to tunneling time (see Section 2 of Supplement 1).

For direct comparison with the experiment, analytic calculations are done for the Fourier component, $\vec{k}$, that maximizes $|\langle \vec{k}|\Psi\rangle|^2$, corresponding to the peak of the electron momenta distribution, from which the tunneling time is experimentally extracted. The tunneling process acts as a momentum filter that maps different Fourier components of the bound-state wavefunction onto different momenta, $\vec{k}$, at the tunnel exit with probability $\propto \exp(-k_\perp^2/2\sigma_\perp^2)$ [17,19], where $k_\perp$ is the momentum transverse to the direction of tunneling. The maximum of $|\langle \vec{k}|\Psi\rangle|^2$ is given by the transmission of a $\Phi(x, k_\perp = 0)$ component, in the partial Fourier transform [29] of the bound-state wavefunction: $\Psi_b(x,y,z) = \frac{1}{2\pi} \iint \Phi(x, \vec{k}_\perp)e^{i r \cdot \vec{k}_\perp} dk_y dk_z$, where x is the major axis of polarization. The tunneling times were calculated for this component $\Phi(x)$ within the short-range potential approximation [29], taking account of nonadiabatic effects. Nonadiabatic effects arise when electrons absorb energy from the laser field. These effects are therefore expected to become more significant at lower intensities (corresponding to higher γ), where multiphoton contributions play a bigger role. We found the analytic results to be robust to variation in barrier shape (resulting, for example, from a Coulomb correction or nonadiabatic effects), as long as the barrier width did not change significantly. In short, small variations in barrier shape result in correspondingly small variations in tunneling time. The contribution of nonadiabatic effects to tunneling time estimates is relatively small (particularly at lower γ), even when the ionization rates are substantially offset from the quasi-static. This is partly due to the exponential dependence of ionization probability on barrier width, versus the linear dependence of tunneling time [Fig. 3(d)].

## 4. COMPARISON OF EXPERIMENTAL RESULTS WITH THEORETICAL DEFINITIONS OF TUNNELING TIME

The four widely used interpretations of tunneling delay times were calculated by finding the transmission amplitude $\Phi(x)$ for the propagation through the barrier, given by: $T = |T|e^{i\theta}$, and using the definitions $\tau_{BL} = -\hbar\partial \ln|T|/\partial V$; $\tau_{LM} = -\hbar\partial\varphi/\partial V$; $\tau_{PM} = \hbar\partial \ln|T|/\partial E$; and $\tau_{EW} = \hbar\partial\varphi/\partial E + w/k$ for Buttiker–Landauer [3,30], Larmor [5], Pollack–Miller [30], and Eisenbud–Wigner times [4], respectively, where V is barrier height and E is electron energy.

These four alternative interpretational pictures have been derived using very different physical considerations. The Buttiker–Landauer time corresponds to the time it would take a classical particle to propagate through an inverted potential barrier. The physical argument as to why it should be considered tunneling time rests on the fact that the ratio of τ_{BL} to the period of barrier modulation serves as a nonadiabaticity parameter (much as the Keldysh γ), and therefore must correspond to whether the electron sees a static or an oscillating field while it is traversing the barrier. The Larmor time corresponds to the degree of rotation of a spin-polarized electron inside a magnetic potential barrier. The Pollack–Miller time was derived using flux–flux correlation functions and represents an average correlation time in a collision. The Eisenbud–Wigner time follows the peak of a near-chromatic wavepacket, calculating the delay of this peak due to the presence of a potential. Hence, an additional term, w/k, is present in τ_{EW}, where w and k are the barrier width and electron velocity, respectively. This additional term corresponds to the propagation of the electron in the barrier region if that barrier were absent, and has to be added to get the total time [2], since the first term only gives a *relative* time shift [4].

The Eisenbud–Wigner time has been used extensively [31,32] to explain the relative single photon ionization delay between ionization of valence and core electrons in Neon and Argon, first observed experimentally [33,34]. Perhaps counterintuitively, it is not the actual time to absorb a photon, but rather an additional phase shift in the peak of the propagating wave packet induced by the presence of the ionic potential *after* that photon is absorbed. Calculating the shift in the peak is straightforward in single-photon ionization, where the total energy of the electron is above threshold, leading to a well-defined single peak and propagation of the entire wavepacket. However, the Eisenbud–Wigner time is much more disputed in tunneling [1], where the peak is absent inside the barrier [2], and moreover, a large part of the wavefunction remains confined. Further discussion of the four tunneling times in the context of strong field ionization can be found in Section 3.1 of [35].

The four tunneling times are shown in Fig. 3(a), where we only consider the experimental range corresponding to $\gamma \leq 2$, where multiphoton contributions are believed to be relatively small [16]. Although these times were derived using very different physical models, they can be expressed as expectation values using the tunneling time probability amplitude, $f(\tau)$, constructed with Feynman Path Integrals (FPIs) [11,30]. The FPI approach is particularly appealing, because the total transmitted wavefunction can be expressed as a sum of all possible paths, each path corresponding to a deterministic tunneling time and contributing $\exp(iS[x(t)]/\hbar)$. The quantity $f(\tau)$ represents the contribution to the total transmission amplitude of only those paths that spend an amount of time, τ, inside the barrier, such that $T = \int_0^\infty f(\tau)d\tau$. The ambiguity in interpretation of tunneling time using this approach arises because the tunneling time probability amplitudes, $f(\tau)$, are complex and interfere. As pointed out by Landauer and Martin [1], while no one disputes the construction's accuracy, it is not clear what procedure to use for calculating relevant physical quantities with FPIs.
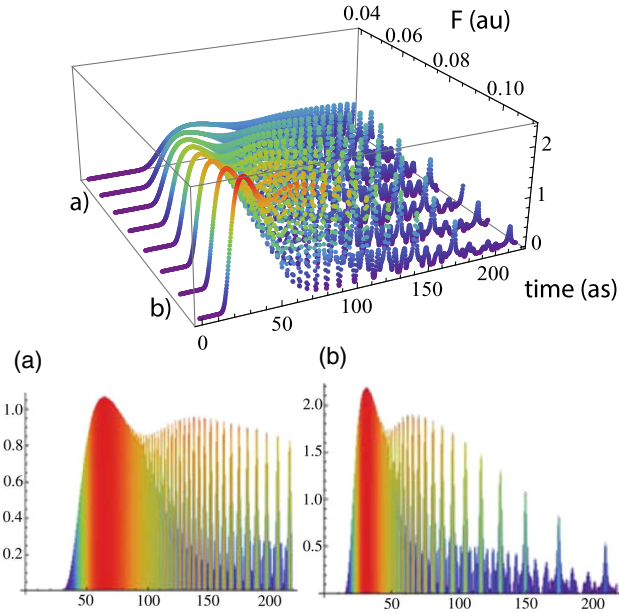
Fig. 4. Normalized distribution where each probability value corresponds to an integer number of attoseconds of tunneling time. Top, 3D probability distribution of tunneling times for intensities ranging from 1 to 7.5×10^{14} W/cm^2, corresponding to field strengths of 0.04–0.11 au. The highly oscillatory structure is due to interference and shows tunneling probability peaking sharply at discrete values as tunneling time increases. (a) Probability distribution at intensity = 1.625×10^{15} W/cm^2, FWHM $\approx$ 80 as, and skewness = 0.9. (b) Probability distribution at intensity = 6.5×10^{14} W/cm^2, FWHM $\approx$ 50 as, and skewness = 1.09.

The four tunneling delay time definitions shown in Fig. 3 can be viewed as expectation values, rather than deterministic quantities [1,2,11,30]. In particular, the Buttiker–Landauer and the Larmor times correspond to the absolute and the real parts, respectively, of the following complex-valued average [1,11]: $\langle \tau \rangle = \int_0^\infty \tau f(\tau) d\tau / T$. This definition has been widely used, in part because it can be expressed as the transition element [1] $\langle \tau \rangle = \langle \Psi_i | \tau | \Psi_T \rangle$, where Ψ_i and Ψ_T are the normalized incident and transmitted parts of the wavefunction, respectively. Perhaps surprisingly, $\langle \Psi_i | \tau | \Psi_T \rangle$ is far too large and only the real part of $\langle \tau \rangle$, equivalent to τ_{LM}, is within our experimental uncertainty. The agreement of the Larmor time with our experimental data suggests that phase accumulated before the electron appears at the tunnel exit (which is typically lost when using saddle-point or WKB-type approximations) is significant in determination of tunneling time.

In addition to computing expectation values with $f(\tau)$, we use it directly to construct the probability distribution of tunneling times, adapting a known method [12], shown in Fig. 4. The peak of this probability distribution is shown along with other theoretical predictions in Fig. 3. This peak corresponds better to the experimental observable (which is the peak of the recorded electron momenta distribution) than the expectation value given by the other tunneling time definitions. This is because trajectories that begin to tunnel at the peak but have longer or shorter tunneling times than the most probable trajectory will not end up at the peak of the momenta

distribution, but will nevertheless be included in any averaging procedure that extracts the expected value of tunneling time.

5. CONCLUSION

Historically, measured tunneling time varied with the nature of the experiment. Besides the attoclock measurements, only one other experiment was done at the single-particle level [36], thereby avoiding the possibility of a pulse-reshaping process [1]. Our findings are consistent with this single-photon experiment [36], in that a particle moving through a potential barrier takes significantly less time than free propagation over the same distance. Therein this yielded superluminal velocities [36]; we get tunneling times that are just a small fraction of the free propagation time [though not superluminal, as Fig. 3(d) shows] for electrons with kinetic energies characteristic of electron motion in Helium.

As Fig. 3 shows, of the five theoretical approaches, two cannot be excluded: the Larmor time and the probability distribution of tunneling times constructed using FPIs. These two are not mutually exclusive. In particular, the correctness of Larmor time (viewed as an average, rather than a deterministic, quantity) allows the existence of a probability distribution of tunneling times. This view is further supported by the correspondence between Larmor time and the weak measurement value of tunneling time, given by $\tau_{LM} = \text{Re}\langle \Psi_i | \tau | \Psi_T \rangle$ [37]. The probability distribution shown in Fig. 4 has a long asymmetric tail that lengthens, along with an increase in the position of the peak and the full width-half-maxima (FWHM), as intensity decreases. This suggests that both uncertainty and expected duration of tunneling time increase at lower intensities, corresponding to a larger barrier width.

Our results imply that the probability distribution of tunneling time, at all measured intensities, may add significant uncertainty to reconstruction of attosecond electron dynamics after strong field ionization. In particular, the FWHM is larger or comparable, depending on intensity, to the "universal attosecond response to removal of an electron" of about 50 as, found computationally [38]. A second important issue is the loss of coherence of the hole if tunneling time is probabilistic rather than deterministic. A hole is created due to a superposition of states formed during the tunneling process. This hole subsequently evolves on the timescale determined by the energy splitting of nearby valance orbitals from which tunneling takes place. The loss of coherence will depend on the time scale of the evolution of a hole [9] relative to the uncertainty in tunneling time. Hence, relatively slow hole dynamics (such as 6.2 fs in Krypton [9,10]) will result in little loss of coherence. On the other hand, in some cases, (such as CO_2 where the hole period is as short as around 1.2 fs [8]) the loss of coherence can be significant. As Fig. 4 shows, the long tail of the distribution can extend to a substantial fraction of a hole period, implying a substantial loss of coherence.

The timescale of tunneling, once an unresolvable question for theorists of the foundations of quantum mechanics, therefore meaningfully affects the reconstruction of electron dynamics using HHG [8] or pump–probe experiments [18], which is

the primary goal of ultrafast science. The implications for both ultrafast experiment and theory, especially for molecules and at time resolutions of current and future interest [39], are at once fundamental, practical, and approachable with existing technology.

REFERENCES

1. R. Landauer and T. Martin, "Barrier interaction time in tunneling," Rev. Mod. Phys. **66**, 217 (1994).
2. E. H. Hauge and J. A. Støvneng, "Tunneling times: a critical review," Rev. Mod. Phys. **61**, 917–936 (1989).
3. M. Buttiker and R. Landauer, "Traversal time for tunneling," Phys. Rev. Lett. **49**, 1739–1742 (1982).
4. E. P. Wigner, "Lower limit for the energy derivative of the scattering phase shift," Phys. Rev. **98**, 145–147 (1955).
5. M. Büttiker, "Larmor precession and the traversal time for tunneling," Phys. Rev. B **27**, 6178–6188 (1983).
6. D. Shafir, H. Soifer, B. D. Bruner, M. Dagan, Y. Mairesse, S. Patchkovskii, M. Y. Ivanov, O. Smirnova, and N. Dudovich, "Resolving the time when an electron exits a tunnelling barrier," Nature **485**, 343–346 (2012).
7. M. Lein, "Atomic physics: Electrons get real," Nature **485**, 313–314 (2012).
8. O. Smirnova, Y. Mairesse, S. Patchkovskii, N. Dudovich, D. Villeneuve, P. Corkum, and M. Y. Ivanov, "High harmonic interferometry of multi-electron dynamics in molecules," Nature **460**, 972–977 (2009).
9. E. Goulielmakis, Z. H. Loh, A. Wirth, R. Santra, N. Rohringer, V. S. Yakovlev, S. Zherebtsov, T. Pfeifer, A. M. Azzeer, M. F. Kling, S. R. Leone, and F. Krausz, "Real-time observation of valence electron motion," Nature **466**, 739–743 (2010).
10. A. Wirth, M. T. Hassan, I. Grguras, J. Gagnon, A. Moulet, T. T. Luu, S. Pabst, R. Santra, Z. A. Alahmed, A. M. Azzeer, V. S. Yakovlev, V. Pervak, F. Krausz, and E. Goulielmakis, "Synthesized light transients," Science **334**, 195–200 (2011).
11. D. Sokolovski and L. M. Baskin, "Traversal time in quantum scattering," Phys. Rev. A **36**, 4604–4611 (1987).
12. D. Sokolovski, S. Brouard, and J. N. L. Connor, "Traversal-time wave-function analysis of resonance and nonresonance tunneling," Phys. Rev. A **50**, 1240–1256 (1994).
13. P. Eckle, A. N. Pfeiffer, C. Cirelli, A. Staudte, R. Dörner, H. G. Muller, M. Büttiker, and U. Keller, "Attosecond ionization and tunneling delay time measurements in helium," Science **322**, 1525–1529 (2008).
14. A. N. Pfeiffer, C. Cirelli, M. Smolarski, D. Dimitrovski, M. Abusamha, L. B. Madsen, and U. Keller, "Attoclock reveals natural coordinates of the laser-induced tunnelling current flow in atoms," Nat. Phys. **8**, 76–80 (2012).
15. L. V. Keldysh, "Ionization in the field of a strong electromagnetic wave," Sov. Phys. JETP **20**, 1307–1314 (1965).
16. G. L. Yudin and M. Y. Ivanov, "Nonadiabatic tunnel ionization: Looking inside a laser cycle," Phys. Rev. A **64**, 013409 (2001).
17. M. V. Ammosov, N. B. Delone, and V. P. Krainov, "Tunnel ionization of complex atoms and of atomic ions in an alternating electromagnetic field," Sov. Phys. JETP **64**, 1191–1194 (1986).
18. M. Uiberacker, T. Uphues, M. Schultze, A. J. Verhoef, V. Yakovlev, M. F. Kling, J. Rauschenberger, N. M. Kabachnik, H. Schröder, M. Lezius, K. L. Kompa, H.-G. Muller, M. J. J. Vrakking, S. Hendel, U. Kleineberg, U. Heinzmann, M. Drescher, and F. Krausz, "Attosecond real-time observation of electron tunnelling in atoms," Nature **446**, 627–632 (2007).
19. M. Meckel, D. Comtois, D. Zeidler, A. Staudte, D. Pavicic, H. C. Bandulet, H. Pépin, J. C. Kieffer, R. Dörner, D. M. Villeneuve, and P. B. Corkum, "Laser-induced electron tunneling and diffraction," Science **320**, 1478–1482 (2008).
20. H. Akagi, T. Otobe, A. Staudte, A. Shiner, F. Turner, R. Dörner, D. M. Villeneuve, and P. B. Corkum, "Laser tunnel ionization from multiple orbitals in HCl," Science **325**, 1364–1367 (2009).
21. R. Dörner, V. Mergel, O. Jagutzki, L. Spielberger, J. Ullrich, R. Moshammer, and H. Schmidt-Bocking, "Cold target recoil ion momentum spectroscopy: a 'momentum microscope' to view atomic collision dynamics," Phys. Rep. **330**, 95–192 (2000).
22. D. H. Parker and A. T. J. B. Eppink, "Photoelectron and photofragment velocity map imaging of state-selected molecular oxygen dissociation/ionization dynamics," J. Chem. Phys. **107**, 2357 (1997).
23. P. Eckle, M. Smolarski, P. Schlup, J. Biegert, A. Staudte, M. Schöffler, H. G. Muller, R. Dörner, and U. Keller, "Attosecond angular streaking," Nat. Phys. **4**, 565–570 (2008).
24. M. Wollenhaupt, M. Krug, J. Kohler, T. Bayer, C. Sarpe-Tudoran, and T. Baumert, "Three-dimensional tomographic reconstruction of ultrashort free electron wave packets," Appl. Phys. B **95**, 647–651 (2009).
25. C. H. R. Ooi, W. Ho, and A. D. Bandrauk, "Photoionization spectra by intense linear, circular, and elliptic polarized lasers," Phys. Rev. A **86**, 023410 (2012).
26. A. S. Landsman, C. Hofmann, A. Pfeiffer, C. Cirelli, and U. Keller, "A unified approach to probing Coulomb effects in tunnel ionization for any ellipticity of laser light," Phys. Rev. Lett. **111**, 263001 (2013).
27. A. S. Landsman and U. Keller, "Tunneling time in strong field ionization," J. Phys. B **47**, 204024 (2014).
28. A. M. Perelomov, V. S. Popov, and M. V. Terentev, "Ionization of atoms in an alternating electric field," Zh. Eksp. Teor. Fiz. **50**, 1393 (1966).
29. R. Murray, W. K. Liu, and M. Y. Ivanov, "Partial Fourier-transform approach to tunnel ionization: atomic systems," Phys. Rev. A **81**, 023413 (2010).
30. N. Yamada, "Unified derivation of tunneling times from decoherence functionals," Phys. Rev. Lett. **93**, 170401 (2004).
31. S. Nagele, R. Pazourek, J. Feist, K. Doblhoff-Dier, C. Lemell, K. Tökési, and J. Burgdörfer, "Time-resolved photoemission by attosecond streaking: extraction of time information," J. Phys. B **44**, 081001 (2011).
32. J. M. Dahlström, A. L'Huillier, and A. Maquet, "Introduction to attosecond delays in photoionization," J. Phys. B **45**, 183001 (2012).
33. M. Schultze, M. Fiess, N. Karpowicz, J. Gagnon, M. Korbman, M. Hofstetter, S. Neppl, A. L. Cavalieri, Y. Komninos, T. Mercouris, C. A. Nicolaides, R. Pazourek, S. Nagele, J. Feist, J. Burgdorfer, A. M. Azzeer, R. Ernstorfer, R. Kienberger, U. Kleineberg, E. Goulielmakis, F. Krausz, and V. S. Yakovlev, "Delay in photoemission," Science **328**, 1658–1662 (2010).
34. K. Klünder, J. M. Dahlström, M. Gisselbrecht, T. Fordell, M. Swoboda, D. Guenot, P. Johnsson, J. Caillat, J. Mauritsson, A. Maquet, R. Taïeb, and A. L'Huillier, "Probing single-photon

ionization on the attosecond time scale," Phys. Rev. Lett. **106**, 143002 (2011).

35. A. S. Landsman and U. Keller, "Attosecond science and the tunneling time problem," Phys. Rep., doi: 10.1016/j.physrep.2014.09.002 (in press).

36. A. M. Steinberg, P. G. Kwiat, and R. Y. Chia, "Measurement of the single-photon tunneling time," Phys. Rev. Lett. **71**, 708–711 (1993).

37. Y. Aharonov, D. Z. Albert, and L. Vaidman, "How the result of a measurement of a component of the spin of a spin-1/2 particle can turn out to be 100," Phys. Rev. Lett. **60**, 1351–1354 (1988).

38. J. Breidbach and L. S. Cederbaum, "Universal attosecond response to the removal of an electron," Phys. Rev. Lett. **94**, 033901 (2005).

39. O. Smirnova and M. Ivanov, "Ultrafast science towards a one-femtosecond film," Nat. Phys. **6**, 159–160 (2010).

optica

Mid-infrared integrated waveguide modulators based on silicon-on-lithium-niobate photonics

JEFF CHILES[1] AND SASAN FATHPOUR[1,2,*]

[1]CREOL, The College of Optics and Photonics, University of Central Florida, Orlando, Florida 32816, USA

[2]Department of Electrical Engineering and Computer Science, University of Central Florida, Orlando, Florida 32816, USA

*Corresponding author: fathpour@creol.ucf.edu

Heterogeneous integration techniques, such as direct bonding, have enabled solutions to many problems facing integrated photonics. In particular, the relatively new field of mid-infrared (mid-IR) integrated photonics has been hindered by the availability of functional, transparent substrates in this wavelength range. The key to achieving compact, high-performance optical modulation and frequency conversion is the monolithic integration of silicon photonics with a material with high second-order nonlinear susceptibility. By transferring large areas of thin, monocrystalline silicon to bulk lithium niobate ($LiNbO_3$) substrates, the first silicon-based platform to exploit the Pockels or linear electro-optic effect in the mid-IR range is achieved. Integrated Mach–Zehnder interferometer modulators with an extinction ratio of ∼8 dB, a half-wave voltage-length product of 26 V · cm, and an on-chip insertion loss of 3.3 dB are demonstrated at a wavelength of 3.39 μm. Ultrathin optical waveguides fabricated and characterized on this platform exhibit a low transverse electric mode linear propagation loss of 2.5 dB/cm. Future capabilities such as wideband difference frequency generation for integrated mid-IR sources are envisioned for the demonstrated silicon-on-lithium-niobate platform.　© 2014 Optical Society of America

OCIS codes: (130.4110) Modulators; (230.7370) Waveguides; (250.3140) Integrated optoelectronic circuits; (250.4110) Modulators; (130.3730) Lithium niobate.

http://dx.doi.org/10.1364/OPTICA.1.000350

1. INTRODUCTION

The mid-infrared (mid-IR) region of the optical spectrum (3–8 μm) is an important range for applications in remote sensing, free-space communications, and defense technology [1]. Integrated photonics offers the best outlook for achieving these functions at low cost, while maintaining good yield and consistent performance. For the targeted applications, it is desirable to use a platform that exhibits transparency at least through the first atmospheric transmission window of 3–5 μm. Although the silicon-on-insulator (SOI) platform has proven highly effective for near-infrared (near-IR) photonics [2], the presence of the buried silicon dioxide (SiO_2) layer limits its usefulness in the mid-IR range due to the onset of optical

absorption [3]. Many mid-IR silicon-based platforms have been proposed and demonstrated to replace SOI, including silicon-on-sapphire [4,5], silicon-on-nitride [6], and all-silicon membrane waveguides (the all-silicon optical platform) [7].

However, the choice of a photonic platform in the mid-IR should not be restricted merely to transparency considerations. A multielement photonic circuit such as an on-chip beam combiner [8] may be composed of numerous passive and active elements, such as tunable phase shifters, optical modulators, passive routers and spectrum filters, and possibly wavelength conversion elements for accessing more efficient detectors. The materials available on the platform determine the means available to achieve these effects. Silicon photonic platforms typically enable a high integration density of passive filtering

and routing elements due to the high index contrast available in their waveguides. Additionally, third-order optical non-linearities [9–12] are made possible by the low multiphoton absorption in the mid-IR region, but the pump power to achieve these effects is still relatively high.

Phase shifting and optical modulation has been achieved through the thermo-optic effect in silicon at speeds up to 70 kHz in the near-IR [13] and the mid-IR range at 23.8 kHz [14] on the SOI platform, but significant increases to these speeds are constrained by trade-offs with power consumption and propagation loss of the waveguides.

An alternative means to achieving on-chip phase shifts with silicon is by plasma dispersion [15], a highly CMOS-compatible approach which has been used to fabricate optical modulators in the near-IR with half-wave voltage products below $3 \text{ V} \cdot \text{cm}$ and data rates ranging from 10 to 50 Gbit/s [16,17]. However, higher bandwidths are achieved at the expense of extinction ratio in such devices; for instance, in Ref. [17], the bit rate of 10 Gbit/s achieves 18 dB extinction ratio, but in Ref. [16], the higher bit rate of 50 Gbit/s is accompanied by an extinction ratio of only 3.1 dB, which is not useful for long-distance communication applications. It is thus useful to consider a figure of merit for the modulation performance as the product of the maximum data rate and the extinction ratio at that rate. The modulators mentioned above exhibit products of 180 and 155 dB · Gbit/s, respectively.

Furthermore, the characteristics of plasma-dispersion-based modulators will be substantially different at longer wavelengths, as is investigated in Ref. [18]. Because of the stronger electroabsorption, a waveguide with a π phase shift induced from electrorefraction by free carriers would encounter an unavoidable absorption loss of 1.17 dB when operating at a wavelength of 4 μm. This means that pure phase modulation is unachievable with this effect in the mid-IR, limiting its usefulness for applications such as on-chip beam combining, or communication links with phase-shift-keying schemes.

Strained silicon can exhibit the Pockels effect in submicrometer waveguides in the near-IR [19], albeit with a high half-wave voltage product of $100 \text{ V} \cdot \text{cm}$. With larger waveguide cross-sections in the mid-IR, inducing strain is expected to be even more difficult.

Evidently, silicon alone may not be able to simultaneously provide all the functions required for high-performance mid-IR integrated photonics. By hybridizing it with other materials, new functions can be performed. For instance, to provide enhanced modulation performance in the near-IR, silicon organic hybrid waveguides have been fabricated with low-drive voltages down to $0.52 \text{ V} \cdot \text{mm}$ [20].

Meanwhile, lithium niobate (LiNbO$_3$) is a mid-IR compatible material (transparent up to 5 μm wavelength) with a high electro-optic coefficient, low refractive index (~2.1), and high second-order optical nonlinearity. Thanks to the fast response of the Pockels effect, near-IR LiNbO$_3$ optical modulators have achieved speeds exceeding 100 GHz [21], though with a $V_\pi \cdot L$ of ~$10 \text{ V} \cdot \text{cm}$. In addition, commercially available LiNbO$_3$ modulators such as the Mach-40 005 from Covega can provide modulation speeds of 40 Gbit/s while maintaining an extinction ratio of 13 dB, giving a modulation performance product

of 520 dB · Gbit/s, which is much higher than the aforementioned values in SOI-based devices. An optical modulator operating at a speed of 1.8 GHz and at a wavelength of 3.39 μm has been reported in Ti-diffused LiNbO$_3$ waveguides decades ago [22], but the low index contrast available in this platform greatly limits integration density and increases the device lengths since wide gaps are required for the electrodes.

To obtain a higher index contrast, the integration of silicon and LiNbO$_3$ has been explored for near-IR applications. One approach is top-side bonding [23,24], in which small pieces of thin LiNbO$_3$ films are bonded on top of a silicon waveguide, so that the optical mode partially overlaps the LiNbO$_3$ top cladding. However, this approach requires extra per-device processing and is only suitable for near-IR wavelengths, as it is performed on SOI substrates. Additionally, Ref. [24] utilizes a polymer bonding agent, which would induce loss in the mid-IR. Amorphous silicon has also been investigated in the near-IR based on its direct deposition on LiNbO$_3$ substrates [25,26], but the intrinsic linear loss of this material and its increasing material loss toward longer wavelengths [27] makes it unsuitable for the mid-IR spectral region.

We have recently demonstrated thin-film LiNbO$_3$ hybrid high-index contrast waveguides and modulators on oxidized silicon substrates in the near-IR [28]. The advantages over the mentioned top-side bonding approach include coupling light into LiNbO$_3$ waveguide core (rather than cladding) regions, as well as fabrication based on robust full-wafer bonding techniques rather than bonding small pieces with unreliable polymers. Unfortunately, similar to SOI, the expected loss of the oxide bottom cladding layer prohibits using our LiNbO$_3$-on-Si hybrid platform for mid-IR wavelengths.

In this work, to avoid material loss problems and to retain reliable wafer-scale processing capabilities, we have achieved the integration of crystalline silicon on LiNbO$_3$ substrates through direct wafer bonding and thin-film transfer techniques. We recently proposed and utilized this novel silicon-on-lithium-niobate (SiLN) platform (Fig. 1) to demonstrate passive waveguides at near-IR wavelengths [29]. In contrast to the discussed LiNbO$_3$-on-Si platform, SiLN employs a top silicon layer as the waveguide core material, and LiNbO$_3$ as the lower cladding. The SiLN platform has numerous practical advantages, including uninterrupted low-loss transmission

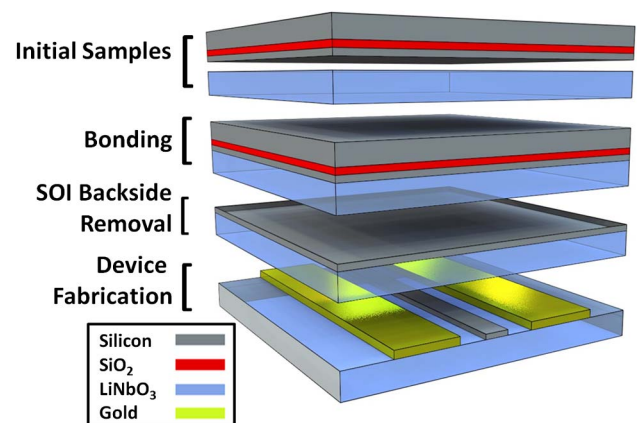**Fig. 1.** Process used to prepare SiLN chips.

throughout the wavelength range of 1.2–5 μm, compatibility with silicon-processing techniques, and a strong effective second-order optical nonlinearity, which will greatly reduce the intensity threshold for achieving certain wavelength conversion functions.

In this work, mid-IR integrated waveguide modulators based on the SiLN platform are demonstrated, representing the first silicon-based photonic devices exploiting the Pockels effect in this wavelength region. First, the design and fabrication of the modulators and SiLN substrates will be described. Next, the results for passive waveguides and active devices at lower frequencies will be presented. AC modulation results at the maximum available detector speed will then be presented, followed by conclusions and remarks on the outlook of the SiLN platform.

2. METHODS

A. Design

The SiLN platform consists of a bulk X-cut LiNbO$_3$ substrate, 500 μm thick, with a 210 nm thick layer of monocrystalline silicon fusion-bonded on the top surface. This silicon layer thickness provides a large optical mode overlap with the LiNbO$_3$ substrate, while retaining sufficient mode confinement to avoid excessive bending loss at our measurement wavelength of 3.39 μm. COMSOL-based simulations of the modulator are shown in Fig. 2, with laterally spaced gold electrodes creating a horizontal electric field along the z axis underneath the fully etched silicon channel waveguide, in order to access the largest attainable electro-optic coefficient of LiNbO$_3$, $r_{33} \approx 31$ pm/V. The optical mode propagates along the y axis, with a simulated effective mode index of 2.15 for 2.1 μm wide single-mode waveguides. The gold electrodes are spaced by 8.5 μm to avoid loss induced by optical mode overlap with the metal, with an allowance for some alignment tolerance during fabrication. The optical mode overlap into the LiNbO$_3$ substrate is 56%. The simulated $V_\pi \cdot L$ is 13 V · cm for a push–pull configured modulator. The advantage of this modulator configuration is that there is no need to dope the silicon waveguide core (which would introduce optical loss),
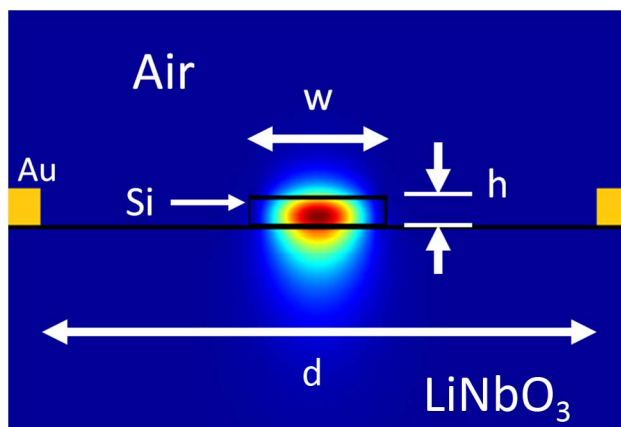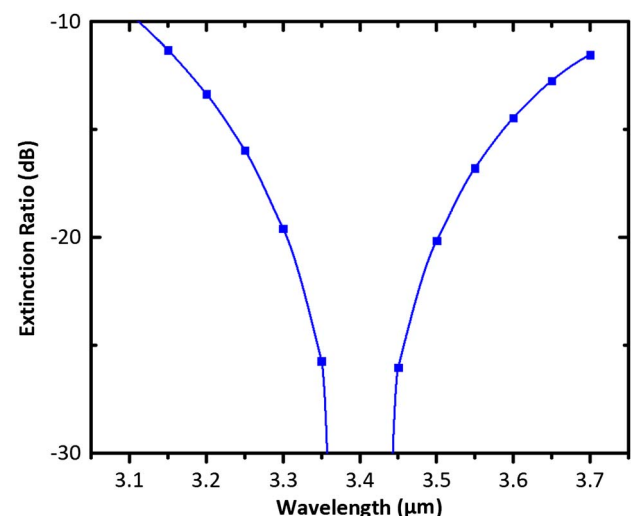
and it can in principle be operated at speeds well above 10 GHz by designing the electrodes for velocity matching as in conventional LiNbO$_3$ travelling wave modulators in the near-IR [30]. This is possible because the mechanism of modulation is the same for both SiLN and conventional LiNbO$_3$ waveguides. Additionally, due to the large optical bandwidth of MZIs, this modulator is simulated to achieve greater than 10 dB extinction ratio over an optical bandwidth of more than 500 nm with respect to center operation at 3.39 μm (Fig. 3). The bandwidth is limited by the wavelength dependence of the mode overlap into the LiNbO$_3$ substrate, which changes the $V_\pi \cdot L$ as the wavelength moves away from the center.

B. SiLN Substrate Preparation

The fabrication process for preparing SiLN substrates is schematically depicted in Fig. 1. First, an SOI die and a LiNbO$_3$ die, about 1.5 cm × 1.5 cm each, were obtained. The dies were then ultrasonically cleaned in standard solvents. To activate the surfaces for direct bonding [31], they were subjected to a low-power argon plasma (with some additional oxygen in the plasma mixture to prevent out-diffusion of oxygen atoms from the LiNbO$_3$ substrates) in an inductively coupled plasma (ICP) reactive-ion etching (RIE) chamber. The dies were then heated to 100°C and bonded such that the SOI top silicon layer was in direct contact with the LiNbO$_3$ substrate, and then annealed at 170°C for 1.5 days to strengthen the bond. Then, the backside of the SOI die was removed via rapid wet-etching with a mixture of hydrofluoric acid (HF), nitric acid (HNO$_3$), and water. The newly exposed (formerly "buried" on the SOI) SiO$_2$ layer was selectively removed using buffered oxide etchant, leaving a fully intact, crystalline thin film of silicon on the top surface of the LiNbO$_3$ substrate.

C. Waveguide and Modulator Fabrication

The SiLN dies were lithographically patterned into a set of MZI modulators based on Y junction splitters and combiners, separate straight waveguides, and a small number of long-path spiral waveguides to accurately assess the propagation loss on

Fig. 2. Simulated mode profile (red is the peak intensity) and modulator dimensions: $w = 2.1$ μm, $h = 210$ nm, $d = 8.5$ μm. The gold rectangles represent the edges of the electrodes used for modulation.

Fig. 3. Simulated optical bandwidth of the SiLN modulator for a center operation wavelength of 3.39 μm. Blue squares show discrete simulation points and the blue line is spline-fitted to these points.
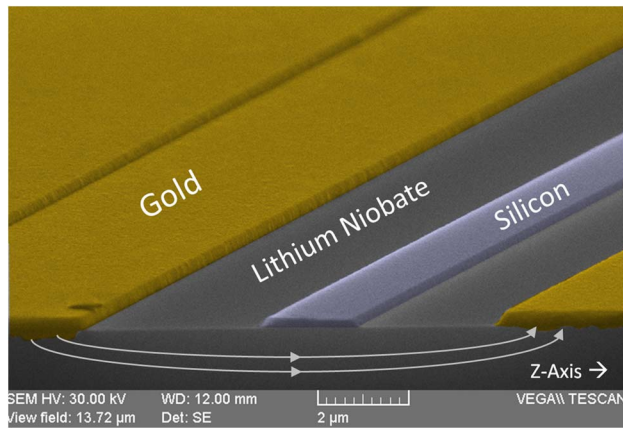
Fig. 4. Scanning electron micrograph of the cross-section of a SiLN modulator. The white lines crossing underneath the silicon represent the direction of the applied electric field during modulation.

Fig. 5. Optical micrographs of a SiLN modulator chip: (a) wide view of chip showing half-etched (left) and full-etched (right) regions, (b) fiber-to-waveguide grating coupler, and (c) Y junction and modulator electrodes.

each sample. Light was coupled in and out of the fabricated chip via 20 µm wide, 1.7 µm period grating couplers followed by 630 µm long linear tapers to 2.1 µm wide, 210 nm thick waveguides. The active modulator section is 5 mm long.

The fabrication started with spin-coating the SiLN dies with ZEP-520A electron-beam resist. Electron-beam lithography was performed to open trenches in the resist. A 100 nm thick layer of SiO_2 was deposited into the trenches via electron-beam evaporation and liftoff, forming a hard mask for etching. The silicon was etched once with ICP-RIE by 110 nm, followed by masking of the grating couplers and an identical etch to form fully etched channel waveguides elsewhere on the chip. The SiO_2 hard-mask was then removed via dilute HF, and the die was subjected to low-temperature wet oxidation at 400°C for 1.5 hours to passivate the silicon surface with a ~3 nm thin oxide layer (this is discussed further in Section 3.A). Next, the metal electrodes with a gap of 8.5 µm were patterned via standard photolithography and liftoff of a 20 nm thin chromium adhesion layer followed by 216 nm of gold. Finally, the metal contacts were subjected to rapid thermal annealing at a temperature of 400°C for 30 s. A scanning electron micrograph of a finished sample is shown in Fig. 4, as well as optical micrographs of another sample in Fig. 5.

3. RESULTS AND DISCUSSION

A. Passive and Low-Frequency Characterization

The SiLN measurement setup is depicted in Fig. 6. A 2 mW continuous-wave helium–neon (HeNe) laser operating at 3.39 µm was used as the mid-IR source, coupled in through a fiber with an 18 µm core diameter at the input and coupled out through a large-area 400 µm core fiber to ease the alignment process. The output light was detected by a lead selenide (PbSe) detector with a specified bandwidth in the 10 kHz range. The light was chopped and then processed through a lock-in amplifier initially, but the chopper was removed once good fiber-to-grating coupler alignment was achieved.

First, the waveguide linear propagation loss was characterized. Straight waveguides 5.6 mm long were placed next to
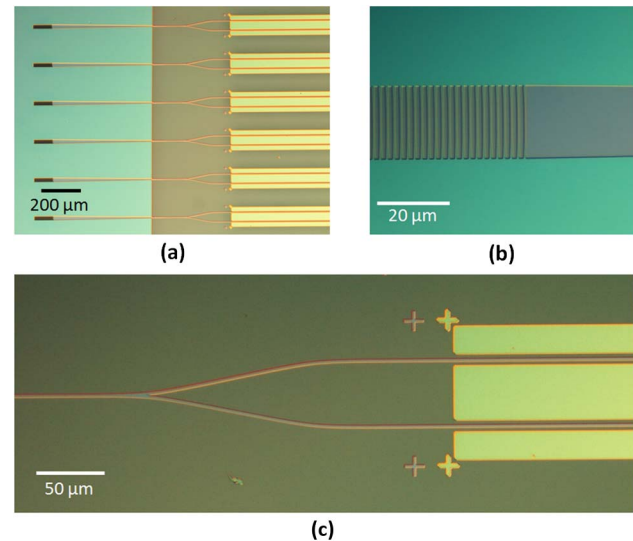
compact spiral waveguides which were 5.1 mm longer, using a bending radius of 300 µm. A propagation loss of 2.5 ± 0.7 dB/cm for the transverse electric mode is obtained by the cutback method after measuring two pairs of such waveguides. The loss figure presented is most likely not a consequence of etching-induced sidewall roughness, estimated here to be <50 nm rms, since the waveguides presented are relatively wide and measurements of earlier-produced half-etched SiLN waveguides yielded similar losses of 3–4 dB/cm. The loss may be due to contamination at the waveguide surface. The measurement wavelength of 3.39 µm exhibits strong optical absorption with hydrocarbons, which could affect the surface of the waveguide that is exposed to air during measurements. The 400°C wet oxidation step was crucial to reducing the propagation loss. Waveguides fabricated without this step exhibit propagation losses above 10 dB/cm. The mechanism of loss reduction is thought to be the passivation of dangling bonds at the silicon surface, reducing its adsorption of contaminants. Ultimately, the contamination-induced loss may be
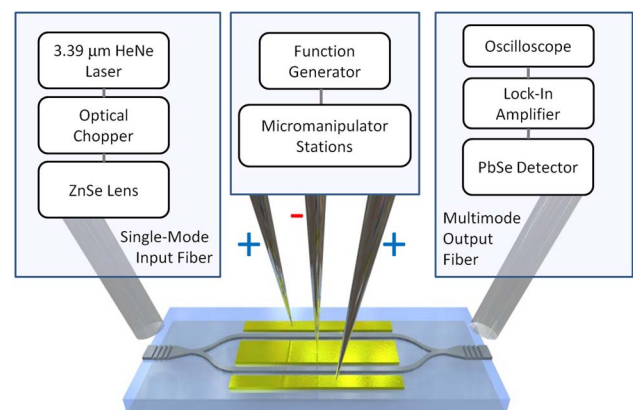
**Fig. 6.** Measurement setup used for characterization.
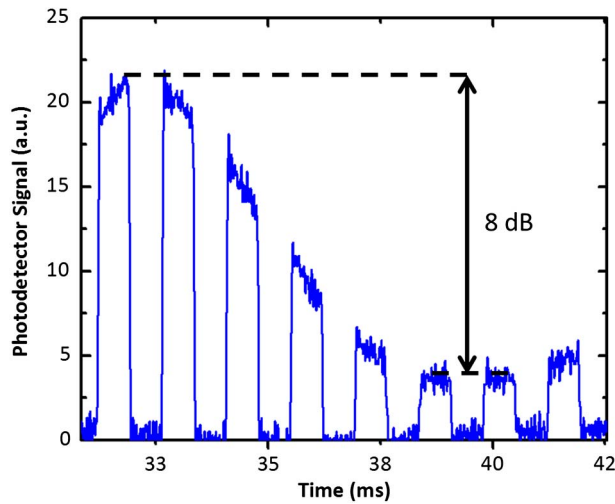
Fig. 7. Transmission through the device during simultaneous optical chopping at 700 Hz and optical modulation at 70 Hz. The photodetector signal (blue data line) has been shifted to emphasize the envelope.

Fig. 8. SiLN modulator response. The red line is the modulator drive voltage divided by a factor of 20, and the blue line is the optical signal transmitted through the modulator, shifted for visibility. The inset shows the frequency response, limited by the detector speed.

mitigated with use of mid-IR compatible cladding materials such as chalcogenide glasses [32] deposited on the waveguide surface, or by hermetic packaging of the devices in an inert atmosphere.

Next, the modulators were characterized to determine the extinction ratio. The modulators were contacted with microprobes as shown in Fig. 6. A triangle-waveform voltage was applied to the modulator at 1/10 the frequency of the 700 Hz optical chopper used in the setup. Consequently, the square-wave chopper signal acquired a sinusoidal modulation envelope. By comparing the square-wave amplitude at the minimum and maximum of this envelope, we were able to obtain an AC characterization of the extinction ratio (Fig. 7). The chopper is necessary in this setup to obtain the relative values of maxima to minima. The measured extinction ratio is ~8 dB, which is lower than that predicted in Section 2.A. This can be attributed to an intensity mismatch between the two arms in the interferometer, probably resulting from small isolated interfacial bonding defects at the Si-LiNbO$_3$ interface. By using commercial vacuum wafer bonding systems, the density of these defects can be greatly reduced, resulting in higher-quality surfaces and better device performance.

The total on-chip insertion loss of the particular modulator under consideration was determined by comparing its unmodulated transmission to that of a straight waveguide of the same length. In addition to the modulator's propagation loss of 1.4 dB, an excess loss of 1.9 dB was observed. This can be attributed to several sources, such as point defects present in the lithography on that particular device, imperfections in the nanotip of the Y junction splitter, and increased metal electrode proximity resulting from an alignment error of 1 μm. Because of the close proximity of the standalone straight waveguides and the modulators, the coupling loss is nearly identical (verified by repeated measurements) and thus factored out. The on-chip insertion loss of the modulator is measured to be 3.3 ± 0.7 dB.
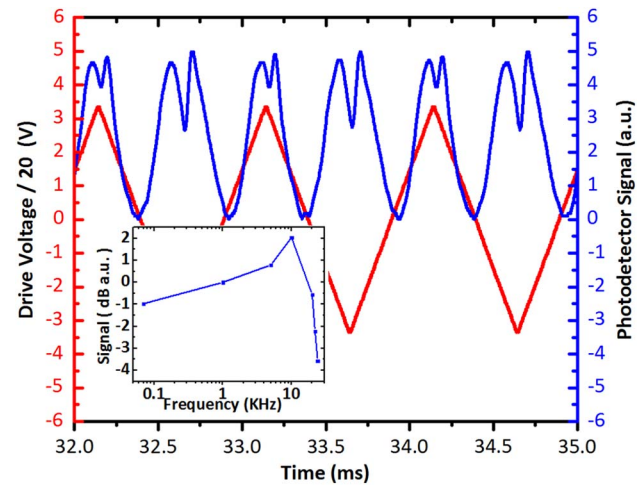
B. AC Modulation

The measurement of the half-wave voltage-length product, $V_\pi \cdot L$, was performed at 1 kHz (Fig. 8). The modulator was also measured out to the limit of the photodetector's bandwidth at 23 kHz (inset of Fig. 8), revealing an uneven frequency response of the detector at its limit. The slight distortion in the peaks of the signal is due to this behavior. The modulation speed measured in this experiment was limited by the speed of the detector available. With faster detectors and probes, and with travelling-wave electrode design, high-speed performance (>10 GHz bandwidth) mid-IR modulators are in principle feasible similar to conventional near-IR LiNbO$_3$ devices. Finally, to rule out the possibility of leakage effects and heating-induced phase changes, a multimeter was inserted into the voltage drive circuit, but no current flow was detected (sensitivity limit was 0.1 μA), indicating negligible power consumption at low frequencies.

The obtained $V_\pi \cdot L$ value from the modulation response is 26 V · cm, which is larger than the 13 V · cm value predicted in simulations. This difference is most likely not a result of dispersion in the r_{33} coefficient (which is negligible) [22]. One possible explanation could be the well-known phenomenon of domain realignment in LiNbO$_3$ after exposure to high-energy electron beams [33] such as the one used in pattern writing. Accordingly, the domains underneath the waveguide could be misaligned with respect to the polarization axis, causing a lowered effective electro-optic coefficient. Future studies with photolithography-patterned devices can investigate this possibility in order to resolve the discrepancy between measured and simulated values of $V_\pi \cdot L$.

4. CONCLUSION

In this work, we have demonstrated optical modulation in the mid-IR range on the proposed SiLN platform, utilizing the Pockels effect. A maximum modulation frequency of 23 kHz was observed (limited only by the detector speed), with an

extinction ratio of ~8 dB, an on-chip insertion loss of 3.3 dB, and a $V_\pi \cdot L$ of 26 V·cm, at a measurement wavelength of 3.39 µm. In addition, optical waveguides were characterized on the SiLN platform in the mid-IR, showing low TE-mode propagation losses of 2.5 dB/cm. With its compact waveguides, high electro-optic sensitivity, and strong second-order nonlinearities, this platform will enable high-performance photonic chips to be created for mid-IR applications.

REFERENCES

1. R. Soref, "Mid-infrared photonics in silicon and germanium," Nat. Photonics **4**, 495–497 (2010).
2. B. Jalali and S. Fathpour, "Silicon photonics," J. Lightwave Technol. **24**, 4600–4615 (2006).
3. R. A. Soref, S. J. Emelett, and W. R. Buchwald, "Silicon waveguided components for the long-wave infrared region," J. Opt. A **8**, 840–848 (2006).
4. T. Baehr-Jones, A. Spott, R. Ilic, A. Spott, B. Penkov, W. Asher, and M. Hochberg, "Silicon-on-sapphire integrated waveguides for the mid-infrared," Opt. Express **18**, 12127–12135 (2010).
5. R. Shankar, I. Bulu, and M. Lončar, "Integrated high-quality factor silicon-on-sapphire ring resonators for the mid-infrared," Appl. Phys. Lett. **102**, 051108 (2013).
6. S. Khan, J. Chiles, J. Ma, and S. Fathpour, "Silicon-on-nitride waveguides for mid- and near-infrared integrated photonics," Appl. Phys. Lett. **102**, 121104 (2013).
7. J. Chiles, S. Khan, J. Ma, and S. Fathpour, "High-contrast, all-silicon waveguiding platform for ultra-broadband mid-infrared photonics," Appl. Phys. Lett. **103**, 151106 (2013).
8. H.-K. Hsiao, K. A. Winick, J. D. Monnier, and J.-P. Berger, "An infrared integrated optic astronomical beam combiner for stellar interferometry at 3-4 µm," Opt. Express **17**, 18489–18500 (2009).
9. B. Jalali, V. Raghunathan, R. Shori, S. Fathpour, D. Dimitropoulos, and O. Stafsudd, "Prospects for silicon mid-IR Raman lasers," IEEE J. Sel. Top. Quantum Electron. **12**, 1618–1627 (2006).
10. D. Borlaug, S. Fathpour, and B. Jalali, "Extreme value statistics in silicon photonics," IEEE Photon. J. **1**, 33–39 (2009).
11. R. K. W. Lau, M. R. E. Lamont, A. G. Griffith, Y. Okawachi, M. Lipson, and A. L. Gaeta, "Octave-spanning mid-infrared supercontinuum generation in silicon nanowaveguides," Opt. Lett. **39**, 4518–4521 (2014).
12. B. Kuyken, P. Verheyen, P. Tannouri, X. Liu, J. Van Campenhout, R. Baets, W. M. J. Green, and G. Roelkens, "Generation of 3.6 µm radiation and telecom-band amplification by four-wave mixing in a silicon waveguide with normal group velocity dispersion," Opt. Lett. **39**, 1349–1352 (2014).
13. A. Densmore, S. Janz, R. Ma, J. H. Schmid, D.-X. Xu, A. Delâge, J. Lapointe, M. Vachon, and P. Cheben, "Compact and low power thermo-optic switch using folded silicon waveguides," Opt. Express **17**, 10457 (2009).
14. M. Nedeljkovic, S. Stankovic, C. J. Mitchell, A. Z. Khokhar, S. A. Reynolds, D. J. Thomson, F. Y. Gardes, C. G. Littlejohns, G. T. Reed, and G. Z. Mashanovich, "Mid-infrared thermo-optic modulators in SoI," IEEE Photon. Technol. Lett. **26**, 1352–1355 (2014).
15. R. Soref and J. Larenzo, "All-silicon active and passive guided-wave components for λ = 1.3 and 1.6 µm," IEEE J. Quantum Electron. **22**, 873–879 (1986).
16. X. Tu, T.-Y. Liow, J. Song, X. Luo, Q. Fang, M. Yu, and G.-Q. Lo, "50-Gb/s silicon optical modulator with traveling-wave electrodes," Opt. Express **21**, 12776–12782 (2013).
17. D. J. Thomson, F. Y. Gardes, S. Liu, H. Porte, L. Zimmermann, J.-M. Fedeli, Y. Hu, M. Nedeljkovic, X. Yang, P. Petropoulos, and G. Z. Mashanovich, "High performance Mach–Zehnder-based silicon optical modulators," IEEE J. Sel. Top. Quantum Electron. **19**, 85–94 (2013).
18. M. Nedeljkovic, R. Soref, and G. Z. Mashanovich, "Free-carrier electrorefraction and electroabsorption modulation predictions for silicon over the 1–14-µm infrared wavelength range," IEEE Photon. J. **3**, 1171–1180 (2011).
19. B. Chmielak, M. Waldow, C. Matheisen, C. Ripperda, J. Bolten, T. Wahlbrink, M. Nagel, F. Merget, and H. Kurz, "Pockels effect based fully integrated, strained silicon electro-optic modulator," Opt. Express **19**, 17212–17219 (2011).
20. R. Palmer, S. Koeber, D. L. Elder, M. Woessner, W. Heni, D. Korn, M. Lauermann, W. Bogaerts, L. Dalton, W. Freude, J. Leuthold, and C. Koos, "High-speed, low drive-voltage silicon-organic hybrid modulator based on a binary-chromophore electro-optic material," J. Lightwave Technol. **32**, 2726–2734 (2014).
21. K. Noguchi, O. Mitomi, and H. Miyazawa, "Millimeter-wave Ti:LiNbO₃ optical modulators," J. Lightwave Technol. **16**, 615–619 (1998).
22. R. A. Becker, R. H. Rediker, and T. A. Lind, "Wide-bandwidth guided-wave electro-optic intensity modulator at λ = 3.39 µm," Appl. Phys. Lett. **46**, 809–811 (1985).
23. Y. S. Lee, G.-D. Kim, W.-J. Kim, S.-S. Lee, W.-G. Lee, and W. H. Steier, "Hybrid Si-LiNbO₃ microring electro-optically tunable resonators for active photonic devices," Opt. Lett. **36**, 1119–1121 (2011).
24. L. Chen, Q. Xu, M. G. Wood, and R. M. Reano, "Hybrid silicon and lithium niobate electro-optical ring modulator," Optica **1**, 112–118 (2014).
25. M. Solmaz and C. K. Madsen, "Silicon-on-lithium niobate waveguides for mid-infrared, " Proc. SPIE **6386**, 63860F (2006).
26. L. Cao, A. Aboketaf, Z. Wang, and S. Preble, "Hybrid amorphous silicon (a-Si:H)–LiNbO₃ electro-optic modulator," Opt. Commun. **330**, 40–44 (2014).
27. U. D. Dave, S. Uvin, B. Kuyken, S. Selvaraja, F. Leo, and G. Roelkens, "Telecom to mid-infrared spanning supercontinuum generation in hydrogenated amorphous silicon waveguides using a thulium doped fiber laser pump source," Opt. Express **21**, 32032–32039 (2013).
28. P. Rabiei, J. Ma, S. Khan, J. Chiles, and S. Fathpour, "Heterogeneous lithium niobate photonics on silicon substrates," Opt. Express **21**, 25573–25581 (2013).
29. J. Chiles and S. Fathpour, "Silicon on lithium niobate: A hybrid electro-optical platform for near- and mid-infrared photonics," in *Conference on Lasers and Electro-Optics*, OSA Technical Digest (online) (Optical Society of America, 2014), paper STh1M.6.
30. E. L. Wooten, K. M. Kissa, A. Yi-Yan, E. J. Murphy, D. A. Lafaw, P. F. Hallemeier, D. Maack, D. V. Attanasio, D. J. Fritz, G. J. McBrien, and D. E. Bossi, "A review of lithium niobate modulators for fiber-optic communications systems," IEEE J. Sel. Top. Quantum Electron. **6**, 69–82 (2000).
31. M. M. R. Howlader, T. Suga, and M. J. Kim, "Room temperature bonding of silicon and lithium niobate," Appl. Phys. Lett. **89**, 031914 (2006).
32. H. Lin, L. Li, Y. Zou, S. Danto, J. D. Musgraves, K. Richardson, S. Kozacik, M. Murakowski, D. Prather, P. T. Lin, V. Singh, A. Agarwal, L. C. Kimerling, and J. Hu, "Demonstration of high-Q mid-infrared chalcogenide glass-on-silicon resonators," Opt. Lett. **38**, 1470–1472 (2013).
33. H. Ito, C. Takyu, and H. Inaba, "Fabrication of periodic domain grating in LiNbO₃ by electron beam writing for application of nonlinear optical processes," Electron. Lett. **27**, 1221–1222 (1991).

optica

Ultra-high-efficiency metamaterial polarizer

Bing Shen,[1] Peng Wang,[1] Randy Polson,[2] and Rajesh Menon[1,*]

[1]Department of Electrical and Computer Engineering, University of Utah, Salt Lake City, Utah 84112, USA

[2]Utah Nanofabrication Facility, University of Utah, Salt Lake City, Utah 84112, USA

*Corresponding author: rmenon@eng.utah.edu

Conventional polarizers operate by rejecting undesired polarization, which limits their transmission efficiency to much less than 50% when illuminated by unpolarized light. We designed, fabricated, and characterized a multilevel metamaterial linear polarizer that rotates light with polarization perpendicular to its principal axis by 90 deg. Light with polarization parallel to its principal axis is transmitted undisturbed. Thereby, such a polarizer is able to output linearly polarized light from unpolarized input with a transmission efficiency that is substantially higher than the theoretical upper limit of 50%. A nonlinear optimization algorithm was used to design the polarizer, while multilevel focused-ion-beam lithography was used to fabricate it in silicon for the vacuum wavelength, $\lambda_0 = 1550$ nm. We experimentally confirmed that the fabricated device enhances the transmission of the desired linear polarization by 100% compared to an unpatterned film, corresponding to a transmission efficiency of ~74% at the design wavelength. Since our method allows for the generalized manipulation of the amplitude, phase, and polarization of light with high transmission efficiency using ultrathin elements, it should enable the efficient generation of complex vector distributions of light.   © 2014 Optical Society of America

OCIS codes: (350.4238) Nanophotonics and photonic crystals; (050.1970) Diffractive optics; (350.3950) Micro-optics.

http://dx.doi.org/10.1364/OPTICA.1.000356

1. INTRODUCTION

Manipulation of the polarization of light is extremely important for a variety of applications ranging from communications [1] to imaging [2–4]. Conventional polarization selection devices (or polarizers) use absorption or reflection to discard the unwanted polarization [5]. In these polarizers, the maximum achievable transmission efficiency of the desired polarization is 50%. Commercial polarizers typically demonstrate transmission efficiencies that are lower [6]. In this article, we apply a new approach to designing a metamaterial polarizer that rotates one polarization by 90 deg, while the orthogonal polarization is transmitted undisturbed. Thereby, such a polarizer allows for substantially higher transmission efficiencies in the desired polarization. Furthermore, we show that our design methodology is applicable to metamaterials in general, and could enable unique and diverse photonic functions in lossless dielectric substrates.

Most conventional polarizers are based upon form birefringence [7] or total internal reflection effects in crystals or polymers, which cause phase retardation between the two orthogonal polarizations. Recently, a variety of novel approaches to polarization rotation have been proposed. Some of these employ surface gratings, whose scattering vectors are different from the polarization state of the incident light to achieve polarization manipulation [8,9]. Other devices achieve polarization manipulation using metasurfaces, i.e., carefully designed antennae that impart an abrupt phase change at an interface [10–12]. An alternative approach is to use subwavelength structures to manipulate polarization across a wavefront (inhomogeneous polarization) [13]. Polarization-manipulation devices have been utilized for a variety of applications [14–17]. Recently, these ideas have been generalized by combining conventional computer-generated holography [18] with subwavelength control for manipulation of the phase, amplitude, and polarization of light [19,20]. Related work described optical transmission by reflectionless metasurfaces. Polarization rotation of zero-order transmitted light through a perforated metal film was also recently demonstrated [21]. Experimental
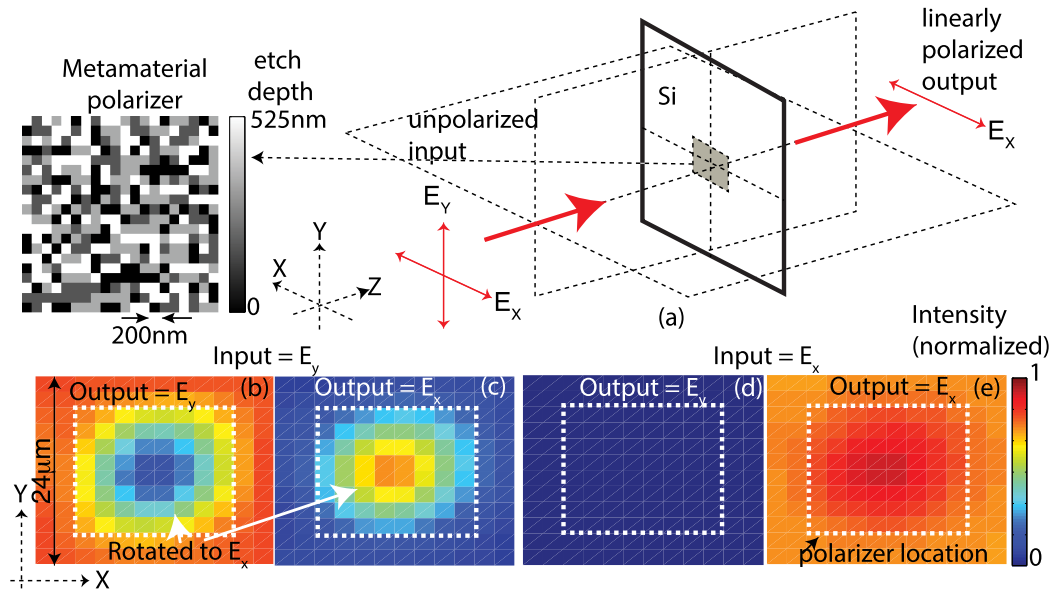
Fig. 1. (a) High-efficiency metamaterial polarizer. The design (left) is composed of etched square pixels in silicon. (b)–(e) Simulated light intensity distributions after transmission through the polarizer for (b) E_y and (c) E_x under E_y input and for (d) E_y and (e) E_x for E_x input. The white dashed lines in (b)–(e) indicate the boundaries of the finite device (Media 2, Media 3, Media 4, Media 5, Media 6, Media 7, Media 8, Media 9, Media 10, Media 11, Media 12, Media 13, Media 14, Media 15, Media 16, Media 17, Media 18, Media 19).

demonstration in the microwave regime was also given [22,23]. These approaches utilize metallic antennae on a single surface, which suffer from parasitic absorption. Nevertheless, only one polarization is manipulated in all previous devices, resulting in less than 50% transmission efficiency, when illuminated by both polarizations.

In contrast, our device is based upon an all-dielectric material that is patterned at subwavelength dimensions so as to enable independent manipulation of both polarizations. To illustrate the principle, we designed, fabricated, and characterized a metamaterial polarizer that operates by allowing one polarization to transmit undisturbed while rotating the orthogonal polarization.

2. DESIGN

Our design goal is to determine the etch depth of each pixel such that a desired phase, amplitude, and polarization distribution of light is obtained upon transmission through the device. We constrained our pixel size to 200 nm × 200 nm to enable fabrication. For computational expediency, we limited the device size to 20 × 20 pixels, corresponding to a total dimension of 4 μm × 4 μm. Furthermore, periodic boundary conditions were applied along the X and Y directions that allowed the unit to be repeated in 2D. We also constrained the maximum aspect ratio for ease of fabrication (Supplement 1).

The design was performed by a modified version of the direct-binary-search (DBS) algorithm. Previously, we have successfully utilized this algorithm to design nanophotonic light-trapping geometries [24,25] as well as broadband nonimaging diffractive optics [26–28]. Details of the algorithm are included in Supplement 1. Here, our optimization variables are the etch depths of each of the 200 nm × 200 nm pixels in our device. The algorithm attempts to maximize a figure of merit, which

we define as the transmission efficiency at the desired polarization (E_x in Fig. 1), when the polarizer is illuminated by both polarizations (E_x and E_y) with equal amplitude. The optimized design is shown on the top left of Fig. 1(a). Although the design was performed using periodic boundary conditions, our fabricated device was composed of 4 × 4 unit cells (total size of 16 μm × 16 μm). In other words, the polarizer was surrounded by unpatterned silicon. We simulated the performance of this fabricated device and summarized the results in Figs. 1(b)–1(e) (see Supplement 1). When illuminated by collimated linearly polarized light with polarization along the Y axis (E_y source), the output light intensity in E_y decreases [Fig. 1(b)], while that in E_x increases as shown in Fig. 1(c). In other words, the input field oriented along the Y axis after propagation through the polarizer is substantially rotated such that it is oriented along the X axis. On the other hand, when the device is illuminated with light polarized along the X axis (E_x source), it transmits mostly undisturbed as shown in Figs. 1(d) and 1(e). Small perturbations of the fields in the output are due to diffraction at the boundary of the polarizer, where the periodic boundary conditions are not satisfied. Spatial nonuniformity of the transmitted fields is expected, since the unit cell does not exhibit any symmetry. We further confirmed using simulations that only 13% of the incident light is reflected, while 74% of the incident light is transmitted into the desired E_x polarization (Supplement 1). Compared to the surrounding unpatterned silicon, the transmission of E_x is enhanced by 110%, and the ratio of the transmitted power at E_x to that at E_y at the output is calculated to be 8.8.

3. EXPERIMENTS

The device was fabricated by etching into silicon using focused-ion-beam lithography using gallium ions. Different etch depths are achieved by varying the deposited energy or
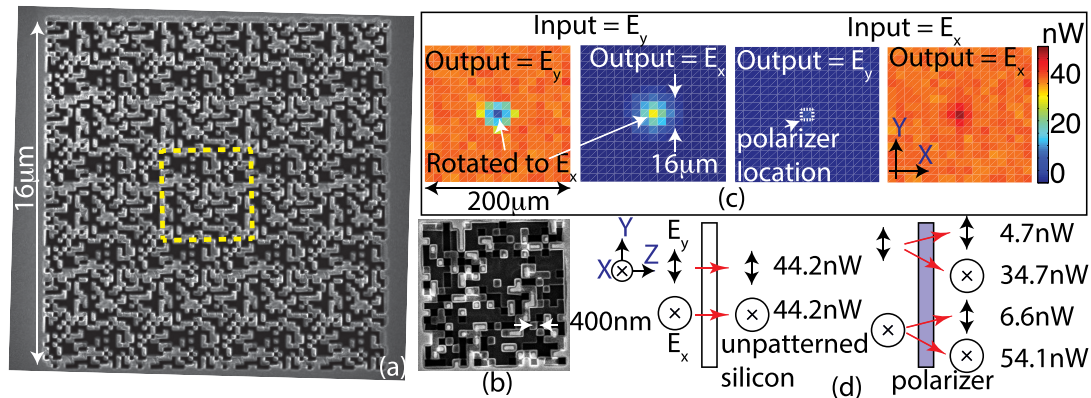
Fig. 2. (a) Scanning-electron micrograph of the metamaterial polarizer. One unit cell is 4 μm × 4 μm (yellow dashed lines). (b) Magnified view shows pixels with a period of 400 nm. (c) Measured transmitted power as a function of position in the X–Y plane. The left two images correspond to the E_y source, while the right two images correspond to the E_x source. Within the device area (dashed white square), E_y is rotated to E_x. (d) Comparison of the measured peak transmitted power in E_x and E_y between unpatterned silicon and the metamaterial polarizer.

exposure dose at each location (see Supplement 1). Figure 2(a) shows the scanning-electron micrograph of a fabricated device composed of 4 × 4 unit cells, where each unit cell is 4 μm × 4 μm (denoted by dashed yellow lines). A magnified view of one unit cell in Fig. 2(b) shows the multiple etch depths and the square pixels.

In order to characterize the polarizer, we illuminated it with collimated linearly polarized light from a 1550 nm laser (Hewlett Packard model No. 8168E). The transmitted power was measured using a lens and a photodetector from a spot of size 14 μm on the sample (Fig. S2 of Supplement 1). A conventional polarizer was placed at the output to measure the power at the two orthogonal polarizations separately. A half-wave plate and a polarizer were used at the input to first align the direction of polarization to the Y axis of the metamaterial polarizer. Then, the device was stepped in the X–Y plane using a stage, while the photodetector registered the transmitted signal. The resulting image is shown in Fig. 2(c). The dashed white square shows the location of the metamaterial polarizer. Behind the device, the power in the E_x polarization is dramatically increased while that in the E_y polarization is correspondingly reduced. The experiment was repeated after aligning the incident polarization to the X axis of our polarizer. As shown in Fig. 2(c), the transmitted power is almost entirely in the E_x polarization, since the electric field oriented along the X axis is transmitted undisturbed. Figure 2(d) schematically compares the transmitted power between the metamaterial polarizer and unpatterned silicon. When illuminated by both polarizations, the metamaterial polarizer transmits a total of 88.8 nW in E_x compared to just 44.2 nW for unpatterned silicon. This increase is primarily due to the incident power in E_y being rotated 90 deg into E_x upon transmission. The measured results agree well with the simulated enhancement of 110%. The measured ratio of the transmitted power at E_x to that at E_y at the output is 7.8, which agrees with the simulated value of 8.8.

4. DISCUSSION OF RESULTS

It has been reported that polarization rotation occurs when the scattering vector is different from the polarization of the incident light [8,9]. The scattering structure, defined by our design, consists of a large number of locally varying scattering vectors. The scattering vectors vary with position not only in the planes perpendicular to the propagation direction but also along the propagation direction. The transmitted light after the metamaterial polarizer is the superposition of light scattered from all these elements. The optimization process is thus attempting to create a distribution of scattering vectors such that the cumulative effect after transmission is that one polarization state (E_x) is allowed to pass through with low loss, while the orthogonal polarization state (E_y) is rotated by 90 deg. We analyzed the electric fields within the device and show that the rotation of the E_y modes is primarily due to the near-field coupling between multiple resonant-guided modes that are excited upon illumination, similar to what has been reported in photonic crystals [29,30]. By analyzing the time-averaged intensity distribution in each layer of our device (see Fig. S10 of Supplement 1), we can readily show that when illuminated by a source polarized along the Y axis, dipoles that are polarized along the X axis are excited at the corners of each isolated pillar in the first layer. Such dipoles then couple energy into the structures in the adjacent layers of the metamaterial polarizer. Eventually, the last (third) layer of the polarizer radiates energy into the far field, still maintaining the polarization along the X axis. This is further confirmed by analyzing the time-dependent field variation in the X–Z and Y–Z planes in the vicinity of the hot spots as discussed in Supplement 1 and as illustrated in Media 2–19.

It is interesting to note that there is an apparent decrease in entropy due to the conversion of randomly polarized input light into linearly polarized output with high efficiency [31]. This is not really true, since the decrease of the polarization degree of freedom is accompanied by a larger increase in the spatial frequencies of the output wavefront. In other words, although the incident light is collimated, the transmitted light radiates in multiple directions (see Fig. S10 of Supplement 1).

We also performed careful analysis of the tolerance of the metamaterial polarizer to fabrication errors (Supplement 1). We show that the devices are robust to fabrication errors
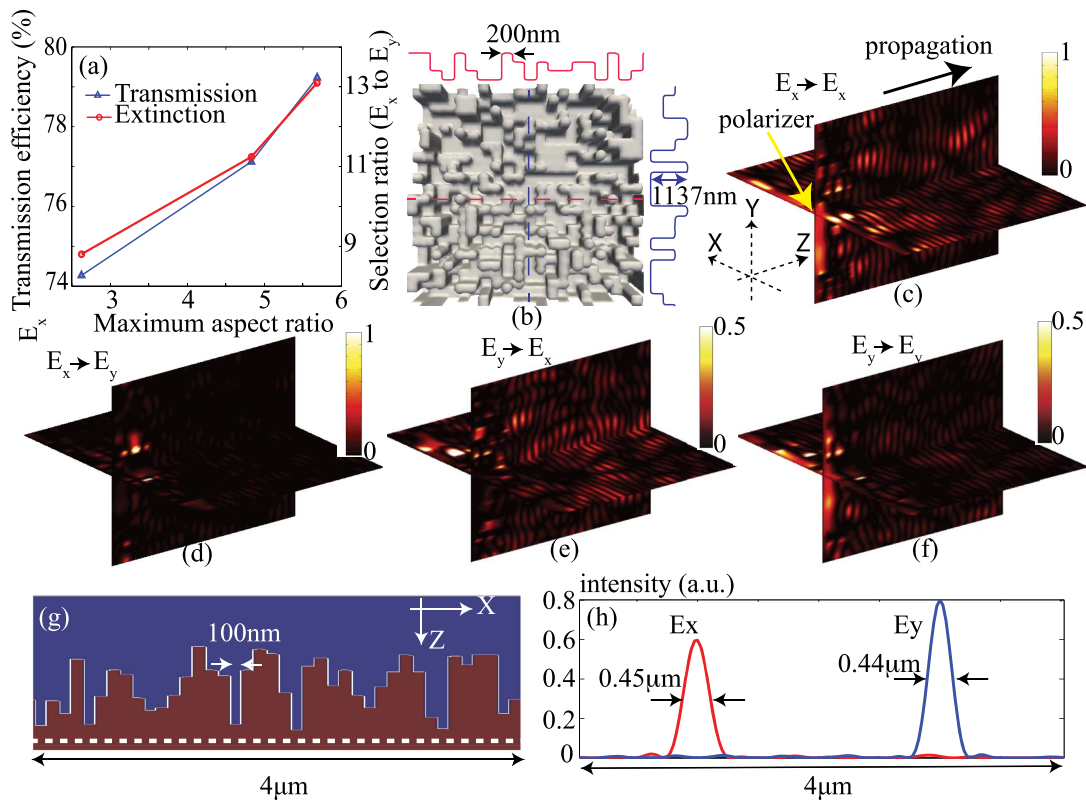
Fig. 3. (a) Transmission efficiency (at E_x) and selection ratio (power in E_x to power in E_y) as a function of maximum aspect ratio. (b) Device with transmission efficiency of 80% and maximum aspect ratio of 5.7. (c)–(f) Time-averaged intensity distributions after the device for (c), (d) E_x source and (e), (f) E_y source. The polarizer is located in the X–Y plane at the left edge. (g) 2D device designed for polarization separation and focusing. (h) Intensity distribution along the dashed white line in (g) when the device is illuminated by E_x and E_y simultaneously.

corresponding to about 8% of the pixel size. Small slopes in the sidewalls of the pixels also introduce only minor changes to the performance of the device. Although our device was designed for a single wavelength, we calculated the bandwidth to be ~20 nm (see Fig. S3 of Supplement 1). By incorporating a broadband source during design, it is possible to increase the device bandwidth further.

In order to ensure ease of fabrication, we applied a constraint on the maximum aspect ratio (defined as the ratio of the maximum etch depth to the pixel size). For the fabricated device, the maximum aspect ratio was 2.6. We performed a series of designs with higher maximum aspect ratios and realized that the performance of the device can be enhanced. Figure 3(a) shows the transmission efficiency at E_x and the selection ratio (power in E_x to power in E_y) as a function of the maximum aspect ratio. As the aspect ratio is increased, the transmission efficiency at E_x under unpolarized input can increase to almost 80%. The design for a maximum aspect ratio of 5.7 is shown in Fig. 3(b). The simulated electric-field distributions in the X–Z and Y–Z planes after transmission through the metamaterial polarizer are shown in Figs. 3(c) and 3(d) for the E_x source, and in Figs. 3(e) and 3(f) for the E_y source. Figures 3(c) and 3(e) show the electric-field distributions polarized along X, while Figs. 3(d) and 3(f) show the electric-field distributions polarized along Y. As expected, the polarizer rotates the incident E_y fields into E_x at the output, while the incident E_x fields transmit undisturbed. Note that no

attempt was made to control amplitude in this case, and, hence, the transmitted intensity shows nonuniformity in the X–Y plane.

As we mentioned earlier, our design can be extended to control the phase, amplitude, and polarization of light. To demonstrate this capability, we designed a device that spatially separates and localizes fields according to their polarization in the plane normal to the direction of propagation (Supplement 1). In order to simplify the computation, this device was designed in 2D, and the optimized design is illustrated in Fig. 3(g). When this device is illuminated by an unpolarized source from above propagating from top to bottom, the electric fields are spatially separated along the X axis as shown by the intensity distributions in Fig. 3(h). The input field was uniform along the X axis for both polarizations. However, at the output, E_x becomes confined to a 0.45-µm-wide region on the left half (red line), while E_y is confined to a 0.44-µm-wide region on the right half (blue line). Note that this polarization separation is achieved within a propagation distance of only 1500 nm (less than the free-space wavelength of 1550 nm).

5. CONCLUSION

We designed, fabricated, and characterized a new metamaterial polarizer that rotates one polarization by 90 deg, while allowing the orthogonal polarization to transmit unperturbed.

We experimentally showed that this polarizer is able to enhance the transmission of one polarization by 100% compared to an unpatterned film. Appropriate design of these devices can achieve absolute transmission efficiencies at one desired polarization of almost 80% at the design wavelength (1.55 μm). Our approach is readily generalized to manipulate the phase, amplitude, and polarization state of electromagnetic fields at the subwavelength scale. The demonstrated device could have significant implications in imaging systems and displays (when extended to visible wavelengths). Although the extinction ratio for our device is smaller than conventional polarizers, the metamaterial polarizer could be useful where transmission efficiency is particularly important. Other interesting applications include the ability to efficiently generate complex modes that may be useful in quantum entanglement [32] and expanded bandwidth in telecommunications [33].

REFERENCES

1. J. N. Damask, *Polarization Optics in Telecommunications* (Springer, 2004).
2. D. S. Kliger, J. W. Lewis, and C. E. Randall, *Polarized Light in Optics and Spectroscopy* (Academic, 1990).
3. V. V. Tuchin, L. V. Wang, and D. A. Zimnyako, *Optical Polarization in Biomedical Applications* (Springer, 2006).
4. Y. P. Svirko and N. I. Zheludev, *Polarization of Light in Nonlinear Optics* (Wiley, 1998).
5. S. W. Ahn, K. D. Lee, J. S. Kim, S. H. Kim, J. D. Park, S. H. Lee, and P. W. Yoon, "Fabrication of a 50 nm half-pitch wire grid polarizer using nanoimprint lithography," Nanotechnology **16**, 1874–1877 (2005).
6. Commercial polarizers in Thorlabs, http://www.thorlabs.us/newgrouppage9.cfm?objectgroup_id=4984.
7. R. C. Tyan, A. A. Salvekar, H. P. Chou, C. C. Cheng, A. Scherer, P. C. Sun, F. Xu, and Y. Fainman, "Design, fabrication, and characterization of form-birefringent multilayer polarizing beam splitter," J. Opt. Soc. Am. A **14**, 1627–1636 (1997).
8. N. K. Grady, J. E. Heyes, D. R. Chowdhury, Y. Zeng, M. T. Reiten, A. K. Azad, A. J. Taylor, D. A. R. Dalvit, and H. T. Chen, "Terahertz metamaterials for linear polarization conversion and anomalous refraction," Science **340**, 1304–1307 (2013).
9. J. Elliott, I. I. Smolyaninov, N. I. Zheludev, and A. V. Zayats, "Polarization control of optical transmission of a periodic array of elliptical nanoholes in a metal film," Opt. Lett. **29**, 1414–1416 (2004).
10. Y. N. Fang, P. Genevet, M. A. Kats, F. Aieta, J. P. Tetienne, F. Capasso, and Z. Gaburro, "Light propagation with phase discontinuities: generalized laws of reflection and refraction," Science **334**, 333–337 (2011).
11. F. Aieta, P. Genevet, N. Yu, M. A. Kats, Z. Gaburro, and F. Capasso, "Out-of-plane reflection and refraction of light by anisotropic optical antenna metasurfaces with phase discontinuities," Nano Lett. **12**, 1702–1706 (2012).
12. N. Yu, F. Aieta, P. Genevet, M. A. Kats, Z. Gaburro, and F. Capasso, "A broadband, background-free quarter-wave plate based on plasmonic metasurfaces," Nano Lett. **12**, 6328–6333 (2012).
13. S. Pancharatnam, "Generalized theory of interference, and its applications," Proc. Ind. Acad. Sci. A **44**, 247–262 (1956).
14. A. Niv, G. Biener, V. Kleiner, and E. Hasman, "Spiral phase elements obtained by use of discrete space-variant subwavelength gratings," Opt. Commun. **251**, 306–314 (2005).
15. A. Niv, G. Biener, V. Kleiner, and E. Hasman, "Propagation-invariant vectorial Bessel beams obtained by use of quantized Pancharatnam–Berry phase optical elements," Opt. Lett. **29**, 238–240 (2004).
16. G. Biener, A. Niv, V. Kleiner, and E. Hasman, "Geometrical phase image encryption obtained with space-variant subwavelength grating," Opt. Lett. **30**, 1096–1098 (2005).
17. G. Biener, A. Niv, V. Kleiner, and E. Hasman, "Near-field Fourier transform polarimetry by use of a quantized space-variant subwavelength grating," J. Opt. Soc. Am. A **20**, 1940–1948 (2003).
18. P. Hariharan, *Optical Holography: Principles, Techniques and Applications* (Cambridge University, 1996).
19. J. Lin, P. Genevet, M. A. Kats, N. Antoniou, and F. Capasso, "Nano-structured holograms for broadband manipulation of vector beams," Nano Lett. **13**, 4269–4274 (2013).
20. X. Ni, A. V. Kildishev, and V. M. Shalaev, "Metasurface holograms for visible light," Nat. Commun. **4**, 1–6 (2013).
21. S. Wu, Z. Zhang, Y. Zhang, K. Zhang, L. Zhou, X. Zhang, and Y. Y. Zhu, "Enhanced rotation of the polarization of a light beam transmitted through a silver film with an array of perforated S-shaped holes," Phys. Rev. Lett. **110**, 207401 (2013).
22. C. Pfeiffer and A. Grbic, "Metamaterial Huygens' surfaces: tailoring wave fronts with reflectionless sheets," Phys. Rev. Lett. **110**, 197401 (2013).
23. F. Monticone, N. M. Estakhri, and A. Alu, "Full control of nanoscale optical transmission with a composite metascreen," Phys. Rev. Lett. **110**, 203903 (2013).
24. P. Wang and R. Menon, "Optimization of generalized dielectric nanostructures for enhanced light trapping in thin-film photovoltaics via boosting the local density of optical states," Opt. Express **22**, A99–A110 (2014).
25. P. Wang and R. Menon, "Optimization of periodic nanostructures for enhanced light-trapping in ultra-thin photovoltaics," Opt. Express **21**, 6274–6285 (2013).
26. G. Kim, J. A. Dominguez-Caballero, and R. Menon, "Design and analysis of multi-wavelength diffractive optics," Opt. Express **20**, 2814–2823 (2012).
27. G. Kim, J. A. Dominguez-Caballero, H. Lee, D. Friedman, and R. Menon, "Increased photovoltaic power output via diffractive spectrum separation," Phys. Rev. Lett. **110**, 123901 (2013).
28. P. Wang and R. Menon, "Three-dimensional lithography via digital holography," in *Frontiers in Optics 2012/Laser Science XXVIII*, OSA Technical Digest (online) (Optical Society of America, 2012), paper FTu3A.4.
29. V. Liu, D. A. B. Miller, and S. Fan, "Ultra-compact photonic crystal waveguide spatial mode converter and its connection to the optical diode effect," Opt. Express **20**, 28388–28397 (2012).
30. J. Lu and J. Vučković, "Objective-first design of high-efficiency, small-footprint couplers between arbitrary nanophotonic waveguide modes," Opt. Express **20**, 7221–7236 (2012).
31. C. Brosseau, *Fundamentals of Polarized Light: A Statistical Optics Approach* (Wiley, 1998).
32. S. Franke-Arnold, L. Allen, and M. Padgett, "Advances in optical angular momentum," Laser Photonics Rev. **2**, 299–313 (2008).
33. N. Bozinovic, Y. Yue, Y. Ren, M. Tur, P. Kristensen, H. Huang, A. E. Willner, and S. Ramachandran, "Terabit-scale orbital angular momentum mode division multiplexing in fibers," Science **340**, 1545–1548 (2013).